NONLINEAR VIBRATION ANALYSIS OF A ROTOR-HYDRODYNAMIC BEARING SYSTEM: GEAR AND THERMAL BOW-INDUCED VIBRATION

A Dissertation

by

DONGIL SHIN

Submitted to the Office of Graduate and Professional Studies of
Texas A&M University
in partial fulfillment of the requirements for the degree of

DOCTOR OF PHILOSOPHY

Chair of Committee,	Alan B. Palazzolo
Committee Members,	Steve Suh
	Won-Jong Kim
	Moo-Hyun Kim
Head of Department,	Andreas A. Polycarpou

December 2020

Major Subject: Mechanical Engineering

ABSTRACT

This dissertation presents a novel approach for modeling and analyzing a geared rotor-bearing system including nonlinear forces in the gear set and the supporting fluid film journal bearings. Co-existing, steady-state, autonomous and non-autonomous responses are obtained in an accurate and computationally efficient manner utilizing the multiple shooting and continuation algorithms. The results reveal a dependence of the gear set contact conditions and system nonlinear response characteristics, i.e. jump, co-existing responses, subharmonic resonances and chaos on the choice of journal bearing parameters.

The Morton effect (ME) is caused by uneven viscous heating of the journal in a fluid film bearing, which causes thermal bending, especially in rotors with an overhung disc or coupling weight. This work investigates the influence of misaligned journal bearing effects on the thermally induced rotor instability problem. The simulation results indicate that the amplitude of the misalignment angle affects the instability speed range caused by the Morton effect under certain conditions.

This work also treats the unconventional application of the SFD for the mitigation of ME-induced vibration. Installing a properly designed squeeze film damper may change the rotor’s critical speed location, damping and deflection shape, and thereby suppress the vibration caused by the ME. The effectiveness of the SFD on suppressing the ME is tested via linear and nonlinear simulation studies. The influence of SFD cage stiffness is evaluated.

The influence of tilting pad journal bearing's pivot design on the severity and instability speed range of the ME vibration was investigated. The friction between pad and pivot, which only exists in the spherical pivot, is taken into account and its impact on the ME is also tested. Nonlinear transient simulations are carried out for a wide operating speed range with varying pivot design parameters. Simulation results indicate that the predicted ME instability is sensitive to the pivot shape, pivot flexibility, and pad-pivot friction.

The Morton effect test rig was built, and its vibration test results are presented. The vibration increases of the rotor at constant operating speed reveals that the existence of the Morton effect in the designed rotor-bearing test rig.

DEDICATION

To God who knows all things and my wife Hannah and my son Isaac

ACKNOWLEDGEMENTS

I would like to thank Dr. Palazzolo for his advising and support throughout the course of my Ph.D. degree at Texas A&M University. I also thank my committee members, Dr. Steve Shu, Dr. Won-Jong Kim and, Dr. Moo-Hyun Kim for their guidance and advising for this research.

I also thank my colleagues in the lab and the department faculty and staff for making my time at Texas A&M university an invaluable experience. I also thank the Turbomachinery Research Consortium for their financial support throughout my Ph.D. degree.

I also want to extend my gratitude to my parents and parents in law for their support, love and patience.

Finally, thanks to my wife, Hannah for her patience and support. Thanks to my son, Isaac.

CONTRIBUTORS AND FUNDING SOURCES

Contributors

This work was supervised by a dissertation committee consisting of Professor Dr. Alan B. Palazzolo and Professor Steve Suh and Professor Won-Jong Kim of the Department of Mechanical engineering and Professor Moo-Hyun Kim of the Department of Ocean engineering.

Xiaomeng Tong from Texas A&M University suggested an idea for the work in section 4. Works presented in section 6 have been conducted with Anthony Hresko and Jongin Yang from Texas A&M University. All other works conducted for the dissertation were completed independently by the student.

Funding Sources

The dissertation research was supported by the TRC (Turbomachinery Research Consortium) of Texas A&M University.

TABLE OF CONTENTS

Page

ABSTRACT ii

DEDICATION iv

ACKNOWLEDGEMENTS v

CONTRIBUTORS AND FUNDING SOURCES vi

TABLE OF CONTENTS vii

LIST OF FIGURES x

LIST OF TABLES xviii

1. INTRODUCTION 1

  1.1. Nonlinear vibration induced by gear nonlinearities 1
  1.2. Thermal bow induced vibration (Morton effect) of rotor-bearing system 6
    1.2.1. Journal misalignment effect on rotordynamics 8
    1.2.2. Squeeze film damper suppression of rotor vibration 9
    1.2.3. Tilting pad pivot friction effect on Morton effect 11

2. NONLINEAR ANALYSIS OF A GEARED ROTOR SYSTEM SUPPORTED BY FLUID FILM JOURNAL BEARINGS 14

  2.1. Introduction 14
  2.2. Modeling of a geared rotor system supported by fluid film journal bearings 15
    2.2.1. Five-degree-of-freedom gear-bearing-rotor model 15
    2.2.2. Finite element model of plain journal bearing 23
  2.3. Nonlinear steady-state solution methods 26
    2.3.1. Multiple shooting method 26
    2.3.2. Arc-length continuation 28
    2.3.3. Stability identification based on the shooting method 30
    2.3.4. Lyapunov exponents for identifying chaos 30
  2.4. Numerical example 32
    2.4.1. Parametric resonances and jump phenomenon 33
    2.4.2. Chaotic response 47
    2.4.3. Effect of gear mesh stiffness on oil whirl 54

3. TILTING PAD JOURNAL BEARING MISALIGNMENT EFFECT ON THERMALLY INDUCED SYNCHRONOUS INSTABILITY (MORTON EFFECT) 61

- 3.1. Introduction 61
- 3.2. Modeling and ME prediction algorithms 61
    - 3.2.1. Tilting pad journal bearings 61
    - 3.2.2. Thermal model – 3D energy equation 68
    - 3.2.3. Thermal deformation of the shaft and bearing 69
    - 3.2.4. Thermal boundary conditions on the shaft and pads 70
    - 3.2.5. Rotor dynamic model 71
- 3.3. Morton effect computation algorithm 73
- 3.4. Simulation results 76
    - 3.4.1. Effect of misalignment ratio 95
    - 3.4.2. Effect of different pad-pivot types 99

4. SQUEEZE FILM DAMPER SUPPRESSION OF THERMAL BOW – MORTON EFFECT INSTABILITY 103

- 4.1. Introduction 103
- 4.2. Modeling and ME prediction algorithms 104
    - 4.2.1. Centrally grooved squeeze film damper 104
    - 4.2.2. Tilting pad journal bearing model 108
    - 4.2.3. Thermal models 109
    - 4.2.4. Flexible rotor with SFD in series with a TPJB 112
    - 4.2.5. Morton effect prediction algorithm 114
- 4.3. Simulation results 115
    - 4.3.1. Linear analysis 117
    - 4.3.2. Morton effect benchmark simulation 125
    - 4.3.3. Effects of SFD at different cage stiffness 131
    - 4.3.4. Comparison between with and without SFD 137

5. TILTING PAD PIVOT FRICTION AND DESIGN EFFECTS ON THERMALLY INDUCED VIBRATION (MORTON EFFECT) 141

- 5.1. Introduction 141
- 5.2. Rotor-bearing modeling 142
    - 5.2.1. Pad-pivot design 142
    - 5.2.2. Reynolds and energy equations 146
    - 5.2.3. TPJB and flexible rotor dynamic equations 148
- 5.3. Simulation results 150
    - 5.3.1. Linear analysis 152
    - 5.3.2. Effect of pivot geometry 154
    - 5.3.3. Effect of pivot stiffness 158

5.3.4. Effect of pivot friction 164

6. MORTON EFFECT EXPERIMENTAL RIG BUILDING AND TESTING 172

6.1. Introduction 172
6.2. Test rig building and analysis.. 173
6.3. Vibration measurement 183

7. CONCLUSIONS 194

REFERENCES 200

LIST OF FIGURES

Page

Figure 2.1 Gear set supported by hydrodynamic journal bearings..................................16

Figure 2.2 Spur gear pair model including hydrodynamic journal bearing 16

Figure 2.3 Comparison of dynamic transmission error with experimental measurements in [4] (reprinted from [34]) 22

Figure 2.4 Axial mid-plane section of a journal bearing...23

Figure 2.5 Mesh and boundary conditions for finite element journal bearing film model 25

Figure 2.6 Pseudo arc-length continuation method..29

Figure 2.7 Effect of backlash (a) peak-peak displacement of DTE (b) time response at 2,000 rpm 35

Figure 2.8 Effect of (a) applied torque and (b) bearing L/D ratio on the peak-peak displacement of DTE through the fundamental resonance (solid line: stable, dotted line: unstable) 36

Figure 2.9 Bifurcation diagrams of (a) 1,000 Nm torque and (b) 1,500 Nm torque cases in Figure 2.8 (a)..38

Figure 2.10 Effect of lubricant viscosity on the peak-peak response of DTE (a) Bearing L/D = 0.3 and (b) Bearing L/D = 1 (solid line: stable, dotted line: unstable)..39

Figure 2.11 Effect of bearing clearance on the peak-peak response of DTE (a) Bearing L/D = 0.3 and (b) Bearing L/D = 1 (solid line: stable, dotted line: unstable)..40

Figure 2.12 Multiple co-existing responses using the shooting method (L/D = 1, $\boldsymbol{\mu} =$ 90 mPa s, T_1=1,500 N m). (a) Frequency-amplitude diagram (b) Phase portrait at 1,850 rpm (Solid line: stable, dotted line: unstable) 41

Figure 2.13 Co-existing mesh deformation $\rho(t)$ responses: (a) Response 1 (b) Response 4 (c) Response 5 42

Figure 2.14 Repelling motion of the unstable orbit (response 2) at fundamental resonance region (a) Response 2 → Response 1 (b) Response 2 → Response 3 (solid line: stable, dotted line: unstable) 43

Figure 2.15 Effect of (a) applied torque and (b) bearing L/D ratio on the peak-peak response of DTE of subharmonic resonance (solid line: stable, dotted line: unstable) 44

Figure 2.16 Waterfall diagrams (a) 750 N m Torque, run-up, (b) 750 N m Torque, run-down, (c) L/D = 0.6, run-up, (d) L/D = 0.6, run-down 45

Figure 2.17 Effect of (a) lubricant viscosity and (b) bearing clearance on the peak-peak response of DTE for subharmonic resonance (solid line: stable, dotted line: unstable) 46

Figure 2.18 Time response of multiple co-existing response of DTE (a) Response 1, (b) Response 2, (c) Response 3 47

Figure 2.19 Bifurcation diagrams vs. operating speed for varying parameter values (a) applied torque (100 , 1,000 and 2,000 N m) (b) lubricant viscosity (10, 40 and 70 mPa s) , and (c) Bearing clearance (74, 105 and 184 μm) 48

Figure 2.20 Bifurcation diagrams and Poincaré attractors at different speeds, for a lubricant viscosity 40 mPa s case in Fig. 19 (b) 50

Figure 2.21 Bifurcation and MLE diagrams vs. (a) applied torque (0~2,400 N m), (b) bearing clearance (60 ~185 μm) and (c) lubricant viscosity (5 ~90 mPa s) 51

Figure 2.22 Frequency spectra, phase portraits and Poincaré attractors of dynamic transmission error (DTE) for different bearing clearances (a) 80 μm (b) 74 μm (c) 61 μm in Figure 2.21 (b) 53

Figure 2.23 Run-up and run-down simulations using direct numerical integration (a) mesh stiffness 1e7 N/m (b) mesh stiffness 1e9 N/m 55

Figure 2.24 Bifurcation diagram using shooting/continuation method with mesh stiffness 1e7 N/m and applied torque 1,000 N m: (a) Bifurcation diagram using continuation algorithm, (b) result from continuation algorithm compared with numerical integration, (c) revolution speed versus response frequency and (d) zoom of (c) 56

Figure 2.25 Bifurcation diagrams with various mesh stiffness values (1e7, 1e8 and 1e9 N/m) and with an applied torque of 1,000 N m 58

Figure 3.1 (a) Model for journal dynamics and (b) Thermal expansion of pad/shaft......63

Figure 3.2 Permanent misalignment angle α_y 65

Figure 3.3 Configuration of journal misalignment phase directions (a) $r_\alpha = 90°$ and (b) $r_\alpha = 270°$ 66

Figure 3.4 Spherical pad-pivot type tilting pad dynamic model......................................67

Figure 3.5 Diagram illustrating the HFEM rotor structural model 69

Figure 3.6 Thermal boundary conditions on rotor and bearing surfaces 70

Figure 3.7 Algorithm for Morton effect transient simulation 73

Figure 3.8 Example rotor-bearing configuration...76

Figure 3.9 Rotor 1 (a) imbalance response amplitude and phase lag, and (b) mode shape of the third critical speed at 6,343 rpm..79

Figure 3.10 Rotor 1’s damped unbalance responses for aligned and misaligned cases...81

Figure 3.11 Comparison of Rotor 1 (a) pk-pk vibration at the NDE bearing position and (b) minimum film thickness ratio 82

Figure 3.12 Comparison of (a) peak journal $\boldsymbol{\Delta T}$ and (b) pk-pk vibration amplitude vs. rpm and axial position for the Rotor 1 case 84

Figure 3.13 Comparison of (a) pk-pk vibration at NDE bearing position and (b) minimum film thickness ratio for Rotor 2 case 85

Figure 3.14 Comparison of (a) peak journal $\boldsymbol{\Delta T}$ and (b) pk-pk vibration amplitude vs. rpm and axial position for the Rotor 2 case 86

Figure 3.15 Effects of misalignment on (a) 1x polar plot, (b) pk-pk vibration at NDE bearing position, (b) Film thickness ratio and (d) journal $\boldsymbol{\Delta T}$ of Rotor 1 case at 6,120rpm 87

Figure 3.16 Effect of misalignment on (a) 1x polar plot, (b) pk-pk vibration at NDE bearing position, (b) Film thickness ratio and (d) journal $\boldsymbol{\Delta T}$, and (e)&(f) FFT of pk-pk vibration at NDE bearing position of Rotor 1 case at 6,570rpm..89

Figure 3.17 Responses at 6,750 rpm: (a) High and hot spot phase angles, (b) Phase lag angle of hot spot behind high spot, (c) Journal surface temperature distribution at three different times 91

Figure 3.18 Comparison of (a) temperature distribution at bearing mid-plane, (b) thermal bow and (c) shaft thermal expansion ratio, at 6,570rpm, for the aligned (left) and misaligned (right) cases 93

Figure 3.19 Pad film thickness distribution at 6,570rpm (a) aligned journal and (b) misaligned $r_m = \mathbf{0.3}$, $r_\alpha = \mathbf{90}°$ 94

Figure 3.20 Comparison of (a) pk-pk vibration at NDE bearing position of Rotor 1, (b) minimum film thickness ratio of Rotor 1 (c) pk-pk vibration at NDE bearing position of Rotor 2, (d) minimum film thickness ratio of Rotor 2 with different misalignment ratio 96

Figure 3.21 Comparison of (a) peak journal $\boldsymbol{\Delta T}$ and (b) minimum film thickness ratio across rotor axial positions for Rotor case 2 with different misalignment ratios 97

Figure 3.22 Comparison of (a) film thickness ratio of Rotor 1, (b) pk-pk vibration at NDE bearing position of Rotor 1, (c) thermal bow of Rotor 1, (d) 1x polar plot with $r_m = \mathbf{0.1}$, $r_\alpha = \mathbf{90}°$, (e) 1x polar plot with $r_m = \mathbf{0.2}$, $r_\alpha = \mathbf{90}°$, (f) 1x polar plot with $r_m = \mathbf{0.3}$, $r_\alpha = \mathbf{90}°$ at 6,570 rpm 98

Figure 3.23 Comparison of (a) peak journal $\boldsymbol{\Delta T}$ and (b) pk-pk vibration amplitude for aligned and misaligned journals, for Rotor 1 with spherical pad-pivot model 100

Figure 3.24 Comparison of cylindrical and spherical pivot model (a) peak journal $\boldsymbol{\Delta T}$ and (b) pk-pk 1x vibration polar plot of Rotor 1 case, at 6,570 rpm 101

Figure 3.25 Comparison of pad rolling motions of spherical pivot-type model for (a) aligned journal, (b) misaligned journal ($r_m = \mathbf{0.3}$, $r_\alpha = \mathbf{90}°$), and (c) film thickness distribution of misaligned journal $r_m = \mathbf{0.3}$, $r_\alpha = \mathbf{90}°$ of Rotor 1 case at 6,570 rpm 102

Figure 4.1 Axial mid-plane of SFD 104

Figure 4.2 Comparison of (a) damping and (b) added mass coefficient with reference [69] (adapted from [69]) 106

Figure 4.3 Schematics of series combination of TPJB and SFD and SFD groove geometry (not to scale) 107

Figure 4.4 Thermal boundary conditions on TPJB pads and shaft outer surfaces 110

Figure 4.5 Example rotor-bearing-SFD configuration 112

Figure 4.6 Morton effect prediction algorithm...114

Figure 4.7 Campbell diagram of rotors with SFD and without SFD (No SFD indicates rigidly mounted TPJB) 117

Figure 4.8 Bending mode of the example rotor at 7,644 rpm 118

Figure 4.9 Distribution of unbalance response amplitudes along the length of the rotor for with and without SFD cases (No SFD indicates rigidly mounted TPJB) 119

Figure 4.10 Linear analysis: Damped first forward critical speed and TPJB housing eccentricity ratio 119

Figure 4.11 Linear analysis: damping ratio and damping coefficient change with different SFD cage stiffness...120

Figure 4.12 Linear analysis: Unbalance response (a) pk-pk vibration amplitude at Rotor end node (b) pk-pk vibration amplitude at bearing node......................121

Figure 4.13 Nonlinear transient simulation result of journal surface ΔT at steady state condition with different cage stiffness (without thermal bow effect) 122

Figure 4.14 Linear analysis with SFD parameter variation (radial clearance and lubricant viscosity) (a) damping ratio of rotor, (b) damping coefficient of SFD, (c) Damped first forward critical speed, (d) added mass coefficient of SFD..123

Figure 4.15 Distribution of unbalance response amplitudes along the length of the rotor for different SFD parameters (No SFD indicates rigidly mounted TPJB) 124

Figure 4.16 Nonlinear steady-state simulation: pk-pk vibration amplitude vs. rpm at the bearing node with different SFD parameter sets..................................125

Figure 4.17 Nonlinear steady-state simulation: pk-pk vibration amplitude vs. rpm at bearing node..125

Figure 4.18 Nonlinear steady-state simulation: Comparison of (a) journal surface ΔT and (b) pk-pk vibration amplitude vs. rpm and rotor axial position (with thermal bow effect) 127

Figure 4.19 Nonlinear transient simulation: 1X filtered polar plot at 8,000 and 8,500 rpm (with thermal bow effect) 128

Figure 4.20 Nonlinear transient simulation: journal surface peak-peak ΔT at 8,000 and 8,500 rpm (with and without thermal bow effect) 130

Figure 4.21 Nonlinear transient simulation: temperature distribution at bearing mid-plane of the with thermal bow case at 8,500 rpm after 25 minutes 131

Figure 4.22 Nonlinear steady-state simulation: pk-pk vibration amplitude vs. rpm at bearing node with different cage stiffness 132

Figure 4.23 Nonlinear transient simulation: 1X polar plot at critical speed with different cage stiffness 133

Figure 4.24 Nonlinear transient simulation: 3D orbit shapes at critical speed after 25 minutes with different cage stiffness 134

Figure 4.25 Nonlinear transient simulation: thermal bow of shaft at critical speed after 25 minutes with different cage stiffness 134

Figure 4.26 Nonlinear transient simulation: (a) pk-pk vibration amplitude vs. rpm at bearing node at critical speed after 25 minutes (b) zoom of (a) 135

Figure 4.27 Nonlinear transient simulation: (a) pk-pk vibration amplitude (b) SFD damping and added inertia force from Case 3 at critical speed 137

Figure 4.28 Nonlinear transient simulation: hot spot location change with time at critical speed (No SFD indicates rigidly mounted TPJB) 139

Figure 4.29 Nonlinear transient simulation: temperature distribution at bearing mid-plane at 25 minutes with SFD 140

Figure 5.1 (a) Schematic of cylindrical type pad-pivot (b) Schematic of spherical type pad-pivot 142

Figure 5.2 Friction mechanism between pad and pivot 144

Figure 5.3 Schematics of journal and pad dynamics 146

Figure 5.4 Schematics of rotor and bearing configurations 150

Figure 5.5 Linear unbalance responses and pivot stiffness of cylindrical and spherical pivots 152

Figure 5.6 Steady-state ME simulations with rigid pivot from 7,500 rpm to 9,500 rpm (a) Minimum film thickness ratio (b) pk-pk vibration amplitude at rotor end (node 19) 154

Figure 5.7 Transient ME simulation at 8,600rpm (a) 1X polar plot at journal location (b) minimum film thickness ratio of TPJB (c) pad pitching angular displacement (d) pk-pk Journal ΔT 155

Figure 5.8 Journal temperature at 8,600 rpm (4 minute 32 seconds) (a) spherical pivot (b) cylindrical pivot 157

Figure 5.9 Steady-state ME simulations with rigid and flexible pivots from 7,000 rpm to 9,500 rpm (a) Minimum film thickness ratio (b) pk-pk vibration amplitude at journal 158

Figure 5.10 Steady-state ME simulations of pk-pk journal ΔT from 7,000 rpm to 9,500 rpm (a) spherical type with rigid pivot (b) spherical type with flexible pivot 160

Figure 5.11 Transient ME simulation at 7,700 rpm and 8,600 rpm (a) 1X polar plot at 7,700 rpm (b) k-pk Journal ΔT at 7,700 rpm (c) 1X polar plot at 8,600 rpm (d) pk-pk Journal ΔT at 8,600 rpm 161

Figure 5.12 Pivot stiffness at 7,700 rpm with time (a) cylindrical pivot (b) spherical pivot 162

Figure 5.13 Transient ME simulation at 7,700 rpm (a) pk-pk vibration amplitude across rotor axial direction for 30 minute (b) temperature distribution of bearing mid-plane at 30 min 163

Figure 5.14 Steady-state ME simulations of pk-pk vibration amplitude at journal with different pivot friction coefficients (a) spherical type with rigid pivot (b) spherical type with flexible pivot 164

Figure 5.15 Transient ME simulation of rigid pivot at 8,600 rpm (a) 1X polar plot (b) pk-pk Journal ΔT 166

Figure 5.16 Steady-state ME simulations of flexible pivot: pk-pk journal ΔT across rotor axial direction (a) no friction (b) friction coefficient 0.4 167

Figure 5.17 Transient ME simulation at 7,700 rpm and 7,900 rpm (a) 1X polar plot at 7,700 rpm (b) pk-pk Journal ΔT at 7,700 rpm (c) 1X polar plot at 7,900 rpm (d) pk-pk Journal ΔT at 7,900 rpm 168

Figure 5.18 Transient simulation results at 7,900rpm after 40 minutes (a) 3D orbits of rotor (b) thermal bow amplitude with different friction coefficients (c) phase lag between hot and high spots (d) temperature distribution at bearing mid-plane of FC 0.4 170

Figure 6.1 Morton effect test rig and Tilting pad journal bearing 173

Figure 6.2 Schematic of an axisymmetric shaft-disk model 174

Figure 6.3 Stress calculations at 6,000 rpm (a) Von Mises stress (b) hoop stress (c) radial stress 177

Figure 6.4 (a) Photo of test rig shaft for free-free mode testing (b) shaft model based on ANSYS APDL 177

Figure 6.5 Comparison of first three mode shapes between Euler beam and ANSYS APDL 179

Figure 6.6 Measured shaft position from 240 rpm to 3,600 rpm 181

Figure 6.7 (a) Installation of RTD sensors on the shaft and (b) RTD numbering at journal mid-plane 182

Figure 6.8 Measured journal temperatures at (a) 3,000 rpm and (b) 4,200 rpm operating speed 183

Figure 6.9 (a) Rotor vibration amplitude and (b) temperatures of oil for the first test (4,800 rpm) 185

Figure 6.10 (a) Bode (overhung end) and (b) 1x polar (bearing outboard X) plots for the first test (4,800 rpm) 186

Figure 6.11 (a) Rotor vibration amplitude and (b) temperatures of oil for the second test (5,640 rpm) 187

Figure 6.12 (a) Bode (overhung end) and (b) 1x polar (bearing outboard X) plots for the second test (5,640 rpm) 188

Figure 6.13 1x polar (bearing outboard X) plots at 5,640 rpm 189

Figure 6.14 (a) comparison between experimental measurements and simulation results (b) zoom of (a) 191

Figure 6.15 Simulated rotor vibration at each rotor node with time 192

LIST OF TABLES

Page

Table 2.1 Comparison of calculated natural frequencies with [93] (adapted from [93])........22

Table 2.2 Parameters of the spur gear pair and journal bearings........33

Table 2.3 Oil whirl onset speed with different torque and mesh stiffness........59

Table 3.1 Parameter values for the example system........78

Table 3.2 Instability speed range (ISR) with different misalignment ratio ($r_m = \sqrt{r_x^2 + r_y^2}$ in Figure 3.2)........96

Table 4.1 Thermal boundary conditions on pad and shaft........111

Table 4.2 Parameter values for the example system........116

Table 4.3 Phase lag between high and hot spots (Case 1: no thermal bow and no SFD, Case 2: with thermal bow and no SFD, Case 3: with thermal bow and with SFD)........138

Table 5.1 Parameter values for the example system........151

Table 6.1 Maximum stresses and safety factor at 0 rpm........175

Table 6.2 Maximum speed without disk separation........176

Table 6.3 Comparison of calculated free-free modes........178

Table 6.4 Vibration amplitude and phase of test rig after balancing........180

Table 6.5 Parameters of Morton effect test rig........184

Table 6.6 Vibration amplitude and phase changes at 5,640 rpm........190

1. INTRODUCTION

1.1. Nonlinear vibration induced by gear nonlinearities

Gearing system speeds and operating torques continue to increase in high-performance machinery. This amplifies the effects of nonlinearities in the gears including tooth backlash and time-varying mesh stiffness. Backlash describes the intentional clearance provided between mating teeth to prevent binding and to include a thin lubricant film between the teeth for heat removal and reduced wear. Backlash causes intermittent loss of contact between the teeth creating a nonlinear force and torque. The mesh stiffness varies periodically with time due to the variation of the number of tooth pairs in contact, and the variation of the point of contact along with the tooth profiles. The time-varying stiffness of the meshing teeth may lead to parametric resonances, which are principal sources of internal excitations and vibrations in gear transmission systems. The backlash forces and time-varying stiffness interact yielding a complex nonlinear, parametrically excited system with both torsional and lateral vibration. Accurate and computationally efficient gear dynamic models, including nonlinear forces and parametric excitations, are required for the effective design of gear sets and the machinery in which they form a critical component.

Significant prior research has been performed on the nonlinear dynamic response of geared systems. Kahraman and Singh [1] analyzed the effect of backlash on a single-degree-of-freedom gear model employing both analytical and numerical simulations.

They validated their model by comparison with experimental results and found that the nonlinear characteristics caused chaotic and subsynchronous resonance responses. Kahraman and Singh [2] examined interactions between gear backlash nonlinearity and the bearing clearances and identified chaotic and subharmonic responses. Kahraman and Singh [3] included time-varying stiffness and clearance nonlinearity in their numerical model of geared systems and identified strong coupling effects between these characteristics. Blankenship and Kahraman [4] presented an experimental – analytical correlation study of a geared system including backlash nonlinearity and parametric excitation. Their predictions of co-existing solutions with the harmonic balance method were confirmed experimentally. Kahraman and Blankenship [5] observed subharmonic resonances in a geared system experiment, which were demonstrated to be strongly dependent on damping ratio and stiffness variation of the gear mesh. Kahraman and Blankenship [6] experimentally observed chaotic vibration, jump phenomena, and subharmonic response due to parametric and backlash excitations. Ranghothama and Narayanan [7] employed an incremental harmonic balance method, arc-length continuation, Floquet theory, and Lyapunov exponents to examine the bifurcation characteristics of a three-degree-of-freedom geared rotor-bearing model. Theodossiades and Natsiavas [8] introduced a new analytical method for a gear system with time-varying stiffness and backlash using perturbations techniques. Al-shyyab and Kahraman [9, 10] investigated the nonlinear response of a multi-mesh gear system using a multi-term harmonic balance method. The effects of gear parameters on the nonlinear behavior were studied for both period-one and sub-harmonic motions. Liu et al. [11] analyzed the effect of gear mesh damping and backlash amplitude on the states of gear meshing and nonlinear behaviors of a gear pair. Yang et al. [12, 13] predicted the nonlinear vibration of a gear system subjected to multi-frequency excitations utilizing a multiple time scales method. They confirmed the interaction between different harmonic excitations and the complex nonlinear behaviors caused by the multi-frequency excitations. Yang et al. [14] performed parametric studies to investigate the influence of the contact ratio, spacing error, transmitted load and mesh damping of a gear using a fifth-order Runge-Kutta method. Wang et al. [15] analyzed the effect of modulation internal excitation on the gear system and verified the accuracy of the prediction by comparing its results with the experimental measurements.

Nonlinear vibration in different types of gears has been investigated. Motahar et al. [16] performed a numerical, nonlinear dynamics study of a bevel gear system. Tip and root modifications were introduced to study their influence on gear vibration. Yang and Lim [17] developed a hypoid gear model considering time varying mesh stiffness, backlash nonlinearity and time-varying bearing stiffness. They showed that the backlash nonlinearity could suppress parametric instability induced by the time-varying bearing stiffness, under certain operating conditions. Wang and Lim [18] studied the effect of gear mesh stiffness asymmetry for the drive and coast sides of the hypoid gear system, and confirmed that the mesh stiffness at the drive side has more significant effect on the nonlinear dynamics. Ambarisha and Parker [19] investigated nonlinear dynamics of a planetary gear system. They applied the profile of the time-varying mesh stiffness obtained from a finite element analysis to improve accuracy. Zhao and Ji [20] performed numerical simulations of a wind turbine gearbox having two planetary gear trains. Complex nonlinear responses of the gearbox were shown to result from a time-varying mesh stiffness, backlash nonlinearity and static transmission error. Xinghui et al. [21] analyzed parametric resonance of a planetary gear subjected to speed fluctuations. The gear model considers time-varying mesh stiffness, and the instability boundaries for the fundamental and combinations resonances were derived based on a perturbation analysis.

Some researchers have explored approaches to suppress vibrations induced by gear nonlinearities. Cheon's [22] simulation study investigated the effect of a one-way clutch to reduce the dynamic transmission error of a geared system. Cheon [23] employed a phasing approach to reduce time-varying mesh stiffness and the resulting vibration, especially at the fundamental resonance.

Stochastic methods have been applied to study the effects of uncertainty in gear parameters. Bonori and Pellicano [24] utilized a stochastic model to analyze the effect of manufacturing error on nonlinear gear dynamics and showed that this could induce chaotic vibrations in the gear system. Wei et al. [25] included modeling uncertainties of a gear system, such as mesh stiffness and damping, and determined the resulting response levels using an interval harmonic balance method.

Various analytical and modeling methods have been applied to gear dynamics simulation. Kim et al. [26] investigated the effect of smoothing functions on clearance nonlinearity of an oscillator and showed how the adjustment of a regulating factor associated with the smoothing functions yielded more reliable predictions. Farshidianfar and Saghafi [27] applied a Melnikov type analysis to investigate homoclinic bifurcations and chaotic responses in a geared system. Gou et al. [28] employed a cell mapping theory to analyze the multi-parameter coupling characteristics of gear parameters. Li et al. [29] used an incremental harmonic balance method to analyze gear systems with internal and external periodic excitations.

Hydrodynamic journal bearings are widely employed in geared systems with high speed and load requirements due to their relatively high stiffness and damping. Theodossiades and Natsiavas [30] investigated the effect of gear and journal bearing parameters on bifurcation, chaos and oil whirl. They represented the journal bearing force with a finite-length impedance method. Baguet and Jacquenot [31] developed a finite element shaft model to study the interactions between a helical gear and a finite-length bearing and showed that a linearized bearing coefficient model does not provide accurate predictions of gear vibrations, especially at high speed and load conditions. Fargère and Velex [32] investigated the effects of the bearing oil inlet location and thermal response on the gear system dynamics. These effects change the journal static equilibrium position, which in turn alters the dynamic response of the system. Liu et al. [33] studied the interactions between tooth wedging effect and journal bearing clearance using the approximate short journal bearing theory. Simulation results showed that varying the operating speed or applied torque may cause the occurrence of oil whirl response of the rotordynamic systems. The effect of tooth wedging on the vibration level of the geared-rotor system is also presented.

Kim and Palazzolo [34, 35] employed shooting with deflation to study the nonlinear response of a Jeffcott rotor supported by floating ring bearings. The effects of changing parameters such as bearing length-to-diameter (L/D) ratio and including the thermal effect of the lubricant were presented. Kim and Palazzolo [36] studied the bifurcation of a heavily loaded rotor with five-pad tilting pad bearings. A shooting/arc-length continuation approach was utilized to obtain quasi-periodic and chaotic motions, the latter being confirmed by maximum Lyapunov exponents.

1.2. Thermal bow induced vibration (Morton effect) of rotor-bearing system

Eccentric, synchronous vibrations in rotating machinery cause asymmetric temperature distribution around the circumference of the journal in a hydrodynamic bearing (HB). This produces thermal bow in the shaft, and under some conditions increasing vibration and inevitable shutdown of the machinery. This “Morton Effect” ME is becoming increasingly observed due to the higher performance requirements of modern machinery and the increasing use of a HB [37]. The ME is the nonlinear synchronous vibration induced by differential viscous shearing of the HB’s lubricant, which gives rise to hot and cold spots on the journal circumference. This increased bow, in particular with overhung rotors, results in larger inertial force and more heating induced by viscous shearing. The viscous shearing, the thermal bow, and the inertial force may form a positive feedback loop, driving the rotor system into a limit cycle vibration, or rubbing between the journal and bearing bushing.

The ME instability phenomenon is highly sensitive to operating and physical parameters [37]. Therefore, even minor changes in parameters and conditions may suppress or induce the ME in the machine. This explains why only a single machine may experience the ME while other “identical” machines operate free from the ME. The axial film thickness asymmetry due to journal misalignment is prevalent in turbomachinery systems due to inevitable installation/manufacturing errors and deflections /distortions caused by applied loads. Therefore, there is a need for the present investigation of the effect of bearing misalignment on the ME, given its known sensitivity to parameter variations.

De Jongh and Hoeven [38] reported an experimental ME case of an overhung rotor showing high vibration levels due to a thermal instability caused by journal differential heating. The instability problem was mitigated by installing a heat barrier sleeve to prevent the heat input into the shaft. Keogh and Morton [39] modeled the journal differential heating with a short bearing theory, iso-viscous, thermo-hydro-dynamic THD model. Lee and Palazzolo [40] developed a ME model based on a variable viscosity Reynolds equation, a 2D energy equation, and a heat conduction equation. Long time-constant, cyclically varying, large amplitude vibration caused by asymmetric journal heating is predicted, using a transient simulation method. Suh and Palazzolo [41-44] developed the first high-fidelity ME prediction model utilizing finite length, 3D thermo-elasto-hydro-dynamic tilting pad journal bearing TPJB models, and performed parametric studies. Tong and Palazzolo [45-47] further expanded the high-fidelity ME model to include distributed thermal bow and a double overhung type rotor configuration. The same authors measured journal circumferential temperature distributions and verified the accuracy of the high-fidelity model, compared with simplified prediction models in [48]. The same authors theoretically showed that the ME can be induced in a gas bearing supported machinery in [49].

1.2.1. Journal misalignment effect on rotordynamics

Misalignment effects on HB have been investigated in many research studies. Bouyer and Fillon [50] presented experimental results for a misaligned plain journal bearing. Their measurements at the bearing mid-plane showed the bearing performance, i.e., maximum pressure, temperature distribution, oil flow rate, and minimum film thickness was significantly affected by misalignment. Sun and Changlin [51] showed that shaft deformation-induced bearing misalignment had a significant effect on bearing performance.

El-Butch and Ashour [52] proposed an improved fidelity, tilting pad journal bearing TPJB, THD model with journal misalignment and pad elastic/thermal distortion effects, which was solved with transient simulation. Sun and Deng [53] showed that thermal and surface roughness effects play a vital role in the performance predictions for a misaligned journal bearing, especially for large eccentricity ratios. Xu and Geng [54] showed that misalignment significantly affects journal bearing performance at large eccentricity ratios, utilizing a THD model. Suh and Choi [55] presented a study on the combined effects of misalignment and tilting pad journal bearing pivot type on static performance. Their theoretical study showed that spherical pivots having tilting, pad yaw and rolling motions, compensates misalignment effects.

1.2.2. Squeeze film damper suppression of rotor vibration

Squeeze film dampers (SFD) are widely used to enhance the stability of a rotor-bearing system and suppress vibration by providing viscous damping. Leader et al. [15] and Edney and Nicholas [56] examined steam turbines experiencing high synchronous vibration and mitigated the vibration utilizing SFD in series with TPJBs. Kanki et al. [57] investigated a steam turbine exhibiting subsynchronous vibration and overcame the instability by installing SFD at the bearing. Ferraro et al. [58] and Ertas et al. [59] adopted an integral squeeze film damper (ISFD) to suppress the subsynchronous vibration of steam turbines. The ISFD alleviated the vibration and provided stable operation of the rotor.

The effects of SFD parameters such as damping properties and cage stiffness on the rotor vibration were presented in the literature. Gunter et al. [60] demonstrated an optimum damping value for rotor-bearing systems, which depends on the rotor’s stiffness ratio between the bearing support and the shaft bending stiffness. Chu and Homes [61] examined the effect of cage stiffness and SFD damping on the location of the critical speed and vibration level, both theoretically and experimentally.

The SFD is commonly equipped with a supply groove for sufficient lubricant flow into the film gap. The added mass induced by the groove has a substantial influence on the dynamic response of a grooved SFD and has been analyzed extensively [62-64]. The force coefficients of SFD with a central groove were experimentally verified in [65-68]. Delgado and San Andres [69, 70] presented a linear fluid inertia bulk flow model for the analysis of the centrally grooved SFD. An effective clearance ratio was adopted based on the measured data from the test rig to replace the actual groove clearance. Linear analysis, which uses linearized stiffness and damping coefficients, maintains its accuracy when the shaft whirling motion is relatively small.

Retrofitting of an existing bearing to install a SFD would depend on the original bearing support structure. Quite often, the bearing housing is cylindrical in shape and slides into a mating hole in the machinery casing. The hole may be split or continuous depending on the design of the machine. Installation of the SFD would then require increasing the bore diameter of the hole to provide for the oil gap of the SFD. In addition, modifications for sealing the SFD with O-rings or by another means or collecting the oil in the case of an open-ended SFD, would be required. This approach will minimize the need for a larger envelope for the bearing modified to include the SFD.

Simulation of a rotor-journal bearing system under a high dynamic loading condition requires a nonlinear simulation for accurate prediction. Bonello et al. [72] studied the interaction between the SFD and flexible rotor based on a harmonic balance method and found that the cavitation effect increases with higher static eccentricity of the SFD and affects the damping capability of the SFD. He [73] utilized an improved harmonic balance method to analyze the flexible rotor with a SFD. Cao et al. [74] simulated the nonlinear short SFD model in series with a fluid film bearing and applied this to a coupled lateral-torsional rotor system. The nonlinear time transient solutions were obtained via the Runge-Kutta method.

1.2.3. Tilting pad pivot friction effect on Morton effect

Suh and Choi [55] conducted a dynamic performance comparison between the spherical and cylindrical pivots under a misaligned journal. The tilt, pitch, and yaw motions of a spherical pivot type ware considered while the cylindrical type only allowed the tilt motion due to its pivot geometry. The spherical pivot showed the invariant bearing performance regardless of the level of misalignment.

The dynamic characteristics of a TPJB are sensitive to its pivot design. The pivot acts as an elastic spring between the pad and housing and significantly alters the bearing characteristics such as lubricant film thickness, eccentricity ratio, etc. Rigid pivot assumption is often used for simplicity of analysis, but this assumption may result in a significant error in the bearing performance prediction. Prior studies [75-79] indicate the importance of considering pivot flexibility for accurate prediction of the TPJB performance. In their analyses, the model with the flexible pivot showed significantly enhanced accuracy than the rigid pivot in predicting the TPJB's static and dynamic characteristics. The analytical model of the TPJB's nonlinear pivot stiffness was derived based on Hertzian contact theory in [80, 81], and the influence of nonlinear pivot stiffness on the dynamic coefficients was investigated in [82]. Shi et al. [83] tested the nonlinear pivot stiffness effect on the dynamic characteristics of a Jeffcott rotor. In the analysis, the nonlinear pivot greatly affected the orbit size of the rotor, lubricant film thickness, and film pressure. The level of the impact was sensitive to the amplitudes of static and dynamic loads applied.

The pad-pivot friction exists in the spherical pivot type TPJB where the pad slides over the pivot surface depending on the journal motion. Many experimental and numerical studies have been carried out regarding the influence of pad-pivot friction. Wygant et al. [84, 85] measured the dynamic coefficients of TPJBs with spherical pivots. The equilibrium position of the bearing showed curved loci along with attitude angles, which confirms the existence of cross-coupled stiffness and damping due to the pad-pivot friction. Pettinato and De Choudhury [86, 87] measured the power loss, pad temperatures, and the equilibrium position of two TPJBs with different pivot types. The equilibrium positions with moderate attitude angles were identified for the spherical pivot TPJB while negligible attitude angles were observed in the cylindrical pivot. Brechting et al. [88] tested the spherical pivot TPJB, and their results showed that the cross-coupled stiffness and damping are present especially at low operating speeds and loads, and those values reduce with increasing speeds. Kim and Kim [89] established a mathematical model for pad-pivot friction and then conducted numerical simulations, verifying that the pivot friction significantly affects the pressure distribution, film thickness of a lubricant, and often induces rotor instability. He [90] adopted a conformal contact model for the prediction of pivot-pad friction. The non-synchronous vibration of pads induced by the friction was observed, and the effect of the pivot radius was investigated. Kim and Palazzolo [91] performed a nonlinear dynamic analysis of a spherical pivot TPJB considering the pad-pivot friction effect. The analytical Stribeck friction model [92] was employed to include the pad angular velocity-dependent friction coefficients. Numerous nonlinear phenomena such as Hopf bifurcation, limit cycles, and non-synchronous vibration appeared in both autonomous and non-autonomous conditions.

2. NONLINEAR ANALYSIS OF A GEARED ROTOR SYSTEM SUPPORTED BY FLUID FILM JOURNAL BEARINGS[*]

2.1. Introduction

Prior models for coupled gearset-bearing vibration generally utilized lower fidelity or steady-state bearing models and presented results in less rigorous nonlinear dynamics formats. This may have been motivated by the high computational expense of employing higher fidelity bearing models and presenting results in advanced nonlinear dynamics formats. Bearing forces were typically represented with linear spring and damping constants, or were obtained using short bearing theory, with highly simplified oil film cavitation models. The simplified approaches may lead to significant prediction error especially for steady-state responses with orbits that are relatively large (>15%) with respect to the bearing clearance. The present approach provides a highly accurate, finite element-based solution of the finite-length, Reynold's equation accounting for cavitation at each time step in the numerical integration. Additionally, results are presented in advanced nonlinear dynamics formats including bifurcation diagrams, maximum Lyapunov exponent plots, and Poincaré attractor plots. Computation time is held within practical limits utilizing multiple shooting and continuation algorithms, and

---

[*] Reprinted with permission from "Nonlinear analysis of a geared rotor system supported by fluid film journal bearings" by Shin, D., and Palazzolo, A., 2020. Journal of sound and vibration, 475, Copyright [2020] by Elsevier B.V.

with the use of embedded C++ components in the MATLAB code, and parallel processing.

The highlight and original contribution of the work is to provide a computationally efficient, high fidelity and rigorously presented modeling approach for the dynamics of the five-degree-of-freedom dual shaft-gear pair system supported on fluid film bearings. This approach involves finite-length bearing models, advanced multiple shooting and continuation methods, gear flexibility and transmission error effects, bifurcation and Poincaré attractor diagrams, and maximum Lyapunov exponents for identifying chaotic behavior. Finally, this approach is applied to parametric studies with varying journal bearing and gear mesh stiffness parameters.

2.2. Modeling of a geared rotor system supported by fluid film journal bearings

2.2.1. Five-degree-of-freedom gear-bearing-rotor model

Figure 2.1 shows a centered gear pair attached to parallel rotors that are each supported by fluid film journal bearings. The model is composed of two rigid rotors having mass elements m_i, radii R_i and polar moments of inertia J_i. The subscript i denotes the driving ($i = 1$) and driven ($i = 2$) geared rotors.

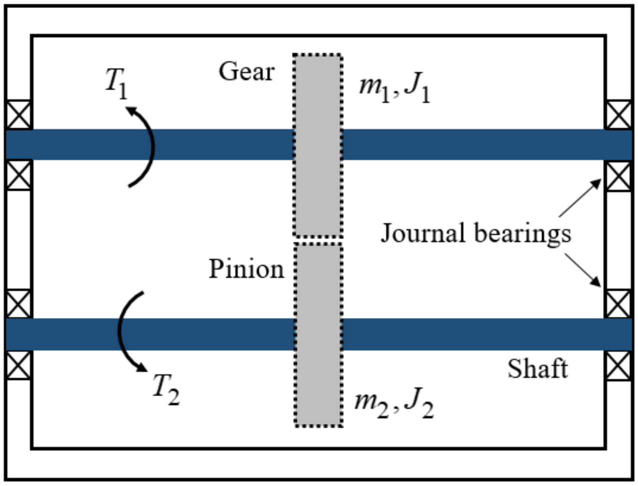

Figure 2.1 Gear set supported by hydrodynamic journal bearings

An external torque T_1 is applied to the driving gear. A nonlinear mesh coupling consisting of tooth backlash and time-varying stiffness is modeled to transmit torque between driving and driven gears. The motion coordinates for the model include (θ_1, θ_2, x_1, x_2, y_1, y_2) as shown in Figure 2.2

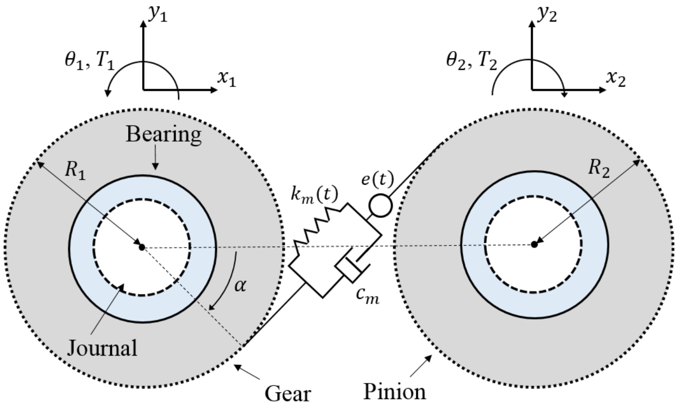

Figure 2.2 Spur gear pair model including hydrodynamic journal bearing

The dynamic transmission error (DTE), $\delta(t)$ is given by

$$\delta(t) = R_1\theta_1 - R_2\theta_2 + x_1\sin(\alpha) - x_2\sin(\alpha) + y_1\cos(\alpha) - y_2\cos(\alpha) - e_r(t) \tag{2.1}$$

where $e_r(t)$ represents the static transmission error. The analytical description of the time-varying mesh stiffness and the static transmission error can be expressed in the form of Fourier series as [3]

$$\begin{aligned} k_m(t) &= k_0 + \sum_{i=1}^{\infty} s_i k_0 \cos(i\omega_g t - \phi_i) \\ e_r(t) &= e_0 + \sum_{j=1}^{\infty} p_j e_0 \cos(j\omega_g t - \psi_j) \end{aligned} \tag{2.2}$$

where k_0 is a mean mesh stiffness, e_0 is a mean static transmission error, and s_i and p_j are the amplitude of the Fourier series components. The phase angles of the Fourier series are represented by ϕ_i and ψ_j, respectively.

The term ω_g is the gear mesh frequency represented by

$$\omega_g = N_i \omega_i \tag{2.3}$$

where N_i is the number of gear teeth, ω_i is rotor operating frequency and $i = 1, 2$. For this study $\omega_1 = \omega_2 = \omega$ is used, which follows the convention in the related literature [33]. The pressure angle α is assumed to remain constant during operation. Plain journal bearings support both rigid shafts, and their nonlinear fluid film force models are explained in section 2.2.

As noted in [26], a tooth backlash model defined with a piecewise linear function in the governing nonlinear differential equations may result in convergence difficulties when employing a Newton-Raphson method. Therefore, the following smoothening function presented in the same reference is also used in the present study.

$$\rho(t) = \frac{1}{2}\{(\delta(t) - b)[1 + \tanh(\sigma(\delta(t) - b))]\} + \frac{1}{2}\{(\delta(t) + b)[1 + \tanh(-\sigma(\delta(t) + b))]\} \qquad (2.4)$$

where $\rho(t)$ represents relative gear mesh displacement considering backlash, b is the half-length of the tooth backlash amplitude ($b = \frac{b_0}{2}$) and σ is a modulating factor which affects the accuracy of the backlash representation and convergence [26]. The value $\sigma = 100$ is selected for this study.

The coupling force between the driving and driven gear mesh is given by

$$F_{\mathrm{m0}} = k_m(t)\delta(t) + c_m\dot{\delta}(t) \qquad (2.5)$$

where c_m represents mesh damping, and it is assumed to be constant in this study. $\delta(t)$ represents the dynamic transmission error in Eq. (2.1), and $\dot{\delta}(t)$ is its derivative.

The equations of motion for the six-degree-of-freedom gear-bearing rotor system are

$$\begin{aligned}
&J_1\ddot{\theta}_1 + k_m(t)(R_1\theta_1 - R_2\theta_2 + x_1\sin(\alpha) - x_2\sin(\alpha) + y_1\cos(\alpha) - y_2\cos(\alpha) - e_r(t))R_1 + c_m\dot{\delta}(t)R_1 = T_1 \\
&J_2\ddot{\theta}_2 - k_m(t)(R_1\theta_1 - R_2\theta_2 + x_1\sin(\alpha) - x_2\sin(\alpha) + y_1\cos(\alpha) - y_2\cos(\alpha) - e_r(t))R_2 - c_m\dot{\delta}(t)R_2 = -T_2 \\
&m_1\ddot{x}_1 + k_m(t)(R_1\theta_1 - R_2\theta_2 + x_1\sin(\alpha) - x_2\sin(\alpha) + y_1\cos(\alpha) - y_2\cos(\alpha) - e_r(t))\sin(\alpha) + c_m\dot{\delta}(t)\sin(\alpha) = F_{\mathrm{b1x}} \\
&m_1\ddot{y}_1 + k_m(t)(R_1\theta_1 - R_2\theta_2 + x_1\sin(\alpha) - x_2\sin(\alpha) + y_1\cos(\alpha) - y_2\cos(\alpha) - e_r(t))\cos(\alpha) + c_m\dot{\delta}(t)\cos(\alpha) = F_{\mathrm{b1y}} - m_1 g \\
&m_2\ddot{x}_2 - k_m(t)(R_1\theta_1 - R_2\theta_2 + x_1\sin(\alpha) - x_2\sin(\alpha) + y_1\cos(\alpha) - y_2\cos(\alpha) - e_r(t))\sin(\alpha) - c_m\dot{\delta}(t)\sin(\alpha) = F_{\mathrm{b2x}} \\
&m_2\ddot{y}_2 - k_m(t)(R_1\theta_1 - R_2\theta_2 + x_1\sin(\alpha) - x_2\sin(\alpha) + y_1\cos(\alpha) - y_2\cos(\alpha) - e_r(t))\cos(\alpha) - c_m\dot{\delta}(t)\cos(\alpha) = F_{\mathrm{b2y}} - m_2 g
\end{aligned} \qquad (2.6)$$

By replacing the term $k_m(t)(R_1\theta_1 - R_2\theta_2 + x_1\sin(\alpha) - x_2\sin(\alpha) + y_1\cos(\alpha) - y_2\cos(\alpha) - e_r) + c_m\dot{\delta}(t)$ with F_{m0}, the equations become

$$\begin{aligned}
&J_1\ddot{\theta}_1 + R_1 F_{\mathrm{m0}} = T_1 \\
&J_2\ddot{\theta}_2 - R_2 F_{\mathrm{m0}} = -T_2 \\
&m_1\ddot{x}_1 + F_{\mathrm{m0}}\sin(\alpha) = F_{\mathrm{b1x}} \\
&m_1\ddot{y}_1 + F_{\mathrm{m0}}\cos(\alpha) = F_{\mathrm{b1y}} - m_1 g \\
&m_2\ddot{x}_2 - F_{\mathrm{m0}}\sin(\alpha) = F_{b2x} \\
&m_2\ddot{y}_2 - F_{\mathrm{m0}}\cos(\alpha) = F_{b2y} - m_2 g
\end{aligned} \tag{2.7}$$

where F_{bix} and F_{biy} represents the i th bearing forces in the x and y directions, and $m_1 g$ and $m_2 g$ terms represent gravity forces. By multiplying each of equations with R_1 and R_2, the first two become

$$\begin{aligned}
&J_1 R_1\ddot{\theta}_1 + R_1^2 F_{m0} = R_1 T_1 \\
&J_2 R_1\ddot{\theta}_2 - R_2^2 F_{m0} = -R_1 T_2
\end{aligned} \tag{2.8}$$

Divide the two equation with J_1 and J_2 respectively, and then subtracting the second equation from the first one, to obtain

$$R_1\ddot{\theta}_1 - R_1\ddot{\theta}_2 + \left(\frac{R_1^2}{J_1} + \frac{R_2^2}{J_2}\right)F_{\mathrm{m0}} = \frac{R_1}{J_1}T_1 + \frac{R_2}{J_2}T_2 \tag{2.9}$$

Substituting $p = R_1\theta_1 - R_2\theta_2$ and manipulating the equation yields

$$\ddot{p} + \left(\frac{J_2 R_1^2 + J_1 R_2^2}{J_1 J_2}\right)F_{\mathrm{m0}} = \frac{R_1}{J_1}T_1 + \frac{R_2}{J_2}T_2 \tag{2.10}$$

Dividing through by $\left(\frac{J_2 R_1^2 + J_1 R_2^2}{J_1 J_2}\right)$ yields

$$\left(\frac{J_1 J_2}{J_2 R_1^2 + J_1 R_2^2}\right)\ddot{p} + F_{\mathrm{m0}} = \left(\frac{J_1 J_2}{J_2 R_1^2 + J_1 R_2^2}\right)\left(\frac{R_1}{J_1}T_1 + \frac{R_2}{J_2}T_2\right) \tag{2.11}$$

Substitute J_e for $(\frac{J_1 J_2}{J_2 R_1^2 + J_1 R_2^2})$ to obtain

$$J_e \ddot{p} + F_{\mathrm{m0}} = T_e \tag{2.12}$$

where $T_e = J_e(\frac{R_1}{J_1}T_1 + \frac{R_2}{J_2}T_2)$ is an equivalent input torque term

The term $\delta(t)$ was inserted into Eq. (2.4) to include the backlash nonlinearity effect. Then, from Eq. (2.4) and (2.5), the gear meshing force including the backlash nonlinearity effect becomes

$$F_m = k_m \rho(t) + c_m \dot{\delta}(t) \tag{2.13}$$

Finally, the equations including the backlash nonlinearity, time-varying mesh stiffness and the static transmission error become

$$\begin{aligned}
&J_e \ddot{p} + F_m = T_e \\
&m_1 \ddot{x}_1 + F_m \sin(\alpha) = F_{\mathrm{b1x}} \\
&m_1 \ddot{y}_1 + F_m \cos(\alpha) = F_{\mathrm{b1y}} - m_1 g \\
&m_2 \ddot{x}_2 - F_m \sin(\alpha) = F_{\mathrm{b2x}} \\
&m_2 \ddot{y}_2 - F_m \cos(\alpha) = F_{\mathrm{b2y}} - m_2 g
\end{aligned} \tag{2.14}$$

where J_e is the equivalent inertia of two gears, i.e. $(\frac{J_1 J_2}{J_2 R_1^2 + J_1 R_2^2})$. The torsional natural frequency ω_n of the system is defined as $\sqrt{\frac{k_0}{J_e}}$.

For validation purposes, the simulation result are compared with experimental measurements [4] in Figure 2.3. The experiment was conducted using relatively stiff ball bearings so the x and y journal motions are assumed fixed in the simulation. The gear parameters for backlash, Fourier coefficients of time varying mesh stiffness and amplitude of static transmission error from [4] are employed in the simulation. The root mean square (RMS) value of the dynamic transmission error is plotted with respect to operating speed, showing good agreement between prediction and test results.

Table 2.1 provides a second validation case through comparison of the five-degree-of-freedom gear-bearing dynamic model's predicted natural frequencies with those provided in [15]. Since natural frequencies are characteristics of a linear model, the backlash and time varying stiffness were omitted and the bearing forces were represented by the stiffness and damping provided in the reference. The correlation is shown in the table and confirms excellent agreement.

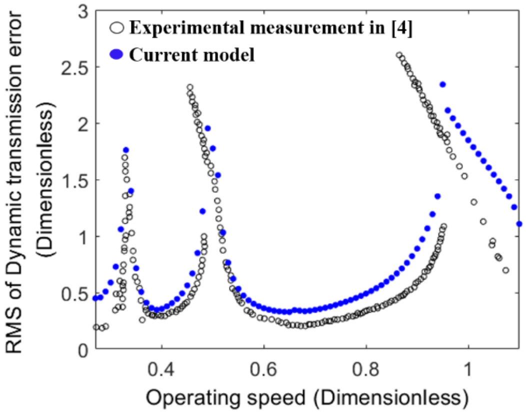

Figure 2.3 Comparison of dynamic transmission error with experimental measurements in [4] (reprinted from [34])

	Calculated natural frequencies in [93]	Natural frequencies based on current model
1st mode	0 Hz	0 Hz
2nd mode	1,149 Hz	1,149.3 Hz
3rd mode	1,293 Hz	1,293.6 Hz
4th mode	1,604 Hz	1,604.3 Hz
5th mode	1,799 Hz	1,799.1 Hz
6th mode	5,043 Hz	5,043.7 Hz

Table 2.1 Comparison of calculated natural frequencies with [93] (adapted from [93])

2.2.2. Finite element model of plain journal bearing

The Reynolds equation [34] for an incompressible lubricant combines the fluid continuity and momentum equations into a partial differential equation for film pressure, and is given by

$$\frac{\partial}{\partial\theta}\left(\frac{h^3}{12\mu}\frac{\partial p}{\partial\theta}\right)+\frac{\partial}{\partial z}\left(\frac{h^3}{12\mu}\frac{\partial p}{\partial z}\right)=\frac{R_J\omega_J}{2}\frac{\partial h}{\partial\theta}+\frac{\partial h}{\partial t} \tag{2.15}$$

where ω_J is the rotating speed of the journal, and R_J and μ represent the radius of the journal and the viscosity of the lubricant, respectively. The centers of the bearing and the journal are O_B and O_J in Figure 2.4, respectively.

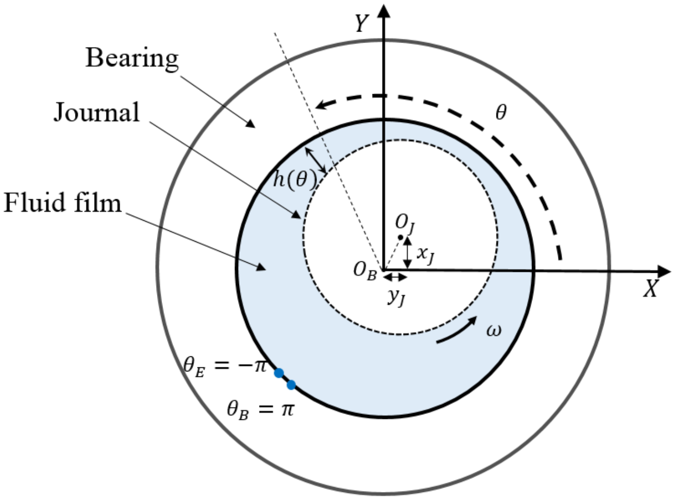

Figure 2.4 Axial mid-plane section of a journal bearing

The displacements of the journal center relative to the bearing center in the x and y directions are x_J and y_J, respectively, and p is the pressure in the lubricant film. Expressions for fluid film thickness h and its derivative $\frac{\partial h(\theta)}{\partial t}$ at θ are given by

$$\begin{aligned} h(\theta) &= C_B - x_J \cos\theta - y_J \sin\theta \\ \frac{\partial h(\theta)}{\partial t} &= -\dot{x}_J \cos\theta - \dot{y}_J \sin\theta \end{aligned} \tag{2.16}$$

where C_B represents the bearing radial clearance.

The mathematical model assumes rigid shafts and rigid attachments between the bearings and ground. Therefore, the journal motions x_J and y_J are identical to their respective gear centerline motions. Thus x_1, y_1 are identical to x_{J1} and y_{J1}, and x_2, y_2 are identical to x_{J2} and y_{J2}.

The finite element mesh of a fluid film is illustrated in Figure 2.5. The coordinate θ corresponds to the circumferential direction of the film and the direction of rotation is from the left (θ_B) to the right (θ_E). The axial coordinate is represented with z and only a half-length ($\frac{L}{2}$) of the film is modeled due to its symmetry. The pressure on the bottom ($z=0$) side of the mesh are set to ambient pressure P_{ambient}. Continuous pressure and flow condition are imposed on the left and right sides of the mesh. The zero-flow condition at the symmetric side ($z=\frac{L}{2}$) and the continuous pressure and pressure gradient conditions at left/right sides are applied as follows

$$v_{z=L/2} = 0,\ P_{\theta=\pi} = P_{\theta=-\pi},\ \frac{\partial p}{\partial \theta_{\theta=\pi}} = \frac{\partial p}{\partial \theta_{\theta=-\pi}} \tag{2.17}$$

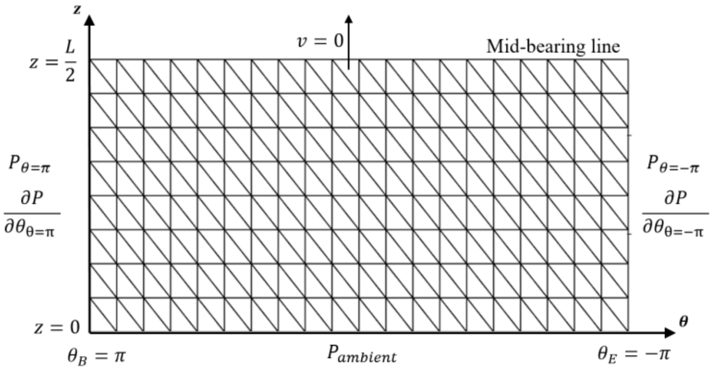

Figure 2.5 Mesh and boundary conditions for finite element journal bearing film model

The Reynolds equation is solved with a mesh of triangular simplex finite elements, which interpolate the two-dimensional pressure distribution in the film domain. The instantaneous reaction force on a journal is obtained by integrating the pressure distribution. Considering that symmetry condition the journal reaction force becomes

$$F_{\text{bi}} = \begin{Bmatrix} F_{\text{bix}} \\ F_{\text{biy}} \end{Bmatrix} = 2\int_0^{L/2}\int_{-\pi}^{\pi} p \begin{Bmatrix} \cos\theta \\ \sin\theta \end{Bmatrix} d\theta dz \tag{2.18}$$

2.3. Nonlinear steady-state solution methods

2.3.1. Multiple shooting method

The shooting method (SM) is a numerical procedure that utilizes an iterative algorithm and numerical integration of the nonlinear differential equations to locate co-existing, periodic equilibrium states. The SM provides a guided iterative search to locate the state vectors that repeat after a specified, or unknown in the case of autonomous systems, period. The single shooting method (SSM) is widely used in nonlinear dynamics research because of its simplicity. However, SSM may experience convergence problems, especially at saddle-node points. Multiple shooting methods (MSM) improves the numerical stability of the SSM by dividing time intervals into smaller ones. Compared to SSM, the MSM shows more robust convergence to periodic states and is less sensitive to the selection of initial state guesses. In addition, MSM is more suitable for parallel computing, thus making it desirable for systems with a large number of degrees of freedom.

The MSM algorithm is explained in this section. The non-autonomous nonlinear equations of motion can be represented by the first order form as

$$\frac{d}{d\tau}\mathbf{x} = \mathbf{x}' = \mathbf{h}(\mathbf{x}, \tau, p) \qquad (n \times 1) \tag{2.19}$$

where $\mathbf{x}$ is a state vector, τ is an explicit time variable in the forcing term and p represents the physical parameters of a system. The period of the steady-state harmonic response defined by a user is represented by the minimum period P_F and a rational number R in the non-autonomous case

$$P_R = RP_F \tag{2.20}$$

The solution at the end of the period P_R is represented

$$\mathbf{x}_{\mathbf{T}_\mathbf{R}} = \mathbf{x}(\tau = P_R, \mathbf{x}(0) = \mathbf{x_0}) \tag{2.21}$$

where x_0 is the initial condition state vector. If x_0 is a solution on an orbital equilibrium state of the period P_R, it will result that

$$\begin{gathered} \mathbf{x}_{\mathbf{T}_\mathbf{R}} = \mathbf{x}(\tau = P_R, \mathbf{x}(0) = \mathbf{x_0}) = \mathbf{x_0} \\ \mathbf{x_0} = \mathbf{g} + \mathbf{e} \end{gathered} \tag{2.22}$$

where g is a user-defined guess of initial conditions, and e is an error term.

Unlike SSM which requires the single end-point constraint ($\mathbf{x}_{T_R} = \mathbf{x}_0$) as explained above, MSM divides P_R into smaller intervals and generates multiple constraints as follows:

$$\begin{gathered} \mathbf{x}_{P_1} = \mathbf{x}(\tau = P_1, \mathbf{x}(0) = \mathbf{x}_0) = \mathbf{x}_1 \\ \mathbf{x}_{P_2} = \mathbf{x}(\tau = P_2, \mathbf{x}(0) = \mathbf{x}_1) = \mathbf{x}_2 \\ \vdots \\ \mathbf{x}_{P_{m-1}} = \mathbf{x}(\tau = P_{m-1}, \mathbf{x}(0) = \mathbf{x}_{m-2}) = \mathbf{x}_{m-1} \\ \mathbf{x}_{P_m} = \mathbf{x}(\tau = P_m, \mathbf{x}(0) = \mathbf{x}_{m-1}) = \mathbf{x}_m = \mathbf{x}_0 \end{gathered} \tag{2.23}$$

where divided time intervals are $0 = P_0 < P_1 < \cdots < P_m = P_R$. Note that m is the number of time intervals defined by a user. A multi-dimensional Newton-Raphson method is applied to update $\mathbf{x}_0$.

For an autonomous system, the additional phase condition should be defined since the point of the periodic solution at a specific time is not unique. In this study, a phase condition that sets the DTE from Eq. (2.1) as zero is used [94].

$$\begin{gathered} \mathbf{H}(\mathbf{x}_0, P_A) = \mathbf{g}(\mathbf{x}_0, P_A) - \mathbf{x}_0 = 0 \\ \mathbf{c}(\mathbf{x}_0) = 0 \end{gathered} \tag{2.24}$$

where P_A is a period of an autonomous system orbit to be identified along with an initial condition $\mathbf{x}_0$.

2.3.2. Arc-length continuation

The shooting method may take considerable computation time, especially when plotting co-existing solution loci versus system parameters. “Continuation algorithms” have been developed to generate the loci (branch plots) with significantly increased efficiency relative to conducting independent SM searches for each parameter value. The Arc-length Continuation (AC) method [94] is applied in this research. AC provides robust solution searches even in high curvature regions by utilizing the trajectory of the solution curves along an arc-length as shown in Figure 2.6.

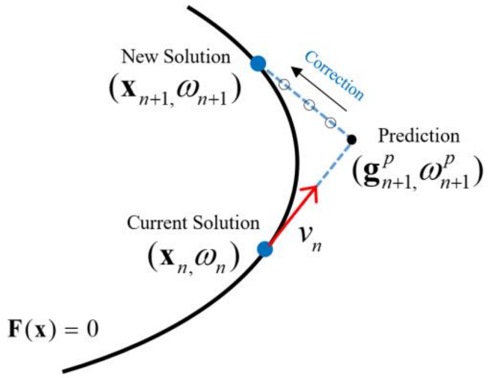

Figure 2.6 Pseudo arc-length continuation method

An additional unknown ω is involved in the iteration search. The next solution is

$$\begin{Bmatrix} \tilde{\mathbf{g}}_n^{i+1} \\ \omega_n^{i+1} \end{Bmatrix} = \begin{Bmatrix} \tilde{\mathbf{g}}_n^{i} \\ \omega_n^{i} \end{Bmatrix} + \begin{bmatrix} \tilde{\mathbf{J}}_g^i & \mathbf{J}_\omega^i \\ \dfrac{\partial \mathbf{k}_n^{i^T}}{\partial \mathbf{x}} & \dfrac{\partial \mathbf{k}_n^{i}}{\partial \omega} \end{bmatrix} \begin{Bmatrix} -\mathbf{f}(\tilde{\mathbf{g}}_n^i, \omega_n^i) \\ -\mathbf{q}(\tilde{\mathbf{g}}_n^i, \omega_n^i, s) \end{Bmatrix} \tag{2.25}$$

where ω and s are operating parameters and arc-length of the solution curve, respectively, n is a current step number, $\mathbf{J}_\omega$ is Jacobian matrix with regard to ω, and k is the constraint imposed on the solution procedures as

$$\mathbf{k}(\mathbf{x}, \omega, s) = v \left\| \tilde{\mathbf{g}}_{n+1}^i - \tilde{\mathbf{g}}_n \right\|_2^2 + (\omega_{n+1}^i - \omega_n)^2 - (\Delta s)^2 \tag{2.26}$$

where v is a relaxation factor, and Δs is an arc-length.

Then Newton-Raphson iteration is performed until the convergence criteria are satisfied. A continuation of periodic solution searches is carried out to plot a frequency response in the excitation frequency range of interest, including bifurcation points. The phase condition in Eq. (2.24) is added to Eq. (2.25) for the autonomous system continuation algorithm.

2.3.3. Stability identification based on the shooting method

The Jacobian matrix of the shooting method is calculated to determine the local stability of periodic solutions. More specifically, the eigenvalues of the Jacobian matrix at a steady-state solution identifies the solution's stability and its bifurcation type. Perturbed solutions are computed to generate the Jacobian matrix entries. The system is considered unstable if the maximum magnitude of the eigenvalues is larger than unity.

2.3.4. Lyapunov exponents for identifying chaos

Various approaches are used to identify the presence of chaos in the response of a nonlinear dynamical system. The most widely used approach is to calculate Maximum Lyapunov exponent (MLE, $\mu_{\max}$). Lyapunov exponents indicate the rate of separation of two infinitesimally close trajectories in the local phase space [94]. A total of n initial separation vectors with different directions are used for a system with n states, to obtain a spectrum of n Lyapunov exponents (LE, $\mu_i (i = 1, 2, ..., n)$) for calculating the rates of separation. The simultaneous numerical integrations of nonlinear differential equations and linearized form of them are required for the MLE calculation.

$$\text{Nonlinear differential equations : } \dot{\mathbf{x}} = \mathbf{g}(\mathbf{x}) \tag{2.27}$$

$$\text{Linearized form of Eq. (2.27) : } \dot{\boldsymbol{\beta}} = \mathbf{L}(\boldsymbol{\beta}) \tag{2.28}$$

The actual and linearized trajectories with perturbed initial conditions are calculated from Eq. (2.27) and Eq. (2.28), respectively, at various times along the nonlinear system trajectory. Deviation distances are obtained from the difference between the nonlinear trajectory and linearized trajectories.

$$\mathbf{\Delta}(t) = \sqrt{\delta \mathbf{x}_1^2 + \delta \mathbf{x}_1^2 + \cdots + \delta \mathbf{x}_n^2} \tag{2.29}$$

An appropriate time interval t_f is selected for the numerical integrations to avoid a numerical error. Sets of orthonormalized perturbed vectors are obtained from a Gram-Schmidt procedure as

$$\tilde{\boldsymbol{\beta}}_1 = \frac{\boldsymbol{\beta}_1(t_f)}{\left\|\boldsymbol{\beta}_1(t_f)\right\|}, \ \tilde{\boldsymbol{\beta}}_2 = \frac{\boldsymbol{\beta}_2(t_f) - (\boldsymbol{\beta}_2(t_f)\bullet\tilde{\boldsymbol{\beta}}_1)\tilde{\boldsymbol{\beta}}_1}{\left\|\boldsymbol{\beta}_2(t_f) - (\boldsymbol{\beta}_2(t_f)\bullet\tilde{\boldsymbol{\beta}}_1)\tilde{\boldsymbol{\beta}}_1\right\|} \text{ and } \tilde{\boldsymbol{\beta}}_m = \frac{\boldsymbol{\beta}_m(t_f) - \sum_{i=1}^{m-1}(\boldsymbol{\beta}_m(t_f)\bullet\tilde{\boldsymbol{\beta}}_i)\tilde{\boldsymbol{\beta}}_i}{\left\|\boldsymbol{\beta}_m(t_f) - \sum_{i=1}^{m-1}(\boldsymbol{\beta}_m(t_f)\bullet\tilde{\boldsymbol{\beta}}_i)\tilde{\boldsymbol{\beta}}_i\right\|} \tag{2.30}$$

After conducting the integrations of of Eq. (2.28), (2.29), and (2.30) for r times, the Lyapunov exponents are obtained as

$$\mu_i = \frac{1}{rt_f}\sum_{k=1}^{r}\ln(\Delta_i^k(t_k)) \tag{2.31}$$

where $\Delta_i^k(t_k)$ is the denominator of the orthonormal vector $\boldsymbol{\beta}_i^k$, k denotes the k_{th} time step and i represents i th vector element.

The MLE is used as a quantitative measure to determine the chaotic response of a nonlinear dynamical system as follows.

- $\mu_{\max} > 0$: System is chaotic (necessary but not a sufficient condition for chaos)
- $\mu_{\max} < 0$: System attracts to a fixed point or a stable periodic orbit (asymptotically stable) (2.32)
- $\mu_{\max} = 0$: The orbit is quasi-periodic.

2.4. Numerical example

The five-degree-of-freedom geared rotor-bearing model of Figure 2.2 and Eq. (2.14) is utilized to demonstrate various nonlinear phenomena induced by gear and journal bearing nonlinearities. The multiple shooting/continuation method and Lyapunov exponents discussed in section 3 are utilized along with direct numerical integration. MATLAB ODE15s was used with a relative tolerance of 10^{-9} for computing the Jacobian matrix in the shooting/continuation procedure. Embedded C++ coding and parallel processing are utilized in the MATLAB program to accelerate the execution. The results are divided into 3 sections (1) parametric resonances/jump phenomena and the effect of journal bearing parameter variations on those phenomena, and (2) chaotic responses due to gear nonlinearity and the effect of journal bearing parameters on the responses, and (3) the effect of gear mesh stiffness on the hydrodynamic stability of the gear system supported by journal bearings. Solid and dashed lines indicate stable and unstable responses, respectively in all figures. Table 2.2 summarizes the parameters of the spur gear pair and journal bearings used in this study.

Gear parameters	
Mass	$m_1 = m_2 = 9.3276$ kg
Moment of inertia	$J_1 = J_2 = 0.03187\,\mathrm{kg \cdot m^2}$
Radius of gears	$R_1 = R_2 = 0.0982$ m
Pressure angle	$\alpha = 20°$
Backlash amplitude	$b_0 = 100$ μm
Mean mesh (tooth) stiffness	$k_0 = $ 1e8 N/m
Mesh damping ratio	$\zeta_m = 0.01 \sim 0.025$
Number of gear teeth	$\mathrm{N_1 = N_2 = 28}$
Applied torque (T_1)	100~3,000 N m
Journal bearing parameters	
Bearing diameter	$D_B = 0.092$ m
Bearing clearance	$C_B = 74 \sim 184$ μm
Bearing L/D ratio	0.3~2
Lubricant viscosity	$\mu = 10 \sim 90$ mPa s

Table 2.2 Parameters of the spur gear pair and journal bearings

2.4.1. Parametric resonances and jump phenomenon

This section presents results for parametric instability, including fundamental and subharmonic resoanances induced by time varying mesh stiffness. Both the fundamental and subharmonic resonances are parametric resonances since they are removed when the time varying component of the gear mesh stiffness is removed. Parametric resonance and jump phenomena of a spur gear system with backlash nonlinearity and time-varying mesh stiffness were treated in [1-8] and more recently in [15, 9-14]. However, the effects of journal bearing parameters on the nonlinear response of the geared system needs further investigation. Parametric instability of the fundamental and double-period subharmonic frequencies is presented below including journal bearing effects. Applied torque input is considered as an excitation source, and time-varying mesh stiffness with the frequency corresponding to gear mesh frequency ω_g in Eq. (2.3) is included. No imbalance excitation and static transmission error $e_r(t)$ in Eq. (2.2) are applied in this section. The non-autonomous, multiple shooting/continuation methods in section 3 are applied to the system equations to analyze the influence of journal bearing parameters on nonlinear responses. Only the first Fourier coefficient of the time-varying mesh stiffness s_1 in Eq. (2.2) was included, and it was set equal to 0.2, since values from 0.1 to 0.3 are employed in the literatures [1-15]. The bearing L/D ratio is 1, the radial clearance is 105 μm, the lubricant viscosity is 30 mPa s, and a applied torque of 1,250 N m is used for the nominal values of the simulation. Each parameter is varied to investigate its effect on the softening effect due to gear nonlinearities. Direct numerical integrations with initial conditions determined from the shooting/continuation procedure are performed to obtain peak-to-peak displacement amplitude vs. rotor operating speed plots. At the same time, the stability of the periodic solutions is presented and obtained from the shooting method’s Jacobian matrix eigenvalues.

Fundamental resonance

Figure 2.7 shows the response amplitude regarding operating speed for the non-dimensional peak-to-peak displacements of DTE ($\frac{\delta}{b_0}$) where δ is defined from Eq. (2.1). The applied torque is 1,100 N m in this case. The linear system resonance will occur when the gear mesh frequency $\omega_g = N\omega = \omega_n = \sqrt{\frac{k_0}{J_e}}$. This occurs at around 2500 rpm in this case.

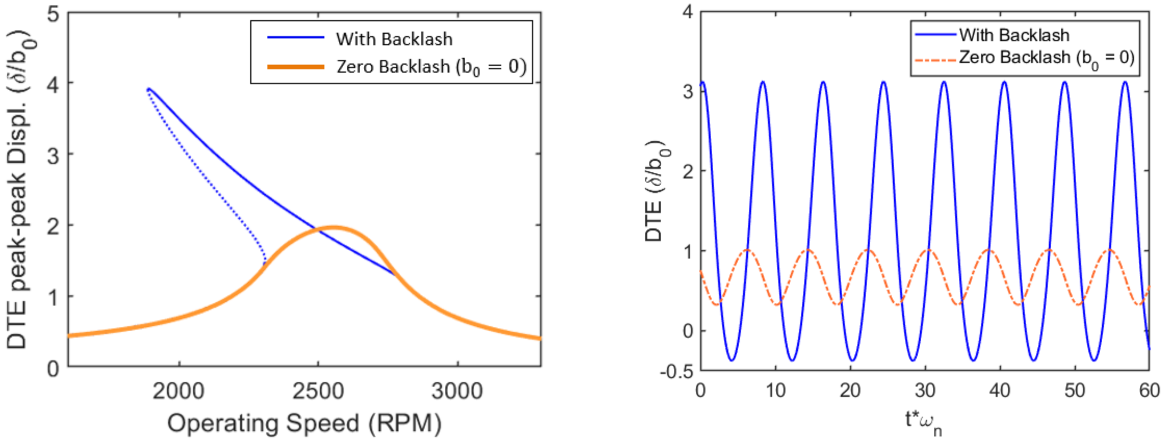

(a) (b)

Figure 2.7 Effect of backlash (a) peak-peak displacement of DTE (b) time response at 2,000 rpm

Including backlash causes a softening effect related left-leaning backbone curve with an unstable branch occurring between 1,800 and 2,300 rpm in Figure 2.7 (a). Multiple co-existing solutions are seen to occur when the rotor speed is in the vicinity of $\frac{\omega_n}{N}$ where N represents the number of gear teeth. The presence of co-existing solutions is clearly seen to result from including backlash, and the peak DTE severity is seen to nearly double when backlash is included. Note that the time-varying stiffness effect is included in both the with and without backlash cases. The increased DTE caused by the gear nonlinearity is also confirmed by the time response of both cases at 2,000 rpm in Figure 2.7 (b).

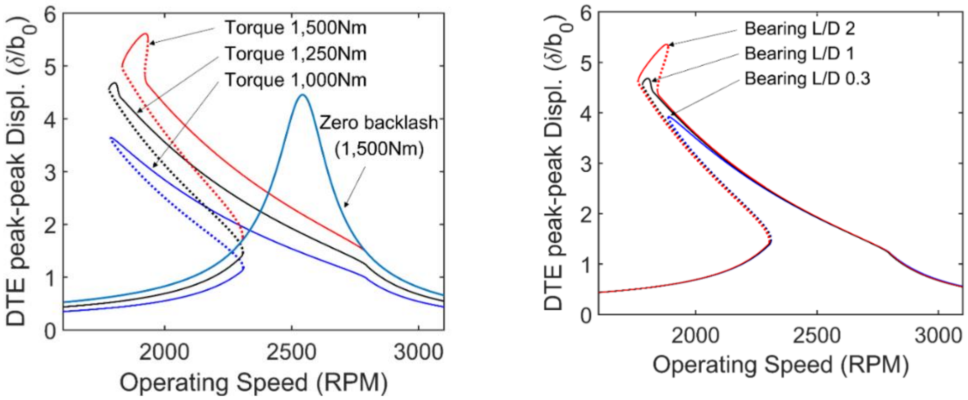

(a) (b)

Figure 2.8 Effect of (a) applied torque and (b) bearing L/D ratio on the peak-peak displacement of DTE through the fundamental resonance (solid line: stable, dotted line: unstable)

The results in Figure 2.8 are obtained for three different applied torques T_1, i.e., 1,000, 1,250 and 1,500 N m ($T_2 = 0$), where T_1 is for driving gear and T_2 is for driven gear. All three cases exhibit a fundamental parametric resonance caused by the time-varying mesh stiffness, with a softening effect starting from near 2,300 rpm. The amplitudes of the forced steady-state harmonic response increase with increased torque inputs. In all cases of Figure 2.8 (a), the unstable responses emerge through saddle-node bifurcations around 2,300 rpm. Three or five multiple, co-existing steady-state responses occur between 1700 – 2300 rpm depending on the applied torque values. The critical rpm (2300 rpm) for jump-up behavior is nearly independent of applied torque variation, but in contrast, the critical rpm for jump-down behavior is more sensitive to applied torque variation. The critical rpm of jump-down behavior tends to increase with increasing drive torque. The separation between the jump-up and jump-down rpm is reduced with increasing applied torque. The emergence of the right-leaning portion of the response curves, which observed at the highest applied torque 1,500 N m may be explained in terms of the backlash forces. Three different meshing states can exist depending on the maximum DTE; no impact, single-sided impact, and double-sided impact. In Figure 2.8 (a), the system shows only a single-sided contact with the 1,000 N m applied torque, which is the source of the primary softening effect. Increasing the applied input torque gives rise to a hardening effect, which introduces additional co-existing responses and jump-up/down frequencies. The peak-peak response at 1,500 N m shows a clear hardening effect along with the softening effect. The number of multiple co-existing responses increased from three to five with the applied torque increased from 1,000 to 1,500 N m. The figure also shows a tendency of the response curve to move rightwards towards the zero-backlash response as the DTE increases. This is consistent with a greater engagement of teeth as the amplitude increases. These results are consistent with the experimental and numerical results in [4], which used a single-degree-of-freedom gear model considering only torsional motion. Prior research utilized a simple rigid or linear stiffness and damping bearing model, or analytical short bearing theory, or finite-length impedance method, which precluded the accurate investigation of nonlinear bearing parameter effects on the response. In this study, utilizing the finite element method for the nonlinear fluid film force of the finite-length bearing, the bearing L/D ratio is varied from 0.3 to 2 in Figure 2.8 (b). The peak-peak DTE displacements in the frequency range away from the resonance region are not significantly affected by the bearing L/D ratio variation. However, similar to the applied torque input case, the jump-down frequency is influenced by the L/D ratio variation, since the jump-down event occurs at a relatively lower frequency range with higher L/D ratio. The jump down speed is lowered by about 100 rpm for $L/D = 2$ compared with $L/D = 0.3$. Figure 2.9 presents the bifurcation diagrams corresponding to the input torques 1,000 and 1,500 N m in Figure 2.8 (a), in a manner that highlights the jump phenomena and multiple co-existing solutions.

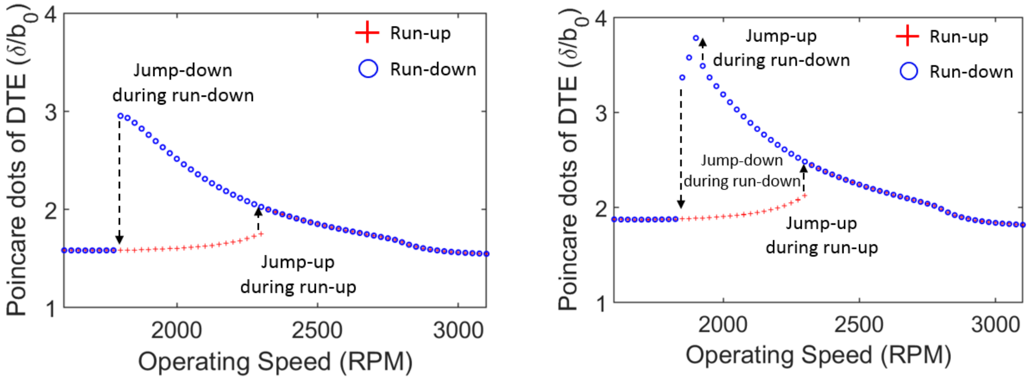

(a) (b)

Figure 2.9 Bifurcation diagrams of (a) 1,000 Nm torque and (b) 1,500 Nm torque cases in Figure 2.8 (a)

Figure 2.10 illustrates the effect of varying bearing lubricant viscosity on steady-state, nonlinear harmonic response. Lubricant viscosities of 10 and 90 mPa s, in addition to the nominal value of 30 mPa s, are simulated for two L/D ratio (L/D = 0.3 and 1). Increasing the viscosity decreases the jump-down frequencies and increases the peak resonant amplitude in both L/D cases.

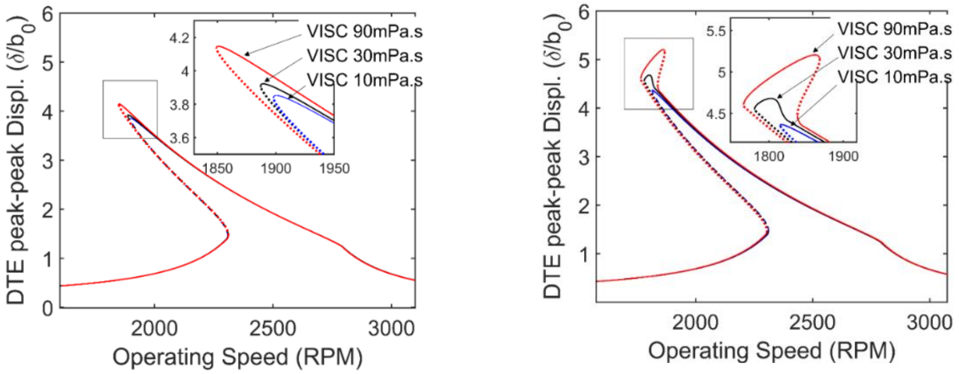

(a) (b)

Figure 2.10 Effect of lubricant viscosity on the peak-peak response of DTE (a) Bearing L/D = 0.3 and (b) Bearing L/D = 1 (solid line: stable, dotted line: unstable)

Figure 2.11 shows the frequency-amplitude diagram with radial bearing clearances of C_B = 184 μm and C_B = 74 μm, along with nominal C_B = 105 μm. The results with the smallest clearance, i.e., C_B = 74 μm, show a broader range of co-existing solutions region compared to other values in both the L/D = 0.3 and the L/D = 1 cases. The C_B = 74 μm and L/D = 1 case displays a double-sided impact and resulting in hardening effect in Figure 2.11 (b). The L/D = 1 case shows more reduction in jump-down frequency as compared to the L/D = 0.3 case. This reduction may be attributed to the fact that the L/D = 1 geometry has more fluid film area than for L/D = 0.3, and hence greater force to affect the parametric resonance.

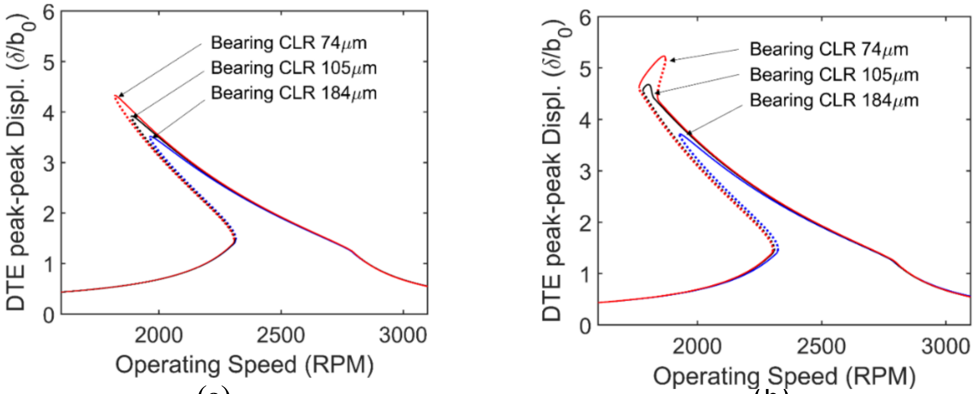

(a) (b)

Figure 2.11 Effect of bearing clearance on the peak-peak response of DTE (a) Bearing L/D = 0.3 and (b) Bearing L/D = 1 (solid line: stable, dotted line: unstable)

Figure 2.12 shows five co-existing steady-state responses in the frequency and phase plane domain for C_B=74 μm case in Figure 2.11 (b). For the phase portrait, the rotor spin speed equals 1850 rpm, and it is obtained via the non-autonomous MSM developed in section 3. The excitations include the time-varying mesh stiffness and the applied torque. Periodic responses 1, 3 and 5 are stable and 2 and 4 are unstable as predicted by the eigenvalues of the Jacobian matrix of the MSM. Note that the unstable forced harmonic responses cannot be obtained by direct numerical integration, but only with a directed search approach such as the MSM.

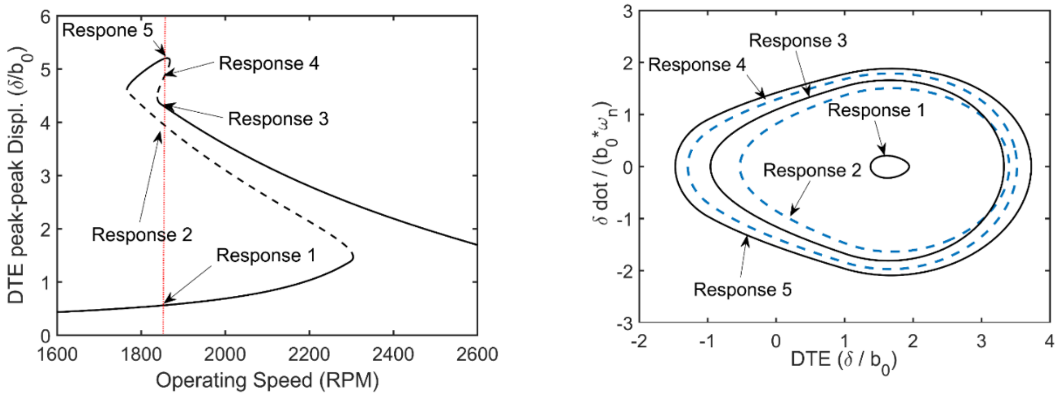

(a) (b)

Figure 2.12 Multiple co-existing responses using the shooting method (L/D = 1, μ = 90 mPa s, T_1=1,500 N m). (a) Frequency-amplitude diagram (b) Phase portrait at 1,850 rpm (Solid line: stable, dotted line: unstable)

The mesh deformation $\rho(t)$ in Eq. (2.4) corresponding to the multiples responses in Figure 2.12 are shown in Figure 2.13. The mesh deformation in Figure 2.13 (a) has static and dynamic components and never loses contact. The response in Figure 2.13 (b) has zero mesh deformation for most of the period and demonstrates the effect of single-sided contact induced by the backlash nonlinearity. Figure 2.13 (c) shows double-sided contact cycling between positive, zero and negative mesh deformation states. The result of this contact behavior is a net hardening effect as evidenced by the right-leaning secondary bend in the response 5 curve of Figure 2.12.

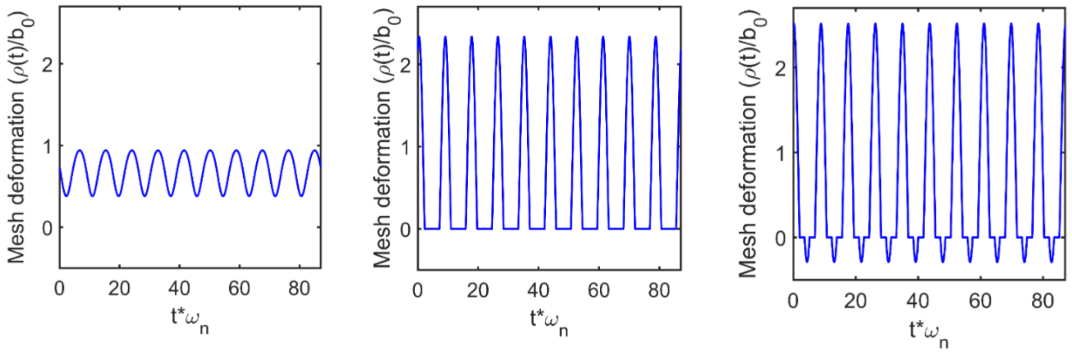

(a) (b) (c)

Figure 2.13 Co-existing mesh deformation $\rho(t)$ responses: (a) Response 1 (b) Response 4 (c) Response 5

Figure 2.14 illustrates the repelling/attracting motions among stable and unstable forced harmonic response orbits at 1850 rpm. The unstable Response 2 is repelled towards the stable attractors, i.e. Response 1 (Figure 2.14 (a)) or Response 3 (Figure 2.14 (b)). Thus, the unstable manifold (the dotted line) initiated by a saddle-node bifurcation in Figure 2.12 acts as a border manifold, which provides information about the convergence route in phase space.

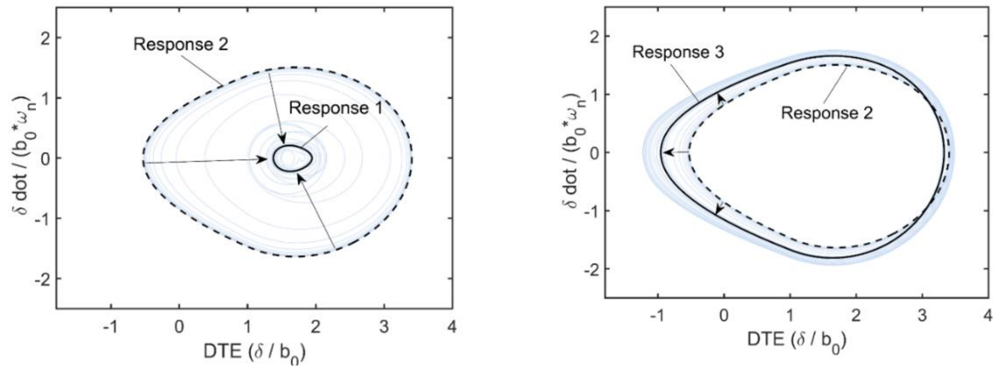

(a) (b)

Figure 2.14 Repelling motion of the unstable orbit (response 2) at fundamental resonance region (a) Response 2 → Response 1 (b) Response 2 → Response 3 (solid line: stable, dotted line: unstable)

Subharmonic resonances

Prior work [3, 95, 96] revealed that subharmonic resonance of geared systems is highly dependent on the amplitude of time-varying mesh stiffness, mesh damping ratio and static applied torque. The focus here is to demonstrate the effect of journal bearing parameters on the subharmonic vibrations occurring for a rotor speed in the vicinity of $\frac{2\omega_n}{N}$. The maximum rpm is extended from 3,100 rpm for the fundamental resonance case to 5,500 rpm to observe the subharmonic resonances. Figure 2.15 (a) shows that increasing torque increases the peak-peak DTE amplitude, the backlash nonlinearity generally causes a softening (left-leaning resonance) effect, but a double-sided contact is evidenced by the right-leaning, hardening peak at 750 N m torque, similar with the fundamental resonance in Figure 2.8.

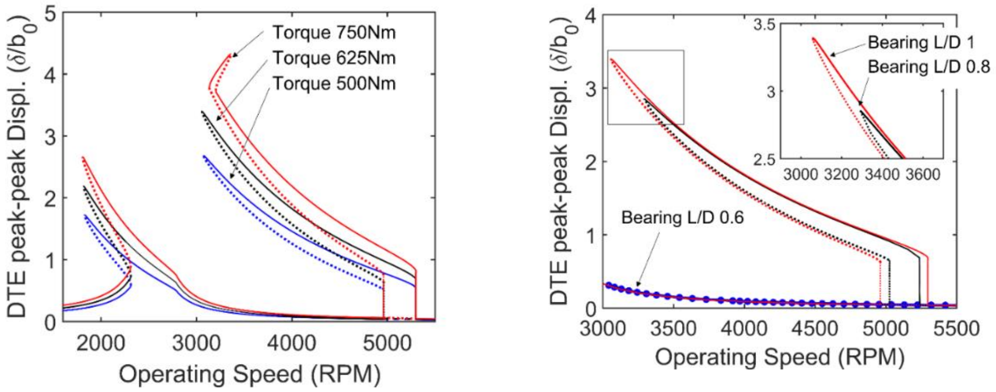

(a) (b)

Figure 2.15 Effect of (a) applied torque and (b) bearing L/D ratio on the peak-peak response of DTE of subharmonic resonance (solid line: stable, dotted line: unstable)

Figure 2.16 provides waterfall diagrams corresponding to the 750 N m torque case in Figure 2.15 (a) and the bearing L/D = 0.6 case in Figure 2.15 (b). Figure 2.16 (a) and (b) correspond to run-up and run-down in speed for the 750 N m torque case with L/D = 1. Figure 2.16 (c) and (d) correspond to run-up and run-down in speed for the bearing L/D = 0.6 case with 625 N m torque input. The figures show jump-up and jump-down bifurcations near 2,500 rpm, and the presence of a sub-harmonic resonance and a 0.5x gear mesh frequency response.

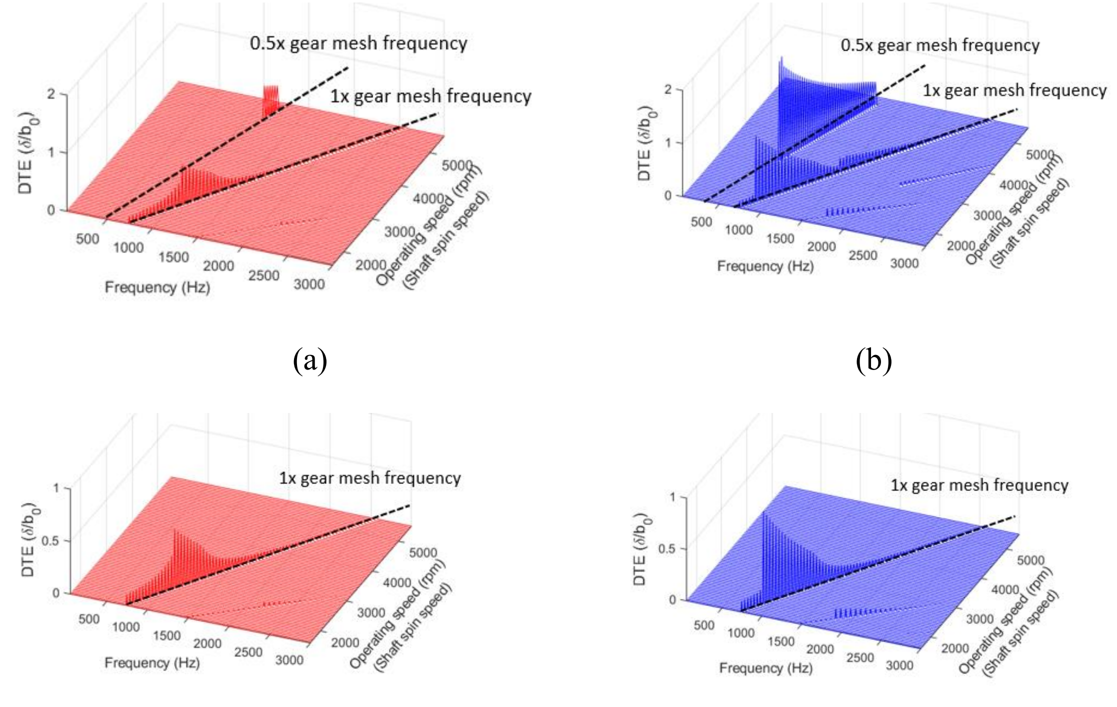

(a) (b)

(c) (d)

Figure 2.16 Waterfall diagrams (a) 750 N m Torque, run-up, (b) 750 N m Torque, run-down, (c) L/D = 0.6, run-up, (d) L/D = 0.6, run-down

In Figure 2.15, unstable branches appear as a period-doubling bifurcation emerges near 5,000 rpm, which corresponds to twice the fundamental resonance frequency rotor speed ($\frac{2\omega_n}{N}$). A saddle-node bifurcation occurs as the period-doubled unstable branches reach their peak amplitude, yielding a stable branch. As a result, one stable solution with the gear mesh frequency (ω_g) and two unstable/stable solutions with half gear mesh frequency ($0.5\omega_g$) coexist in the operating speed range between 3,000 and 5,000 rpm.

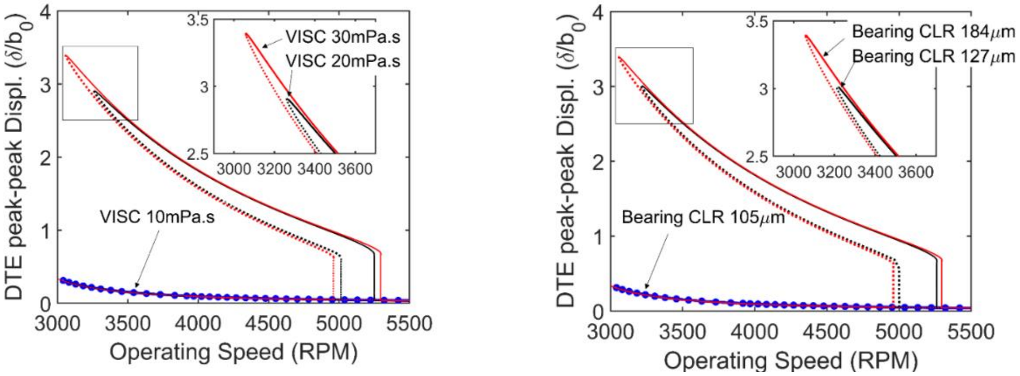

(a) (b)

Figure 2.17 Effect of (a) lubricant viscosity and (b) bearing clearance on the peak-peak response of DTE for subharmonic resonance (solid line: stable, dotted line: unstable)

Variation of the journal bearing parameters significantly affects the subharmonic resonance as shown in Figure 2.15 (b) and Figure 2.17. The sub-harmonic resonance is seen to vanish when considering a drop in L/D from 0.8 to 0.6. Physically this may result from the more significant force of the larger L/D bearing inducing the subharmonic vibrations. Figure 2.17 (a) shows that increasing the lubricant viscosity extends the frequency overlap range by decreasing the jump-down frequency. Similar trends are also observed in the case of bearing clearance in Figure 2.17 (b). The subharmonic is seen to disappear for the low viscosity (10 mPa s) case and the low clearance (105 μm) case. Figure 2.18 shows multiple co-existing DTE versus time plots for the 30 mPa s case in Figure 2.17 (a): 3575 rpm, L/D = 1, an applied torque of 625 N m, a lubricant viscosity of 30 mPa s and a bearing clearance of 36.8 μm. The $t\omega_n$ in Figure 2.18 is the non-dimensional time variable where the time t is multiplied by the torsional natural frequency ω_n. Note that the Response 1 in Figure 2.18 (a) has the frequency equal to ω_g, while the Response 2 and 3 in Figure 2.18 (b) and (c) have the half frequency of ω_g.

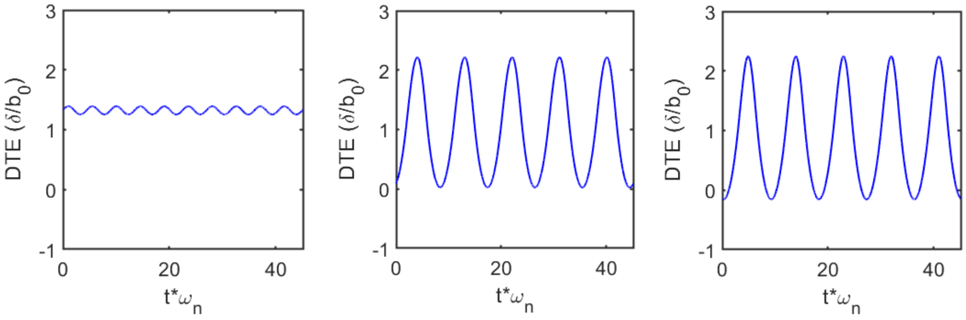

(a) (b) (c)

Figure 2.18 Time response of multiple co-existing response of DTE (a) Response 1, (b) Response 2, (c) Response 3

2.4.2. Chaotic response

The effect of linearized bearing model stiffness and damping coefficients, static transmission error, tooth friction, etc. on the chaotic response of geared systems was investigated in [16, 18, 19, 24, 97, 98], and chaotic behavior was observed experimentally in [6]. The effects of varying journal bearing parameters using a nonlinear bearing model, on the geared system's chaotic response are discussed below. The model parameter values include a low torque load of 200 N m, a light mesh damping ratio of 0.01, $L/D = 0.3$, and the mean static transmission error e_0 is set to b_0, the coefficient of static transmission error p_j in Eq. (2.2) is set to 0.15. Unbalance force is not included in this simulation. The nonlinear equations are solved using MATLAB's ODE 15s with a relative tolerance of 10^{-5}. The time response corresponding to the first

1500 gear mesh periods of the system was discarded from the sampled data to ensure that the responses reached steady-state conditions. The steady-state responses during the last 500 gear mesh periods were employed for the plots shown below. The MLEs of the spur gear system were plotted to identify the onset of chaotic motion. The MLEs converged after 600-time intervals with 0.25 gear mesh periods per interval.

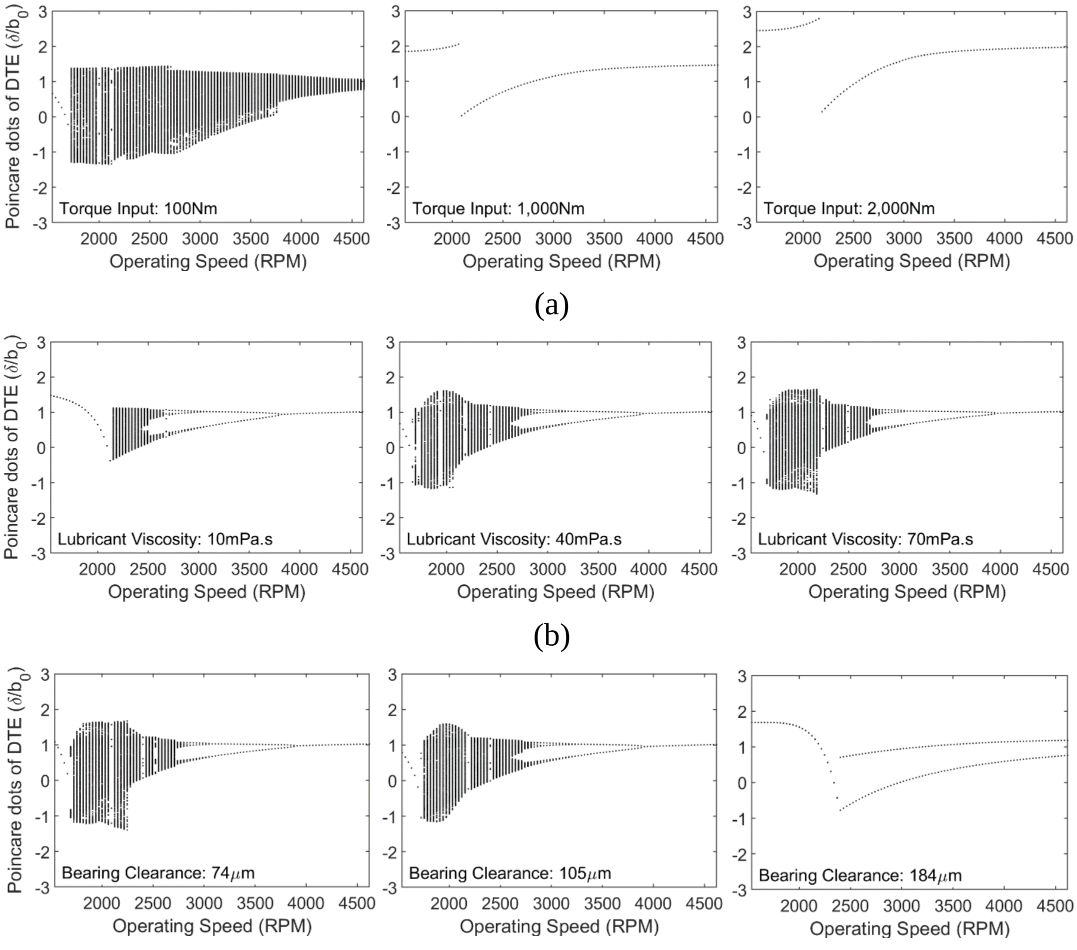

(a)

(b)

(c)

Figure 2.19 Bifurcation diagrams vs. operating speed for varying parameter values (a) applied torque (100 , 1,000 and 2,000 N m) (b) lubricant viscosity (10, 40 and 70 mPa s) , and (c) Bearing clearance (74, 105 and 184 µm)

Figure 2.19 shows DTE bifurcation diagrams versus rotor rpm while varying torque, bearing lubricant viscosity and radial clearance. The viscosity and clearance are held fixed at 40 mPa s and 105 μm, respectively, while varying torque in Figure 2.19 (a). The torque and clearance are held fixed at 1100 N m and 105 μm respectively while varying viscosity in Figure 2.19 (b). The torque and viscosity are held fixed at 1100 N m and 40 mPa s respectively while varying radial clearance in Figure 2.19 (c). The Poincaré dots are sampled at the gear mesh frequency period ($\Delta t = \frac{2\pi}{\omega_g}$).

With a relatively low applied torque (100 N m), the system performs 1x synchronous motions at the gear mesh frequency until the operating speed reaches about 1,800 rpm. Then chaotic responses emerge and are maintained at higher speeds. Note that with increasing applied torque from 1,000 to 2,000 N m, the operating speeds where jump occurs are slightly increased from 2,050 to 2,150 rpm, which implies that the variation of applied torque has an impact on the natural frequencies of the geared system supported by journal bearings, via a torsional-lateral coupling. Comparison of three cases reveals that the increasing torques tend to mitigate the chaotic responses.
Figure 2.19 (b) shows that the chaos in DTE response starts at lower speed and ranges over a larger set of values as the bearing lubricant viscosity increase from 10 to 70 mPa s. In all three diagrams of Figure 2.19 (b), with higher operating speeds over 2,500 rpm, the chaotic responses turn into period four and two motions, and eventually into period one motion. Figure 2.19 (c) shows how the chaotic behavior in DTE occurs with the

radial bearing clearance values from 74 to 184 μm. Period-doubling bifurcations occur with decreasing speeds from 4,500 rpm to lower speeds in the 74 and 105 μm cases, as exemplified by the period one motion turning into period two motion around 3,800 rpm, followed by additional period doubling into chaos. In Figure 2.19 (b) and (c), the lower viscosity and high bearing radial clearance tend to suppress the chaotic behaviors and show relatively stable motions.

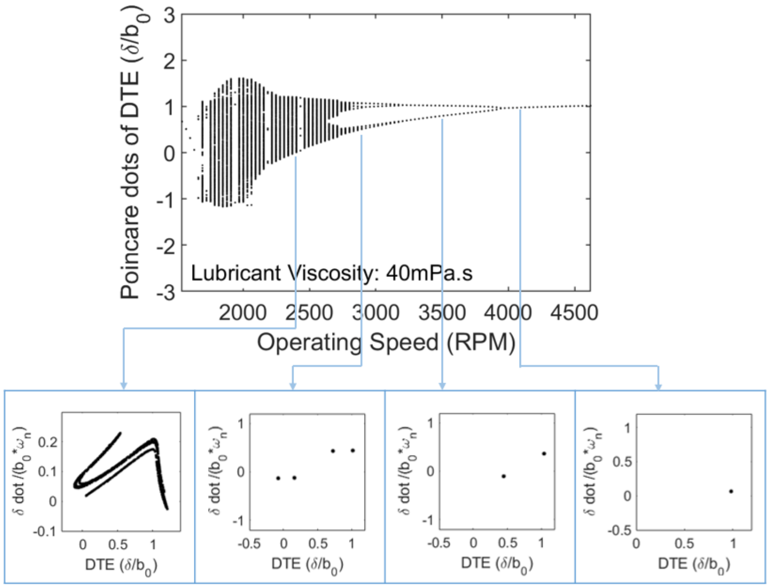

2,300rpm (MLE = 0.056)

2,900rpm (MLE = -0.041)

3,500rpm (MLE = -0.045)

4,100rpm (MLE = -0.041)

Figure 2.20 Bifurcation diagrams and Poincaré attractors at different speeds, for a lubricant viscosity 40 mPa s case in Fig. 19 (b)

Figure 2.20 is included to more clearly illustrate the occurrence of chaotic and period-doubling bifurcations corresponding to the 40 mPa s case in Figure 2.19 (b). Attractors are presented for the four different operating speeds (2,300 rpm, 2,900 rpm, 3,500 rpm and 4,100 rpm). The strange attractor and corresponding positive MLE value of 0.056 both confirm chaotic behavior at 2300 rpm. The number of attractors (4→2→1) confirms the occurrence of period-doubling bifurcations as the speed decreases from 4,100 to 3,500 to 2,900 rpm.

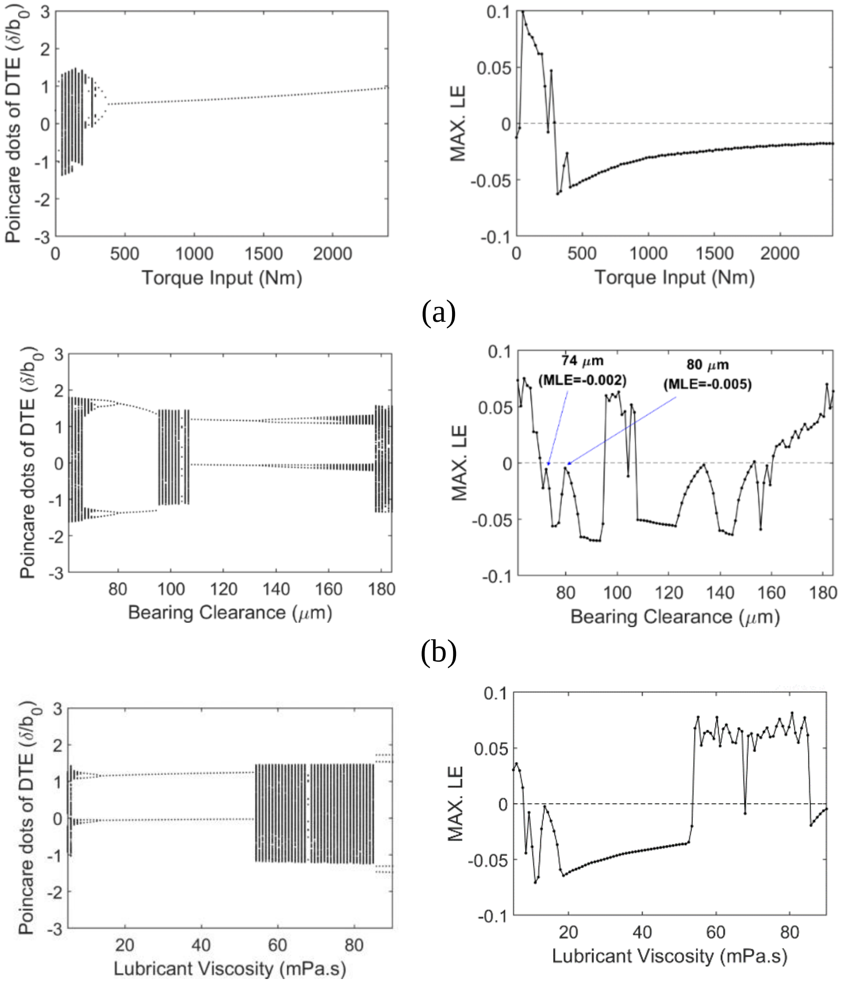

(a)

(b)

(c)

Figure 2.21 Bifurcation and MLE diagrams vs. (a) applied torque (0~2,400 N m), (b) bearing clearance (60 ~185 μm) and (c) lubricant viscosity (5 ~90 mPa s)

Figure 2.21 shows DTE bifurcation and MLE diagrams versus applied torque, journal bearing radial clearance and viscosity, at the fixed operating speed 1,540 rpm. The viscosity is held fixed at 30 mPa s, and the clearance is held fixed at 100 μm while varying torque in Figure 2.21 (a). The Fourier coefficient of the static transmission error in Eq. (2.2) is set to 0.15 and applied to the system. The sampling frequency of Poincaré dots is the gear mesh frequency ω_g.

The MLEs quantitatively confirm the existence of chaotic behavior. Figure 2.21 (a) presents the bifurcation diagram and MLE plot with applied torque ranging from 0 to 2,400 N m. Increasing the applied torque is seen to eliminate chaotic motion, and synchronous 1x motion appears at applied torques above 400 N m. The MLEs show positive values, indicating chaos, with low applied torque (< 400 N m). For instance, at 200 N m, the corresponding MLE has the positive value of $+0.07$.

The radial bearing clearance is varied from 60 to 185 μm in Figure 2.21 (b) with the rotor speed at 1,540 rpm and the lubricant viscosity of 30 mPa s. Chaotic motion occurs in three separate clearance ranges (i.e., 60~70 μm, 95~105 μm, 175~185 μm), and period-doubling routes to chaos with decreasing and increasing parameter values are observed in the ranges 60~80 μm and 130~180 μm, respectively. In Figure 2.21 (c), the applied torque is held fixed at 100 N m, and the clearance is held fixed at 100 μm while varying viscosity. The figure shows chaos appearing in two ranges of lubricant viscosity: over the ranges of 0~7 mPa s and 55~85 mPa s. All bifurcation diagrams in Figure 2.21

display the period-doubling route to chaos, which indicates that the system goes into chaotic states by doubling its period with increasing or decreasing control parameters.

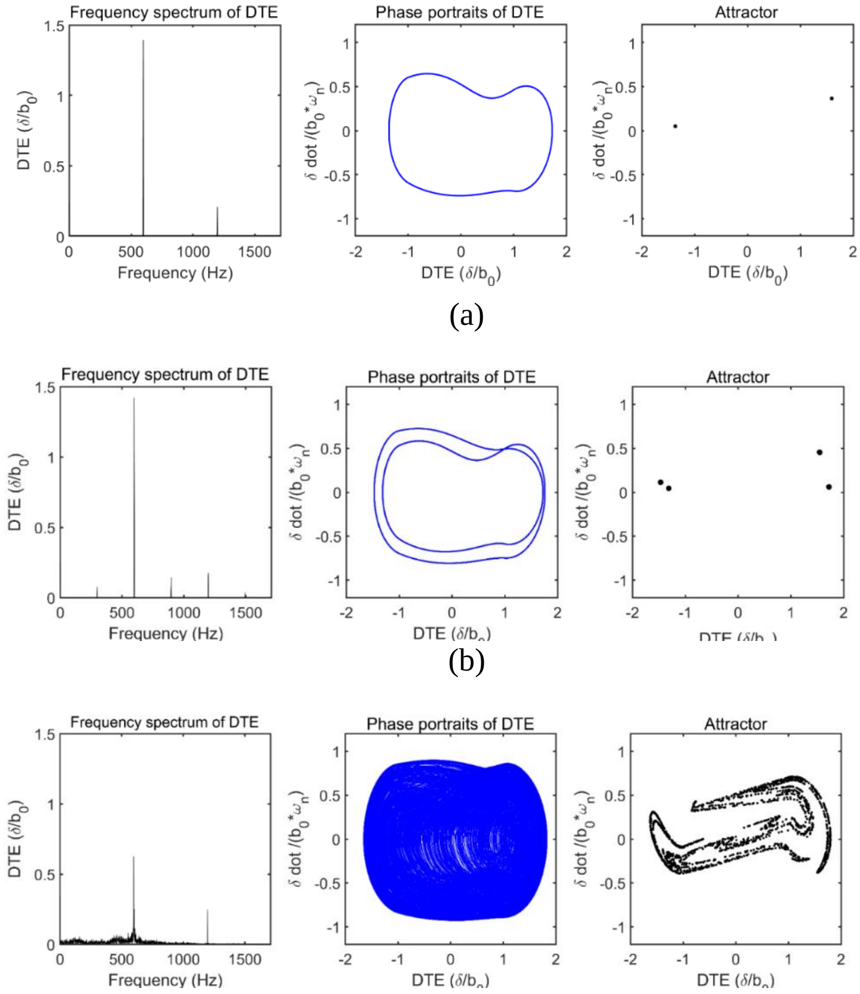

(a)

(b)

(c)

Figure 2.22 Frequency spectra, phase portraits and Poincaré attractors of dynamic transmission error (DTE) for different bearing clearances (a) 80 µm (b) 74 µm (c) 61 µm in Figure 2.21 (b)

The periodic, period-doubling and chaotic DTE behaviors implied in Figure 2.21 (b) for bearing clearance variation, are further confirmed in the frequency spectrum, phase portrait, and Poincaré attractor plots in Figure 2.22. Three radial bearing clearance values, i.e., 80, 74 and 61 μm, are examined. As can be seen by comparing Figure 2.21 (b) and Figure 2.22 (a) and (b), the geared system with MLE = -0.005 (80 μm case) and -0.002 (74 μm case) has period two and period four DTE responses, respectively, confirmed by the Poincaré attractors. The 61 μm bearing clearance case in Figure 2.22 (c) was selected to illustrate chaotic DTE response based on an MLE ($+0.06$), from Figure 2.21 (b). The phase portrait orbit has a clear aperiodic response, the frequency spectrum has a broadband character, and the corresponding Poincaré dots form a strange attractor. These results show that the system experiences period-doubling bifurcation with decreasing bearing clearance as the system transitions into chaotic responses.

2.4.3. Effect of gear mesh stiffness on oil whirl

Oil whirl is a rotor dynamics term describing a self-excited, shaft vibration anomaly common to rotating machinery supported by oil film, fixed pad, journal bearings. The dominant symptom of oil whirl is a sub-synchronous limit cycle vibration that is sustained by the journal bearing forces, as opposed to the external excitation such as rotor mass imbalance. In this section, the effect of gear mesh stiffness on the oil whirl instability is investigated. The bearing supported geared rotor pair is modeled as an autonomous (unforced) system with perfectly balanced rotors, and as such is analyzed utilizing the autonomous shooting method. The multiple shooting/continuation method for autonomous cases developed in section 3 is used for identifying periodic solutions.

This approach for drawing the bifurcation diagrams was incapable of finding the solutions near saddle-node bifurcations without manual assistance. The continuation algorithm was restarted near the saddle-node bifurcation points and the step size was reduced to help the solutions converge. This typically requires two or three restarts to plot one complete bifurcation diagram.

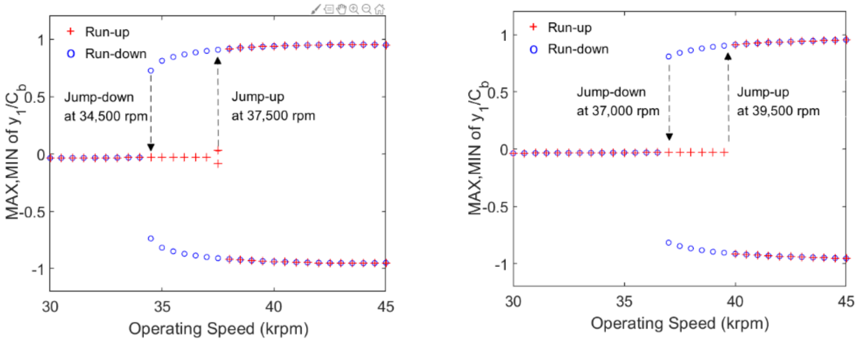

(a) (b)

Figure 2.23 Run-up and run-down simulations using direct numerical integration (a) mesh stiffness 1e7 N/m (b) mesh stiffness 1e9 N/m

Figure 2.23 shows a bifurcation diagram of the non-dimensional maximum and minimum vertical position of the rotor center in the load direction versus operating speed. Results are shown for two mesh stiffness values, i.e., k_0 = 1e7 N/m and 1e9 N/m. The input torque applied to the gear pair is 1,000 N m. Run-up/run-down simulations are conducted separately, using direct numerical integration, and the two results are combined to generate the figure. In Figure 2.23 (a), as the operating speed increases, the jump-up phenomenon is observed at 37,500 rpm, which corresponds to the onset speed of oil whirl. Jump-down frequency is also predicted at 34,500 rpm with run-down simulation, and consequently, the amplitude of vertical rotor response has been abruptly reduced at the same speed. The result with high mesh stiffness value, i.e., 1e9 N/m in Figure 2.23 (b), shows a delayed onset speed of oil whirl compared with 1e7 N/m case, such that the jump-up and jump-down frequencies are predicted at 39,500 and 37,000 rpm, respectively. From this result, it is verified that mesh stiffness variation not only affects the high frequency vibration in a geared system but also may change the characteristics of hydrodynamic stability of a geared system supported by journal bearings.

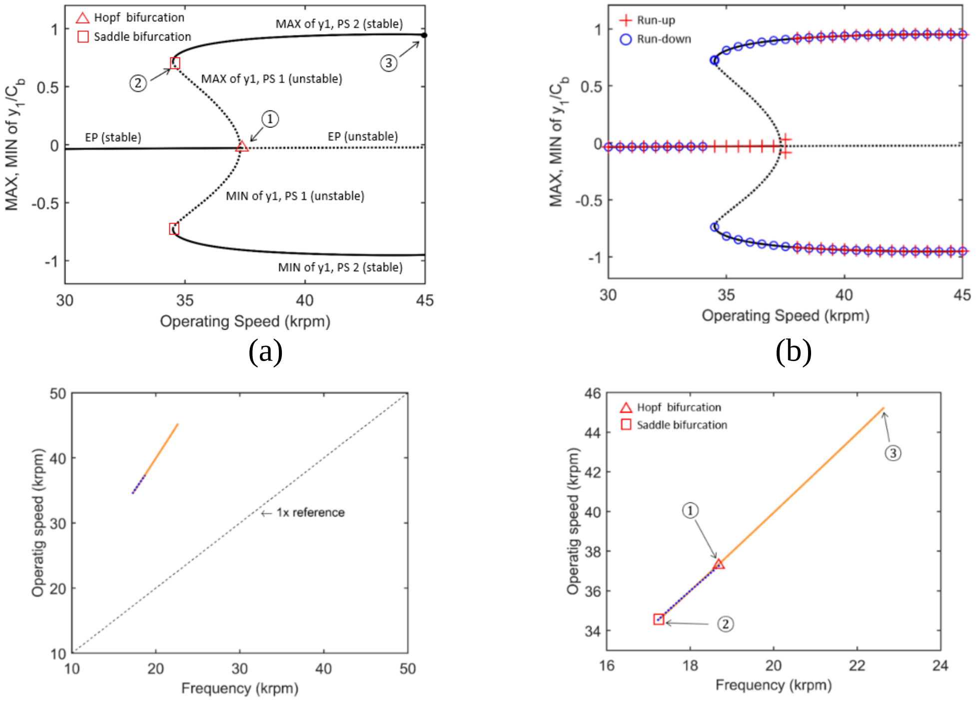

(a)

(b)

(c)

(d)

Figure 2.24 Bifurcation diagram using shooting/continuation method with mesh stiffness 1e7 N/m and applied torque 1,000 N m: (a) Bifurcation diagram using continuation algorithm, (b) result from continuation algorithm compared with numerical integration, (c) revolution speed versus response frequency and (d) zoom of (c)

It should be noted that the result with direct numerical integration is incapable of identifying co-existing solutions and the stability of responses. The bifurcation diagram is obtained with the continuation algorithm and the result is presented in Figure 2.24. In the case of mesh stiffness 1e7 N/m, in Figure 2.24 (a), the stable equilibrium position EP which is maintained over low operating speeds switches to unstable motion after crossing Hopf bifurcation point at 37,210 rpm. The transition from stable to unstable response is verified with the continuation algorithm, which provides the eigenvalues of the Jacobian matrix moving out of the unit circle in the complex plane. The point ① corresponds to a Hopf bifurcation, where an unstable subsynchronous response PS 1 emerges and approaches the saddle bifurcation point ②. The amplitudes of the maximum and minimum responses of PS 1 quickly grow as the speed decreases until the saddle point is reached. After the saddle bifurcation, the subsynchronous branch becomes the stable response PS 2 and its maximum and minimum amplitudes slowly approach the bearing clearance limit. The results using the continuation algorithm are drawn in the same figure with the direct numerical integration results in Figure 2.24 (b). Two results agree well throughout the all speed ranges, except the unstable subsynchronous response PS 1 is only predicted with the continuation algorithm. The vibration frequencies of the branches are shown in Figure 2.24 (c) and its zoomed version in (d). The frequency range where subsynchronous vibration was observed is located between 17,000 and 23,000 rpm, which corresponds to the 45~50% of operating speed.

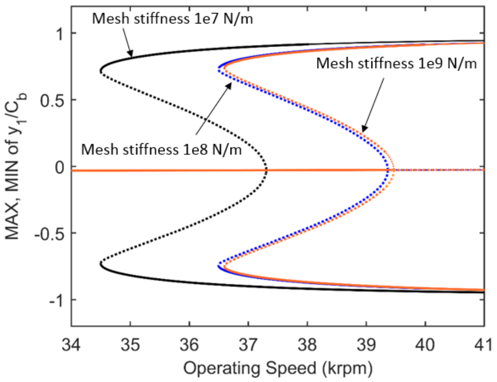

Figure 2.25 Bifurcation diagrams with various mesh stiffness values (1e7, 1e8 and 1e9 N/m) and with an applied torque of 1,000 N m

Bifurcation diagrams with three different mesh stiffness (1e7, 1e8 and 1e9 N/m) at 1,000 N m torque are drawn using the continuation algorithm in Figure 2.25. The onset speed of oil whirl is increased from 37,210 to 39,310 rpm as the mesh stiffness increases from 1e7 to 1e8 N/m. In contrast, the onset speed shift is relatively insignificant (110 rpm) between higher mesh stiffness cases, i.e., 1e8 and 1e9 N/m. This result shows that the gear and the journal bearing parameters are coupled and the variation of gear parameter may affect the hydrodynamic stability characteristics of fluid film bearings.

Applied torque	1e7 N/m	1e8 N/m	1e9 N/m	Onset speed difference
50 N m	10,450 rpm	10,480 rpm	10,490 rpm	40 rpm
200 N m	18,760 rpm	18,890 rpm	18,910 rpm	150 rpm
400 N m	25,360 rpm	25,780 rpm	25,800 rpm	440 rpm
600 N m	30,750 rpm	31,390 rpm	31,410 rpm	660 rpm
800 N m	34,780 rpm	36,070 rpm	36,130 rpm	1,350 rpm
1,000 N m	37,210 rpm	39,310 rpm	39,420 rpm	2,210 rpm

Table 2.3 Oil whirl onset speed with different torque and mesh stiffness (Identified utilizing Continuation algorithm)

The effect of applied torque on oil whirl onset speed was presented in [30, 33], and the results showed that higher applied torque on the geared system delayed the oil whirl onset speed. This aspect of applied torque effect on oil whirl onset speed may be affected by the amplitude of gear mesh stiffness. The interaction between the applied torque and gear mesh stiffness is investigated with various torque and mesh stiffness values in Table 2.3. Six applied torque amplitudes from 50 to 1,000 N m were applied as mesh stiffness varies from 1e7 to 1e9 N/m. The onset speed of oil whirl is identified by employing the continuation algorithm to find the speed where the jump-up phenomenon occurs. As observed in the reference [30, 33], the onset speed generally increases with higher applied torques for all three stiffness cases. From the table, it is also evident that the effect of mesh stiffness magnitude on the onset speed is closely related to the amplitude of torque values. When the lowest applied torque (50 N m) is applied, the onset speed delay caused by the mesh stiffness variation from 1e7 to 1e9 N/m is only 40 rpm. Meanwhile, the speed delay increases up to 2,210 rpm with the application of the highest torque value (1,000 N m). This result confirms that the transition of oil whirl onset speed with different mesh stiffness is less significant at lower applied torques.

3. TILTING PAD JOURNAL BEARING MISALIGNMENT EFFECT ON THERMALLY INDUCED SYNCHRONOUS INSTABILITY (MORTON EFFECT)*

3.1. Introduction

The present study reveals a marked dependence of the ME on tilting pad journal bearing misalignment. This is established utilizing a high-fidelity model described with three-dimensional (3D) THD models of the fluid film, and 3D solid FEM bearing, and shaft structure models discussed in section 2. The journal misalignment model is included in the high fidelity bearing model, and the influence of its asymmetric fluid film distribution on the ME occurrence is investigated. The impact of pad-pivot type on the ME, with journal misalignment, is also considered.

3.2. Modeling and ME prediction algorithms

3.2.1. Tilting pad journal bearings

The Reynolds equation for an incompressible Newtonian fluid with variable fluid viscosity and negligible fluid inertia/shaft curvature is

$$\nabla \cdot (C_1 \nabla P) + \nabla D_2 \cdot U + \partial h / \partial t = 0 \tag{3.1}$$

where C_1 and C_2 are constants related to variable viscosity μ.

$$C_1 = \int_0^h \int_0^z (\xi / \mu) d\xi dz - C_2 \int_0^h (\xi / \mu) d\xi \text{ , } C_2 = \int_0^h \int_0^z (1/\mu) d\xi dz \Big/ \int_0^h (1/\mu) d\xi$$

---

* Reprinted with permission from "Tilting pad journal bearing misalignment effect on thermally induced synchronous instability (Morton effect)" by Shin, D., and Palazzolo, A., 2020. Journal of tribology, 143(3), 031802, Copyright [2020] by ASME

where z is the axial coordinate of the fluid film bearing

This form assumes laminar flow, uniform pressure distribution in the direction of film thickness, constant fluid density, and temperature-dependent variable viscosity. The viscosity-temperature relation is

$$\mu = \mu_0 e^{-\alpha(T-T_0)} \tag{3.2}$$

where α is the coefficient of viscosity, and μ_0 and T_0 are the reference viscosity and temperature, respectively. The fluid film temperature T is solved for with the energy equation which is coupled with the Reynolds equation through the viscosity and velocity terms. The pressure distribution obtained from the Reynolds equation is utilized to obtain the fluid velocity from the relation

$$u = \left(\int_0^z (\xi/\mu)d\xi - \int_0^h (\xi/\mu)d\xi \frac{\int_0^h (1/\mu)d\xi}{\int_0^h (1/\mu)d\xi} \right) \nabla p + \frac{\int_0^z (1/\mu)d\xi}{\int_0^h (1/\mu)d\xi} U \tag{3.3}$$

The ∇p term is calculated in both the circumferential and axial directions for a full 3D thermo-hydro-dynamic analysis. The Reynolds cavitation model, which imposes a zero-pressure gradient at the cavitation boundary is utilized in the Morton effect simulations. This approach is widely utilized in the literature about journal misalignment [55,99,100]. Moreover, significant thermal expansion of the shaft and bearing pad accompanies the Morton effect. This decreases the film thickness significantly, which tends to suppress cavitation, as evidenced in the simulation results. Of course, more sophisticated, and more computationally intensive, cavitation models can be applied. This will be done in future work.

The two types of pad-pivots studied are cylindrical and spherical. The cylindrical pivot has angular pad tilting (pitch), and translational pivot motion (deformation), and the spherical pivot has rolling and yawing motions in addition to those of the cylindrical pivot. The model for journal and pad dynamics is illustrated in Figure 3.1 (a).

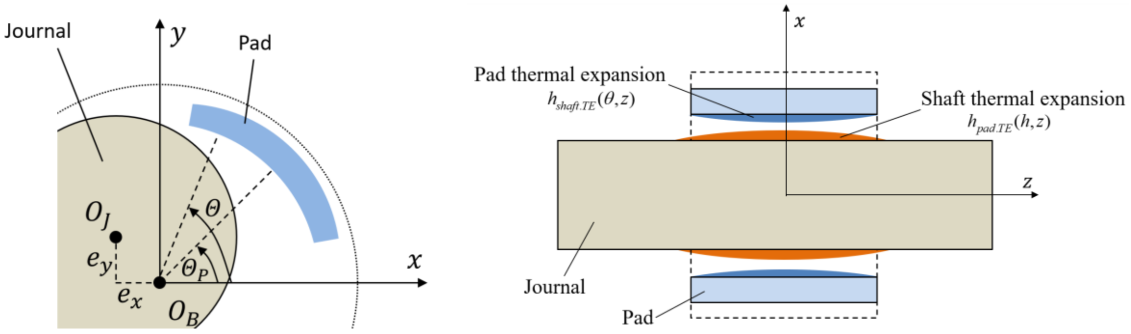

(a) (b)

Figure 3.1 (a) Model for journal dynamics and (b) Thermal expansion of pad/shaft

The film thickness formula for the spherical- type pivot TPJB is

$$\begin{aligned}h(\theta,z) &= C_P - \hat{e}_x\cos(\theta) - \hat{e}_y\sin(\theta) - (C_P - C_b)\cos(\theta-\theta_P)\\ &-\delta_{tilt}R\sin(\theta-\theta_P) - h_{shaft.TE}(\theta,z) - h_{pad.TE}(h,z)\end{aligned} \tag{3.4}$$

where

$$\hat{e}_x = e_x - y_{pvt}\cos\theta_p - z\alpha_{roll}\cos\theta_p - z\beta_{yaw}\cos(\theta_p+\pi/2)\,,$$

$$\hat{e}_y = e_y - y_{pvt}\sin\theta_p - z\alpha_{roll}\sin\theta_p - z\beta_{yaw}\sin(\theta_p+\pi/2)\,.$$

and

- C_p and C_b represent pad and bearing radial clearances.
- y_{pvt}, δ_{tilt}, α_{roll}, β_{yaw} are the pad-pivot deformation, and tilting, rolling and yawing pad angular displacements, respectively.
- z and R are the axial position and the journal radius, respectively.
- θ and θ_p are the circumferential coordinate of the bearing and pivot circumferential positions, respectively as shown in Figure 3.1 (a).

Equation (3.4) considers the journal/bearing pad's asymmetric thermal expansion, the variation of axial and circumferential motions of pads and deformation due to pivot compliance. The terms $h_{shaft.TE}$ and $h_{pad.TE}$ in Eq. (3.4) are the thermal expansions of the shaft and pads as illustrated in Figure 3.1 (b). For the cylindrical pivot-type model, the terms related to roll α_{roll} and yaw β_{yaw} motions are removed from the equation.

Journal misalignment is an imposed shift in angular position of the bearing or shaft. The misalignment term is incorporated into Eq. (3.4) by adding the terms α_x and α_y which represent the journal angular displacements in the $x-z$ and $y-z$ planes, respectively, as illustrated for α_y in Figure 3.2.

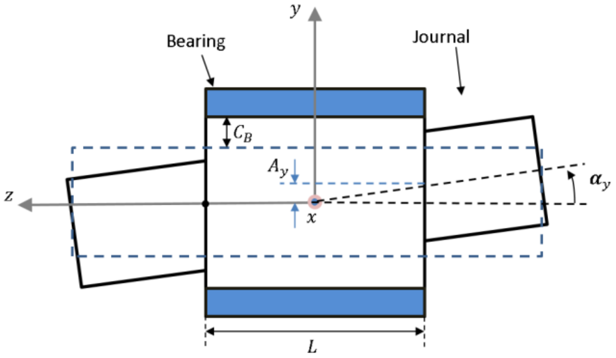

Figure 3.2 Permanent misalignment angle α_y

The misalignment ratio, misalignment angle, and misalignment phase are defined as

$$r_y = \frac{A_y}{C_B},\ r_x = \frac{A_x}{C_B}$$
$$\alpha_y = A_y \frac{2}{L},\ \alpha_x = A_x \frac{2}{L} \tag{3.5}$$
$$r_\alpha = \tan^{-1} \frac{\alpha_y}{\alpha_x}$$

where A_y is the journal/bearing relative, end displacement due to α_y, and C_B L are the bearing radial clearance and length. The misalignment ratio and angle α_x in the $x-z$ plane have similar definitions. For characteristically small misalignment angles $\sin\alpha_y = \alpha_y$ applies. Then the updated equations for $\hat{e}_x$ and $\hat{e}_y$ with the misalignment terms become

$$\hat{e}_x = e_x - y_{pvt}\cos\theta_p - z\alpha_{pitch}\cos\theta_p - z\beta_{yaw}\cos(\theta_p + \pi/2) + z\alpha_x \tag{3.6}$$

$$\hat{e}_y = e_y - y_{pvt}\sin\theta_p - z\alpha_{pitch}\sin\theta_p - z\beta_{yaw}\sin(\theta_p + \pi/2) + z\alpha_y$$

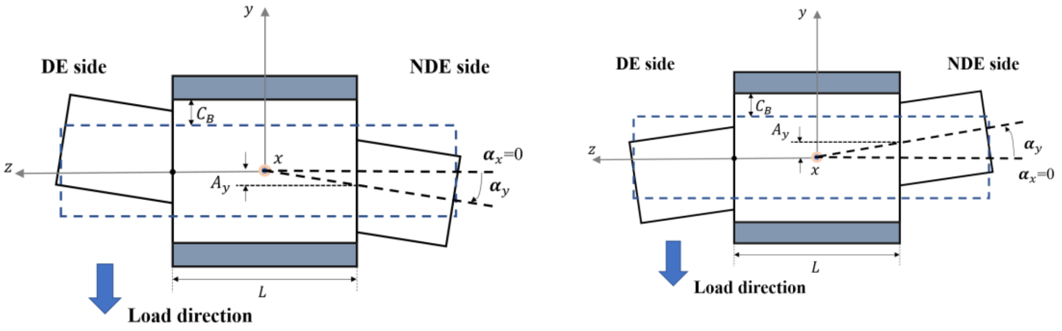

(a) (b)

Figure 3.3 Configuration of journal misalignment phase directions (a) $r_\alpha = 90°$ **and (b)** $r_\alpha = 270°$

Two configurations of misalignment, i.e. $r_\alpha = 90°$ and $270°$ are illustrated in Figure 3.3 to explain the misalignment phase. Note that the right side of the shaft in the figure is the non-drive end (NDE) side while the other side is the drive end (DE). For both configurations, the misalignment ratio in the x direction is zero ($r_x = 0$). If the r_y value is non-zero and positive, the misalignment angle will be 90° from Eq. (3.5), and it corresponds to the case in Figure 3.3 (a).

The 270° misalignment angle case in Figure 3.3 (b) has the same magnitude of misalignment ratio as the 90° case but with opposite sign, and this makes the misalignment phase of this case equal to −90° (=270°) based on Eq. (3.5).

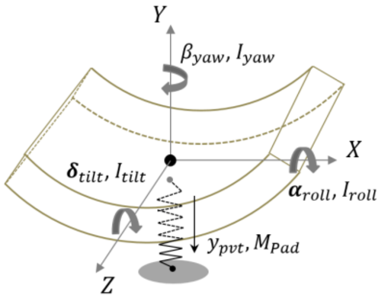

Figure 3.4 Spherical pad-pivot type tilting pad dynamic model

The equations for the tilting pad journal bearing with spherical pivot-type pads in Figure 3.4 with small motions are [55]

$$
\begin{aligned}
M_{pad\_i}\ddot{y}_{pvt} &= -K_P y_{pvt} + F_{pad\_i} \\
I_{tilt\_i}\ddot{\delta}_{tilt} &= MO_{tilt\_i} \\
I_{roll\_i}\ddot{\alpha}_{roll} &= MO_{roll\_i} \\
I_{Yaw\_i}\ddot{\beta}_{yaw} &= MO_{yaw\_i}
\end{aligned}
\qquad (3.7)
$$

where i represent the number of pads, M_{pad_i}, I_{tilt_i}, I_{roll_i} and I_{Yaw_i} are the mass and the tilting/rolling /yawing inertias of each pad, respectively, and F_{pad_i}, MO_{tilt_i}, MO_{pitch_i} and MO_{yaw_i} represent the fluid film force and the tilting/rolling /yawing moments applied to a pad, respectively. The equations can be applied to a cylindrical pivot-type tilting pad journal bearing by removing the rolling and yawing motions from Eq. (3.7).

3.2.2. Thermal model – 3D energy equation

The energy equation

$$\rho c(u\frac{\partial T}{\partial x}+w\frac{\partial T}{\partial z})=k(\frac{\partial^2 T}{\partial x^2}+\frac{\partial^2 T}{\partial y^2}+\frac{\partial^2 T}{\partial z^2})+\mu\left[(\frac{\partial u}{\partial y})^2+(\frac{\partial w}{\partial y})^2\right] \qquad (3.8)$$

is solved utilizing eight-node isoparametric finite elements to obtain the 3D temperature distribution T across the fluid film. The quantities in (8) are the film temperature T, density ρ, specific heat capacity c, thermal conductivity k, circumferential velocity u, and axial velocity v. The convection term in the film thickness direction is not considered due to the assumed thin film (bearing radial clearance 68 μm, bearing radius 40 mm) while the conduction term is considered in all x, y and z directions. This approach is commonly used in the literature [102-104]. The fluid film temperature T is obtained during each journal orbit by solving Eq. (3.8) employing the variable viscosity μ relation in Eq. (3.2), as discussed in section 3. The pad inlet boundary temperature is obtained from the mixing theory in [41]. An up-winding scheme [105] is employed in the finite element solution of Eq. (3.8) to avoid spatial oscillations due to the convective term. The film temperature is modeled as a quasi-steady state problem.

Shaft and pad temperatures are predicted with the Laplace equation

$$\frac{\partial^2 T}{\partial x^2}+\frac{\partial^2 T}{\partial y^2}+\frac{\partial^2 T}{\partial z^2}=\frac{\rho c}{k}\frac{\partial T}{\partial t} \qquad (3.9)$$

assuming constant thermal conductivity. Utilizing 3D eight-node isoparametric FEM, the discrete form of (9), i.e.

$$[C][\dot{T}]+[K][T]=0 \qquad (3.10)$$

The transient solution of Eq. (3.10) is obtained via numerical integration. The solid finite element, thermal model extends 7 times the journal length, either side of the journal, in the present model. This is based on simulations that showed little change in temperatures incurred by larger extensions. Of course, the extension lengths could be varied in actual applications. Convection to ambient atmosphere is assumed to occur outside of the journal.

3.2.3. Thermal deformation of the shaft and bearing

The hybrid beam and solid element, structural finite element model HFEM shown in Figure 3.5 is employed to determine deformations resulting from the asymmetric temperatures in the journal and adjacent rotor segments while exploiting the computational efficiency of beam finite elements.

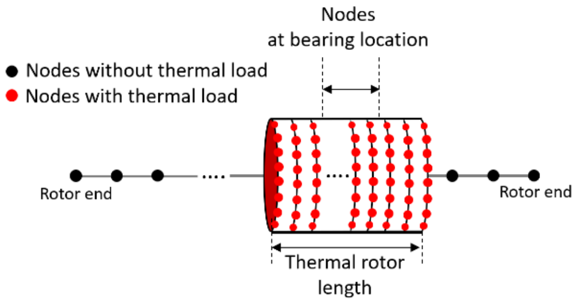

Figure 3.5 Diagram illustrating the HFEM rotor structural model

The solid finite element model extends 7 times the journal length in the present model based on simulations that showed little change incurred by larger extensions. Of course, the extension lengths could be varied in actual applications. Thermal deformations of the shaft and bearing are obtained from discrete FE equation of the form

$$[K_{\Delta T}][D_{\Delta T}]=[F_{\Delta T}] \tag{3.11}$$

where $D_{\Delta T}$ is the nodal displacement vector in x, y and z directions induced by the thermal load vector $F_{\Delta T}$ which is obtained from the temperature fields determined from Eq.(3.10). Details of the thermal bow calculation utilizing the HFEM are provided in [46]. The thermal bow is calculated in the rotating reference frame and becomes a dynamic force in the stationary frame equations of motion.

3.2.4. Thermal boundary conditions on the shaft and pads

Thermal boundary conditions are applied at interfaces between the fluid (lubricant) and structures (bearing pad and journal), and between the shaft and atmosphere as shown in Figure 3.6.

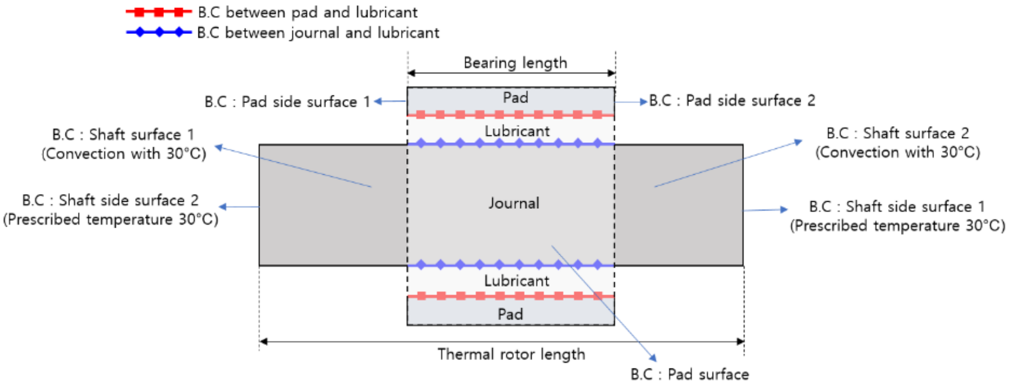

Figure 3.6 Thermal boundary conditions on rotor and bearing surfaces

Heat flux and temperature boundary conditions are imposed at the interface between the lubricant and pad

$$\begin{aligned} &k_L \left.\frac{\partial T_L}{\partial r}\right|_{r=R+H} = k_B \left.\frac{\partial T_B}{\partial r}\right|_{r=R+H} \\ &T_L\big|_{r=R+H} = T_B\big|_{r=R+H} \end{aligned} \tag{3.12}$$

The heat flux and temperature boundary conditions at the lubricant-journal interface are

$$\begin{aligned} &k_L \left.\frac{\partial T_L}{\partial r}\right|_{\theta=0,r=R} = k_J \left.\frac{\partial T_J}{\partial r}\right|_{\theta=-\omega t,r=R} \\ &T_L\big|_{\theta=0,r=R} = T_J\big|_{\theta=-\omega t,r=R} \end{aligned} \tag{3.13}$$

These conditions must be applied in the rotating frame for the journal mesh which is continuously re-oriented during the time transient simulation. Thermal boundary conditions are applied at the following surfaces in Figure 3.6; two bearing pad side surfaces, one bearing pad surface, two shaft side surfaces, and two journal surfaces.

3.2.5. Rotor dynamic model

Lateral dynamics utilizes Euler beam elements, and modal reduction is employed for computational efficiency. The system equations of motion are

$$\left[\dot{U}\right] = [D][U] + [F] \tag{3.14}$$

where $[U] = \begin{bmatrix} \dot{Z} \\ Z \end{bmatrix}$, $[D] = \begin{bmatrix} -M_{ro}{}^{-1}C_{ro} & -M_{ro}{}^{-1}K_{ro} \\ 1 & 0 \end{bmatrix}$, $[F] = \begin{bmatrix} M_{ro}{}^{-1}F_{ro} \\ 0 \end{bmatrix}$. U, M_{ro}, C_{ro} and K_{ro}

are the state vector and mass, damping and stiffness matrices of the rotor, F_{ro} is the force vector including the nonlinear fluidic forces from the bearings, imbalance forces, forces induced by thermal bow and gravity, etc.

Equation (14) is diagonalized utilizing biorthogonality with the right eigenvector ψ_R and left eigenvector ψ_L of the matrix $\left[D\right]$. Equation (14) becomes

$$\left[\dot{Y}\right]=\left[A\right]\left[Y\right]+[\psi_L^T]\left[F\right] \tag{3.15}$$

where $\left[Y\right]=\left[\psi_R\right]\left[U\right]$, $[A]=[\psi_{Lm}^T][D][\psi_{Rm}]=\begin{cases}\lambda_i & if \quad m=n \\ 0 & if \quad m\neq n\end{cases}$. λ_i is the i_{th} eigenvalue of the system. Modes five times larger than spin speed are ignored to reduce the computational complexity. Equations (7) and (15) are solved simultaneously with numerical integration.

3.3. Morton effect computation algorithm

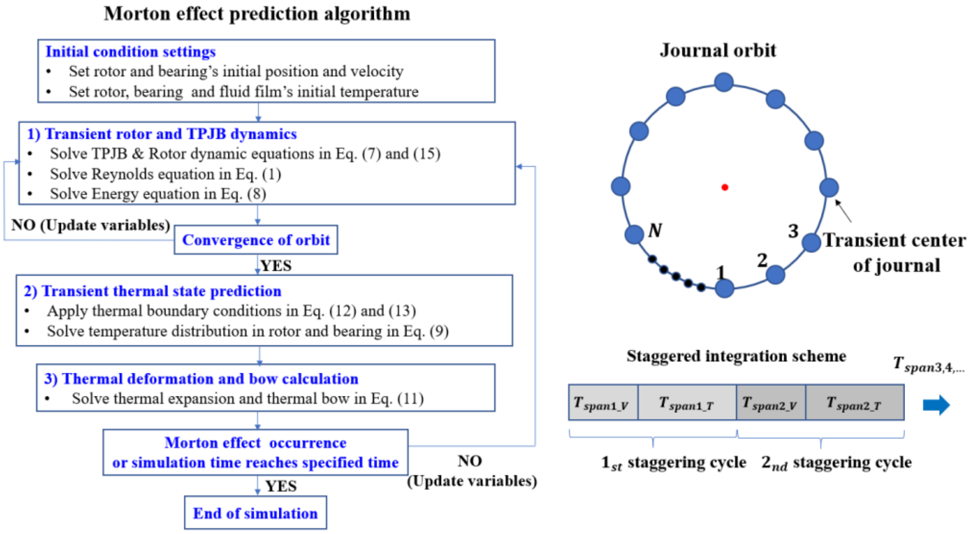

Figure 3.7 Algorithm for Morton effect transient simulation

The diagram describing the ME transient simulation algorithm is presented in Figure 3.7. The initial conditions of the rotor-bearing state variables, lubricant/shaft/bearing pad temperature distribution, and thermal expansion and bow states are specified at the start of the simulation. To perform 1) the transient rotor and TPJB dynamics are solved by numerical integration, until the rotor orbits converge to steady-state, utilizing the rotor-bearing dynamic equations in Eq. (3.7) and (3.15) with the film thickness and journal misalignment formulae in Eq. (3.4), (3.5) and (3.6), the Reynolds equation in Eq. (3.1) and the energy equation in Eq. (3.8). The fluid velocities from Eq. (3.3) are obtained from the Reynolds equation and are employed in the energy equation solution. Each journal orbit is both temporally and spatially divided into N

steps as illustrated in Figure 3.7. The energy equation is solved at the end of each of the N steps, in order to 1) obtain the orbit-averaged lubricant temperature and the flux boundary conditions of fluid-structure interfaces (lubricant/bearing and lubricant/journal), and to 2) update the variable viscosity in Eq. (3.2). Then the Reynolds equation, combined with the dynamic equations, are also solved at every orbit segment with the updated variable viscosity from the previous step. Once the orbit of journal converges to its steady-state the 2) transient thermal state predictions for the shaft and bearing pads are completed based on the lubricant temperature distribution and flux boundary conditions obtained in the previous step 1). The prescribed convective thermal boundary conditions on the shaft and bearing pad outer surfaces, and the lubricant's thermal states obtained at the journal/lubricant and lubricant/bearing pad interfaces in Eq. (3.12) and (3.13), provide the thermal boundary conditions for solving the shaft/bearing pad conduction problems Eq. (3.9).

The thermal expansions of shaft/bearing pads and the thermal bow amplitudes of the shaft are calculated based on Eq. (3.11) in step 3). All steps in 1) – 3) will be repeated until the ME instability criteria discussed in Section 4 are met, or until the limit time is reached. Updated variables are utilized in this process, including the fluid and structural temperature distributions, the new film thickness reflecting the calculated thermal expansion of the shaft and pads, the thermal bow of the shaft, the lubricant viscosity, and the thermal boundary conditions on shaft/pads.

The rotordynamic structural states change with extremely short time constants compared with the thermal variable time constants. Thus, integrating both problems with the same numerical integration time step is computationally impractical and unnecessary, and the staggered–time-integration technique in Figure 3.7 is applied. In the 1_{st} stagger cycle, the rotordynamic equations including the rotor and bearing structures are numerically integrated with the time step of T_{span1_V} , with invariant rotor and bearing temperatures/deformations/bow during the one orbit period. Next, the temperature distributions of the structures are calculated with the larger time constant of T_{span2_V} , while the rotor/bearing motion states are held invariant. The use of different time steps in T_{span1_V} and T_{span2_V} is justified due to the much slower heat transfer process compared with the rotordynamic motions. A quicker simulation is achieved without overly sacrificing accuracy. Heat flux and temperature continuity at the film–solid interfaces are explicitly enforced at all simulation times in our model. In particular, this is performed in the staggered time approach, where the shaft orbit is constant during the thermal solution update.

For the steady-state transient simulation, the transient simulation explained above starts from the lowest speed of interest and simulates the rotor-bearing system response until either steady-state or an unacceptable vibration level (caused by the ME) occurs. Then the process stops and repeats the simulation at the next higher speed. Steady-state occurs if the errors between the temperature and dynamics states of the entire rotor-bearing system at the previous time step, and at the current time step, are less than the specified error criteria. The final temperature/dynamic states of the previous speed are transferred to the initial conditions for the next speed to improve the computational efficiency of the process. When the unstable rotor response is detected, the initial states of the next speed is determined by the average of the final state of the previous step, and the initial states of the highest operating speed just below the instability onset speed. The linear method [46] provides an alternative approach and estimates stiffness and damping coefficients of the bearings and combines them into the rotor matrix to formulate the system matrix. The rotor-bearing dynamic response is calculated at different operating speeds instead of calculating the bearing hydrodynamic forces at each time step as in the nonlinear transient method. The linear method calculates the lubricant temperature and variable viscosity at each orbit segment. However, this method is inherently inaccurate compared with the nonlinear transient method because; 1) the responses determined utilizing the dynamic coefficients calculated at the journal equilibrium position become inaccurate when the orbit size becomes large, and 2) the linear method neglects the inertial forces resulting from the thermal bow caused by the viscous heating.

3.4. Simulation results

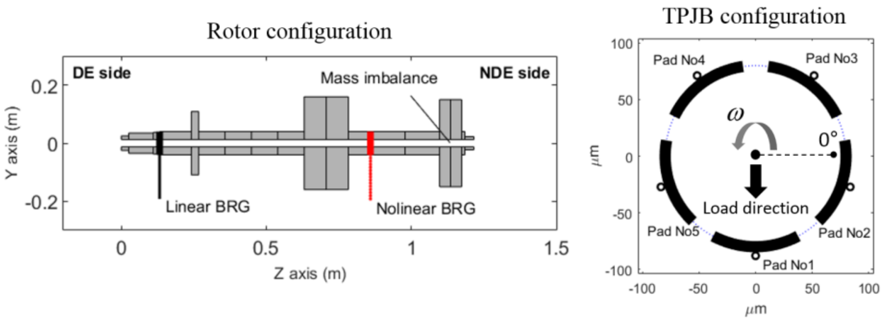

Figure 3.8 Example rotor-bearing configuration

Figure 3.8 shows a single overhung, example rotor with a linear bearing (node 4) at the drive end DE side and a nonlinear bearing (node 13) at the non-drive end NDE side. A mass imbalance is located at node 16 along with the NDE overhung mass of $40kg$. The TPJB at the NDE side has five tilting pads with a load-on-pad configuration as shown in Figure 3.8. The parameters of the example rotor-bearing configuration are listed in Table 3.1. The thermal boundary conditions illustrated in Figure 3.6 are applied on the rotor and the bearing pad surfaces with a convection coefficient of 50 W/m^2K and the ambient temperature of $30°C$. These parameter values are utilized for all simulations except for the Rotor 2 case in section 4, which has an increased bearing radial clearance, compared with that of the original rotor. A case was run with the rotor convection coefficient equal to 250 W/m^2K outside the bearing, and the results showed no influence on the predicted response with the Morton effect. Therefore, all cases utilized 50 W/m^2K . The Rotor 1 case is defined with the original parameter values as shown in Table 3.1. The mesh sizes of the FEM are 40x7x17 (circumferential, radial and axial directions) for both the thermal and temperature predictions, 15x7x7 for the lubricant film and 15x8x8 for the energy equation solvers, and the numerical tolerances of the Matlab ODE are selected as $1e^{-5}$ for absolute and $1e^{-4}$ for relative, respectively. A convergence test was performed with three times the current mesh size, and with tolerances of $1e^{-7}$ and $1e^{-6}$, and the results showed quite similar results with the presented predictions.

Lubricant parameters		**Bearing parameters**	
Viscosity at 50 ℃ [$Ns/m2$]	0.0203	Pad type	Load on pad
Viscosity coefficients [$1/°C$]	0.031	No. pads	5
Supply temperature [$°C$]	50	Radius of shaft [m]	0.04
Inlet pressure [Pa]	$1.32×10^5$	Bearing clearance (C_b) [m]	$6.8×10^{-5}$
Reference temperature [$°C$]	50	Preload	0.25
Rotor Parameters		Bearing length [m]	0.06
Heat capacity [J/kg $°C$]	453.6	Thermal expansion coefficient [$1/°C$]	$1.1×10^{-5}$
Heat conductivity [W/mK]	50	Reference Temperature [$°C$]	30
Thermal expansion coefficient [$1/°C$]	$1.22×10^{-5}$	Pad pivot stiffness [N/m]	4e8
Reference temperature [$°C$]	25	Pivot offset	0.5
Rotor length [m]	1.214	**Linear Bearing**	
Rotor inner diameter [m]	0.0254	Kxx, Kyy [N/m]	$1.7×10^8$
Rotor outer diameter [m]	0.08	Cxx, Cyy [Ns/m]	$1.0×10^5$
Mass of wheel 1 [kg]	6.43	**Thermal boundary conditions**	
Mass of wheel 2 [kg]	90	Temperature on shaft surface [$°C$]	30
Mass of overhung wheel [kg]	40	Temperature on bearing surface [$°C$]	30
Initial(mechanical) imbalance [$kg.m$]	6.5e-5	Convection coefficient [W/m^2K]	50
		Thermal rotor length [m]	0.18

Table 3.1 Parameter values for the example system

The ME is a fully nonlinear phenomenon producing a synchronous 1x instability, as compared with typical linear instability resulting from positive real part eigenvalues. A ME instability is defined here as when the rotor vibration and journal ΔT increases abruptly, and the minimum film thickness drops below 10% of C_b at constant operating speed, while the corresponding system without ME has acceptable vibration and minimum film thickness levels. A linear analysis is conducted to identify the critical speeds, mode shapes, damped unbalance response and damping ratio of the system as shown in Figure 3.9. The linear analysis result is included solely for comparison with the ME response, and is obtained from conventional rotodynamic analysis. The linearized bearing coefficients are obtained from a THD model which includes solutions for temperature and viscosity distributions by solving the energy equations in the film and bearings. The ME thermal bow effect is not included. This utilizes the Rotor 1 bearing's linearized damping and stiffness coefficients as explained in section 3, neglects bearing misalignment, and utilizes a constant imbalance for all speeds. Figure 3.9 (a) shows a large vibration level near the rotor's third critical speed of 6,343 rpm, with corresponding damping ratio 0.05 detected at both the NDE bearing and rotor end locations. Figure 3.9 (b) shows that overhung disc modal displacement are significantly larger than the corresponding bearing components, in the bending (critical speed) mode at 6,343 rpm.

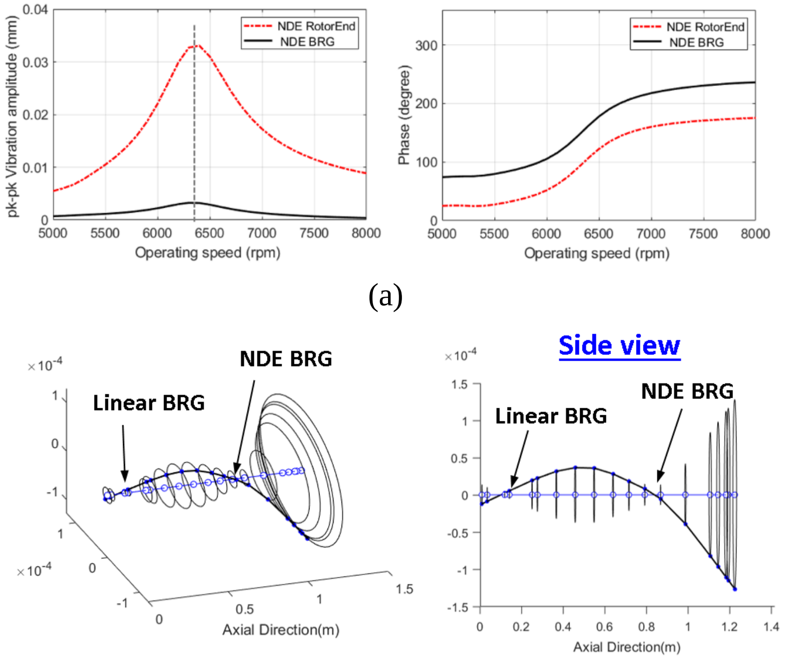

(a)

(b)

Figure 3.9 Rotor 1 (a) imbalance response amplitude and phase lag, and (b) mode shape of the third critical speed at 6,343 rpm

Case histories of the ME [38, 47] showed ME instability near the bending critical speeds of the rotor. The journal *Δ*T (temperature differential across a journal diameter) is the root cause of the thermal bow and is induced by synchronous rotor vibration, which is typically peaks at a critical speed. Prior ME studies [47] revealed that larger imbalance force induces larger orbit size, and journal ΔT. Machines operating near the bending critical speed typically amplify synchronous vibration of the rotor, which could lead to increased journal ΔT, and resultant thermal bow. Then the thermal deflection will more dramatically increase with an overhung bending mode shape, compared with other mode shapes, even with identical values of journal ΔT [47].

Figure 3.10 shows the effect of bearing misalignment on linear unbalance response amplitude. The applied misalignment ratios are $r_x = 0$ and $r_y = 0.3$, respectively, which correspond to a misalignment phase of 90° from Eq. (3.5). Based on Eq. (3.5), and the bearing parameters in Table 3.1, the $r_m = \sqrt{r_x^2 + r_y^2} = 0.3$ misalignment ratio results in a misalignment angle of $\alpha_y = 0.00086\ rad$ and resultant misalignment displacement $A_y = 0.0258mm$. Figure 3.10 shows the vibration amplitudes at the NDE bearing location and the rotor end increase slightly with bearing misalignment. The critical speeds are almost identical with 6,343rpm for the aligned journal and 6,346rpm for the misaligned journal. The increments of vibration level between the aligned and misaligned cases at 6,343 rpm are 0.000146mm at the NDE bearing, and $0.0183mm$ at the rotor end, respectively. The damping ratios of the aligned and misaligned cases are quite similar with 0.05 and 0.0466, respectively. With the slightly smaller damping ratio for with-misalignment, the misaligned rotor's vibration amplitude shows a slightly increased vibration amplitude.

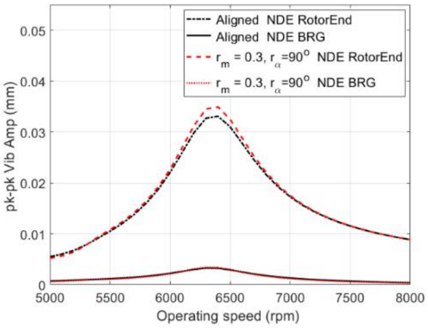

Figure 3.10 Rotor 1's damped unbalance responses for aligned and misaligned cases

Both bearing clearance and misalignment were varied to investigate their influences on the ME utilizing the nonlinear transient model. The rotor with parameters in Table 3.1 is referred to as Rotor 1, and an identical rotor with increased bearing radial clearance is referred to as Rotor 2.

Steady-state simulations, using the nonlinear transient model explained in section 3, were conducted with aligned and misaligned journals at various speeds. The operating speed is varied from 6,000 rpm to 6,700 rpm with speed increment of 10 rpm.

Steady-state transient simulation results for the Rotor 1 case (original parameters) are presented in Figure 3.11 and 12. Figure 3.11 (a) shows the NDE bearing location pk-pk vibration amplitude. For the misaligned journal case, the misalignment ratios are $r_x = 0$ and $r_y = 0.3$, corresponding to 90° of misalignment phase as shown in Figure 3.3. ME instability speed ranges for the aligned and misaligned cases are shown. The simulation terminates if the journal motion reduces the minimum film thickness below 10% of the bearing clearance, since this clearly establishes the occurrence of a severe Morton effect event, with vibration levels far exceeding API recommended shutdown levels. This high vibration is indicative of a near rub condition, however the simulation is terminated before rub actually occurs. The instability onset speed (IOS) is identified as the operating speed where vibration level abruptly increases. The misaligned journal exhibits the IOS at 6,150rpm which is 90 rpm lower than the aligned case (6,240rpm).

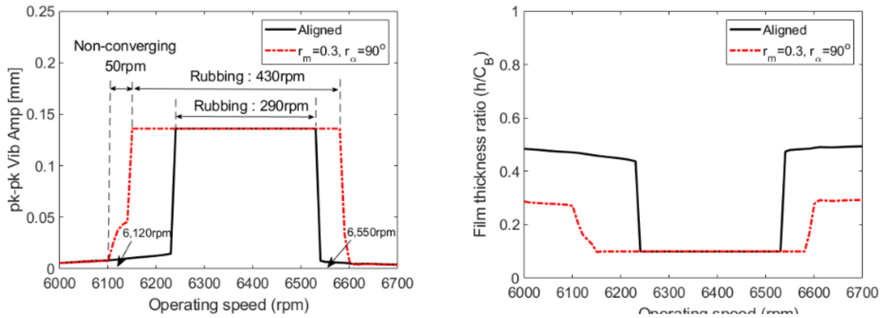

(a) (b)

Figure 3.11 Comparison of Rotor 1 (a) pk-pk vibration at the NDE bearing position and (b) minimum film thickness ratio

The pk-pk vibration of the misaligned journal shows an acceptable level above 6,580rpm. The instability speed range (ISR) of the misaligned case is 430rpm (6,150rpm~6,580rpm) over the operating speed range (6,000rpm~6,7000rpm) while the ISR of the aligned journal is 310rpm (from 6,240 rpm to 6,530 rpm). This shows that the machine with the misaligned journal may experience ME instability at lower speeds, and that the unstable vibration is sustained over a wider speed range compared with the aligned case. The misaligned case also shows a speed range where ME instability occurs but not converge or lead to an unacceptable vibration level, as illustrated between 6,100 to 6,150 rpm in Figure 3.11. Comparison of Figure 3.10 and 11 show that although misalignment has a significant influence on the ME IOS, it has little influence on the critical speed. This stands in contrast to changing other parameters such as lubricant viscosity/temperature, bearing clearance, and overhung mass, which shift the IOS and significantly change the critical speed [47].

Figure 3.11 (b) shows the minimum film thickness ratio for the aligned and misaligned cases. The ISR which corresponds to where the minimum film thickness ratio is 10% of C_b is seen to be identical to the range of large pk-pk vibration in Figure 3.11 (a). It is notable that the minimum film thickness ratios of the misaligned case are less than those of the aligned case in all speed ranges. The decreased minimum film thickness ratio is attributed to the displacements of the journal in the journal misalignment direction. In the linear analysis in Figure 3.10, the damped unbalance response and damping ratio of the aligned and misaligned cases showed quite similar results, indicating no significant vibration level change in the presence of the misalignment. Unlike the linear analysis of Figure 3.10, the nonlinear transient simulation revealed significant ME related vibration is only present in the misaligned journal case at specific speed ranges. This is explained by the induced hot/cold spots and thermal bow effect caused by the decreased minimum film thickness, which can be only captured in the nonlinear transient simulation.

Figure 3.12 (a) shows the peak journal ΔT across the journal diameter vs. the rotor axial position and the rpm. Only rotor axial positions ranging from 0.6488m to 1.068m are presented, since only seven times the bearing length (0.06m) is designated for the thermal shaft, in order to improve computational efficiency, as mentioned in section 3.

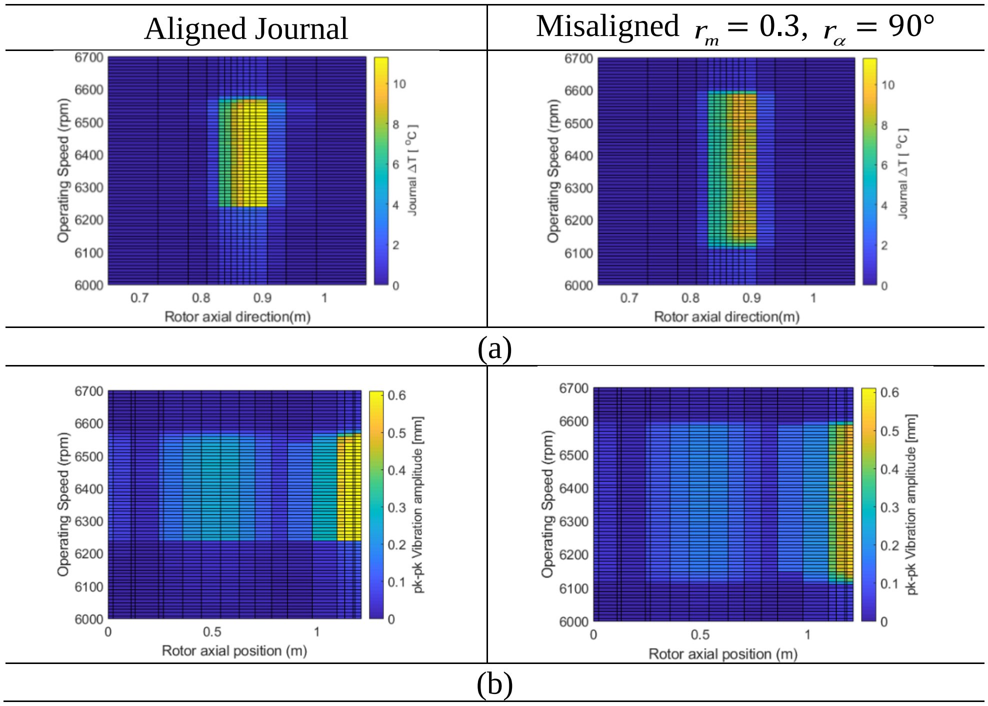

Figure 3.12 Comparison of (a) peak journal ΔT and (b) pk-pk vibration amplitude vs. rpm and axial position for the Rotor 1 case

Compared with the aligned case, the journal high ΔT region is wider with respect to rpm for the misaligned case. The highest journal ΔT of the misaligned case reaches 9.88°C. The high journal ΔT region occurs mainly in the rotor axial length from $0.8288m$ to $0.8888m$ which corresponds to the location of the fluid film bearing. Outside of this region shows relatively small journal ΔT values from 0° to 4° which justifies the thermal shaft length assumption.

The high journal ΔT induces increased thermal bow, decreased minimum film thickness ratio, and large vibrations as shown in Figure 3.12 (b). Large vibration levels are found at the rotor center (from 0.1mm to 0.2mm peak to peak), and the overhung end side (from 0.4mm to 0.6mm peak to peak). This distribution of the pk-pk vibration along the rotor axial direction is consistent with the mode shape in Figure 3.9 which confirms the resonance of this bending mode.

Figure 3.13 and 14 show simulation results for the Rotor 2 case. A comparison of Figure 3.11 and 13 show that the ME instability for the Rotor 1 aligned case is eliminated by increasing the bearing clearance from 68μm for Rotor 1, to 84μm for Rotor 2.

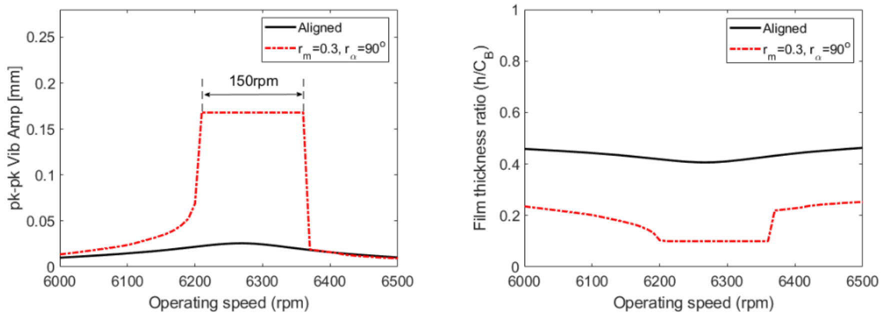

(a) (b)

Figure 3.13 Comparison of (a) pk-pk vibration at NDE bearing position and (b) minimum film thickness ratio for Rotor 2 case

The amount of the bearing radial clearance change is realistic considering the manufacturing tolerances of the bearing and shaft. Assuming the IT7 standard [107] for the shaft and bearing pad thickness, the manufacturing tolerances of the pad thickness and shaft diameter is +-0.018mm and +-0.035mm for pad thickness of 12mm and the shaft diameter of 80mm, respectively. Then the maximum error in the bearing clearance can be up to +-0.0178mm. The Rotor 2 linear model revealed that the third (bending) critical speed occurs at 6,290 rpm which is about 50rpm lower than that of the Rotor 1 case.

Figure 3.13 (a) shows the no ME condition for the Rotor 2 aligned case becomes a severe ME condition for the misaligned bearing case. The ME synchronous instability leading to an unacceptable vibration level is observed from 6,200 rpm to 6,360 rpm. The 160 rpm ISR for the misaligned Rotor 2 case is less than the 430 rpm ISR for the misaligned Rotor 1 case. The increase in ISR between the aligned and misaligned states is nearly the same for Rotor 1 (140 rpm) and Rotor 2 (160 rpm).

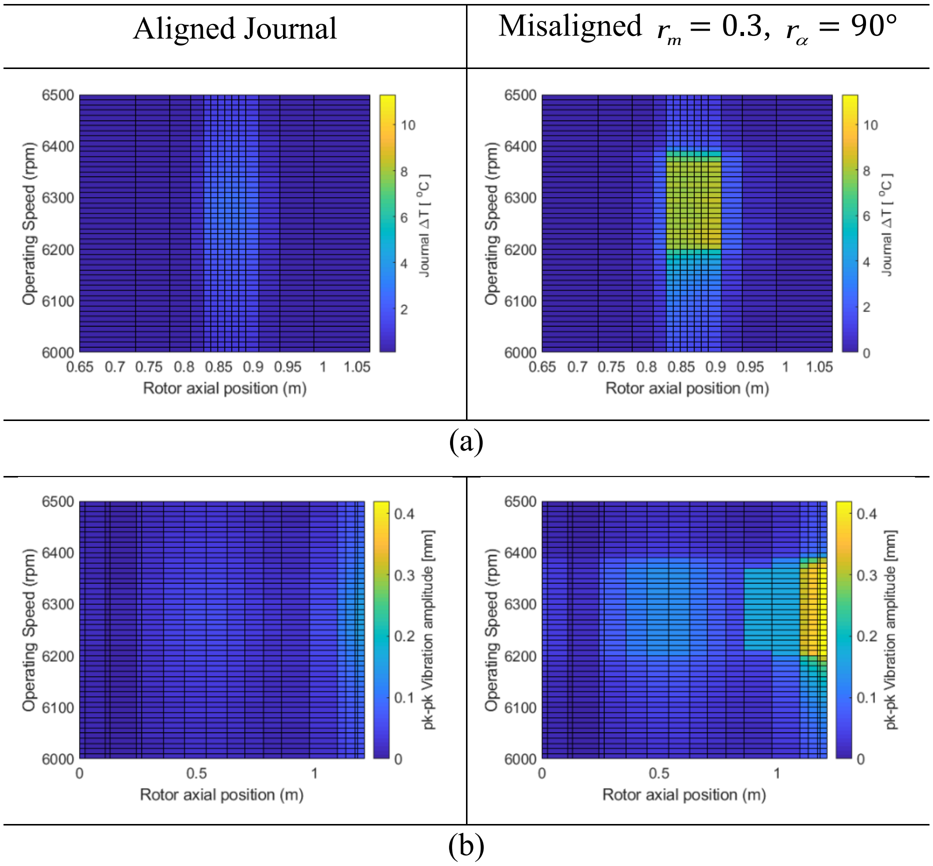

Figure 3.14 Comparison of (a) peak journal ΔT and (b) pk-pk vibration amplitude vs. rpm and axial position for the Rotor 2 case

Figure 3.14 shows a comparison of the pk-pk vibration and journal ΔT vs. rpm and axial position, for the aligned and misaligned journal cases. The highest journal ΔT, 8.5°C, and the highest vibration, up to twice C_B , are seen to occur near the third bending critical speeds of 6,290rpm. Similar to the Rotor 1 case, the vibration distribution level is most significant at the overhung end side, indicating the increased thermal bow at the overhung side, and the resultant ME instability.

Rotor 1 transient simulations were performed at 6,120rpm and 6,570rpm, as shown in Figure 3.15 and 16. All parameter inputs of the rotor-bearing system are identical to the aforementioned steady-state simulation results. The misalignment ratio of 0.3 and the phase of 90° are again utilized for the misaligned journal case.

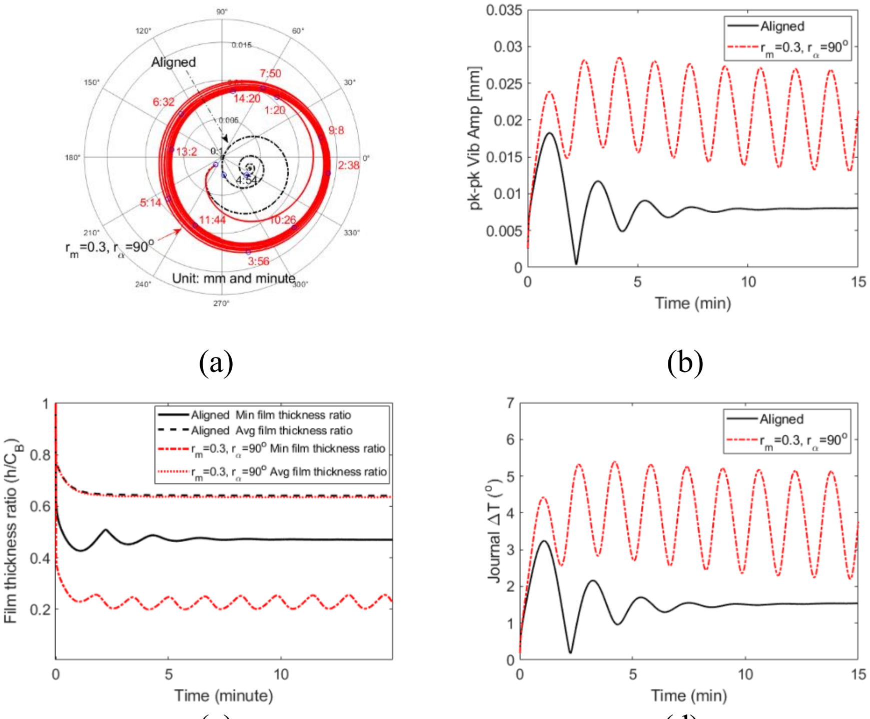

(a) (b)

(c) (d)

Figure 3.15 Effects of misalignment on (a) 1x polar plot, (b) pk-pk vibration at NDE bearing position, (b) Film thickness ratio and (d) journal ΔT of Rotor 1 case at 6,120rpm

Figure 3.15 (a) shows the 1x filtered polar plot at the NDE bearing location at 6,120rpm. The texts on the plot indicate the time (in minutes) when the vibration amplitude and the phase are measured. The misaligned journal produces a relatively large thermal spiral with time-varying pk-pk vibration amplitude. The phase angle with respect to the initial imbalance of the aligned case converges quickly, while that of the misaligned journal keeps varying from 0° to 360° during the entire simulation time. This result agrees with the steady-state results in Figure 3.11 where the vibration of the misaligned does not converge with time, and the aligned case shows less vibration level.

Figure 3.15 (b) shows that the misalignment effect increases the vibration level since the pk-pk vibration amplitudes of the misaligned case oscillate between $28.13\mu m$ and $13.28\mu m$, while the response of the aligned journal decays to its steady-state vibration level of $8\mu m$. The misalignment gives rise to more asymmetric viscous heating in the journal caused by its decreased minimum film thickness.

Figure 3.15 (c) shows that the misaligned journal has reduced the minimum film thickness ratio compared with the aligned case, although the area average (decreased) film thickness ratio of both cases is almost identical. The decreased mean film thickness was calculated by subtracting the thermal expansion of the shaft and pads from the nominal film thickness.

The minimum film thickness ratio of the misaligned journal fluctuates from 0.2 to 0.25 while the ratio of the aligned one is observed between 0.42 and 0.5. The impact of the pad-pivot stiffness and bearing radial clearance on the ME was investigated in [47], which showed that a softer pivot and increased bearing clearance tended to suppress ME. These parameter changes increased the minimum film thickness ratio, causing less viscous heating. Similarly, the decreased minimum film thickness due to the misaligned journal will produce more viscous heating in the journal surface area, especially where the journal is tilted. This may result in an increased shaft/bearing thermal expansion ratio and increased journal ΔT, exacerbating the ME.

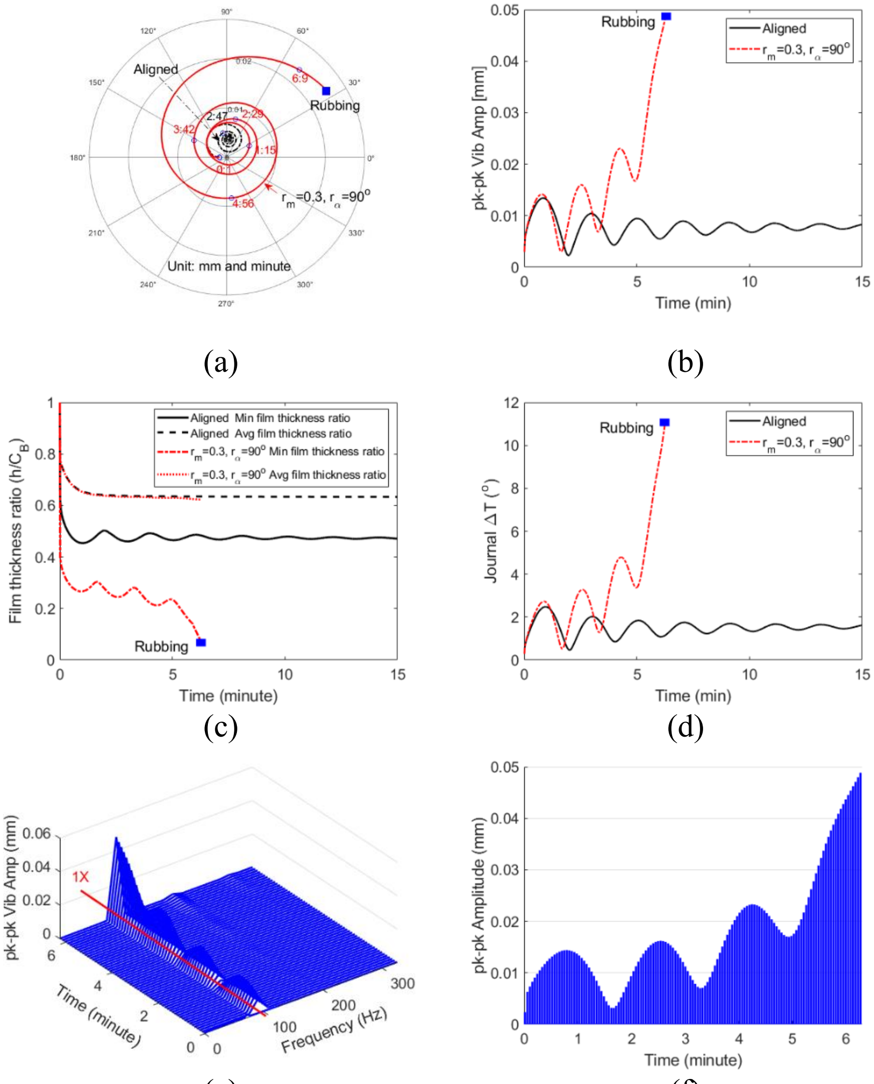

(a) (b)

(c) (d)

(e) (f)

Figure 3.16 Effect of misalignment on (a) 1x polar plot, (b) pk-pk vibration at NDE bearing position, (b) Film thickness ratio and (d) journal ΔT, and (e)&(f) FFT of pk-pk vibration at NDE bearing position of Rotor 1 case at 6,570rpm

The shape of the pk-pk journal surface temperature ΔT at the axial center of the bearing, as shown in Figure 3.15 (d) is similar to the vibration level in Figure 3.15 (a), which demonstrates the coupling between journal temperature and journal motions. The ME unstable vibration in the rotor system is governed by the journal ΔT and its resultant thermal bow amplitude, which is a unique feature of the ME**.**

Figure 3.16 shows the transient simulation results at the higher speed 6,570 rpm. Figure 3.16 (a) shows a diverging spiral shaped 1X polar plot for the misaligned case leading to the unacceptable vibration level at 6min 11s, while the spiral of the aligned journal converges to its steady-state value. Figure 3.16 (b) shows that the corresponding vibration amplitude, with an increasing trend up to $49\mu m$. The unacceptable vibration level occurs at that time and the journal ΔT of the misaligned case reaches $11°C$, which could cause a significant thermal bow. The aligned case results show acceptable levels of vibration, journal ΔT, and minimum film thickness ratio. The FFT of NDE bearing pk-pk vibration at 6,570 rpm is shown in Figure 3.16 (e) and (f), which confirms that the ME vibration is synchronous.

Figure 3.17 (a) illustrates how the high spot leads the hot spot for the misaligned journal case at 6,570 rpm, and time equal to 6 minutes. The hot and high spots are seen to gradually move around the journal circumference as time increases.

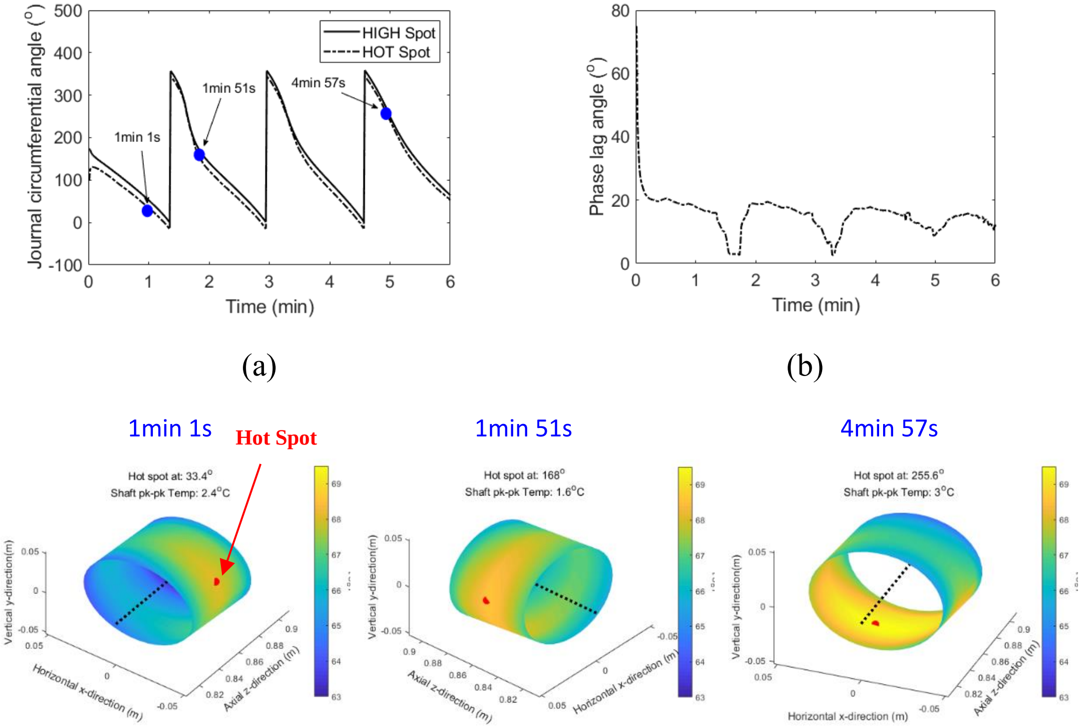

(a) (b)

(c)

Figure 3.17 Responses at 6,750 rpm: (a) High and hot spot phase angles, (b) Phase lag angle of hot spot behind high spot, (c) Journal surface temperature distribution at three different times

Figure 3.17 (b) shows that the phase lag of the hot spot behind the high spot is approximately 20° during most of the simulation time except the times where the phase lag drops then returns. These times correspond to the troughs in vibration amplitude in Figure 3.16 (f). In these instances, the synchronous vibration amplitude gets small so that the temperature asymmetry decreases. Figure 3.17 (c) shows the corresponding journal surface temperature distribution at three different simulation times, including 1min 1s, 1min 51s, and 4min 57s. A major indicator of the ME is the spiral movement of the 1x phasor in the polar plot domain as shown in Figure 3.16 (a). Figure 3.17 (b) shows that the hot spot lags the high spot, but the rotordynamics causes the high spot to follow the heavy spot (imbalance) that is caused by the thermal bow in the plane of the hot spot. Thus, the high spot follows the hot spot which is always lagging the high spot. This feedback mechanism causes the spiral motion of the high spot 1x phasor in the polar plot.

The temperature distribution at the bearing mid-plane, the induced thermal bow, and the shaft thermal expansion ratio are shown in Figure 3.18, for 6,570 rpm, and aligned (left) and misaligned (right) cases. These results are measured at the end of each simulation time (15min for the aligned, 6min 17s for the misaligned case). Figure 3.18 (a) shows a maximum journal ΔT of $13°C$ in the misaligned case, while the isotherms of the aligned journal show a relatively concentric distribution. For the misaligned case, the hot spot is located at 22.7°, which lags about 10° behind the high spot location (32.8°).

The corresponding thermal bow due to the journal ΔT is shown in Figure 3.18 (b). The phase of the thermal bow at the rotor end is 247.7° for the aligned case, which is 185° away from the corresponding hot spot location (62.5°) while that of the misaligned journal is seen at 206.3°, and it is 183.6° away from its hot spot location. The amplitude of the thermal bow at the overhung end is $0.0344mm$ with misalignment, which is about six times larger than that of the aligned case ($0.0054mm$). This increases the synchronous excitation in the system. The thermal expansion of the shaft due to the viscous shearing is presented in Figure 3.18 (c).

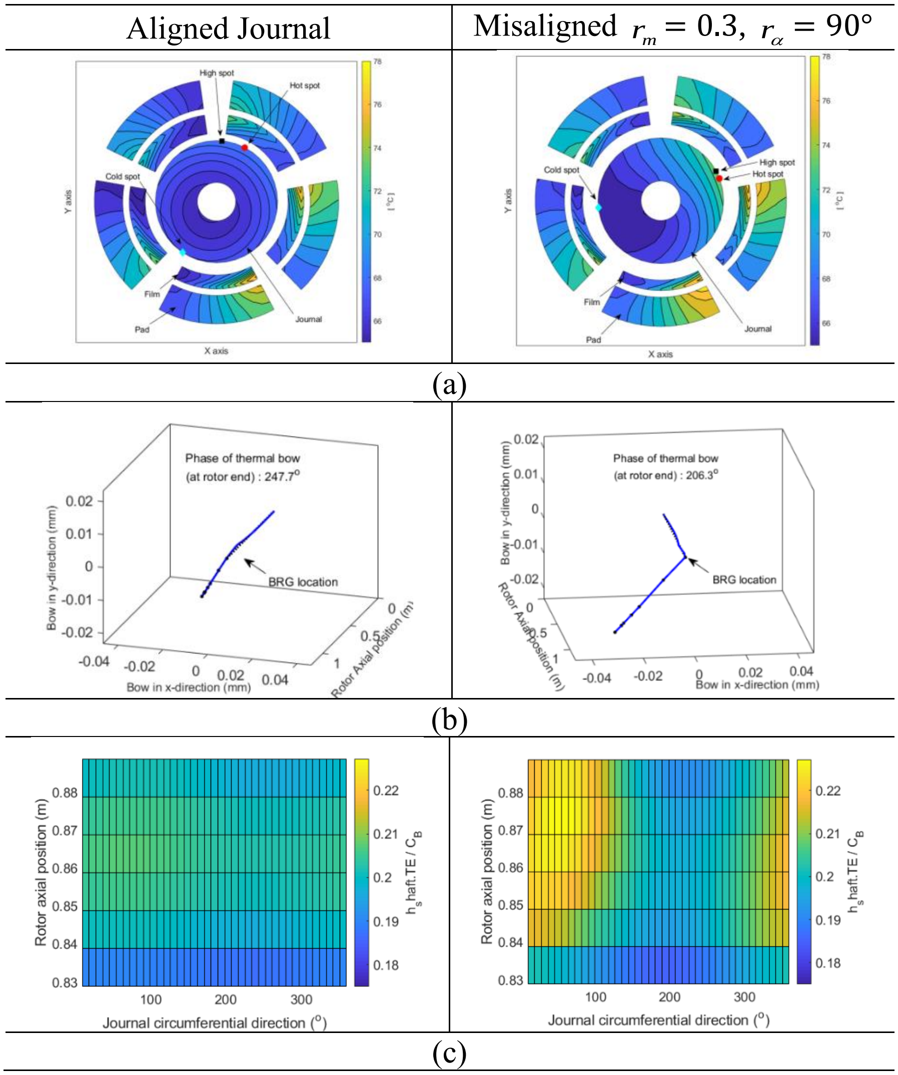

Figure 3.18 Comparison of (a) temperature distribution at bearing mid-plane, (b) thermal bow and (c) shaft thermal expansion ratio, at 6,570rpm, for the aligned (left) and misaligned (right) cases

A relatively high expansion ratio (=0.22) is observed for the misaligned case at circumferential positions ranging from 0° to 90°, which corresponds to the high-temperature region and hot spot location in Figure 3.18 (a). Figure 3.18 shows the thermal expansion only in the rotor axial length matching the bearing location (from $0.8288m$ to $0.8888m$). The steady-state approach (Figure 3.11) was validated by its good agreement with the transient approach for the Rotor 1 case at 6,120 rpm and 6,570rpm, with and without the misalignment effect.

Figure 3.19 shows the film thickness ratio for the five pads at the end of the simulation time. The misaligned case shows an asymmetric distribution along the bearing axial direction while the aligned journal exhibits near symmetry. Figure 3.19 (b) corresponds to the misaligned case with the 90° misalignment phase shown in Figure 3.3 (a), and the pad arrangement in Figure 3.8. A large region has decreased film thickness at the NDE side in pads 1, 2, and 5, while the opposite trend is seen in the same pads at the DE side (a large region with increased film thickness). The damped unbalance response and damping ratio from the linear analysis showed only marginal impact due to misalignment. Therefore, the cause of the film thickness asymmetry along with the decreased minimum film thickness is attributed to the ME induced by the misaligned journal.

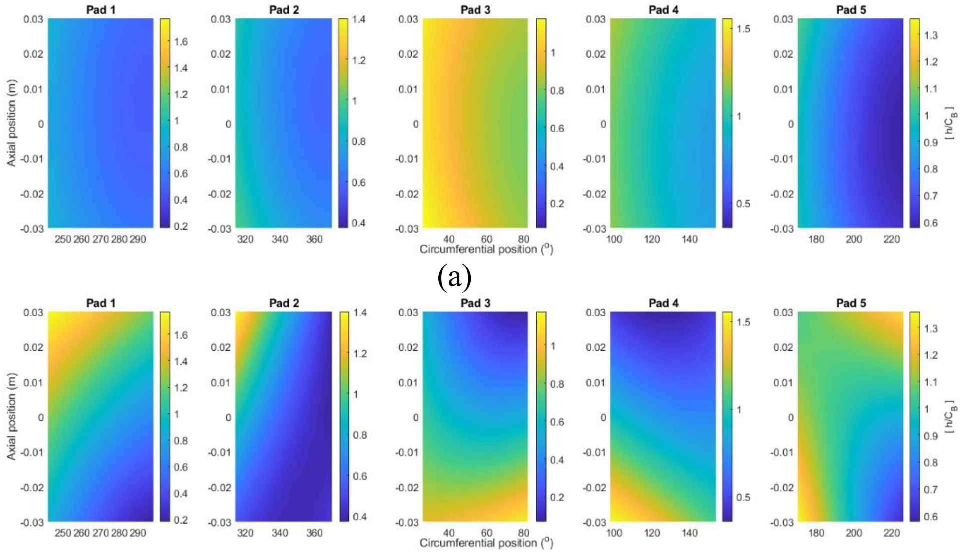

(a)

(b)

Figure 3.19 Pad film thickness distribution at 6,570rpm (a) aligned journal and (b) misaligned $r_m = 0.3,\ r_\alpha = 90°$

3.4.1. Effect of misalignment ratio

The effect of the misalignment ratio ($r_y = \frac{A_y}{C_B}$ in Figure 3.2) on the instability speed range ISR is investigated for both Rotor 1 and Rotor 2 cases, and the steady-state transient simulation results are presented in Figure 3.20. The ratio of the misalignment ratio varied from 0 to 0.3 with an increment of 0.1, and the misalignment phase ($r_\alpha = \tan^{-1}\frac{\alpha_y}{\alpha_x}$ in Figure 3.2) stays constant at 90° for all cases. All other parameter settings are identical with the aforementioned simulation results. The ISR due to the ME increases for both rotor cases as the misalignment ratio increases. The detailed ISR results are listed for different misalignment ratios in Table 3.2. In both rotor cases, the misalignment showed no significant effect when the misalignment ratio = 0.1, as the increase of the ISR is only 10 rpm for Rotor 1, and no ME is induced in Rotor 2. The misalignment effect on the ME becomes more evident when the misalignment ratio increases above 0.2. Table 3.2 shows an increase in ISR by 100rpm and 140rpm compared with that of the aligned journal for Rotor 1, when r_m=0.2 and 0.3. For Rotor 2, the ME is first seen to occur with r_m=0.2, and its ISR is small at 80 rpm. The maximum ISR of the Rotor 2 is 160rpm when the misaligned ratio is further increased to r_m=0.3. Increases of the ISR for Rotor 2 case are 80rpm for r_m=0.2 and 160rpm for r_m=0.1, respectively. The increased ISR with r_m=0.2 and 0.3 for both Rotor 1 (100rpm and 140rpm) and Rotor 2 (80rpm and 160rpm) cases are similar, indicating the bearing radial clearance doesn’t have a significant impact on the misalignment-induced ME. These results demonstrate that the misaligned journal induces more severe ME when its misalignment ratio exceeds a certain level (r_m>0.2 in this case).

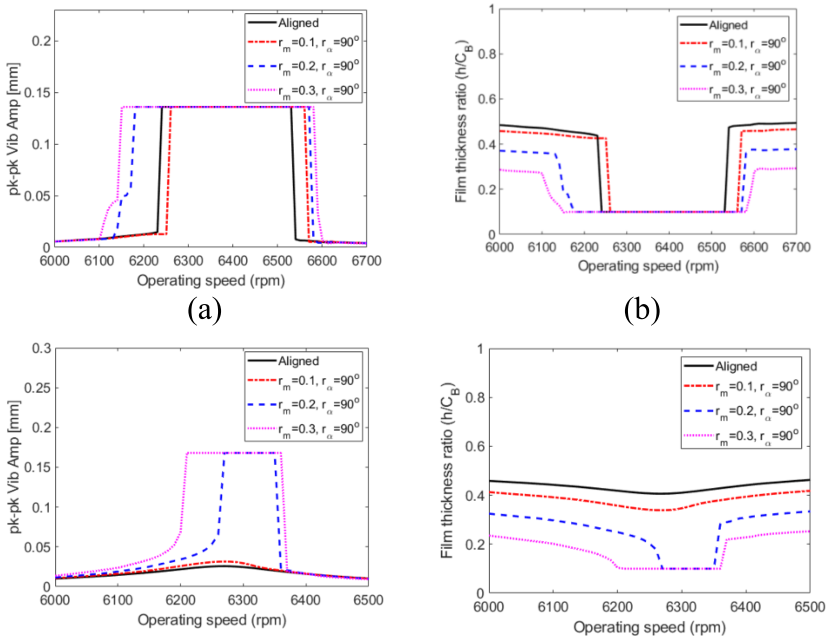

(a) (b)

(c) (d)

Figure 3.20 Comparison of (a) pk-pk vibration at NDE bearing position of Rotor 1, (b) minimum film thickness ratio of Rotor 1 (c) pk-pk vibration at NDE bearing position of Rotor 2, (d) minimum film thickness ratio of Rotor 2 with different misalignment ratio

	Aligned	$r_m = 0.1$, $r_\alpha = 90°$	$r_m = 0.2$, $r_\alpha = 90°$	$r_m = 0.3$, $r_\alpha = 90°$
Rotor 1	6240~6530rpm (290rpm)	6260~6560rpm (300rpm)	6180~6570rpm (390rpm)	6150~6580rpm (430rpm)
Rotor 2	No Morton (0rpm)	No Morton (0rpm)	6270~6350rpm (80rpm)	6200~6360rpm (160rpm)

Table 3.2 Instability speed range (ISR) with different misalignment ratio ($r_m = \sqrt{r_x^2 + r_y^2}$ in Figure 3.2)

The corresponding pk-pk vibration amplitude and the pk-pk shaft temperature distribution along the rotor axial direction for Rotor 2 is illustrated in Figure 3.21. As expected, high pk-pk temperature and vibration are observed in the wider ISR as the misalignment ratio increases.

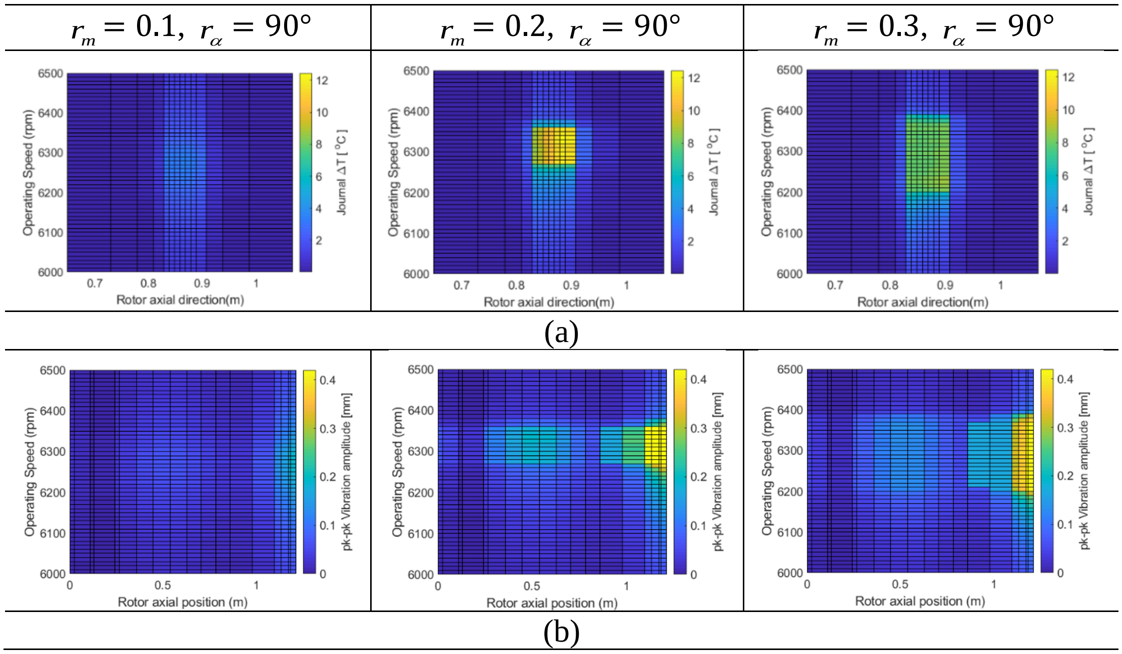

Figure 3.21 Comparison of (a) peak journal ΔT and (b) minimum film thickness ratio across rotor axial positions for Rotor case 2 with different misalignment ratios

Transient simulations of Rotor 1 were conducted at 6,570rpm to validate the steady-state simulation results, as shown in Figure 3.22. The unacceptable vibration level occurs only with $r_m = 0.2$ and 0.3 in Figure 3.22 (a), which agrees with the steady-state results in Figure 3.20. The unacceptable vibration level occurs about 4min faster with r_m=0.3, compared with r_m=0.2. High vibration levels at the NDE bearing location are observed for the two misaligned cases ($r_m = 0.2$ and 0.3) in Figure 3.22 (b). Although an unacceptable vibration level is not observed with r_m =0.1, oscillating vibration with varying phase exists while the aligned case shows converging response to its steady-state position. The corresponding thermal bow amplitude and the phase of the rotor measured from the bearing node to the rotor end node are presented in Figure 3.22 (c). The thermal bow of the aligned case is 0.0056m in magnitude and 247.7° in phase at the rotor end, while 0.0083m and 211.2° for r_m=0.1, 0.031m and 289.4° for r_m=0.2, and 0.0313m and 206.57° for r_m=0.3, at the rotor end.

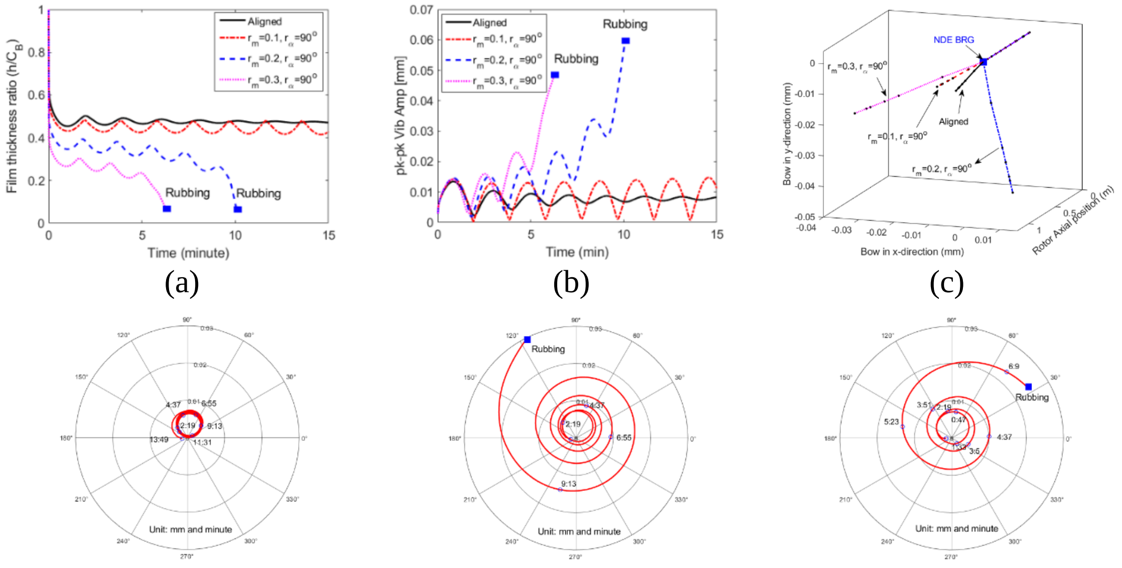

(a) (b) (c)

(d) (e) (f)

Figure 3.22 Comparison of (a) film thickness ratio of Rotor 1, (b) pk-pk vibration at NDE bearing position of Rotor 1, (c) thermal bow of Rotor 1, (d) 1x polar plot with $r_m = 0.1$, $r_\alpha = 90°$, (e) 1x polar plot with $r_m = 0.2$, $r_\alpha = 90°$, (f) 1x polar plot with $r_m = 0.3$, $r_\alpha = 90°$ at 6,570 rpm

The 1x polar plots for r_m=0.1~0.3 are shown in Figure 3.22 (d), (e) and (f). The spiral with r_m=0.1, which is marginally stable with non-diverging vibration response, changes to diverging shapes with increased misalignment ratios of 0.2 and 0.3. The time to reach 10% of C_b is 9min 16s for r_m=0.2 and 6min 10s for r_m=0.3. This indicates increased ME severity with increased misalignment ratio.

3.4.2. Effect of different pad-pivot types

The previously presented models and simulations utilized a cylindrical pad-pivot type which has only pad-tilting motions. The following results compare the effect of including a spherical pad pivot with rolling, yawing and tilting motions. All other rotor and bearing parameters and operating conditions are the same as for the previous models and simulations. Figure 3.23 shows steady-state vibration level and journal ΔT results for the spherical pad-pivot model, performed with different misalignment ratios including $r_m = 0$ (Aligned journal) and $r_m = 0.3,\ r_\alpha = 90°$ (Misaligned journal). The speed ranges of the high vibration and temperature of the aligned case are found from 6,250rpm to 6,550rpm, which is almost identical to the aligned case for the cylindrical-pivot type. The instability speed range ISR for the misaligned case ($r_m = 0.3,\ r_\alpha = 90°$) does not change from the aligned case. The increase of ISR with the same misalignment ratio was 160 rpm for the cylindrical pad-pivot type. This indicates that the additional pad motions (rolling) of the spherical pad-pivot compensates the misalignment effect on the rotor-bearing system.

<table>
<tr><th>Spherical pivot, Aligned Journal</th><th>Spherical pivot, Misaligned
$r_m = 0.3,\ r_\alpha = 90°$</th></tr>
<tr><td>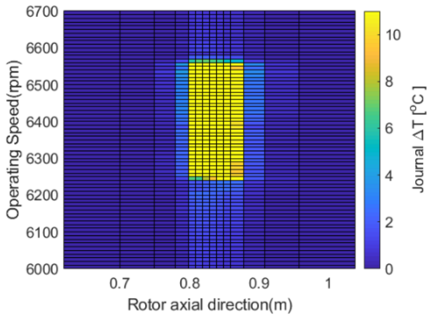
</td><td>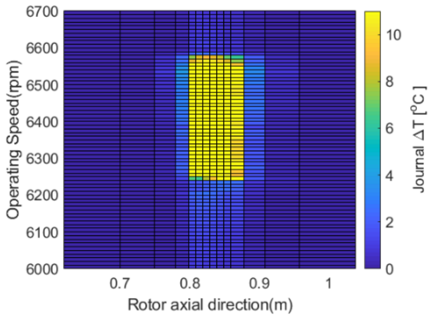
</td></tr>
<tr><td colspan="2">(a)</td></tr>
<tr><td>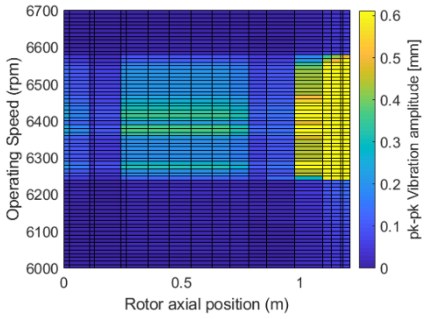
</td><td>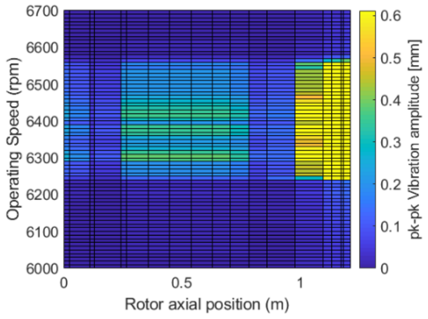
</td></tr>
<tr><td colspan="2">(b)</td></tr>
</table>

Figure 3.23 Comparison of (a) peak journal ΔT and (b) pk-pk vibration amplitude for aligned and misaligned journals, for Rotor 1 with spherical pad-pivot model

The transient simulation was conducted at 6,570 rpm for both pad-pivot types with different misalignment ratios including $r_m = 0$ (Aligned journal) and $r_m = 0.3,\ r_\alpha = 90°$ (Misaligned journal). The journal ΔT and the 1x vibration polar plot results are shown in Figure 3.24 for both pivot types. Note that in the cylindrical pad-pivot case, the misaligned ratio of $r_m = 0.3,\ r_\alpha = 90°$ induces a severe ME leading to the unacceptable vibration level as shown in the journal ΔT and polar plots. In comparison, the spherical pivot model results show almost identical stable journal ΔT and vibration amplitude/phase levels, regardless of the misalignment ratio.

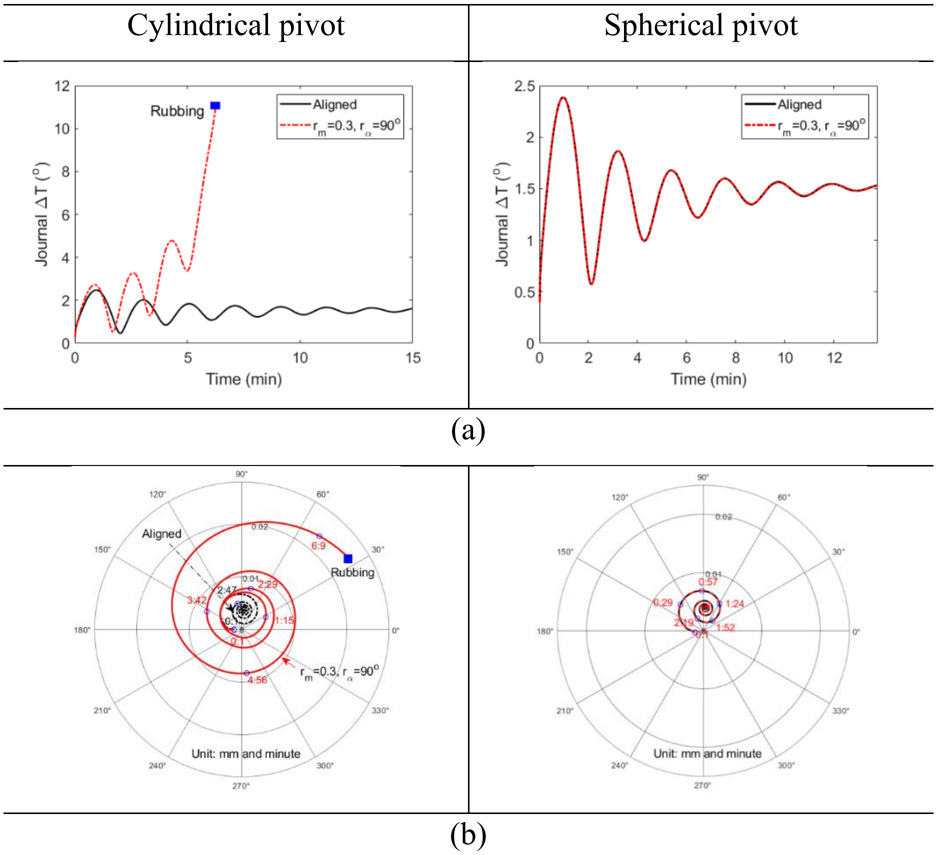

Figure 3.24 Comparison of cylindrical and spherical pivot model (a) peak journal *ΔT* and (b) pk-pk 1x vibration polar plot of Rotor 1 case, at 6,570 rpm

Figure 3.25 (a) and (b) show the rolling motions of the spherical pad-pivot at 6,570rpm for different misalignment ratios. The steady-state angular displacements of the five pad motions are relatively small for the perfectly aligned journal model. However, with the misalignment ratio ($r_m = 0.3,\ r_\alpha = 90°$), the steady-state positions of all five pads have been significantly displaced as shown in Figure 3.25 (b). The increased rolling movements are more evident in pad 1, 3 and 4 than other pads, where the pad locations are shown in Figure 3.3 and Figure 3.8. The tilted journal (with misalignment phase of 90°) affects the minimum film thickness significantly. The corresponding film thickness ratio of pads with the misalignment effect is shown in Figure 3.25 (c). Compared with the misaligned case equipped with the cylindrical pivot in Figure 3.19 (c), no film thickness asymmetry is seen to occur in the figure, indicating the compensated misalignment effect from the spherical pivot motions. This result verifies that the misalignment-induced ME can be avoided by suppressing the film asymmetry with the spherical pivot and also demonstrates that the film asymmetry is the one potential root cause of the misalignment-induced ME.

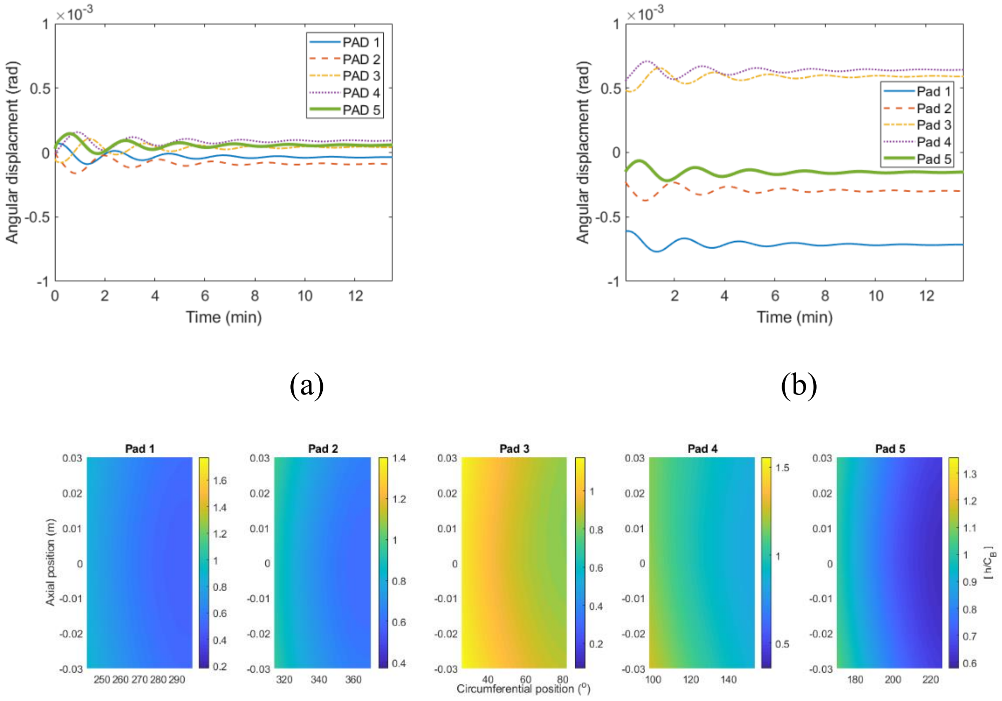

(a)

(b)

(c)

Figure 3.25 Comparison of pad rolling motions of spherical pivot-type model for (a) aligned journal, (b) misaligned journal ($r_m = 0.3$, $r_\alpha = 90°$), and (c) film thickness distribution of misaligned journal $r_m = 0.3$, $r_\alpha = 90°$ of Rotor 1 case at 6,570 rpm

4. SQUEEZE FILM DAMPER SUPPRESSION OF THERMAL BOW – MORTON EFFECT INSTABILITY[*]

4.1. Introduction

Measures to suppress the ME vibration have been limited to changing rotor-bearing parameters such as bearing radial clearance, bearing length, overhung mass, etc. To the best of the authors' knowledge, there has not been any published study regarding the potential of SFD for suppressing the ME. This section presents a computational study of the ME instability and its suppression by including the SFD in series with a tilting pad journal bearing TPJB. A linear response study was conducted in order to provide conventional rotordynamic response as part of a complete description of the example rotor system. Simulated results demonstrate that installing a properly designed squeeze film damper shifts the critical speed and alters the deflection shape of a rotor, which may help attenuate the ME vibration. The present work employs a finite element based SFD model including the inertia effect from a central groove [71], which is similar to the linear bulk-flow model in [69, 70]. The multi-physics ME simulation model includes three-dimensional (3D) THD models of the fluid film, and 3D solid FEM bearing and journal thermal and structural models and flexible shaft dynamics models. Both linear and nonlinear transient simulations are performed to compare the rotor

---

[*] Reprinted with permission from "Squeeze film damper suppression of thermal bow-Morton effect instability" by Shin, D., and Palazzolo, A. and Tong, X., 2020. Journal of engineering for gas turbines and power, Copyright [2020] by ASME

dynamic performances and journal temperature differential with and without the SFD. The linear analysis confirms the shift of critical speed, damping ratio, and the modified mode shape due to the SFD. Optimal parameters of SFD are developed that substantially attenuate the ME vibration in nonlinear simulations.

4.2. Modeling and ME prediction algorithms

4.2.1. Centrally grooved squeeze film damper

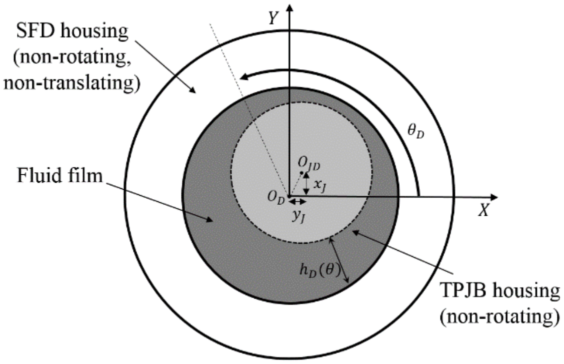

Figure 4.1 Axial mid-plane of SFD

The Reynolds equation (RE) for an incompressible lubricant is employed to obtain the fluid pressure distribution in the SFD film. The RE combines the momentum and fluid continuity equations into the partial differential equation

$$\begin{aligned}&\frac{\partial}{\partial\theta_D}\left(\frac{{h_D}^3}{12\mu_D}\frac{\partial p}{\partial\theta_D}\right)+\frac{\partial}{\partial z}\left(\frac{{h_D}^3}{12\mu_D}\frac{\partial p}{\partial z_D}\right)\\&=\frac{R_J\omega_J}{2}\frac{\partial h_D}{\partial\theta_D}+\frac{\partial h_D}{\partial t}\end{aligned}\tag{4.1}$$

where R_J and μ_D denote the radius of the SFD journal and the viscosity of the lubricant, respectively. The term $\frac{R_J \omega_J}{2}\frac{\partial h_D}{\partial \theta}$ is set to zero for the force calculation of the SFD since its bearing housing is normally fixed in the circumferential direction with an anti-rotation pin or a cage to prevent the bearing housing rotation. In Figure 4.1, x_J and y_J are the bearing housing center displacement with respect to the SFD center O_D.

The film thickness of the fluid and its derivative are expressed as

$$\begin{aligned} h_D(\theta_D) &= C_D - x_J \cos\theta_D - y_J \sin\theta_D \\ \frac{\partial h_D(\theta_D)}{\partial t} &= -\dot{x}_J \cos\theta_D - \dot{y}_J \sin\theta_D \end{aligned} \tag{4.2}$$

where C_D represents the SFD radial clearance and θ_D denotes the circumferential coordinate of the SFD lubricant.

The finite element level form of the Reynolds equation is represented as

$$K_E P_E = S_E + I_E \tag{4.3}$$

where $(K_E)_{ik} = (\frac{h_{DE}{}^3}{12\mu})\int_\Omega (\frac{\partial N_i}{\partial x}\frac{\partial N_k}{\partial x} + \frac{\partial N_i}{\partial y}\frac{\partial N_k}{\partial y})dxdy$ and $i,k = 1,2,3$. The damping source term is $(S_E)_i = (\frac{h_{DE}}{\partial t})\int_\Omega N_i dxdy$, and the fluid inertia term is

$(I_E)_i = (\frac{\rho_D h_{DE}{}^2}{12\mu}\frac{\partial^2 h_{DE}}{\partial t^2})_E \int_\Omega N_i dxdy$.

Triangular simplex finite elements interpolate the two-dimensional film pressure distribution and are expressed with shape functions and node pressure vectors as

$$p(x,y) = N^T P_E$$

$$N^T = (N_1, N_2, N_3) \tag{4.4}$$

$$P_E{}^T = (P_{1E}, P_{2E}, P_{3E})$$

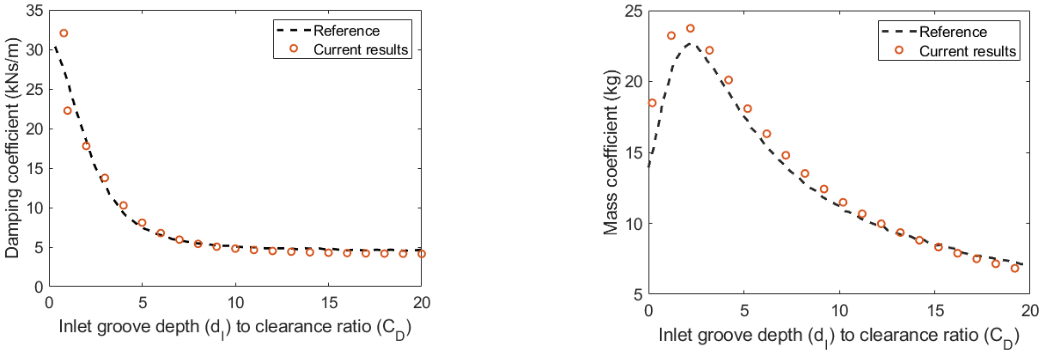

(a) (b)

Figure 4.2 Comparison of (a) damping and (b) added mass coefficient with reference [69] (adapted from [69])

Values obtained from the current model are compared in Figure 4.2 with results from [69], which are based on a linear bulk flow model. The schematic showing the series combination of the journal, tilting pads, TPJB housing, SFD film and outer SFD housing is shown in Figure 4.3. The groove geometry of the SFD including the inlet groove depth (d_I) and film clearance (C_D) used in Figure 4.2 is also illustrated in the figure. The The SFD parameter values, including the pressure boundary conditions, inlet/outlet groove length, and effective groove/film clearance from [69] are applied to the current model. The compared result shows good agreement between the two models.

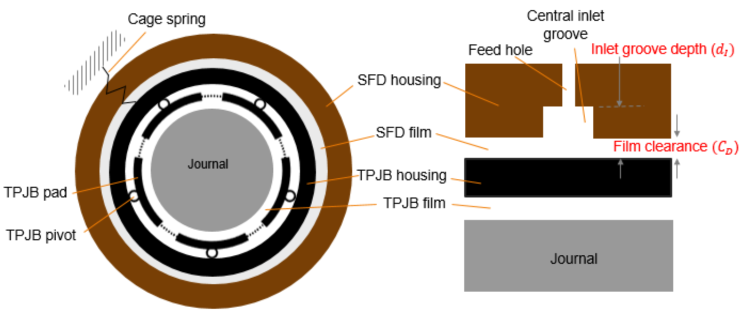

Figure 4.3 Schematics of series combination of TPJB and SFD and SFD groove geometry (not to scale)

The instantaneous reaction force applied to the bearing housing is obtained by integrating the pressure distribution. Considering the half symmetry of the lubricant, the bearing housing reaction force becomes

$$F_D = \begin{Bmatrix} F_{Dx} \\ F_{Dy} \end{Bmatrix} = 2\int_0^{L/2}\int_{-\pi}^{\pi} p \begin{Bmatrix} \cos\theta_D \\ \sin\theta_D \end{Bmatrix} d\theta_D dz_D \tag{4.5}$$

Note that the lubricant temperature variation of the SFD is assumed negligible in the example rotor system because the SFD is prevented from rotation with a cage. In addition, the initial SFD lubricant temperature is assumed to be the same as the TPJB supply oil temperature, and therefore temperature change in the SFD lubricant caused by the supply oil and thermal structures of SFD/TPJB housings are not considered in this study.

4.2.2. Tilting pad journal bearing model

Accurate prediction of the ME phenomenon requires a high-fidelity THD TPJB model. The generalized Reynolds equation for an incompressible fluid with variable lubricant viscosity and negligible fluid inertia/shaft curvature is employed [41, 42]. The temperature-dependent variable viscosity is obtained from the calculated film temperature distribution and the viscosity-temperature relation

$$\mu = \mu_0 e^{-\alpha(T-T_0)} \tag{4.6}$$

where μ_0 , T_0 and α are the reference viscosity, film temperature, and the viscosity coefficient, respectively, and the film temperature T is obtained by solving the energy equation.

A cylindrical pivot with angular pad tilting and pivot translational motions are included in the current analysis. The film thickness formula for the cylindrical pivot is

$$\begin{aligned} & h(\theta, z) = C_P - \hat{e}_x \cos(\theta) - \hat{e}_y \sin(\theta) \\ & -(C_P - C_b)\cos(\theta - \theta_P) - \delta_{tilt} R \sin(\theta - \theta_P) \\ & -h_{shaft.TE}(\theta, z) - h_{pad.TE}(\theta, z) \end{aligned} \tag{4.7}$$

where

$$\hat{e}_x = e_x - y_{pvt}\cos\theta_p\,,\ \ \hat{e}_y = e_y - y_{pvt}\sin\theta_p\,.$$

and C_P , C_b , z , R , θ and θ_P represent pad and bearing radial clearance, film’s axial coordinate, journal radius, bearing circumferential coordinate and pad pivot position, respectively. Note that the film thickness formula considers the asymmetric thermal expansion of the journal ($h_{shaft.TE}$) and pad ($h_{pad.TE}$) and pivot deformation caused by the load on pads.

The dynamic equations of the cylindrical pivot TPJB pads are

$$
\begin{aligned}
M_{pad}{}^{i}\ddot{y}_{pvt} &= -K_p y_{pvt} + F_{pad}{}^{i} \\
I_{tilt}{}^{i}\ddot{\delta}_{tilt} &= N_{tilt}{}^{i}
\end{aligned}
\tag{4.8}
$$

where i denotes the pad number, and $M_{pad}{}^{i}$, $I_{tilt}{}^{i}$, $F_{pad}{}^{i}$ and $N_{tilt}{}^{i}$ are the mass and the tilting inertia of a pad, the fluid film force and the tilting moments applied to a pad, respectively.

4.2.3. Thermal models

The energy equation to calculate the 3D temperature distribution T across the fluid film is

$$
\begin{aligned}
&\rho c(u\frac{\partial T}{\partial x} + w\frac{\partial T}{\partial z}) = k(\frac{\partial^2 T}{\partial x^2} + \frac{\partial^2 T}{\partial y^2} + \frac{\partial^2 T}{\partial z^2}) \\
&+\mu\left[(\frac{\partial u}{\partial y})^2 + (\frac{\partial w}{\partial y})^2\right]
\end{aligned}
\tag{4.9}
$$

where ρ, c, k, u, w are density, specific heat capacity, thermal conductivity, circumferential and axial velocities, respectively. Eq. (4.9) is solved using 3D, eight-node isoparametric finite elements along with an up-winding scheme [43, 44] to prevent spatial oscillations from the convective term.

The Laplace equation is solved using 3D eight-node isoparametric finite elements to predict the temperature distributions of the journal and pads, and its discrete form is

$$
[C][\dot{T}] + [K][T] = [F] \tag{4.10}
$$

where F is time-varying thermal load updated with the thermal solutions of the rotor-bearing system. The time-transient solution of Eq. (4.10) is obtained via numerical integration [43, 44]. The heat conduction of the tilting pads and shaft are considered to calculate the pad and shaft temperature distributions. The transient simulation is conducted with the FE model of the pads and shaft including their thermal masses, and with convection boundary conditions applied as explained in Figure 4.4.

Accurate prediction of the thermal bow amplitude and its phase is critical to accurately determine ME occurrences. The hybrid beam-solid method used in [45] is adopted to determine the deformations resulting from the differential heating in the journal while using the computational efficiency of beam finite elements. The calculated thermal bow in the rotating reference frame is converted into the dynamic excitation in the inertial frame equations of motion.

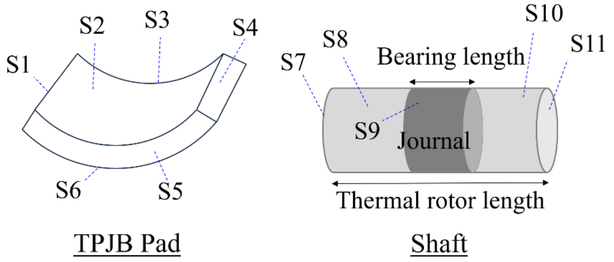

Figure 4.4 Thermal boundary conditions on TPJB pads and shaft outer surfaces

Thermal boundary conditions are imposed on the two interfaces (fluid-pad and journal-fluid), pad surfaces, and four outer surfaces of the shaft exposed to atmosphere, as shown in Figure 4.4. Temperature boundary conditions are applied to the two interfaces. Note that the thermal conditions need to be applied in the rotating frame for the journal surface mesh, and it is continuously re-oriented in the transient simulation. Table 4.1 indicates the thermal boundary conditions applied to the surfaces of TPJB pad and shaft. The convection coefficient of 50 W/m^2K is used for all the surfaces contacting supply oil (supply oil temperature of 50 $°C$) and 30 W/m^2K is used for all the surfaces in contact with air (room temperature of 30 $°C$). Note that a convective boundary condition with supply oil temperature of 50 $°C$ is applied to the back of the tilting pads. The model for the pad inlet boundary temperature is adopted from mixing theory in [41, 42]. The axial length of the solid and thermal finite element models is seven times the journal length. This specific length is determined from the simulation that induces a negligible change in temperature calculated by the much longer length of the finite element model.

Region	Surface	Description	BC types
Pad	S1, S4	Lateral ends	Convection with oil at supply oil temperature
	S2	Pad-Film interface	Prescribed temperature and heat flux from film surface
	S3, S5	Axial ends	Convection with oil at supply oil temperature
	S6	Radial out	Convection with oil at supply oil temperature
Shaft	S7, S11	Axial ends	Prescribed temperature at room temperature
	S8, S10	Radial surfaces	Convection with air at room temperature
	S9	Journal-Film interface	Prescribed temperature and heat flux from film surface

Table 4.1 Thermal boundary conditions on pad and shaft

4.2.4. Flexible rotor with SFD in series with a TPJB

The rotor configuration with a single overhung mass at the non-drive side (NDE) is shown in Figure 4.5.

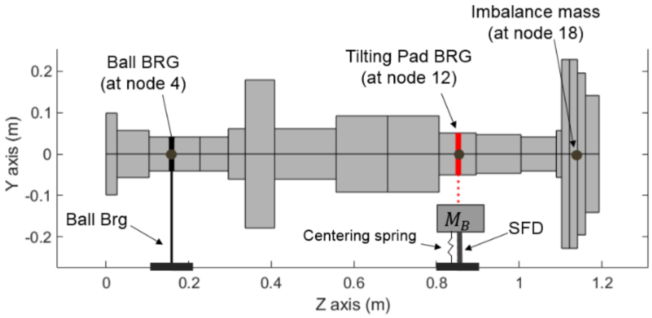

Figure 4.5 Example rotor-bearing-SFD configuration

The flexible, lateral rotordynamics, Euler beam based model of the rotating assembly is represented as

$$\left[\dot{U}\right]=[D][U]+[F] \tag{4.11}$$

where $[U]=\begin{bmatrix}\dot{Z}\\ Z\end{bmatrix}$, $[D]=\begin{bmatrix}-M_{ro}{}^{-1}C_{ro} & -M_{ro}{}^{-1}K_{ro}\\ 1 & 0\end{bmatrix}$, $[F]=\begin{bmatrix}M_{ro}{}^{-1}F_{ro}\\ 0\end{bmatrix}$. U, M_{ro}, C_{ro} and K_{ro} are the state variable vector and mass/damping/stiffness matrices of the system, F_{ro} is the force vector including gravity, fluidic forces $F_{B,x,y}$ from the TPJB, imbalance excitation, and dynamic forces induced by thermal bow. This equation is diagonalized using the right and left eigenvectors and modal reduction. For computational economy, only the modes having frequencies below five times the running speed were employed in the simulation.

The SFD dynamic model including the TPJB housing mass, cage spring stiffness, and nonlinear SFD force is included as

$$\begin{gathered}\begin{bmatrix} M_D & 0 \\ 0 & M_D \end{bmatrix}\begin{bmatrix} \ddot{x}_D \\ \ddot{y}_D \end{bmatrix} = -\begin{bmatrix} K_{Dx} & 0 \\ 0 & K_{Dy} \end{bmatrix}\begin{bmatrix} x_D \\ y_D \end{bmatrix} \\ +\begin{bmatrix} F_{Dx} + M_{Dx} - F_{Bx} \\ F_{Dy} + M_{Dy} - F_{By} \end{bmatrix}\end{gathered} \tag{4.12}$$

where x_D and y_D denotes the x and y displacements of the TPJB housing. M_D, K_{Dx}, K_{Dy}, $F_{D,x,y}$, $F_{B,x,y}$, M_{Dx} and M_D represent the TPJB housing mass, cage stiffness in x and y directions, and the transient SFD damping/added mass force and transient TPJB force in the x and y directions. Note that the TPJB force $F_{B,x,y}$ is the sum of each pad force ${F_{pad}}^i$ in Eq. (4.8)

The coupling between the TPJB and SFD models was achieved by subtracting the TPJB housing displacement x_D and y_D from the journal displacement of the TPJB in Eq. (4.11), and incorporating the TPJB force $F_{B,x,y}$ into Eq. (4.12). The whole rotor-bearing-SFD model consists of the TPJB dynamic equation Eq. (4.8), flexible rotor dynamic equation Eq. (4.11) and the SFD dynamic equation Eq. (4.12). The lowest twenty modes of the rotor are retained and used for numerical integration. The three dynamic equations are coupled with each other and solved simultaneously to investigate the SFD effect on the ME suppression.

4.2.5. Morton effect prediction algorithm

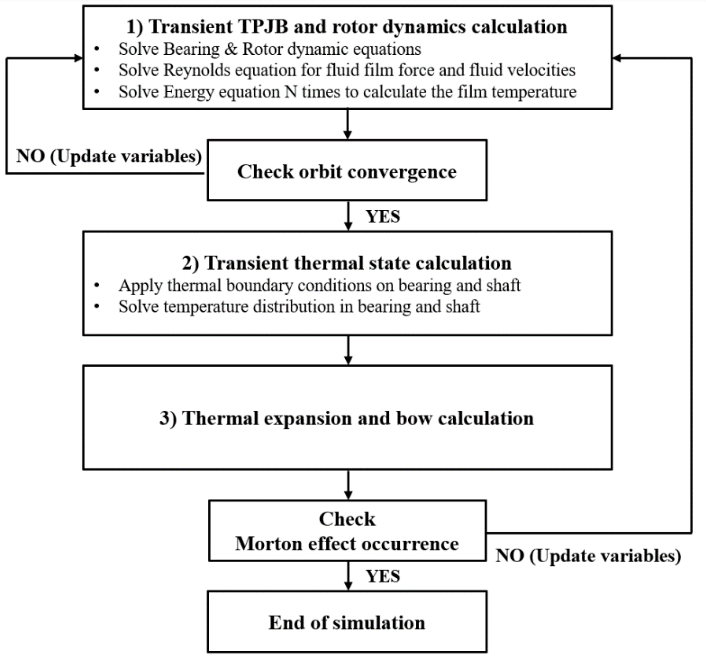

Figure 4.6 Morton effect prediction algorithm

The flow diagram representing the ME prediction algorithm is in Figure 4.6. The initial conditions for the rotor-bearing-SFD dynamic states, the temperature distribution of fluid film/shaft-bearing structures, and the initial thermal bow amplitude are specified at the first step. Then the time-transient solution of the rotor-bearing-SFD system is obtained via numerical integration based on Eq. (4.1), (4.2), (4.5), (4.6), (4.7), (4.8), (4.11), and (4.12) until all the rotor orbits decay to steady-state conditions. Convergence is considered to have occurred only after the orbits at all rotor nodes in the model have converged. The energy equation is solved 40 times per each orbit cycle for computational efficiency, and the lubricant viscosity obtained from the previous step is updated at the next step (updated 40 times per one orbit cycle). The number 40 is based on many simulation results, which showed a negligible difference by using a larger number of steps. Transient thermal states of the bearing-shaft structures are calculated based on Eq. (4.9) and (4.10), after the orbit convergence is ensured. A staggered–time-integration technique is employed [43, 44] for faster simulation, without deteriorating accuracy, since the thermal and vibration related time constants are greatly different in the rotordynamic model.

The steady-state simulation results presented in the following section are also obtained from the transient simulation method explained above. The simulation initiates from the lowest speed of interest and continues until either dynamic/thermal steady state or rubbing (induced by the ME) occurs. Then the process starts again at the next higher speed. The linear method estimates linearized stiffness and damping coefficients of the bearings and incorporates them into the matrix of the Euler beam rotor to formulate the system matrix, and the linear method is used for the calculation of critical speed and unbalance response of the system.

4.3. Simulation results

The rotor configuration with a single overhung mass at the non-drive side (NDE) was shown in Figure 4.5 of section 1.4. The imbalance mass has a magnitude of 135 $g.mm$ and is located at node 18 in the figure. The ball bearing at node 4 has linear stiffness and damping values of $1.7\times10^8 \; N/m$ and $1\times10^5 \; N{\bullet}s/m$, respectively, and these values are assumed invariant with operating speed. The parameters of the TPJB with five pads with a load-on-pad and the SFD at node 12 are given in Table 4.2.

Lubricant parameters		**Bearing parameters**	
Viscosity at 50 °C [Ns/m^2]	0.0203	Pad type	Load on pad
Viscosity coefficients [1/°C]	0.031	No. pads	5
Supply temperature [°C]	50	Radius of shaft [m]	0.0508
Inlet pressure [Pa]	1.32×10^5	Bearing clearance [μm]	74.9
Reference temperature [°C]	50	Preload	0.5
Shaft Parameters		Bearing length[m]	0.0508
Heat capacity [J/kg °C]	453.6	Thermal expansion coefficient [1/°C]	1.3×10^{-5}
Heat conductivity [W/mK]	50	Reference Temperature [°C]	25
Thermal expansion coefficient [1/°C]	1.22×10^{-5}	**Linear Ball Bearing**	
Reference temperature [°C]	25	K_{xx}, K_{yy} [N/m]	1.7×10^8
Thermal rotor length [m]	0.3508	C_{xx}, C_{yy} [$N \bullet s/m$]	1.0×10^5
SFD parameters			
TPJB housing mass [kg]	4	Length [m]	0.0508
Diameter [m]	0.15	Clearance [μm]	100
Viscosity [$Pa.s$]	0.03	Fluid density [kg/m^3]	865
Cage spring stiffness [N/m]	$1\times10^8 \sim 8\times10^8$	Effective groove clearance ratio	20
Inlet groove length [m]	0.0063	Outlet groove length [m]	0.0041

Table 4.2 Parameter values for the example system

The thermal boundary conditions on the pad and shaft surfaces are also listed in the table. The mesh size of the FEM for the thermal and temperature prediction is selected as 40x7x17 (circumferential, radial, and axial directions) for shaft, and 15x10x10 (per one pad) for the Reynolds equation lubricant film and 15x10x10 (per one pad) for the energy equation solver (pad and film). A convergence test with the current mesh size was conducted with three times the current mesh size, and the results showed good agreement with the presented predictions. The mesh size of the squeeze film is 40x15 (circumferential and axial directions). This size is chosen by gradually increasing the mesh size until the SFD force converges. For the numerical integration of the rotor-bearing-SFD system, the Newmark-beta method is employed with 1,000-time steps per one shaft rotation.

4.3.1. Linear analysis

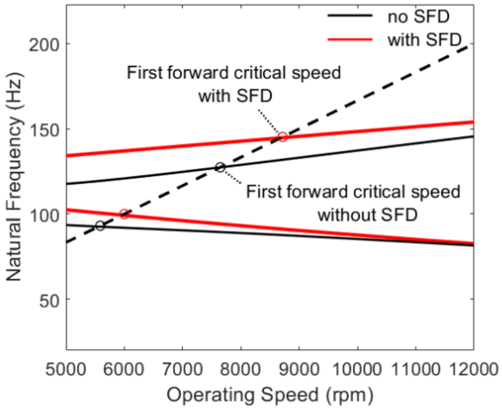

Figure 4.7 Campbell diagram of rotors with SFD and without SFD (No SFD indicates rigidly mounted TPJB)

A linear analysis has been conducted for a more complete description of the example rotor system prior to the nonlinear ME simulation. Note that the method used for the linear analysis is not a linear ME analysis, but a conventional method using linearized dynamic coefficients to calculate the critical speed and unbalance response. Figure 4.7 shows the Campbell diagram of the rotor-bearing system with and without the

SFD using $1\times10^{8}\ N/m$ cage stiffness and nominal parameters in Table 4.2. The damped first forward critical speed of both cases is found at 7,644 rpm for no SFD case and 8,708 rpm for with SFD case. It is sometimes noted that the ME occurs mainly when the rotor speed is near the rotor's first bending mode [37, 38]. This is not always the case, so care must be exercised to search a far wider speed range when designing to prevent the ME. The ME does occur near the critical speed in the example presented, and an increase in the critical speed may help expand the operating speed range being free from the ME vibration.

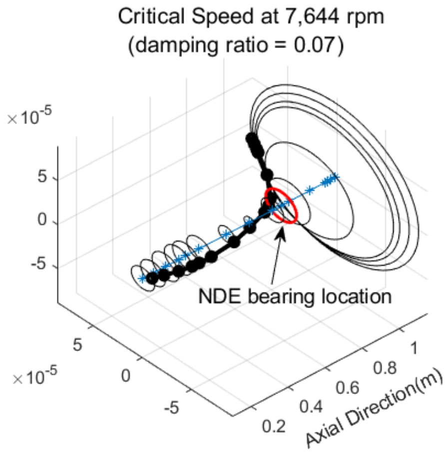

Figure 4.8 Bending mode of the example rotor at 7,644 rpm

The bending mode corresponding to the first forward critical speed without SFD in Figure 4.7 is illustrated in Figure 4.8.

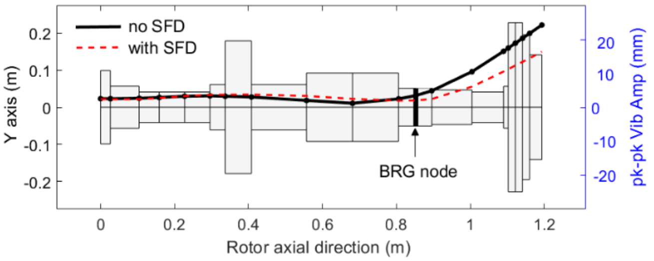

Figure 4.9 Distribution of unbalance response amplitudes along the length of the rotor for with and without SFD cases (No SFD indicates rigidly mounted TPJB)

Figure 4.9 illustrates the deflection shape based on unbalance response of both cases at each critical speed. With the SFD included, the vibration amplitudes at the bearing and the NDE rotor-end nodes have been reduced compared with no SFD case.

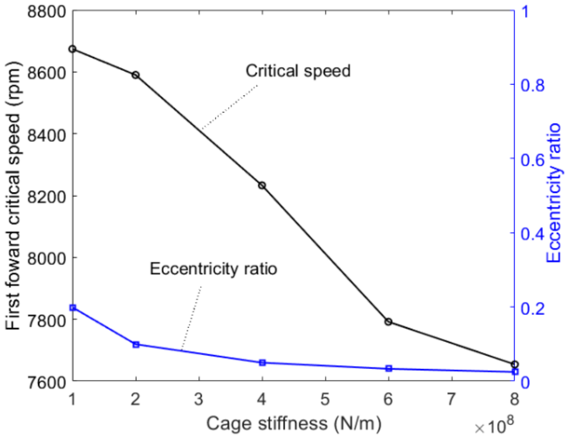

Figure 4.10 Linear analysis: Damped first forward critical speed and TPJB housing eccentricity ratio

In Figure 4.10, the SFD cage stiffness values are varied from $1\text{x}10^8 \ N/m$ to $8\text{x}10^8 \ N/m$ while other SFD parameters are fixed. The figure illustrates the damped first forward critical speed and TPJB housing eccentricities of the SFD with different cage stiffness. The model of the SFD including the cage stiffness assumes that the TPJB bearing housing is centered in the SFD when the bearing load is zero. The bearing load causes the TPJB bearing housing to become slightly eccentric in the SFD when the actual static bearing load is applied. The eccentricity remains very small (<0.2) for all cage stiffness values examined. The SFD damping and inertia coefficients remain nearly constant for this eccentricity range; therefore, the effects of the small eccentricity can be ignored. In the figure, the first forward critical speed shows decreased values with increasing stiffness as opposed to the common conception that high stiffness value leads to an increase in the system's natural frequency.

The trend of decreasing critical speed with higher stiffness is consistent with the observation in [73]. Note that an increase in the cage stiffness shifts the rotor's critical speed near the critical speed without SFD (7,644 rpm) in Figure 4.7.

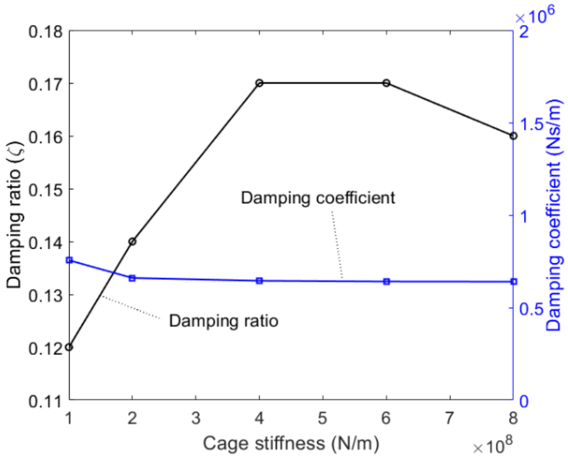

Figure 4.11 Linear analysis: damping ratio and damping coefficient change with different SFD cage stiffness

Figure 4.11 shows the damping ratio and damping coefficient variation with different cage stiffness. The damping ratio increases from the lowest value of 1×10^8 N/m to 4×10^8 N/m and slightly decreases with a further increase to 8×10^8 N/m.

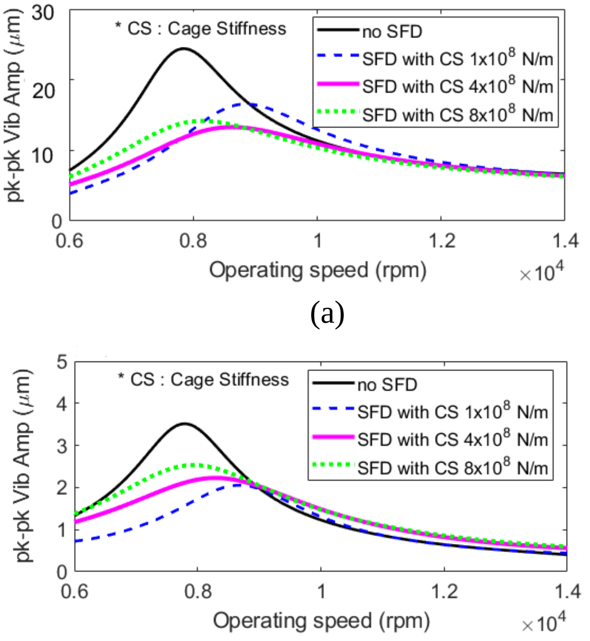

(a)

(b)

Figure 4.12 Linear analysis: Unbalance response (a) pk-pk vibration amplitude at Rotor end node (b) pk-pk vibration amplitude at bearing node

Figure 4.12 depicts the unbalance responses at the bearing and rotor-end via linear analysis. While the higher vibration level at the NDE rotor-end appears with the lower stiffness in Figure 4.12 (a), the vibration at the bearing location increases with the stiffer cage in Figure 4.12 (b).

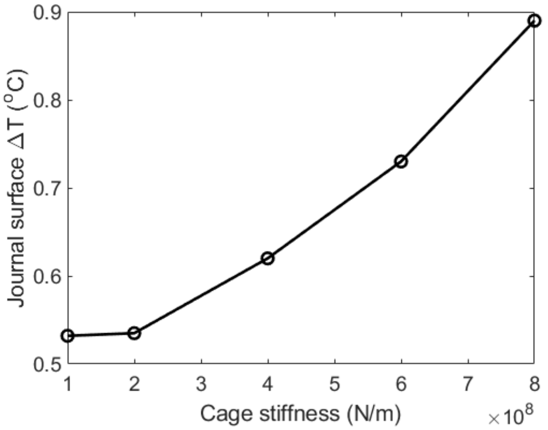

Figure 4.13 Nonlinear transient simulation result of journal surface ΔT at steady state condition with different cage stiffness (without thermal bow effect)

In Figure 4.13, the journal surface ΔT of the rotor with different cage stiffness is presented based on nonlinear transient simulation, which calculates the instantaneous TPJB bearing and SFD forces at each time step. The thermal bow effect is not included in all cases for comparison purposes. In the figure, an increase in cage stiffness induces more journal ΔT (The journal ΔT is calculated by subtracting the minimum temperature value on the journal surface from the maximum value at the bearing mid-plane). The results in Figure 4.12 (b) and 13 imply that for this example, increasing cage stiffness increases the vibration amplitude at the journal, which in turn increases journal ΔT.

This part presents the linear analysis with varying radial clearance and lubricant viscosity of the SFD and investigates the optimal parameters of the SFD in terms of vibration suppression. The nominal parameters in Table 4.2 and 1×10^8 N/m cage stiffness is used for simulation.

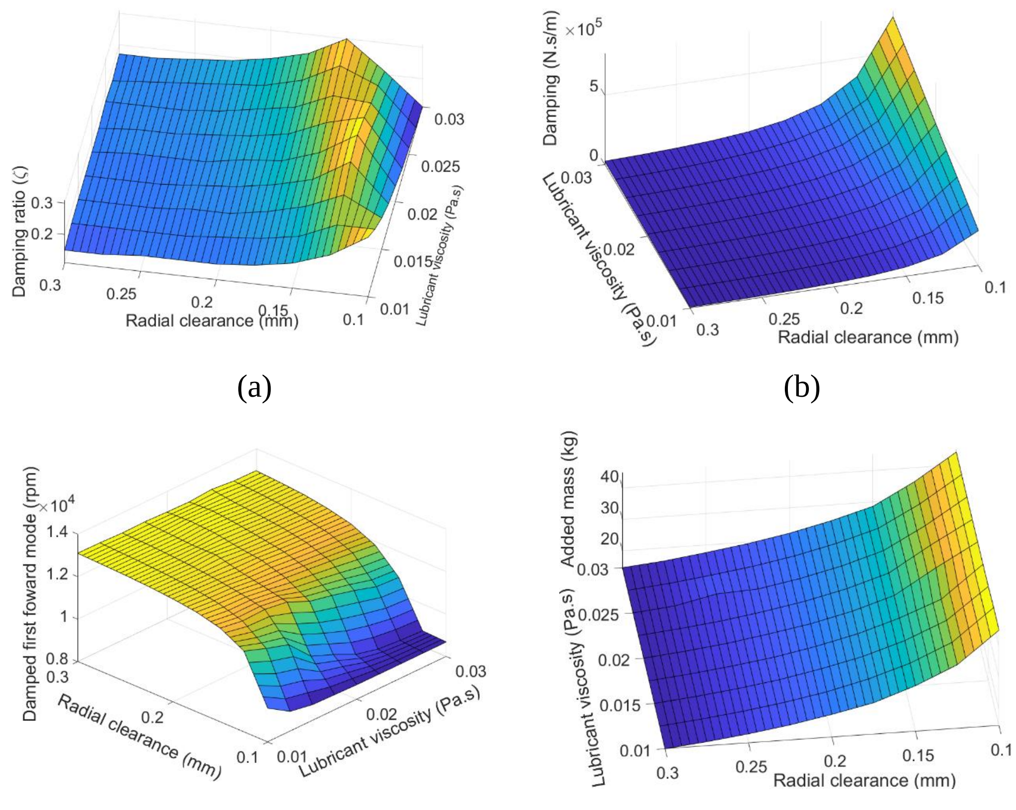

(a) (b)

(c) (d)

Figure 4.14 Linear analysis with SFD parameter variation (radial clearance and lubricant viscosity) (a) damping ratio of rotor, (b) damping coefficient of SFD, (c) Damped first forward critical speed, (d) added mass coefficient of SFD

The map in Figure 4.14 (a) shows a high damping ratio region where the SFD radial clearance ranges from 100μm to 150μm. Figure 4.14 (b) shows the corresponding damping coefficient map obtained via identical parameter variation. Note that the highest damping coefficient of 7.56×10^5 $N{\bullet}s/m$ with 100 μm radial clearance and 0.03 $Pa{\bullet}s$ lubricant viscosity leads to the lowest damping ratio of 0.11 in Figure 4.14 (a). The damping coefficient values corresponding to the high damping ratio range from 2×10^5 $N{\bullet}s/m$ to 2.5×10^5 $N{\bullet}s/m$ in Figure 4.14 (b). Figure 4.14 (c) illustrates the first forward critical speed map with varying parameters. The critical speed shifts up with larger radial clearance, and the highest critical speed reaches up to 13,000 rpm with 300μm radial clearance. Note that the critical speed is inversely proportional to the damping coefficients as higher critical speeds appear with lower damping coefficients, as indicated in Figure 4.14 (b) and (c). Figure 4.14 (d) shows that SFD radial clearance has a dominant effect on the added mass coefficient variation.

Two parameter sets with high damping ratio (Set 1: 0.3 mm radial clearance and 0.015 $Pa\bullet s$ lubricant viscosity and Set 2: 0.1 mm radial clearance and 0.01 $Pa\bullet s$ lubricant viscosity) are chosen from the map in Figure 4.14 (a), and their distribution of unbalance response are drawn in Figure 4.15. Both cases show the reduced deflection at the bearing and rotor-end locations than no SFD case. In addition, a significant reduction in the rotor-end deflection is identified compared with the nominal parameter set (0.3 mm radial clearance and 0.01 $Pa\bullet s$ lubricant viscosity).

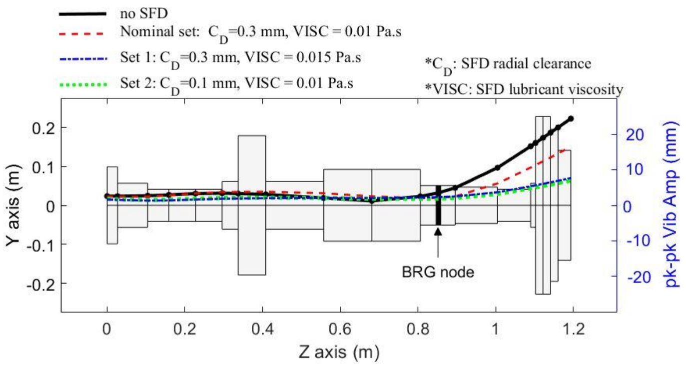

Figure 4.15 Distribution of unbalance response amplitudes along the length of the rotor for different SFD parameters (No SFD indicates rigidly mounted TPJB)

Nonlinear transient simulation is also performed with two selected sets and the nominal set from 7,000 rpm to 10,000 rpm in Figure 4.16. Note that the thermal bow effect is not included in all cases for comparison purposes. The two selected cases show decreased vibration level at the TPJB from 7,500 rpm to 9,500 rpm compared with the nominal set.

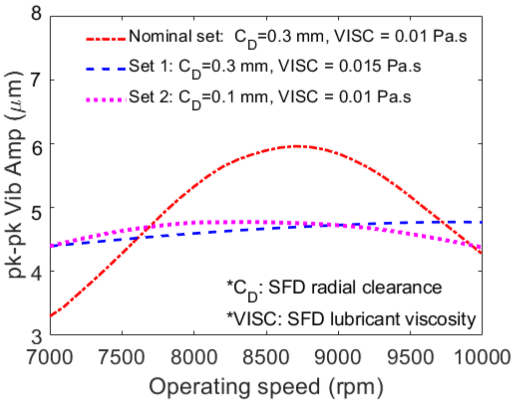

Figure 4.16 Nonlinear steady-state simulation: pk-pk vibration amplitude vs. rpm at the bearing node with different SFD parameter sets

4.3.2. Morton effect benchmark simulation

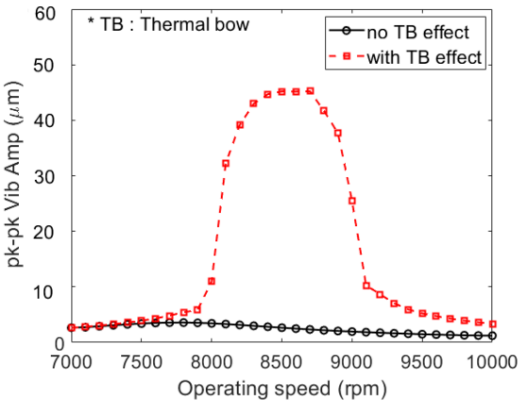

Figure 4.17 Nonlinear steady-state simulation: pk-pk vibration amplitude vs. rpm at bearing node

Morton effect simulations are performed to benchmark the experimentally observed ME case in [38]. Note that the SFD model is not included in the current analysis, and the parameters of the rotor-bearing configuration are from Table 4.2. The ME instability phenomenon is identified by observing a substantial increase in vibration caused by including the thermal bow (TB) effect, while the vibration amplitudes remain low if the TB effect is not included. More detailed descriptions of the ME instability determination are in [45]. Note that the exclusion of the TB is achieved by setting the induced thermal bow amplitude to be zero when the dynamic equations of the rotor are solved. Figure 4.17 illustrates the vibration level of the TPJB at different speeds with and without TB. This result is obtained via the nonlinear steady- state simulation explained in section 1.5. The no TB results in the figure are included to show that the large 1x vibration is caused solely by the ME. The result with TB exhibits much larger vibration amplitude from 8,000 rpm to 9,000 rpm as compared with the no TB model results. Ref. [38] shows high vibrations over a similar speed range. It is notable that the test results in [38] indicate high vibration as low as 7300 rpm, which is not apparent in the simulation model. This may be due to the effects of pedestal flexibility, lack of precise values of pad-pivot parameters or other un-modeled effects.

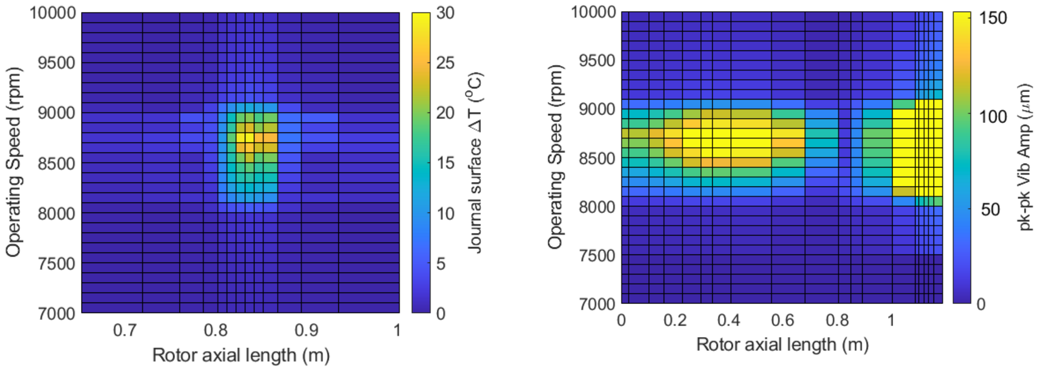

(a) (b)

Figure 4.18 Nonlinear steady-state simulation: Comparison of (a) journal surface ΔT and (b) pk-pk vibration amplitude vs. rpm and rotor axial position (with thermal bow effect)

Figure 4.18 (a) presents the journal temperature differential ΔT across the rotor axial length at different speeds. The journal ΔT is calculated by subtracting the minimum temperature value on the journal surface from the maximum value at the bearing mid-plane. Note that only the rotor's axial length from 0.6522 m to 1.0078 m is presented in the figure since the thermal shaft length is designated to be only seven times the bearing length (0.0508 m), as explained in [43, 44]. The region where large ΔT appears coincides with the bearing's axial location from 0.8022 m to 0.853 m. The largest ΔT of 28 $^\circ C$ is observed at the bearing mid-plane near 0.827 m at 8,700 rpm, where a rub between the journal and pad surfaces occurs, due to the ME. The large ΔT induces thermal bows with large amplitudes, displacing the overhung disk away from its equilibrium centerline. This causes significant imbalance excitation, which in turn causes high vibration of the rotor. The speed range with large ΔT corresponds to that with high vibration in Figure 4.18 (b). The high vibration with amplitudes up to 0.15

mm is observed at the rotor axial position from 0.2 m to 0.6 m and the rotor's NDE overhung side (axial length over 1 m). Note that the bending mode of the rotor showed large deflection on the NDE side at 7,644 rpm in Figure 4.18, which is consistent with the location of the large vibration in the nonlinear simulation results in Figure 4.18 (b). These results indicate that the ME vibration of the example rotor was closely related to its bending mode at 7,644 rpm. The speed range of large vibration is seen to occur above the critical speed and appears from 7,800 rpm to 9,000 rpm.

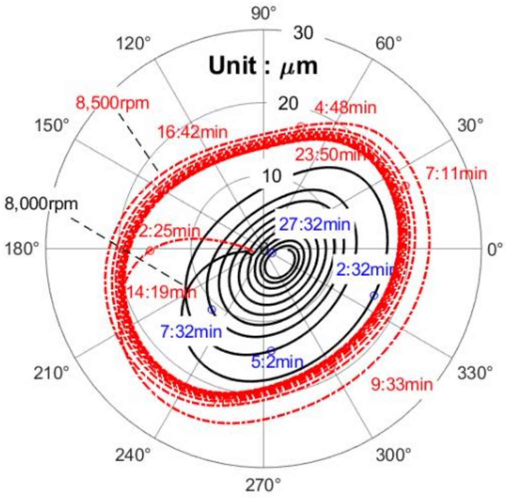

Figure 4.19 Nonlinear transient simulation: 1X filtered polar plot at 8,000 and 8,500 rpm (with thermal bow effect)

Nonlinear transient simulations are performed both at 8,000 and 8,500 rpm, and the results are presented in Figure 4.19 and Figure 4.20. All parameter inputs of the system are identical to the aforementioned nonlinear steady-state simulation, and the SFD is not included. Figure 4.19 displays a 1X filtered polar plot based on the vibration amplitude and phase at the bearing for both speeds. Note that the texts in the plot denote the simulation time at the instance when the vibration amplitude and phase are plotted. At 8,000 rpm, the rotor initially shows a large thermal spiral with time-varying vibration amplitude and phase, which is caused by the large ΔT in Figure 4.18 (a) and its resultant thermal bow. The vibration amplitude reached its maximum value of 20 μm and then dropped to 2.36 μm at 25 minutes, and the phase of the vibration keeps changing from 0° to 360° during the process. This thermal spiral vibration is the main characteristic of the ME and was experimentally observed in [38]. At 8,500 rpm, a larger thermal spiral with the maximum amplitude of 25 μm appears and does not converge with time.

Although the high vibration level accompanied by time-varying phase, without rub between the journal and pads, is consistent with observations in the experiment in [38], the predicted vibration levels are lower than the observed ones in [38]. This may be due to uncertainties in the simulation parameters, including unbalance distribution or other un-modeled effects.

Figure 4.19 demonstrates that the phase angle migration is more severe at 8,500 rpm compared with 8,000 rpm. This occurs even though 8,500 rpm is displaced further from the linear system model's critical speed at 7,644 rpm. This shows that the ME is not strictly a resonance problem. The increase in thermal bow (imbalance) due to the ME at the higher speed dominates over the effect of proximity to the critical speed. This is also reflected in the greater migration of the phase angle at 8,500 rpm seen in Figure 4.19. Having said this, the disappearance of the ME below 6,000 rpm and above 10,000 rpm demonstrates a clear dependency of the ME on proximity to a critical speed.

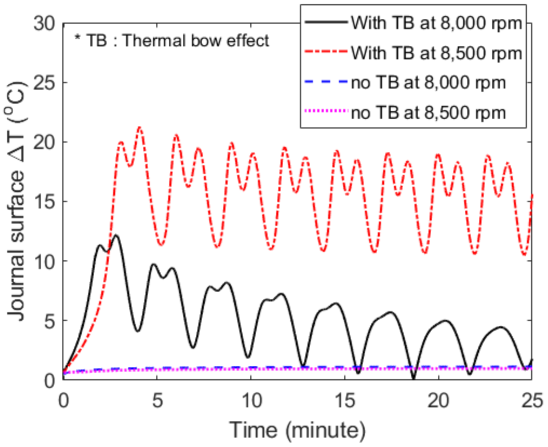

Figure 4.20 Nonlinear transient simulation: journal surface peak-peak ΔT at 8,000 and 8,500 rpm (with and without thermal bow effect)

Figure 4.20 illustrates the corresponding journal ΔT at the bearing mid-plane for the rotors with and without TB at two operating speeds. The journal ΔT at 8,000 rpm shows a smaller value compared with that of 8,500 rpm in most of the simulation, indicating a smaller thermal bow amplitude and less severe vibration at the speed. Note that the temperature oscillations at a fixed location will depend on the proximity of running speed to the critical speed. If running were well below the critical speed in a region of non-resonant forced response, the hot spot would remain fixed circumferentially. The result without the TB shows stable ΔT converging to around 1 ℃ with time at both speeds. This comparison confirms that the violent vibration in Figure 4.19 was induced by the ME. The oscillating amplitude of the ΔT also is consistent with the varying vibration amplitude, as observed in Figure 4.19.

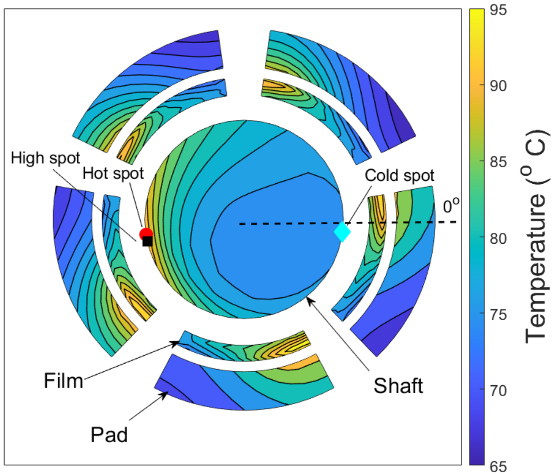

Figure 4.21 Nonlinear transient simulation: temperature distribution at bearing mid-plane of the with thermal bow case at 8,500 rpm after 25 minutes

Figure 4.21 illustrates the corresponding temperature distribution at the bearing mid-plane of the with TB case at 8,500 rpm after 25 minutes. The high journal ΔT of 15.2 ℃ occurs at the hot spot (188.8°) on the journal surface. The high spot denoted with the black rectangular leads the hot spot (192.8°) with 4°. The cold spot is seen at 352.6°, which is 159.8° away from the hot spot.

4.3.3. Effects of SFD at different cage stiffness

To mitigate the vibration induced by the ME, the SFD model developed in section 1.1 is incorporated into the rotor's bearing location, as explained in section 1.4. The conventional SFD consists of the cage stiffness and lubricant film at the gap between the TPJB housing and the SFD housing. Reference [62] shows that the proper selection of cage stiffness is crucial for maximizing the damping capability of the SFD.

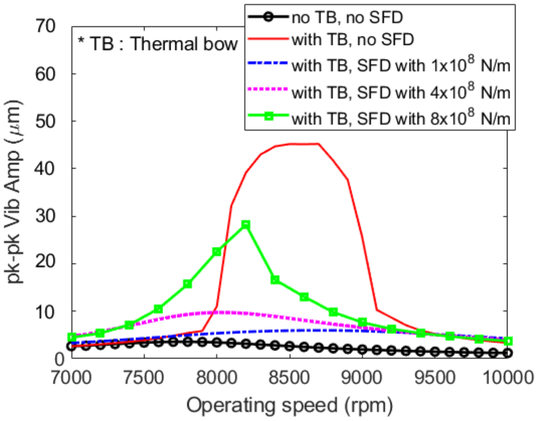

Figure 4.22 Nonlinear steady-state simulation: pk-pk vibration amplitude vs. rpm at bearing node with different cage stiffness

Figure 4.22 compares the vibration level at the bearing with different cage stiffness of the SFD. Nonlinear steady-state simulation is carried out from 7,000 rpm to 10,000 rpm. Although all stiffness cases display relatively reduced vibration amplitudes compared with the rotor “with TB and without SFD case”, they still have higher vibration than when not considering the TB effect. In the figure, the vibration level increases with the stiffer cage, and the $8\text{x}10^8\ N/m$ shows the largest pk-pk vibration amplitude of 28.21 μm at 8200 rpm.

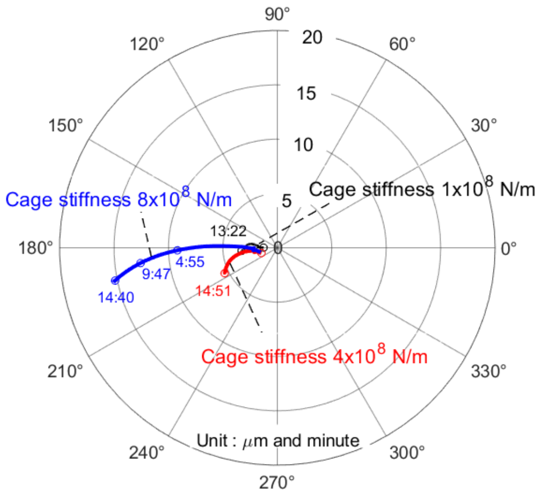

Figure 4.23 Nonlinear transient simulation: 1X polar plot at critical speed with different cage stiffness

Figure 4.23 displays the 1X filtered polar plot with different cage stiffness where the results are obtained at each critical speed. The critical speed is defined here as the speed where the maximum pk-pk vibration occurs. In Figure 4.22, the maximum pk-pk vibration appears at 8,600 rpm for the 1×10^8 N/m cage stiffness, 8,100 rpm for 4×10^8 N/m, and 8,200rpm for 8×10^8 N/m, indicating the shift in critical speed depending on the cage stiffness. Figure 4.23 shows increasing vibration amplitudes for all three cases, while the operating speed and conditions are kept constant. The amount of vibration increase is more significant with higher stiffness values. The phase angles of the vibration also keep changing during the 15min, but they are not as evident as the rotor without the SFD case in Figure 4.19.

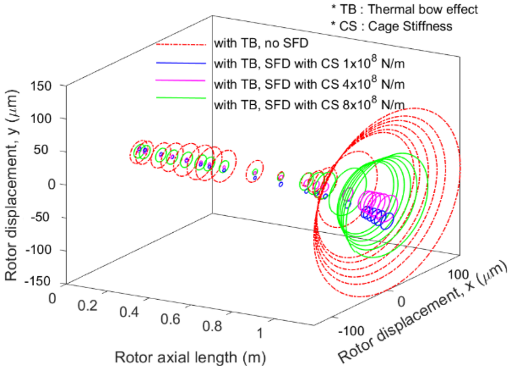

Figure 4.24 Nonlinear transient simulation: 3D orbit shapes at critical speed after 25 minutes with different cage stiffness

Figure 4.24 shows 3D orbit shapes of the rotor with different cage stiffness obtained via nonlinear simulation. The orbits are drawn at each critical speed after 25 minutes. In the figure, the orbit sizes of the rotor keep growing and approach the size of the no SFD case with increasing cage stiffness. Note that the orbits with relativity low cage stiffness ($1\times10^8 \ \ N/m$) are shifted downward in y direction due to the larger static deflection of the cage.

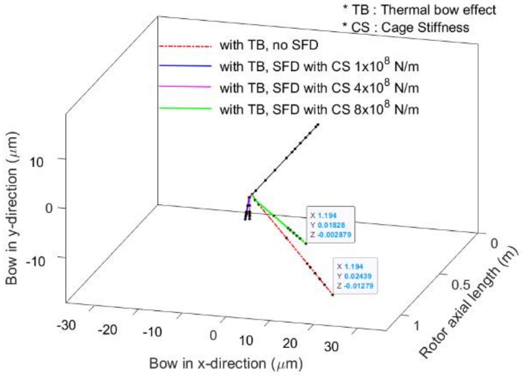

Figure 4.25 Nonlinear transient simulation: thermal bow of shaft at critical speed after 25 minutes with different cage stiffness

Figure 4.25 shows the amplitude of the induced thermal bow corresponding to the result in Figure 4.24. In the no SFD case, a large thermal bow amplitude of 27.5 μm appears at the rotor end, and its corresponding phase angle is 331°, which is 143° away from the hot spot in Figure 4.21. With the SFD, the thermal bow amplitudes are substantially reduced, as shown in Figure 4.25. When the SFD is considered, the most significant thermal bow occurs with the cage stiffness of $8 \times 10^8\ N/m$, and its value is 18.5 μm. Relatively small thermal bow amplitudes are induced with low cage stiffness values. This result confirms that high cage stiffness of the SFD causes increased ME-induced vibration in the example presented. Note that in the linear and nonlinear analysis results in Figure 4.12 and Figure 4.13, the vibration amplitudes at journal location have been reduced with stiffness cage and thus resulting in less journal ΔT.

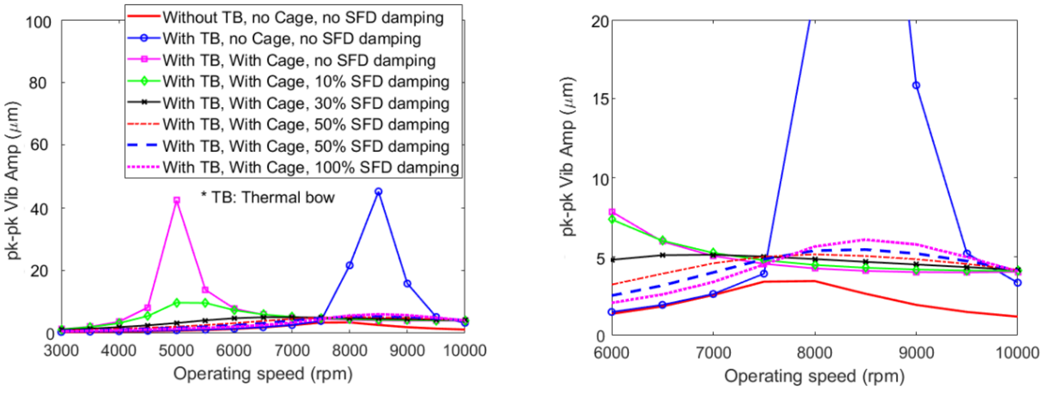

(a) (b)

Figure 4.26 Nonlinear transient simulation: (a) pk-pk vibration amplitude vs. rpm at bearing node at critical speed after 25 minutes (b) zoom of (a)

The higher vibration level with stiffer cage may be due to the decreased effective damping with increasing cage stiffness of bearing support as demonstrated in [108]. Based on the nonlinear simulations, the cage stiffness value of $1\times10^{8}\ N/m$, ensures a low journal eccentricity (<0.2) and small vibration amplitudes. This value is selected for the SFD design and will be used for the simulations in the following discussion. Simulations are performed with varying levels of SFD force, from 0 % to 100 % of the nominal value, to demonstrate that the full SFD force is not required to suppress the ME. The cage stiffness of $1\times10^{8}\ N/m$ and the rotor-bearing-SFD parameters in Table 4.2 are employed for simulation. Figure 4.26 depicts the nonlinear steady-state result from 3,000 rpm to 10,000 rpm. When no SFD force (0 % of SFD force) and only cage stiffness are included in the simulation, a much larger vibration amplitude (42.39 μm)) than the no TB case occurs at 5,000 rpm, indicating ME occurrence. By increasing the SFD force from 10 % up to 100 % of the nominal value, the high vibration level is mitigated compared with 0 % case. Note that the most stable vibration with the smallest pk-pk vibration at its resonance speed occurs with 50 % of SFD force, which confirms the existence of optimal damping in terms of vibration suppression [61]. The linear analysis in Figure 4.14-16 also indicated the existence of optimal SFD parameters, which showed more improved stability of the rotor. The relocation of the critical speed is also observed with the SFD force variation. With the 0 % SFD force and with the cage stiffness, the critical speed at the low speed of 5,000 rpm appears while the counterpart of no SFD case is around 7,600 rpm. By increasing the ratio of the SFD force, the critical speed shifts up to its maximum value of 8,500 rpm with 100 % of the nominal force. The result confirms that the cage stiffness alone is not effective in controlling the ME vibration, and the damping force from the SFD is needed to suppress the ME.

4.3.4. Comparison between with and without SFD

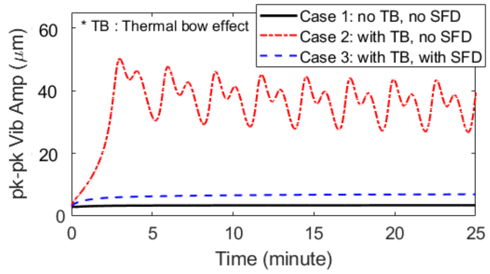

(a)

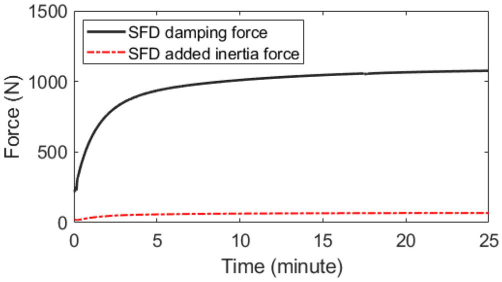

(b)

Figure 4.27 Nonlinear transient simulation: (a) pk-pk vibration amplitude (b) SFD damping and added inertia force from Case 3 at critical speed

Figure 4.27 (a) depicts the pk-pk vibration of the bearing with time at the speed where maximum vibration level appears in nonlinear simulation. Three different cases are considered, i.e., Case 1: no thermal bow and no SFD (TPJB rigidly mounted), Case 2: with thermal bow and no SFD, Case 3: with thermal bow and SFD (cage stiffness of $1\times10^{8}\ N/m$). In Case 3, the high vibration induced by the ME is suppressed to an acceptable level, but the vibration level is still higher than Case 1. In Figure 4.27 (b), the magnitude of the SFD damping and inertia forces from Case 2 increase with time and converge to 1,076 N and 68 N, respectively.

	7500 rpm	8000 rpm	8500 rpm	9000 rpm	9500 rpm
Case 1	6.93 °	8.49 °	9.39 °	6.998 °	3.633 °
Case 2	6.66 °	8.23 °	NC	7.173 °	3.641 °
Case 3	12.32 °	11.83 °	11.23 °	11.72 °	10.8 °

*NC: non-converging

Table 4.3 Phase lag between high and hot spots (Case 1: no thermal bow and no SFD, Case 2: with thermal bow and no SFD, Case 3: with thermal bow and with SFD)

The migration of the hot spot on the journal surface causes the phase-varying thermal bow and thus the varying phase in the induced ME vibration. In the process, the hot spot typically lags the high spot (minimum film thickness) on the journal due to the convection effect in the lubricant film. Therefore, the occurrence of the ME is closely related to the stability of the hot spot. It is known that when the ME occurs, the hot spot moves around the journal circumference, and the phase lag between hot and high spots changes accordingly [37, 38]. In this regard, the phase lag between high and hot spots at various operating speeds are investigated. The phase lag values are measured after 25 minutes via nonlinear simulation in Table 4.3. The comparison between Case 1 and 2 reveals that phase lags are similar regardless of the thermal bow inclusion at the speeds where the ME induced vibration is not evident, as shown in Figure 4.27 (7500, 9000 and

9500 rpm). At 8,000 rpm, the ME starts to influence the rotor vibration in Figure 4.27, and the phase lag changes from 0° to 360° during most of the simulation, and eventually converges to 8.23°, which is similar to that of Case 1.

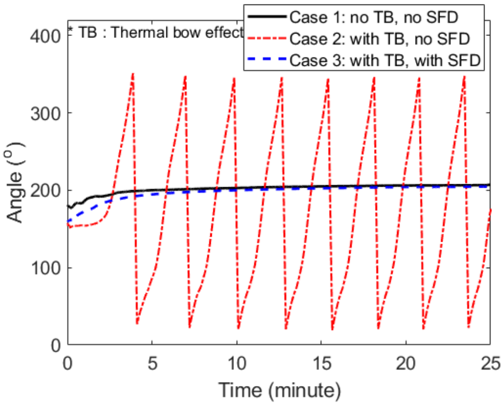

Figure 4.28 Nonlinear transient simulation: hot spot location change with time at critical speed (No SFD indicates rigidly mounted TPJB)

At 8,500rpm, the thermal spiral is non-converging type, and the rotor exhibits the high vibration with varying phase until 25 minutes. The corresponding hot spot location with time is shown in Figure 4.28. The angle shown in the figure provides the angular position of the hot spot relative to the angular position of the original imbalance, which is fixed at 0°, and this is shown in Figure 4.21.

The hot spot angle of Case 2 keeps varying in a wide range and does not converge to a steady-state value, while those of Case 1 and 3 show stable and converging angles with time. Note that Case 3 shows relatively increased and stable phase lags ranging from 10.8° to 12.32° compared with two other cases without the SFD. The stable hot spot angles and increased phase lag may explain the enhanced stability and the ME suppression in the rotor-bearing due to the SFD.

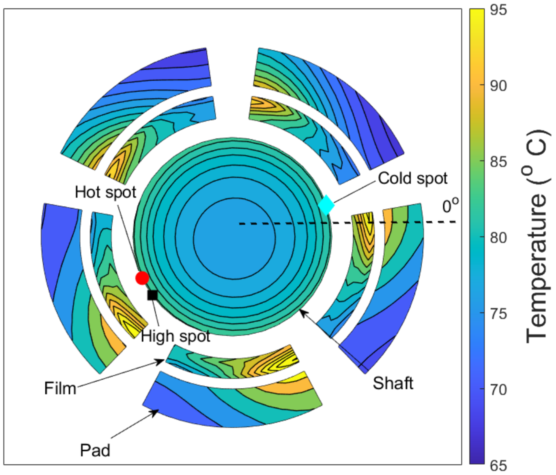

Figure 4.29 Nonlinear transient simulation: temperature distribution at bearing mid-plane at 25 minutes with SFD

Figure 4.29 illustrates the temperature distribution at the bearing mid-plane of Case 3 after 25 minutes of simulation at its critical speed (8,600 rpm), where the high spot leads the hot spot with 11.72°. Comparing with that of Case 2 at the same instance in Figure 4.21 reveals that the induced high ΔT is suppressed in Case 3 as displayed by the concentric distribution of the journal temperature. This may be attributed to the addition of the SFD, which reduced the vibration amplitudes at the journal location as demonstrated from the linear unbalance analysis in Figure 4.12. The reduced synchronous orbits within the journal may result in less asymmetric heating of the journal as evidenced in Figure 4.13.

5. TILTING PAD PIVOT FRICTION AND DESIGN EFFECTS ON THERMALLY INDUCED VIBRATION (MORTON EFFECT)

5.1. Introduction

The effect of pivot designs on the ME instability has not been fully investigated yet. Though the effect of different pivot geometries was considered in [44, 45], their analysis was limited to the TPJB's static performance under the misaligned journal condition [45], and the ME vibration using linear pivot stiffness at the single operating speed [44]. The impact of the pad-pivot friction under dynamic loading conditions was investigated in [89-91]. However, a simple rigid rotor model (Jeffcott rotor) was employed in their analysis, and the only friction moment concerning the tilting motion is considered while the spherical pivot allows both tilting and rolling motions. The present study analyzes the influence of the pad-pivot design effects on the ME vibration with more detailed models of pivots including nonlinear pivot stiffness, spherical pivot's rolling motion, and pad-pivot friction. The improved cooling effect of a spherical pivot compared with the cylindrical pivot will be verified. The nonlinear time-varying pivot stiffness based on Hertzian contact theory is employed, and its effect on the ME will be carried out in a wide operating speed range.

5.2. Rotor-bearing modeling

5.2.1. Pad-pivot design

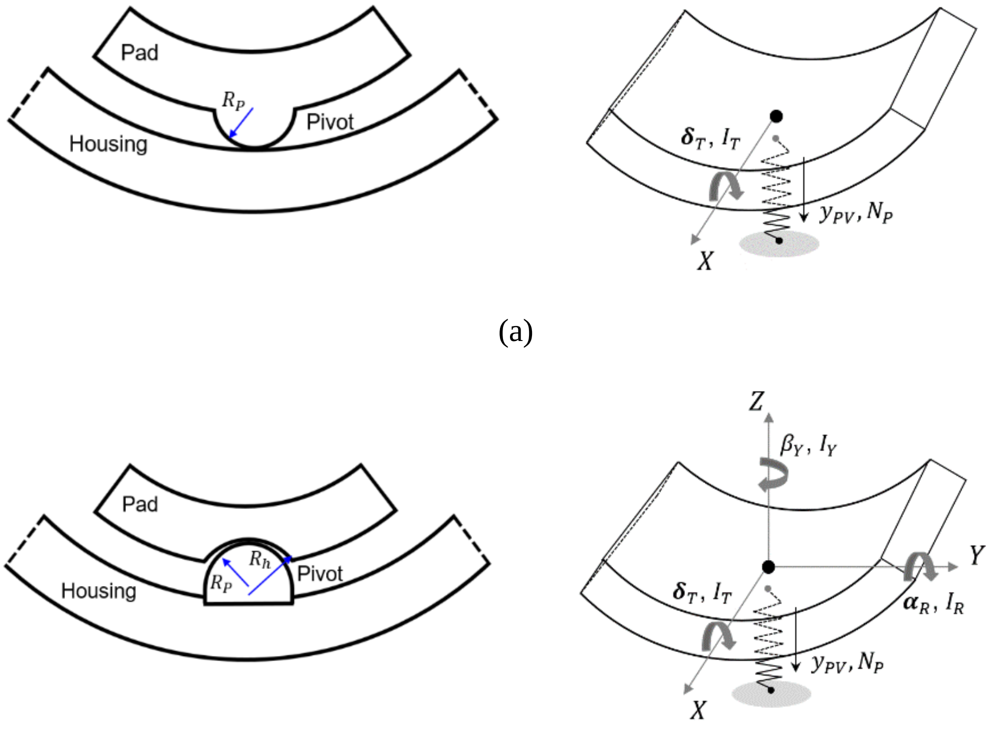

(a)

(b)

Figure 5.1 (a) Schematic of cylindrical type pad-pivot (b) Schematic of spherical type pad-pivot

The two most commonly used pivot types of TPJBs are cylindrical and spherical pivots as illustrated in Figure 5.1. The former has a cylinder-shaped pivot on the backside of a pad. Since the diameter of the pivot in an axial direction (pad rolling direction) is usually much larger than the one in a radial direction, the cylindrical type only allows a tilting motion. Meanwhile, since the spherical pivot has identical pivot diameters in the both axial and radial directions, the pivot type enables both rolling and yawing motions as well as the tilting.

In the current analysis, nonlinear pivot stiffness based on the Hertzian contact theory is employed for each pivot case. From [80, 81], the nonlinear pivot stiffness of the cylindrical type is expressed as

$$K_{CYL} = \frac{EL_{PIV}\pi}{2(1-\nu^2)(\frac{2}{3}+\ln(0.87EL_{PIV}(D_H - D_P))} \tag{5.1}$$

where E and ν represent Young's modulus of pad and housing, and Poisson's ratio respectively. L_{PIV}, D_H and D_P denote the cylindrical pivot's axial length, housing diameter, and pivot diameter, respectively.

The nonlinear pivot stiffness of the spherical pivot [80, 81] also is expressed as

$$K_{SPH} = 1.442\sqrt[3]{\frac{F_P C_1}{C_2{}^2}}, \ C_1 = \frac{D_H D_P}{D_H - D_P}, \ C_2 = \frac{1-\nu_P{}^2}{E_p} + \frac{1-\nu_H{}^2}{E_H} \tag{5.2}$$

where F_P is load applied on a pivot. D, ν, and E represent the diameter of pads and housing, Young's modulus, and Poisson's ratio, respectively. The subscripts P and H represent the pivot and housing, respectively.

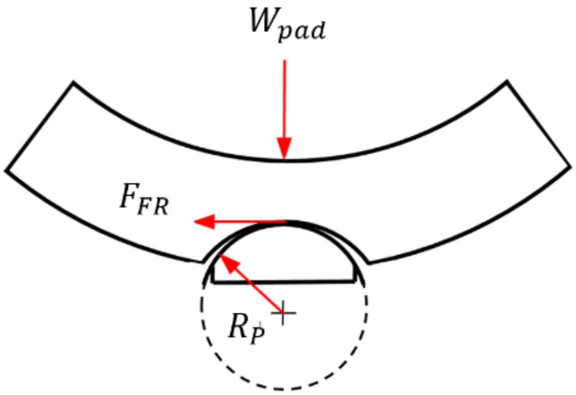

Figure 5.2 Friction mechanism between pad and pivot

In the spherical pivot, the friction between pad and pivot is present since the pad slides on the pivot as shown in Figure 5.2. The mathematical model of pad-pivot friction developed in [89] is employed in the current analysis. The force induced by the friction, F_{FR} , can be determined by the product of normal load applied on the pivot and the friction coefficient between two contact surfaces. Then the friction moment, M_{FR} , which is the product of pivot radius and friction force, is applied to each pad and deters the pad motions. As shown in Eq. (5.3), the friction moment applied to pads are separated into two categories, i.e., 1) pad in sliding motion and 2) pad in stuck, and its equations are as follows

$$M_{FR} = -\frac{\dot{\delta}}{\left|\dot{\delta}\right|}\left|\mu_{FR} R_P W_{pad}\right| \quad \text{if } \dot{\delta} \neq 0$$

$$M_{FR} = \begin{cases} -M_P & \text{if } \left|M_P\right| < \left|\mu_{FR} R_P W_{pad}\right| \\ -\frac{M_P}{\left|M_P\right|}\left|\mu_{FR} R_P W_{pad}\right| & \text{if } \left|M_P\right| \geq \left|\mu_{FR} R_P W_{pad}\right| \end{cases} \tag{5.3}$$

where $\dot{\delta}$ is the angular velocity of tilting or rolling motion of pads. μ_{FR}, R_P and W_{pad} denote the friction coefficient, pivot radius, and load applied on the pad, respectively. M_P is an applied load on the pad by lubricant film pressure. If the pad is in motion, the friction moment is determined by multiplying the friction force ($F_{FR} = \mu_{FR} W_{pad}$) and pivot radius ($R_P$), and its direction is opposite to the pad motion. If the pad is stuck, the friction exerts the moment with the same magnitude applied on the pad by the lubricant (M_P) or the moment with the magnitude of $\mu_{FR} R_P W_{pad}$. The direction is also in the opposite of the external moment on the pad. The angular velocity $\dot{\delta}$ can be either tilting or rolling motion of the pad. Unlike the previous works which only accounted for the friction applied to the pad tilting motion, this study considers the friction moment in both tilting and roll motions while the friction due to yawing motion is assumed negligible. For this, the magnitudes of the pad angular velocities of both motions are determined by the projection of the resultant moment along the pitch and roll axes. Note that the nonlinear stiffness calculation in Eq. (5.1) and (5.2) assumes the frictionless contact between pad and pivot. Therefore, care should be taken when applying the pad-pivot friction along with the nonlinear pivot stiffness model based on the Hertzian contact theory. This may be somewhat unrealistic to use both models together. However, in the following analysis, since the aim of this study is to analyze the friction effect on the ME vibration, both models are used together to investigate the trend of friction effect depending on different pivot flexibility.

5.2.2. Reynolds and energy equations

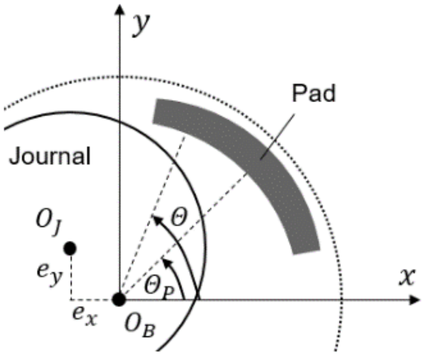

Figure 5.3 Schematics of journal and pad dynamics

The schematic of journal and pad are shown in Figure 5.3. O_J and O_B are centers of journal and bearing, respectively. θ and θ_P denotes the circumferential coordinate and angular position of the pivot, respectively. The equation for lubricant film thickness in the case of the spherical pivot TPJB is

$$\begin{aligned} h(\theta,z) &= C_P - \hat{e}_x\cos(\theta) - \hat{e}_y\sin(\theta) - (C_P - C_b)\cos(\theta-\theta_P) \\ &-\delta_{tilt}R\sin(\theta-\theta_P) - h_{shaft.TE}(\theta,z) - h_{pad.TE}(h,z) \end{aligned} \tag{5.4}$$

where

$$\hat{e}_x = e_x - y_{pvt}\cos\theta_p - z\alpha_{pitch}\cos\theta_p - z\beta_{yaw}\cos(\theta_p + \pi/2),$$

$$\hat{e}_y = e_y - y_{pvt}\sin\theta_p - z\alpha_{pitch}\sin\theta_p - z\beta_{yaw}\sin(\theta_p + \pi/2).$$

and C_P and C_b represent the pad and bearing clearances, respectively. y_{pvt}, δ_{tilt}, α_{pitch} and β_{yaw} denote the pivot displacement and tilting/rolling and pitching motions, respectively. R, $h_{shaft.TE}$ and $h_{pad.TE}$ are journal radius, thermal expansion of shaft and pads, respectively. The thermal expansion is obtained from the 3D FEM which is detailed in [43-45]. In the case of the cylindrical pivot, the terms related to rolling and yawing motions (α_{pitch} and β_{yaw}) in Eq. (5.4) are set to be zero. For the rigid pivot case, the pivot displacement y_{pvt} is also removed from the equation.

The generalized Reynolds equation and 3D energy equation are used to obtain the lubricant film force.

The Reynolds equation for an incompressible, Newtonian fluid and negligible fluid inertia is

$$\begin{gathered} \nabla\cdot(C_1\nabla P) + \nabla D_2\cdot U + \partial h/\partial t = 0 \\ C_1 = \int_0^h\int_0^z(\xi/\mu)d\xi dz - C_2\int_0^h(\xi/\mu)d\xi \\ C_2 = \int_0^h\int_0^z(1/\mu)d\xi dz \Big/ \int_0^h(1/\mu)d\xi \end{gathered} \tag{5.5}$$

where h is lubricant film thickness, μ is a variable viscosity term dependent on lubricant temperature.

The viscosity-temperature relation is applied by

$$\mu = \mu_0 \exp^{-\alpha(T-T_0)} \tag{5.6}$$

where μ_0, T_0 and α are reference viscosity/temperature and viscosity coefficient, respectively. T is lubricant film temperatures obtained from 3D energy equation

The energy equation is solved with

$$\rho c(u\frac{\partial T}{\partial x} + w\frac{\partial T}{\partial z}) = k(\frac{\partial^2 T}{\partial x^2} + \frac{\partial^2 T}{\partial y^2} + \frac{\partial^2 T}{\partial z^2}) + \mu\left[(\frac{\partial u}{\partial y})^2 + (\frac{\partial w}{\partial y})^2\right] \tag{5.7}$$

where ρ, c, k and μ are density, heat capacity, thermal conductivity and viscosity of lubricant film. Note that lubricant velocities in the circumferential direction (u) and axial direction (w) are obtained from the Reynolds equation in Eq. (5.5). The Reynolds equation and energy equations are solved with the FEM using the 2D triangle elements for the former and the 3D isoparametric hexahedron element for the latter. Quadratic up-winding scheme [105] is applied for the FEM calculation of the energy equation to prevent the spatial oscillation problem from the convection term in Eq. (5.7).

5.2.3. TPJB and flexible rotor dynamic equations

The dynamic equations of the spherical pivot TPJB considering the nonlinear pivot stiffness and pad-pivot friction are

$$\begin{aligned}
m_{Pi}\ddot{y}_{PVi} &= -K_{SPHi}y_{PVi} + F_{Pi} \\
I_{Ti}\ddot{\delta}_{Ti} &= M_{Ti} + M_{FRi,T} \\
I_{Ri}\ddot{\alpha}_{Ri} &= M_{Ri} + M_{FRi,R} \\
I_{Yi}\ddot{\beta}_{Yi} &= M_{Yi} + M_{FRi,Y}
\end{aligned} \tag{5.8}$$

where i represents the pad number. m_{Pi}, I_{Ti}, I_{Ri} and I_{Yi} are pad mass and pad inertia of tilting/rolling/yawing degree of freedom. The corresponding coordinates related to pad mass and inertia (y_{PVi}, δ_{Ti}, α_{Ri} and β_{Yi}) are illustrated in Figure 5.1. K_{SPHi} is the nonlinear pivot stiffness of the spherical pivot calculated from Eq. (5.2). Note that the stiffness value is time-varying since the equation is a function of lubricant force applied on each pad (F_{Pi}). The pad-pivot friction moments, M_{FRi}, are applied to the relevant motions and axes. The friction moment on the yawing motion is assumed negligible and set to zero in the simulation. For the cylindrical pivot type, the degree of freedoms corresponding to rolling and yawing motions are removed and the nonlinear pivot stiffness, K_{SPHi}, is replaced with K_{CYLi} in Eq. (5.1). This equation is then combined with the flexible rotor model based on the Euler beam theory. The beam model is reduced with modal reduction, and it is systematically connected to the tilting pad journal bearing equations in Eq. (5.8). Detailed explanations of this procedure are presented in [43, 46].

The algorithms to solve the nonlinear ME simulations are also detailed in [43, 46] where the Reynolds and Energy equations and thermal/dynamic structures of the rotor and the TPJB are systematically coupled, and time-staggering integration is used for the transient simulations of the ME phenomenon.

5.3. Simulation results

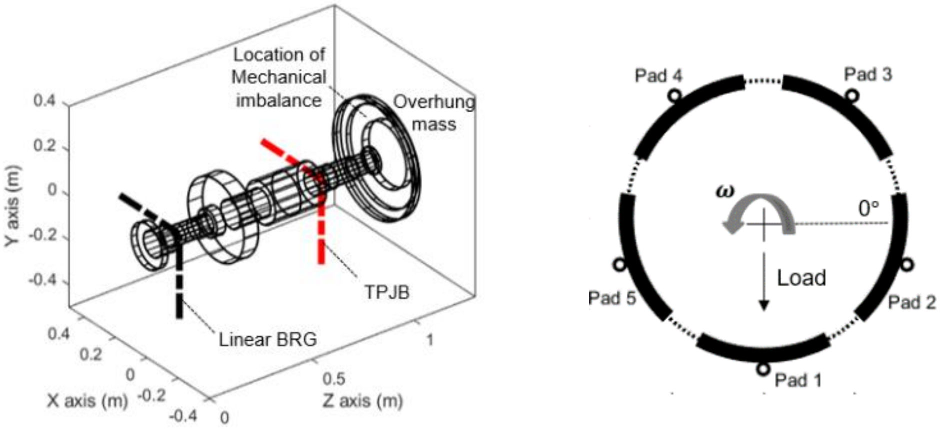

(a) (b)

Figure 5.4 Schematics of rotor and bearing configurations

Figure 5.4 represents the rotor and bearing configurations used for ME simulations. In Figure 5.4 (a), the linear and nonlinear TPJB bearings are located at node 4 and 12, respectively. The initial mechanical imbalance is at the NDE overhung mass of node 18. The stiffness and damping values of the linear ball bearing at node 4 and the amplitude of mechanical imbalance are shown in table 5.1. The TPJB with five pads and load-on-pad configuration are also illustrated in Figure 5.4 (b). The parameters of the rotor-bearing such as shaft diameter, lubricant properties, and TPJB design parameters are listed in Table 5.1. Design parameters of the two different pivot types, i.e., cylindrical (CYL) and spherical pivot (SPH), used for simulations are also shown in the same table.

Lubricant parameters		**Bearing parameters**	
Viscosity at 50 °C [Ns/m^2]	0.0203	Pad type	Load on pad
Viscosity coefficients [1/°C]	0.031	No. pads	5
Supply temperature [°C]	50	Radius of shaft [m]	0.0508
Inlet pressure [Pa]	1.32×10^5	Bearing clearance [μm]	74.9
Reference temperature [°C]	50	Preload	0.5
Shaft Parameters		Bearing length[m]	0.0508
Heat capacity [J/kg °C]	453.6	Thermal expansion coefficient [1/°C]	1.3×10^{-5}
Heat conductivity [W/mK]	50	Reference temperature [°C]	25
Thermal expansion coefficient [1/°C]	1.22×10^{-5}	Pivot radius [mm]	15
Reference temperature [°C]	25	Pivot friction coefficient	0.1~0.4
Thermal rotor length [m]	0.3508	**Linear Ball Bearing**	
		K_{xx}, K_{yy} [N/m]	1.7×10^8
		C_{xx}, C_{yy} [Ns/m]	1.0×10^5
Cylindrical pivot parameters		**Spherical pivot parameters**	
Pivot radius [mm]	62	Pivot radius [mm]	19.98
Pivot housing radius [mm]	55	Pivot housing radius [mm]	20
Length of cylindrical pivot [mm]	40	Elastic modulus of spherical pivot [Pa]	2.1e11
Elastic modulus of pivot [Pa]	2.1e11	Poisson’s ratio of spherical pivot	0.3
Poisson’s ratio of pivot/pivot housing	0.3		

Table 5.1 Parameter values for the example system

5.3.1. Linear analysis

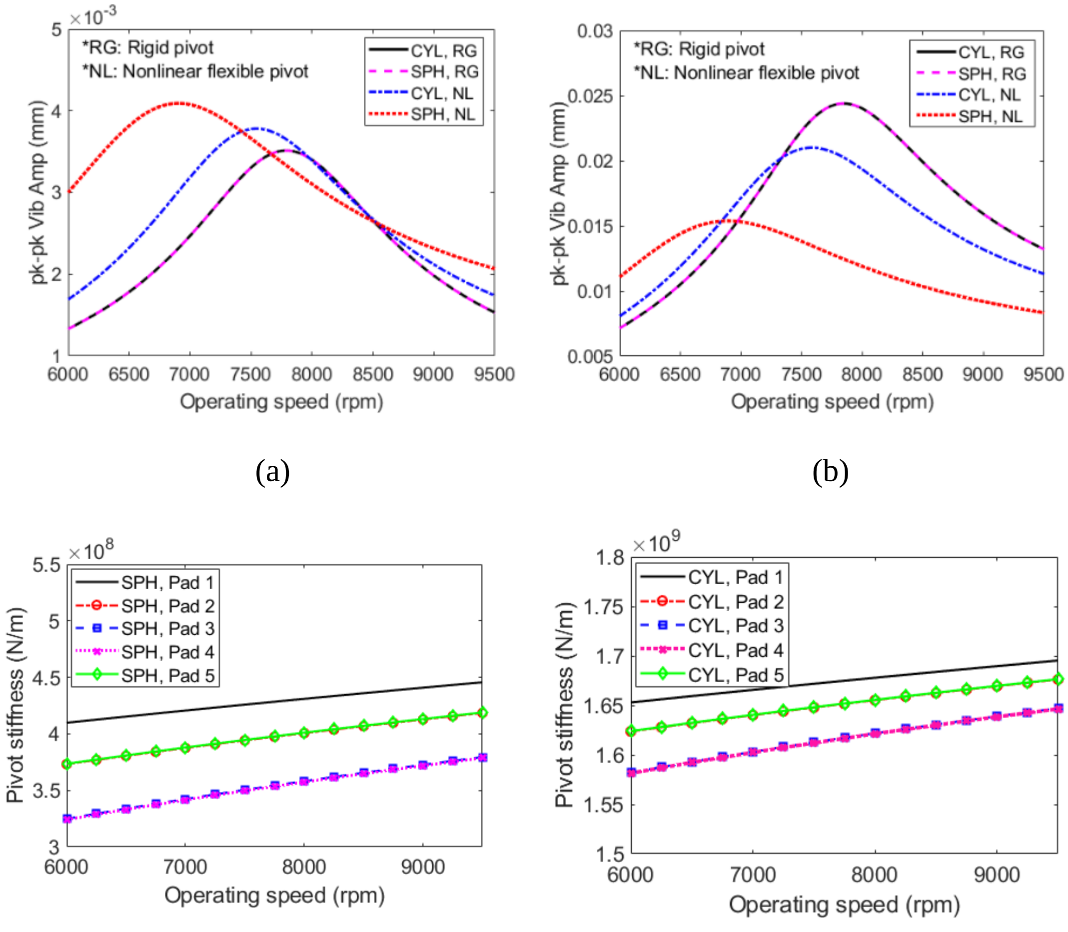

(a) (b)

(c) (d)

Figure 5.5 Linear unbalance responses and pivot stiffness of cylindrical and spherical pivots

Prior to nonlinear ME simulations, linear unbalance responses and pivot stiffness are predicted based on convectional Rotor dynamic analysis using the linearized bearing stiffness and damping coefficients at equilibrium positions. In Figure 5.5, the simulations are conducted from 6,000rpm to 9,500rpm, and the journal equilibrium states are calculated at each speed. The linear unbalance responses at the journal (node

12) and overhung location (node 18) are presented in Figure 5.5 (a) and (b), and the pivot stiffness of five pads predicted at the journal's equilibrium states are shown in Figure 5.5 (c) and (d). Linear unbalance indicates that both pivot cases show almost identical responses when the NL is not considered. With decreasing pivot stiffness of the SPH with nonlinear pivot, the unbalance response at the journal location in Figure 5.5 (a) has increased compared with the rigid pivot, while the vibration amplitude at the overhung location in Figure 5.5 (b) has significantly decreased compared to other cases. When the flexible pivot is considered, the critical speed of both pivots has shifted to a lower speed range. The level of shift is more evident for the SPH case than the CYL. This may be explained by the predicted pivot stiffness in Figure 5.5 (c) and (d). The pivot stiffness of spherical pivots (Figure 5.5 (c)) shows relatively low values ranging from $3.25\times10^{8}\ N/m$ N/m to $4.5\times10^{8}\ N/m$ across the speed range while the CYL (Figure 5.5 (d)) indicates higher pivot stiffness up to $1.7\times10^{9}\ N/m$. This result is consistent with the results in [75] where the rigid pivot assumption significantly overpredicts the bearing's direct stiffness values and critical speed. Also, note that the large discrepancy between stiffness values of two pivots is similar to the predicted results in [76].

5.3.2. Effect of pivot geometry

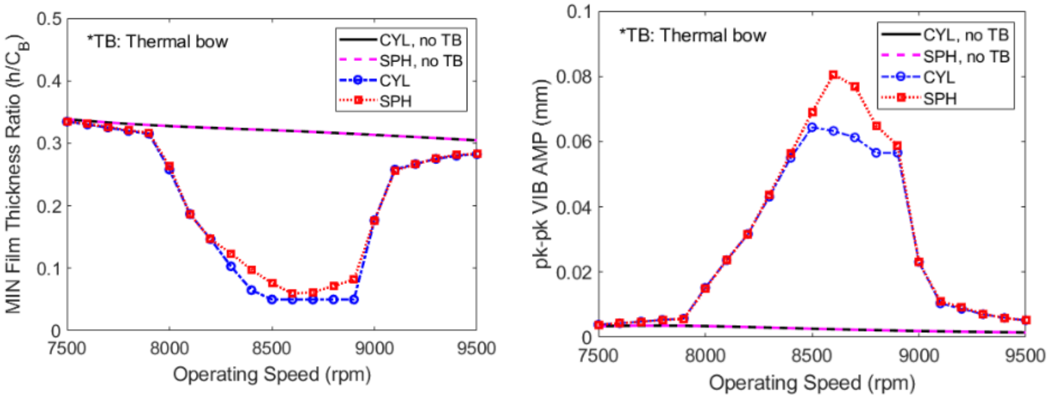

(a) (b)

Figure 5.6 Steady-state ME simulations with rigid pivot from 7,500 rpm to 9,500 rpm (a) Minimum film thickness ratio (b) pk-pk vibration amplitude at rotor end (node 19)

In Figure 5.6, both CYL and SPH types are employed to examine the pivot geometry influence on the ME based on nonlinear steady-state simulations with the assumption of rigid pivots. Note that “no thermal bow (TB)” cases are included in the figure to show that the induced large vibration level is solely caused by the ME, and this has been performed by setting the induced thermal bow amplitudes to be zero during the simulation. In the figure, two “with TB” cases display much thinner minimum film thickness ratios in Figure 5.6 (a) and high vibration level at the rotor end (node 19) in Figure 5.6 (b) from 8,000 rpm to 9,100 rpm compared with the no TB cases, confirming that the induced thermal bow and resultant large vibration are due to the ME. In the speed range where vibration levels are relatively small (7500~7,900 rpm and 9,200~9500 rpm), both pivot types with the TB show marginal differences in the film thickness ratio and vibration level. The difference becomes more evident when severe ME vibration appears from 8,300 to 8,900 rpm. The CYL shows a film thickness ratio of

0.05 and thus rubbing from 8,500 to 8,900 rpm, which is not apparent in the SPH at the same operating speeds. Note that the rubbing between pads and shaft is defined by the minimum film thickness ratio being below 0.05. This assumption is employed to avoid the excessive computation time and consideration of mixed lubrication theory when the minimum film thickness becomes very small. Note that the high vibration level without rubbing has been seen to occur with the SPH while the CYL encounters rubbing from 8,500 to 8,900 rpm.

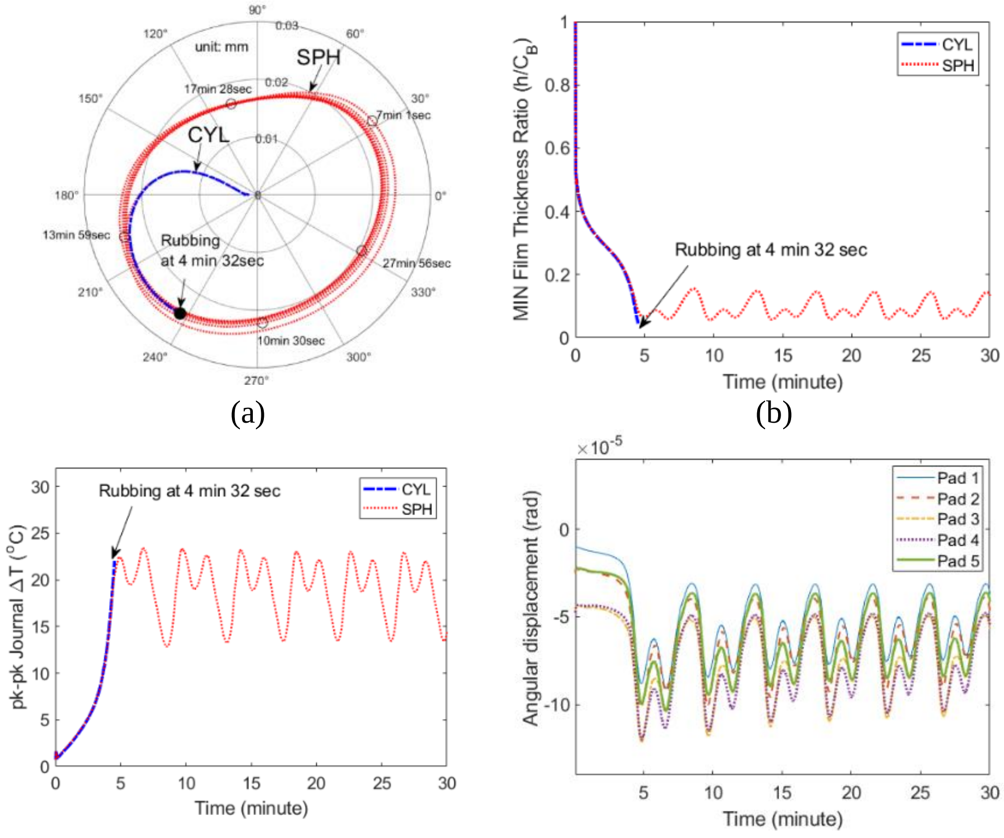

(a) (b)

(c) (d)

Figure 5.7 Transient ME simulation at 8,600rpm (a) 1X polar plot at journal location (b) minimum film thickness ratio of TPJB (c) pad pitching angular displacement (d) pk-pk Journal ΔT

Transient simulation results at 8,600 rpm corresponding to Figure 5.6 are presented in Figure 5.7. In Figure 5.7 (a), for both pivots, spiral vibrations are seen to occur in the 1X polar plot with varying phase angle and amplitude at journal location, and this “spiral vibration” is known to be the main characteristic of the ME. Note that the phase angle is an angle with respect to the initial mechanical imbalance. The phase angle of the SPH keeps changing from 0° to 360° during 30 minutes in Figure 5.7 (a) while the CYL encounters rubbing at 4 minutes 32 seconds, which is confirmed by the minimum film thickness ratio less than 0.05 in Figure 5.7 (b). Journal ΔT defined by the subtraction between the maximum and minimum temperatures across journal circumference is shown in Figure 5.7 (c). High ΔT oscillating between $13^{\circ}C$ and $23^{\circ}C$ confirms that the violent vibration in Figure 5.7 (a) is attributed to the journal asymmetric heating and its resultant thermal bow excitation.

Note that, though two pivot types have the same bearing stiffness and damping values and unbalance responses in Figure 5.5, the rubbing phenomenon is only observed with the CYL. This is because the pad pitching motion of the SPH provides a better cooling effect to the bearing compared with the CYL. The occurrence of the thermal bow would produce an asymmetric film distribution in the axial direction, and the film near the NDE side will be smaller than the DE side film due to the presence of thermal bow at the NDE. The SPH’s pitching motions in Figure 5.7 (d) are assumed to compensate this asymmetric film distribution, and thus resulting in the rotor being free-from the rubbing. In the figure, negative angular displacements are induced for all five pads due to the asymmetric pressure loading applied on the pads, which in turn produces symmetric film thickness in the axial direction. The fluctuations of pitching displacements follow the trend of the vibration, film thickness and journal ΔT trajectories as represented in Figure 5.7 (a), (b), and (c). Note that the times where peak angular displacements occur coincides with the time where high journal ΔT is observed in Figure 5.7 (c), which demonstrates the compensation effect of the pitching motion is more dominant when the larger thermal bow and its excitation is induced in the rotor.

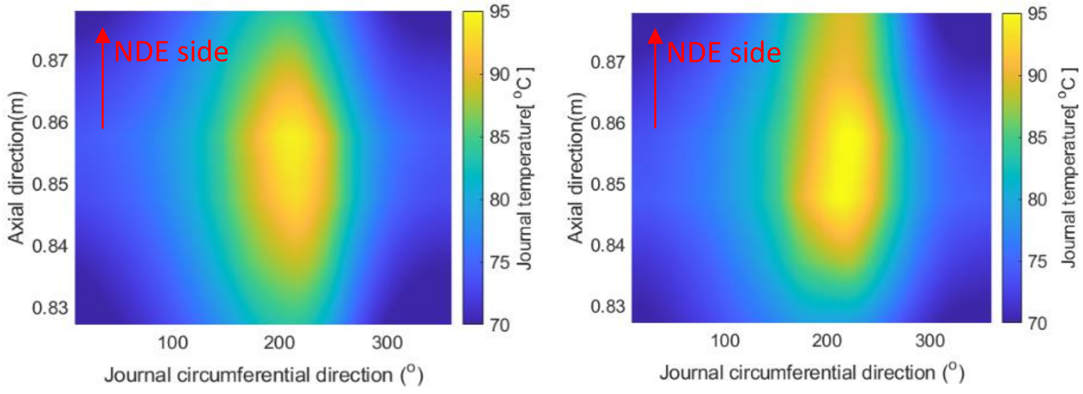

(a) (b)

Figure 5.8 Journal temperature at 8,600 rpm (4 minute 32 seconds) (a) spherical pivot (b) cylindrical pivot

Journal temperature distributions of both pivots at 4 minutes and 32 seconds are compared in Figure 5.8. Note that the y axis in the figure corresponds to the axial location of the journal in the shaft (from 0.8276 m to 0.8776 m). The temperature of the SPH in Figure 5.8 (a) shows symmetrical temperature distribution along the axial direction due to its pitching motion, while the asymmetry distribution appears for the

CYL in Figure 5.8 (b) as the temperature of the NDE side is higher than the DE side temperature. The asymmetric heating in Figure 5.8 (b) is caused by the induced thermal bow effect which decreases the film thickness at the NDE side than the DE one, and this renders the CYL to be more prone to the rubbing than the SPH.

5.3.3. Effect of pivot stiffness

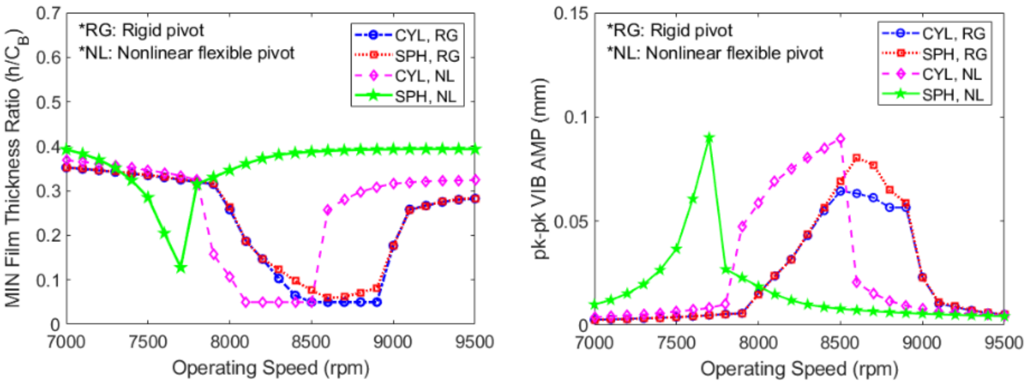

(a) (b)

Figure 5.9 Steady-state ME simulations with rigid and flexible pivots from 7,000 rpm to 9,500 rpm (a) Minimum film thickness ratio (b) pk-pk vibration amplitude at journal

The influences of pivot stiffness on the ME are investigated, and the results are presented in Figure 5.9. Simulations are carried out for both rigid and flexible pivots from 7,000 rpm to 9,500 rpm. Similar to the linear unbalance results in Figure 5.5, the nonlinear pivot of the CYL shifts the ME instability speed range to a lower speed range in Figure 5.9. For the CYL-rigid pivot case, high vibration starts to appear from 8,000 rpm and lasts until 9,100 rpm while for the CYL-flexible pivot case, severe vibration is present from 7,800 rpm to 8,600 rpm. Note that the unstable speed range due to the ME has been reduced with the nonlinear pivot stiffness, i.e., instability speed rage of 1,100 rpm for rigid pivot and 800 rpm for the nonlinear pivot. It is also noteworthy that rubbing occurs for both rigid and flexible pivots of the CYL at its maximum vibration speed (8,600rpm for both cases in Figure 5.9 (b)). The amplitude of vibration where rubbing occurs is higher with the nonlinear pivot, indicating the increased pivot deformation due to the pivot flexibility.

Investigation of the SPH cases suggests that the shift of the ME speed range due to the pivot flexibility is more apparent in the SPH than the CYL. The SPH-nonlinear pivot exhibits a high vibration level around 7,700 rpm, which is about 1,000 rpm lower than that of the SPH-rigid case. This observation is consistent with the critical speed changes presented in the linear unbalance response in Figure 5.5, where the critical speed shift is more significant with the SPH compared with the CYL due to its lower pivot stiffness. The ME is not a strict resonance problem as demonstrated by 1) many reported ME cases occurred far away from the rotor’s critical speed, and 2) ME vibration level at the speed closer to the critical speed is not necessarily more severe than the speed farther from the critical speed. For example, in Figure 5.6 (b), the vibration level at 8,600 rpm is higher than that of the 7,700 rpm, which is very close to the critical speed (7,820 rpm) of the example rotor in the CYL-rigid pivot case. However, the investigation of the pivot stiffness effect in this section also implies that when the ME occurs near rotor’s critical speed, the ME instability speed range is largely affected by the critical speed changes of the rotor, confirmed by the dependency of the ME instability speed change with different pivot stiffness and resultant critical speed change.

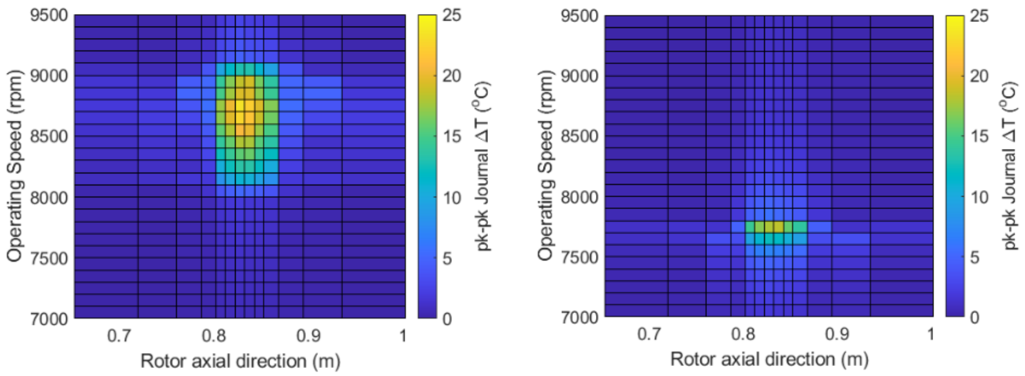

(a) (b)

Figure 5.10 Steady-state ME simulations of pk-pk journal ΔT from 7,000 rpm to 9,500 rpm (a) spherical type with rigid pivot (b) spherical type with flexible pivot

Journal temperature differential (ΔT) with different speeds and rotor axial locations are presented in Figure 5.10. For comparison purpose, the SPH with rigid (Figure 5.10 (a)) and flexible (Figure 5.10 (b)) pivots are shown in the figure. High journal ΔT s are shown from 8,000rpm to 9,000 rpm for the rigid case, and 7,600rpm to 7,800rpm for the nonlinear pivot, and these ranges coincide with the high vibration range in Figure 5.9 (b). This coupled phenomena between the ΔT and vibration indicate that the thermal bow of the shaft induced by ΔT produces additional excitations in the system and causes large vibration. Also note that relatively small pk-pk journal ΔT (up to 18.2 ℃) is predicted for the nonlinear pivot compared with that of the rigid pivot (up to 23.5 ℃), indicating that rigid pivot assumption may over-predict the journal ΔT and vibration level in ME analysis.

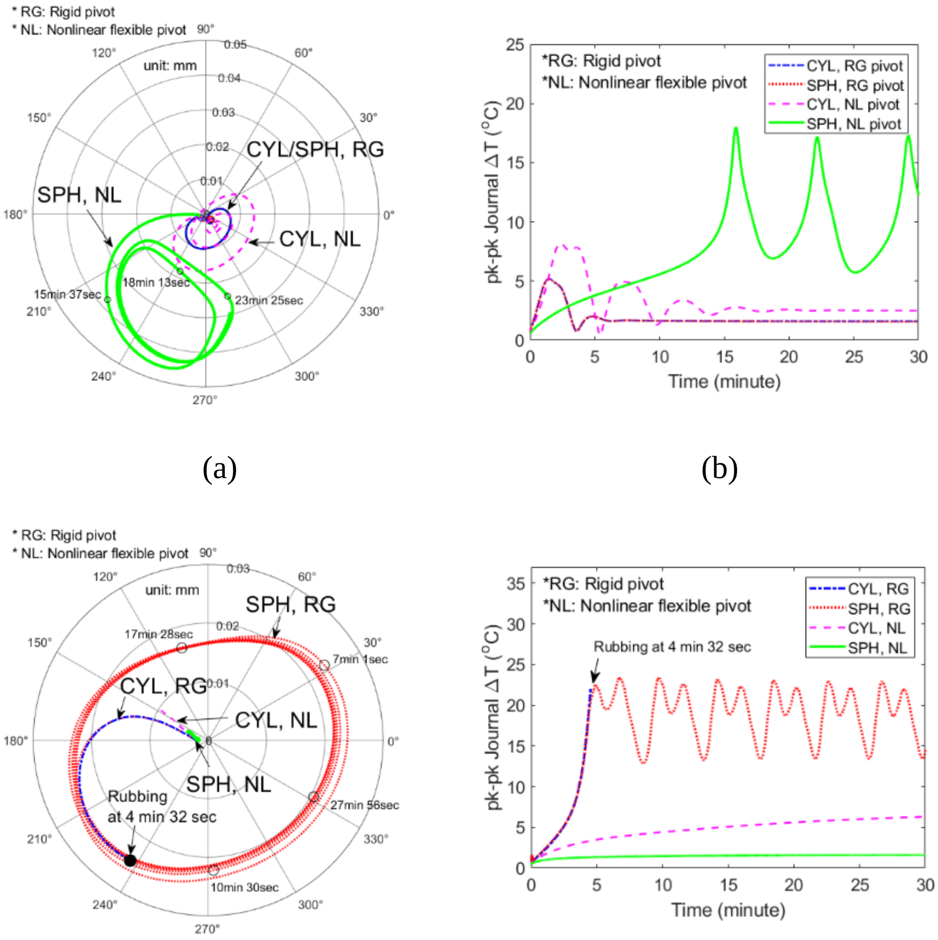

(a)

(b)

(c)

(d)

Figure 5.11 Transient ME simulation at 7,700 rpm and 8,600 rpm (a) 1X polar plot at 7,700 rpm (b) k-pk Journal ΔT at 7,700 rpm (c) 1X polar plot at 8,600 rpm (d) pk-pk Journal ΔT at 8,600 rpm

Transient simulations are conducted for different pivot cases in Figure 5.11. At 7,700 rpm, the most severe vibration level appears with the SPH-nonlinear pivot case with non-converging spiral vibration in Figure 5.11 (a). In Figure 5.11 (b), the high journal ΔT is also seen to occur with fluctuating amplitudes for the same case. The CYL and SPH cases with rigid pivot show relatively small vibration and ΔT at 7,700 rpm compared with the flexible cases. Meanwhile, at 8,600rpm, the rigid pivot cases exhibit more violent vibration and higher ΔT as shown in Figure 5.11 (c) and (d). These results are consistent with the steady-state results in Figure 5.9 and confirms that the shift of the ME instability speed range with different pivot types.

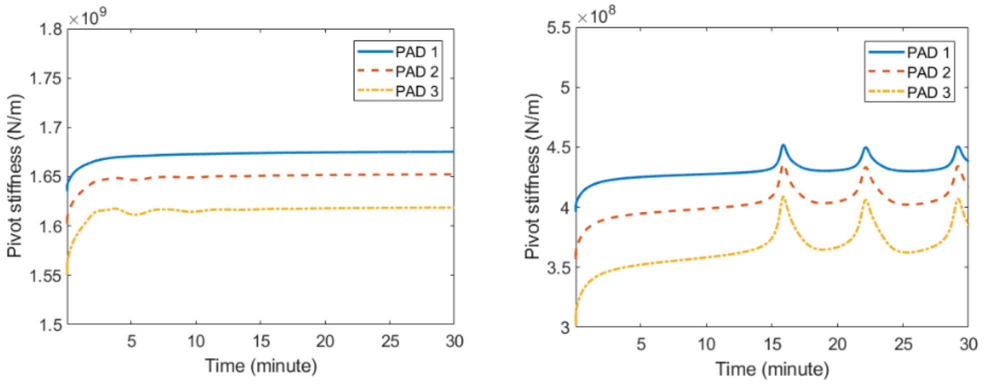

(a) (b)

Figure 5.12 Pivot stiffness at 7,700 rpm with time (a) cylindrical pivot (b) spherical pivot

Pivot stiffness variation of both pivot types corresponding to 7,700 rpm in Figure 5.11 (a) and (b) are illustrated in Figure 5.12. Only three pads are presented as pad 4 and 5 represents the similar responses with the Pad 2 and 3, respectively. During the simulation, the stiffness values of the SPH range from $1.55\times10^{9}\ N/m$ to $1.67\times10^{9}\ N/m$, which is much larger than the SPH case ranging from $3\times10^{8}\ N/m$ to $4.5\times10^{8}\ N/m$ in Figure 5.12 (b). The average stiffnesses of both pivots are similar to the linear analysis in Figure 5.5. Note that the pivot stiffness varies in accordance with the vibration and ΔT changes in Figure 5.11 (a) and (b). As the high vibration occurs after 15 minutes in the

SPH-nonlinear case in Figure 5.11 (b), larger dynamic loads are applied on pads, and the pad-pivot tends to be stiffened due to its nonlinear characteristics in Figure 5.12.

Spherical shape with rigid pivot	Spherical shape with flexible pivot

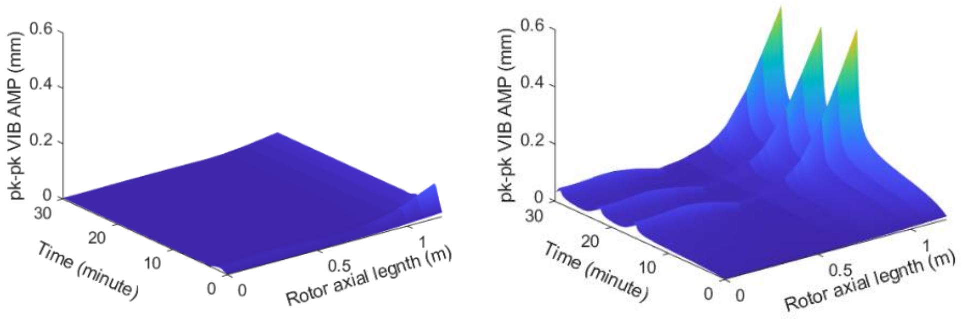

(a)

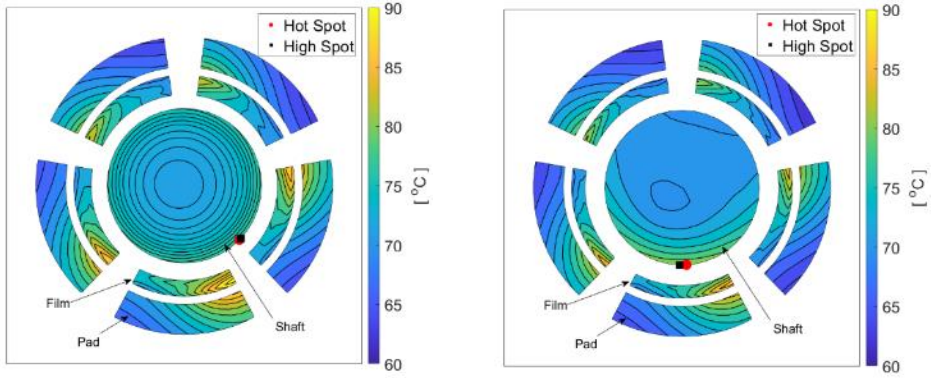

(b)

Figure 5.13 Transient ME simulation at 7,700 rpm (a) pk-pk vibration amplitude across rotor axial direction for 30 minute (b) temperature distribution of bearing mid-plane at 30 min

Figure 5.13 shows transient simulation results of the SPH with both rigid and flexible pivots at 7,700rpm. In Figure 5.13 (a), for the SPH-rigid pivot, the vibration level is relatively small for all rotor axial locations and converges after 5 min. Meanwhile, the SPH-nonlinear pivot displays non-converging vibration after 10 minutes, and especially severe vibration at the rotor axial location over 0.8 m. The amplified vibration level at the NDE overhung compared to other axial locations of the rotor implies that the vibration is induced by the thermal bow at the NDE side. Bearing mid-plane temperature distributions for both cases are shown in Figure 5.13 (b). The shaft of the SPH-rigid pivot shows relatively concentric distribution of temperatures in Figure 5.13 (a) while the SPH-flexible pivot resents the asymmetric temperature distribution in Figure 5.13 (b), which generates the thermal bow in the shaft.

5.3.4. Effect of pivot friction

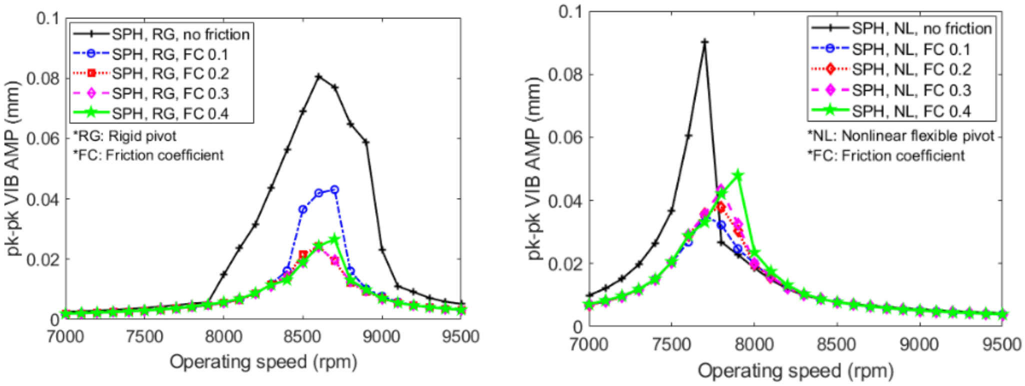

(a) (b)

Figure 5.14 Steady-state ME simulations of pk-pk vibration amplitude at journal with different pivot friction coefficients (a) spherical type with rigid pivot (b) spherical type with flexible pivot

Although there have been many experimental results [44,84-87] that the presence of pad-pivot friction affects the static and dynamic performances of the spherical pivot type TPJBs, the friction effect is often neglected in the transient simulation of the TPJBs for simplicity. To examine the friction effect on the ME, parametric studies are performed with varying friction coefficients (FC) utilizing the rotor model in Figure 5.4.

Since the pivot friction is present only in the spherical pivot type, simulation results employing only the spherical pivot will be presented in the following. Coulomb friction model will be used for simulations, and the friction coefficients of the Coulomb model vary between 0.1 and 0.4. Stribeck friction model used in [91] are also tested and compared with the results based on the Coulomb friction model, and the comparison showed negligible difference between two models. Therefore, only the Coulomb friction model will be used in the following analysis. Figure 5.14 illustrates nonlinear steady-state vibration responses of both rigid and flexible pivots considering the pivot friction. In the rigid pivot case shown in Figure 5.14 (a), the cases considering the friction effect significantly reduces the vibration amplitude and instability speed range of the ME. With FC 0.1, the rotor vibration amplitude at 8,600 rpm is suppressed to 0.04193 mm compared with 0.08052 mm for the no friction case. Further increase of friction coefficient until FC 0.3 reduces the vibration level to 0.0244 mm at the identical operating speed. The rotor vibration amplitude with FC 0.4 slightly increases at 8,700rpm compared with FC 0.2 and 0.3 while the other operating speeds show similar vibration levels regardless of the FCs. For the flexible pivot case in Figure 5.14 (b), the pivot friction also suppresses the rotor vibration in general, but its effect on the ME vibration is not as evident as the rigid pivot as shown in the figure. For the rigid pivot, vibration suppression due to the friction is apparent both above and below the operating speed where maximum vibration level appears (8,600 rpm with no friction). However, for the flexible pivot, the friction effect suppresses the rotor vibration only below the maximum vibration speed (7,700 rpm with no friction) and even increase the vibration level above that speed. With FC 0.1, the vibration level is most significantly mitigated compared with other friction coefficients (0.2~0.4). Above the maximum vibration speed (7,700 rpm with no friction), the vibration level starts to regrow with increasing friction coefficients (from 0.1 to 0.4). The maximum vibration speed also increases with increasing friction coefficients, i.e., from 7,800 rpm (for FC 0.2 and 0.3) to 7,900rpm (for FC 0.4). This result indicates that the rigid pivot assumption may overpredict the pivot friction's vibration suppression effect on the ME vibration. Also, the optimal friction coefficients exist for the pad-pivot friction which best suppresses the rotor vibration, as demonstrated in the nonlinear pivot case in Figure 5.14 (b).

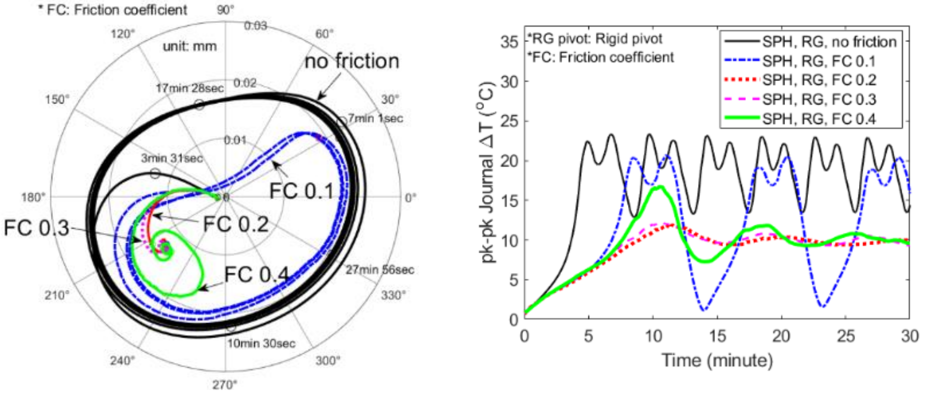

(a)

(b)

Figure 5.15 Transient ME simulation of rigid pivot at 8,600 rpm (a) 1X polar plot (b) pk-pk Journal ΔT

Transient ME analysis of the rigid pivot corresponding to Figure 5.14 (a) at 8,600 rpm is performed and its results are shown in Figure 5.15. With FC 0.1, the spiral shape and journal circumferential ΔT become smaller compared with the no friction but is still non-converging. Note that, in Figure 5.15 (b), the pivot friction has shortened the period of ΔT fluctuation of FC 0.1 compared with the no friction. With FC 0.2 and 0.3, the spiral shapes are further reduced, and they converge to equilibrium points in 1X polar plot, indicating that the stability of the rotor is enhanced with increasing pivot friction. The journal ΔT also shows much reduced amplitudes and converging responses with FC 0.2 and 0.3 as shown in Figure 5.15 (b). If the friction is further increased to 0.4, the trajectory of spiral and ΔT show higher fluctuations while it eventually converges to a similar vibration and ΔT levels with FC 0.2 and 0.3 at the end of the simulation. These results indicate that there exists an optimal level of pivot-friction which effectively suppresses the ME vibration.

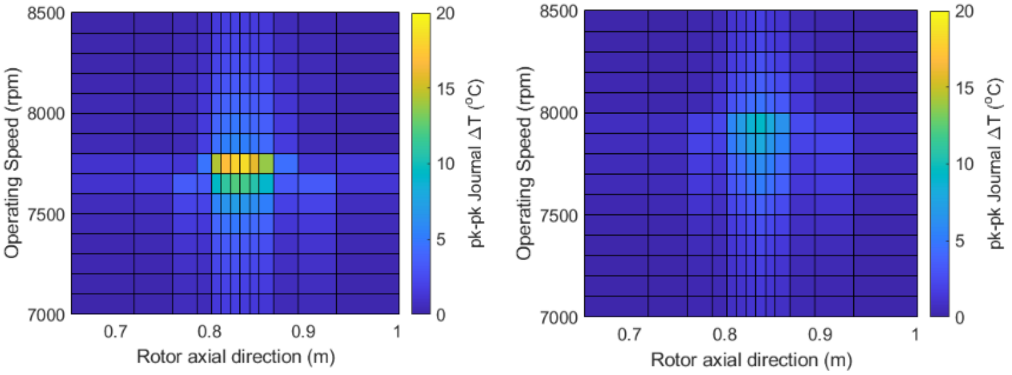

(a) (b)

Figure 5.16 Steady-state ME simulations of flexible pivot: pk-pk journal ΔT across rotor axial direction (a) no friction (b) friction coefficient 0.4

Journal differential heating of two cases, i.e., 1) no friction, 2) FC 0.4, is compared in Figure 5.16. Similar to the vibration reduction trend in Figure 5.14 (b), with the friction effect, the journal ΔT is also decreased, and high ΔT speed range has been shifted up as seen from Figure 5.16 (b). Without the friction, the high ΔT reaches up to 18.4℃ at journal location (axial coordinates from 0.8276 m to 0.8776 m) near 7,700 rpm while maximum ΔT of 9.37 ℃ appears at 7,900 rpm with FC 0.4. These similar trends in vibration and ΔT indicate that the ME vibration is induced by the journal asymmetric heating and its resultant thermal bow. The pivot friction reduces the asymmetric heating in journal circumference and thus reducing the ME vibration in this particular rotor case. This result also implies that the prediction without considering the pivot friction may overpredict the journal circumferential ΔT, which is the most critical value in predicting the ME vibration.

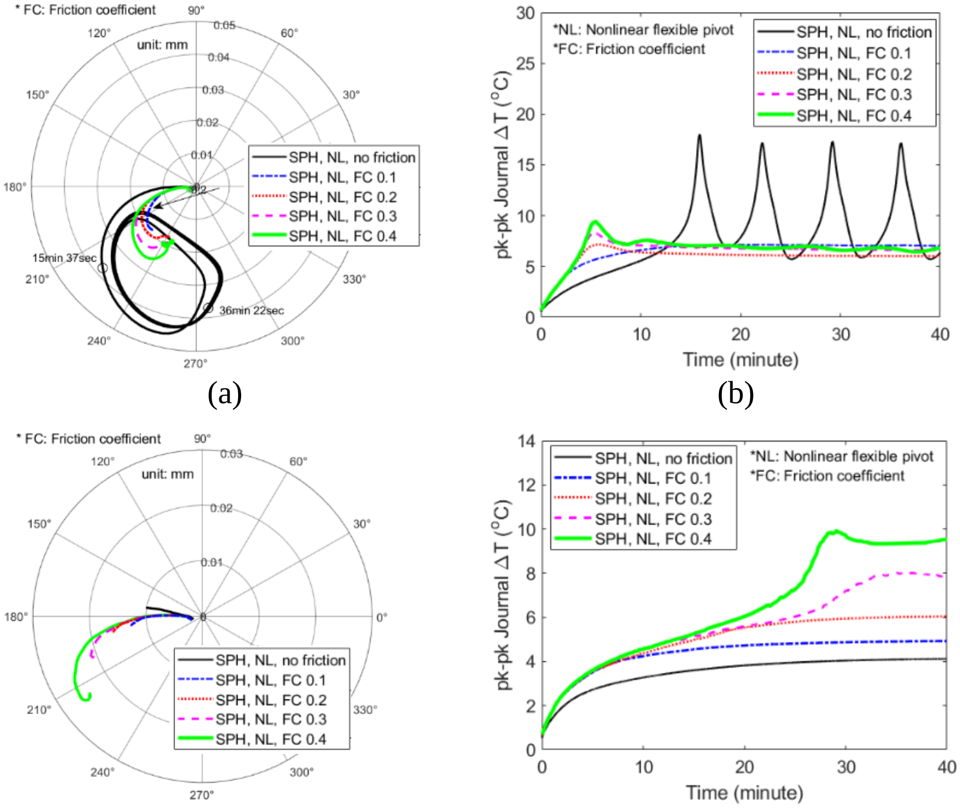

(a) (b)

(c) (d)

Figure 5.17 Transient ME simulation at 7,700 rpm and 7,900 rpm (a) 1X polar plot at 7,700 rpm (b) pk-pk Journal ΔT at 7,700 rpm (c) 1X polar plot at 7,900 rpm (d) pk-pk Journal ΔT at 7,900 rpm

Figure 5.17 shows the simulation results at 7,700 rpm and 7,900 rpm with the nonlinear pivot cases corresponding to Figure 5.14 (b). At 7,700 rpm, FC 0.1 case shows the smallest spiral vibration in Figure 5.14 (a) and ΔT converges in the shortest time period compared with other cases in Figure 5.17 (b). Increasing friction coefficients up to 0.4 amplify the spiral and more fluctuations in ΔT with time in Figure 5.17 (b).

Note that ΔT s are slightly reduced with FC 0.2 and 0.3 than FC 0.1, and it regrows with FC 0.4. At 7,900 rpm, the no friction case shows the most stable spiral and ΔT trajectories with time. Then they start to grow with increasing friction coefficients, and these results are consistent with Figure 5.14 (b). With FC 0.3 and 0.4, the ΔT reaches up to 9.5 $℃$ and 7.8 $℃$ after 40 minutes, and they are still non-converging. These transient simulation results confirm that the reduction of ME below the maximum vibration speed and the increase of ME above that speed as demonstrated in Figure 5.14 (b).

Figure 5.18 illustrates the transient simulation results at 7,900 rpm, corresponding to the results in Figure 5.17 (c) and (d). Note that, at this operating speed, it has been found that the pivot friction-induced more ME vibration with increasing coefficients. The 3D orbits of the rotor after 40 minutes in Figure 5.18 (a) confirm that the rotor orbits are enlarged with increasing pad-pivot friction especially at the NDE overhung side (> 0.8776m) due to the increased thermal bow as shown in Figure 5.18 (b). Note that the thermal bow amplitude ($\sqrt{x_{bow}^2 + y_{bow}^2}$) in Figure 5.18 (b) is calculated at each node location of the rotor. Without the friction, the bow amplitude at the NDE side (node 19) is 0.01135 mm while the counterpart of FC 0.4 is about two times of that, i.e., 0.02254 mm.

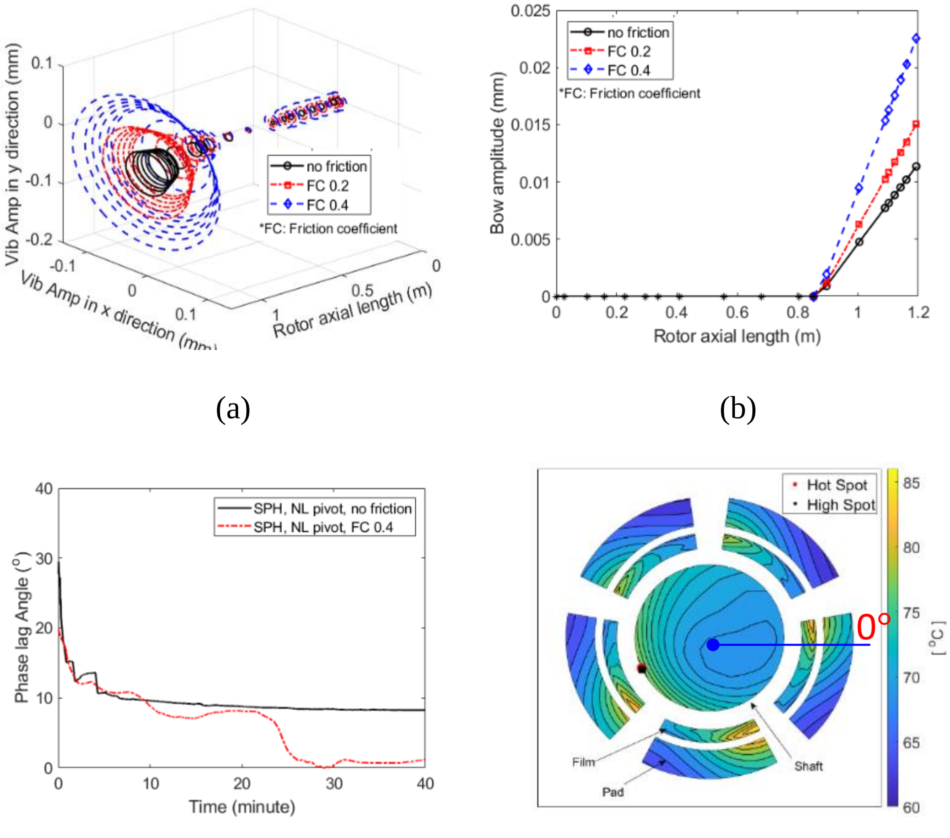

(a) (b)

(c) (d)

Figure 5.18 Transient simulation results at 7,900rpm after 40 minutes (a) 3D orbits of rotor (b) thermal bow amplitude with different friction coefficients (c) phase lag between hot and high spots (d) temperature distribution at bearing mid-plane of FC 0.4

Figure 5.18 (c) and (d) represent the phase lag between hot and high spots across the journal circumference and the bearing mid-plane temperature of FC 0.4 after 40 minutes. The no fiction case with relatively small vibration corresponding to Figure 5.17 (c) shows a stable phase lag angle response with time and converges to 8.282 ° at 40 minutes. Meanwhile, FC 0.4 case with larger vibration shows more fluctuations and reaches to relatively small phase lag of 1.255 ° at 40 minutes. The high and hot spots for the FC 0.4 case are shown in Figure 5.18 (d). Both spots are seen to be located around 190° being away from the 0° location (location of the initial mechanical imbalance) in the figure. Asymmetric temperature distribution with a high circumferential ΔT of 9.5 ° is seen to occur with the friction while relatively small ΔT of 4 ° is reported for the no friction case. These results confirm that at 7,900 rpm the pivot friction induces more asymmetric heating in the journal and causes amplified vibration level in the rotor.

6. MORTON EFFECT EXPERIMENTAL RIG BUILDING AND TESTING

6.1. Introduction

Many researchers have worked on the experimental works to verify the Morton effect and find their root causes. de Jongh and Morton employed a simple rotor design with a tilting pad journal bearing to reproduce the Morton instability [109]. Four RTD sensors were used and inserted into the journal circumferential surface to measure the temperature differential of the journal. It has been found that the journal temperature differential varies in a wide range from 3℃ to 10℃ depending on the operating speed. Also, they verified that the phase lag between hot and high spots varies with the rotor's spin speed. Kirk and Balbahadur [110] measured the vibration during the run-up/down testing. After the run-up of the rotor, the rotor speed was kept constant to observe any symptoms regarding the Morton effect. They found a hysteresis phenomenon where the vibration amplitude of the run-down is much higher than the one of the run-up testing. Panara, et al. [111] measured the journal temperature differential with 8 thermocouples and bearing pad temperature with additional sensors. The effect of the overhung mass on the Morton effect was tested by varying the overhung weight from 7.3 % of the total rotor weight to 12.4 %. From the testing, it has been found that the ME range was sensitive to the overhung mass, and the instability range was lowered with larger and heavier overhung masses. Tong and Palazzolo [48] conducted experimental works to measure the journal circumferential temperature with 20 RTD sensors. The rotor supported with two ball bearings and one tilting pad journal bearing were designed to have an offset of 0.003 inches from the bearing centerline, thus generating a prescribed journal orbit in the rotor. The rotor spin speed, static eccentricities, and oil supply temperature were varied in the testing, and it has been verified that the journal temperature differential is proportional to the rotor spin speeds.

6.2. Test rig building and analysis

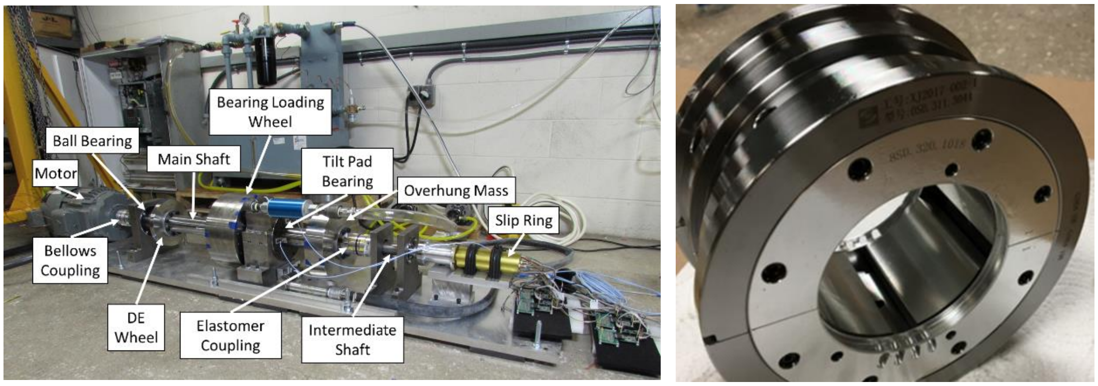

Figure 6.1 Morton effect test rig and Tilting pad journal bearing

Morton effect test rig has been built as shown in Figure 6.1. The total length and diameter of the shaft are 1.215m and 0.08m, respectively. The large mass near bearing housing weighs 90kg (bearing loading wheel in the figure), and it is installed to provide the bearing with sufficient load for operation. The overhung mass at the non-drive end (NDE) has a diameter of 0.3 m and a mass of 40 kg. A slip ring is connected at the end of the NDE. Total of 26 RTD sensors are embedded into the journal circumferential surface to measure the journal temperature differential. Ten vibration sensors are positioned across the rotor. Two sensors at the slip ring, two at overhung mass, four at bearing housing, and two at the mid-shaft between the bearing loading wheel and the motor are installed.

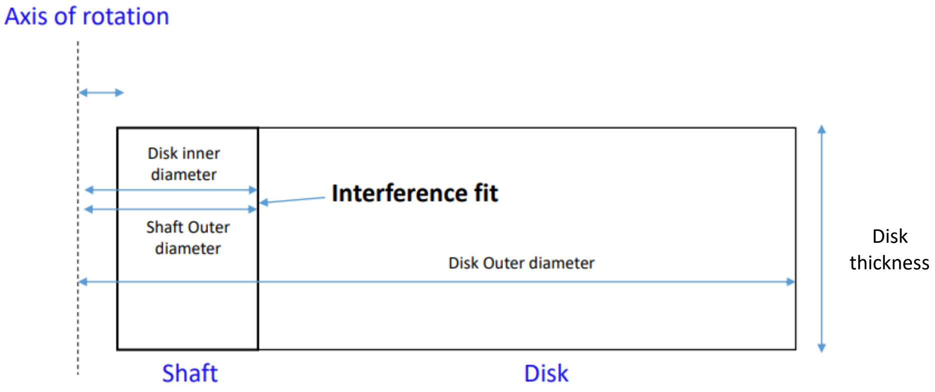

Figure 6.2 Schematic of an axisymmetric shaft-disk model

For safe operation of the test rig, the stress between the shaft and bearing loading wheel is analyzed using ANSYS APDL. If the contact stress at the interface between the shaft and wheel exceeds the yield strength of the shaft and disk materials at 0 rpm, it will lead to the failure of the test rig. Meanwhile, if the contact stress at the interface is below zero at high operating speeds, the separation between the shaft and disk will occur. Therefore, selecting the proper interference fit amplitudes satisfying both stress conditions at 0 rpm and high speeds is important in designing the rotor. The axisymmetric model of the shaft-wheel model is developed based on ANSYS APDL. The schematic of the contact model between the test rig shaft and wheel is shown in Figure 6.2. The operating speed of the rotor is applied to the axis of rotation in the figure. Different amplitudes of interference fit were applied at the contact surface between the shaft and wheel. Maximum Von Mises and hoop stress values at 0 rpm are calculated with different interference fit amplitudes in Table 6.1.

Interference fit		Max. Von Mises stress		Max. Hoop stress	
		Stress	Safety factor	Stress	Safety factor
Case 1	0.1178 mm	375 MPa	1.94-3.1	202 MPa	3.62-5.76
Case 2	0.254 mm	535 MPa	1.36-2.18	288 MPa	2.54-4.05
Case 3	0.3048 mm	642 MPa	1.14-1.81	346 MPa	2.11-3.37
Case 4	0.3556 mm	749 MPa	0.98-1.55	404 MPa	1.81-2.88

Table 6.1 Maximum stresses and safety factor at 0 rpm

The interference fit amplitudes were varied from 0.1178 mm to 0.3556 mm, and the corresponding maximum values of the Von Mises and Hoop stresses are calculated in the table. The safety factor is calculated based on the yield strength values of the 4340 steel. Depending on the heat treatment applied to the steel, the yield strength of the steel varies from 731 MPa to 1,165 MPa. With increasing interference fit values in Table 6.1, the stress at the contact interface increases accordingly, thus lowering the safety factors of the shaft-wheel contact. With the smallest interference fit of 0.1178 mm, higher safety factors are obtained, and the safety factors above 1.94 are ensured for both Von Mises and hoop stresses.

Interference fit		Max. Contact stress at the speed without disk separation
Case 1	0.1178 mm	19 MPa (at 7,500 rpm)
Case 2	0.254 mm	25 MPa (at 9,500 rpm)
Case 3	0.3048 mm	43 MPa (at 10,500 rpm)
Case 4	0.3556 mm	12 MPa (at 11,500 rpm)

Table 6.2 Maximum speed without disk separation

Next, the contact stress analysis at high operating speed is conducted to verify the existence of the contact between the shaft and the wheel during operation. Identical interference fit values in Table 6.1 were used for the analysis. The maximum speeds without separation are determined by gradually increasing the rotor speed until the contact stress at the interface between the shaft and disk becomes zero. The maximum speeds without the wheel separation are summarized along with its contact stress values in Table 6.2. At the interference fit of 0.1178 mm, the contact stress value of 19 MPa exists at the contact interface at 7,500 rpm. Based on the rotordynamic analysis, the first bending mode of the developed rotor-bearing system is predicted to be around 5,500 rpm. The Morton effect model also predicts the Morton effect vibration range around 5,500rpm. Therefore, the maximum speed of 7,500 rpm for 0.1178mm interference is sufficient for the safe operation without the wheel separation in our test rig case. As the interference fit increases, the maximum speed without the separation also increases. However, as shown in Table 6.1, with increasing interference, high-stress values occur at the contact interface and therefore deteriorate the safety factor of the design. The calculated stresses using ANSYS APDL at 6,000 rpm are shown in Figure 6.3

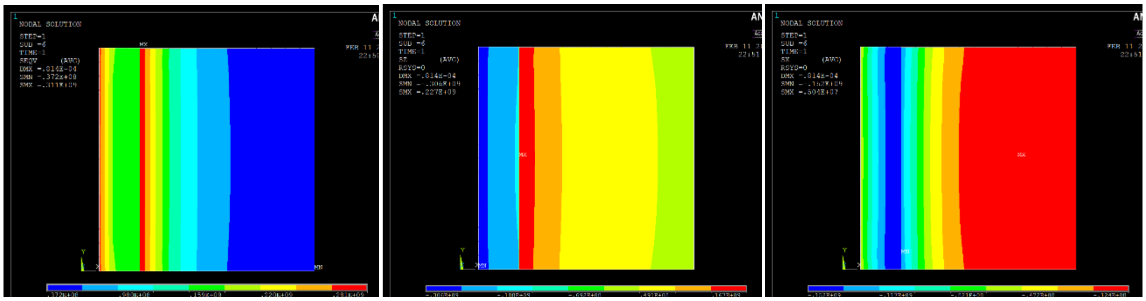

(a) **(b)** **(c)**

Figure 6.3 Stress calculations at 6,000 rpm (a) Von Mises stress (b) hoop stress (c) radial stress

To measure the free-free mode, the shaft was connected with two straps and hung from a gantry as shown in Figure 6.4 (a). The measured natural frequencies are then compared with the calculated natural frequencies. The natural frequencies of the shaft are calculated based on both ANSYS APDL software and developed MATLAB codes.

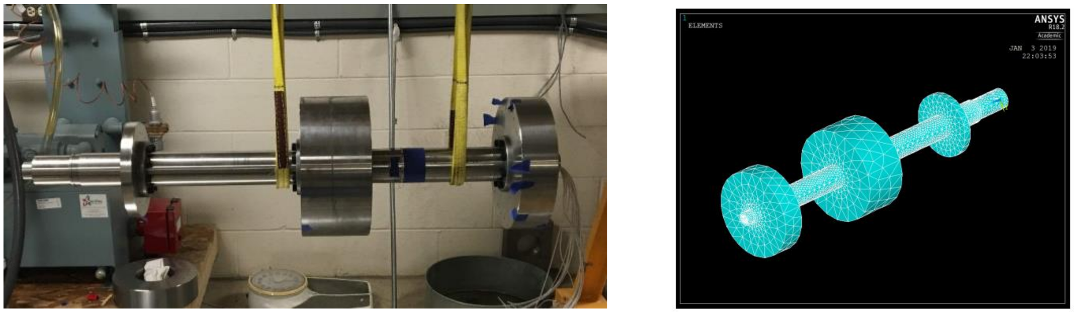

(a) (b)

Figure 6.4 (a) Photo of test rig shaft for free-free mode testing (b) shaft model based on ANSYS APDL

For the ANSYS analysis, three dimensional tetrahedron solid elements were used for the natural frequency calculation. Euler beam model is also developed based on MATLAB software. The comparison between the measured and simulated results are listed in Table 6.3.

	Measured natural frequencies	Calculated with ANSYS APDL	Calculated with Euler beam model
1st mode	8,760 rpm	9,300 rpm	10,080 rpm
2nd mode	23,340 rpm	23,892 rpm	24,900 rpm

Table 6.3 Comparison of calculated free-free modes

As shown in the table, calculated results based on ANSYS APDL and Euler beam model show close agreement with the measured natural frequencies of the shaft. The results from the ANSYS APDL indicates closer agreement with the measured data than the Euler beam model since it employs the high-fidelity three-dimensional FEM method. The first, second and third modes shape of the shaft are drawn with both ANSYS APDL and the Euler beam model, and the results are shown in Figure 6.5. Modes shapes based on both methods show similar shapes as shown in the figure.

	1st Mode	**2nd Mode**	**3rd Mode**
Euler beam	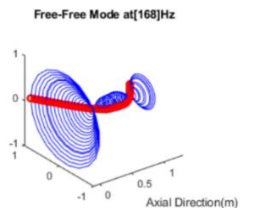	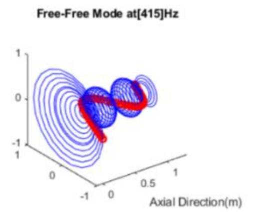	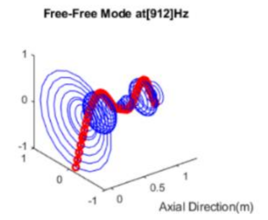
ANSYS	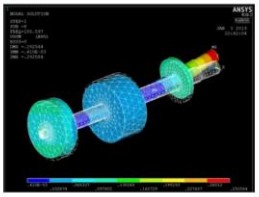	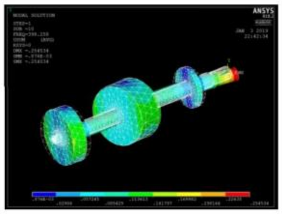	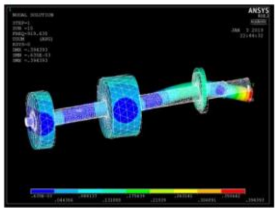

Figure 6.5 Comparison of first three mode shapes between Euler beam and ANSYS APDL

The balancing process was conducted before the Morton effect testing. The vibration amplitude and phase are recorded at 1,800 rpm at the initial test. Then the trial weight was attached at the wheel, and the vibration amplitude and phase were recorded again. Based on the measured vibration data from the two tests, the correction weight of 2.31 ounces at the phase of -7° has been obtained and applied to the wheel. The second balancing process was completed with the new measured vibration data. As a new trial weight, the calculated correction weight from the previous balancing was used. The correction weight of 3.118 ounces was calculated at the second balancing, and it has been attached at the phase of -28.21°. Similar balancing process was also done at the higher operating speed of 3,000 rpm. Multi-plane balancing was then applied at 2,700 rpm to further enhance the vibration levels of the rig. The vibration amplitude and phase of the rotor after the balancing processes are summarized in table 6.4.

Operating speed	Vibration at bearing in x direction		Vibration at bearing in y direction	
	pk-pk amplitude	Phase	pk-pk amplitude	Phase
1,200 rpm	0.001778 mm	-166°	0.00127 mm	-134°
2,400 rpm	0.001524 mm	-72°	0.004572 mm	-120°
2,700 rpm	0.001778 mm	-172°	0.004064 mm	-89°
3,000 rpm	0.00254 mm	-175°	0.004064 mm	-89°

Table 6.4 Vibration amplitude and phase of test rig after balancing

Next, the lift-off of the test rig has been checked. The position of the journal is measured with the proximity sensors. As the rotor spin speed increases, the rotor's vertical position is expected to rise. To test the lift-off, the rotor speed was increased from 240 rpm to 3,600 rpm, and the flow rate of the supply oil was maintained at 2 GPM. At the initial check, the rotor's vertical position increases until 1,800 rpm, but the increase was negligible after the speed as shown in Figure 6.2. The root cause of this phenomenon was identified as the journal misalignment, and it has been corrected in the following test.

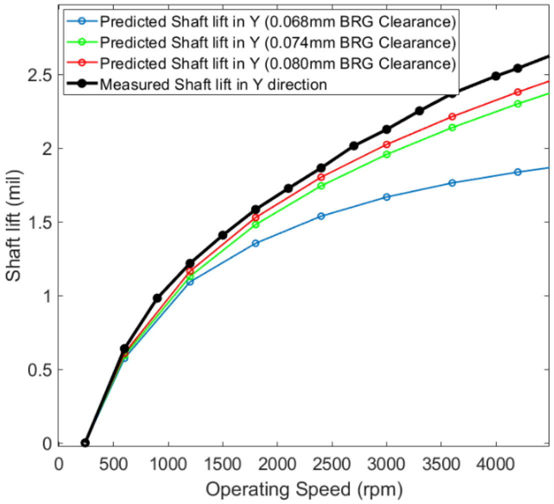

Figure 6.6 Measured shaft position from 240 rpm to 3,600 rpm

Figure 6.6 shows the lift of test after aligning the shaft. To accurately measure the shaft lift amplitude, the thermal expansion of housing is considered. The measured shaft lift-off amplitudes were compared with the simulation results using Morton effect prediction models in the previous sections. The nominal bearing clearance was 0.08 mm, and the measured bearing clearance was measured as 0.068 mm. Therefore, three different values of the bearing clearance including the nominal, measured and average values (0.074 mm) were tested, and its results are presented in Figure 6.6. The results show that the measured shaft lift amplitudes are closely related with the case with nominal bearing clearance of 0.080 mm.

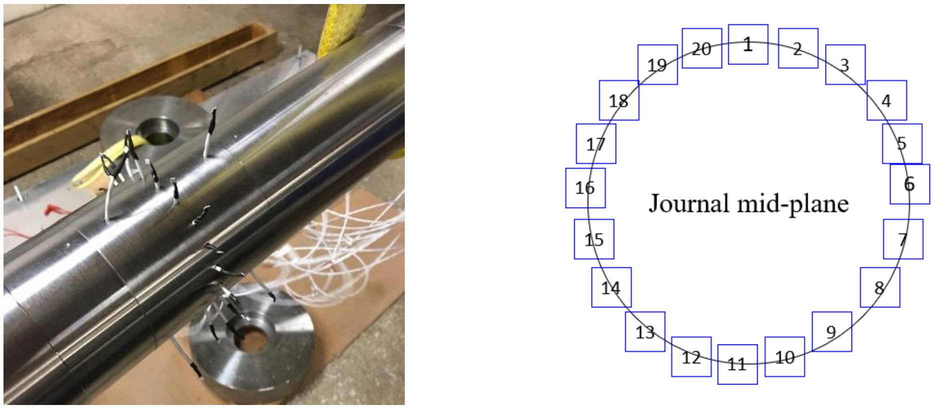

(a) (b)

Figure 6.7 (a) Installation of RTD sensors on the shaft and (b) RTD numbering at journal mid-plane

26 RTD sensors are inserted in the journal of the shaft in Figure 6.7 (a) to measure the temperature variation of the journal circumference when the ME occurs. The RTD holes are covered with epoxy to prevent the damage to sensors from oil. The lubrication system is also installed to control the flow rate and temperature of the supply oil to the journal bearing. A freezer is located between the lubrication system and oil hose to the bearing so that the oil can be cooled with the ice in the freezer. A slip ring is used to measure the signal from the 26 RTD sensors, and it is located at the non-drive end side of the rotor. The configuration and numbering of the 20 RTDs located at the journal mid-plane is shown in Figure 6.7 (b).

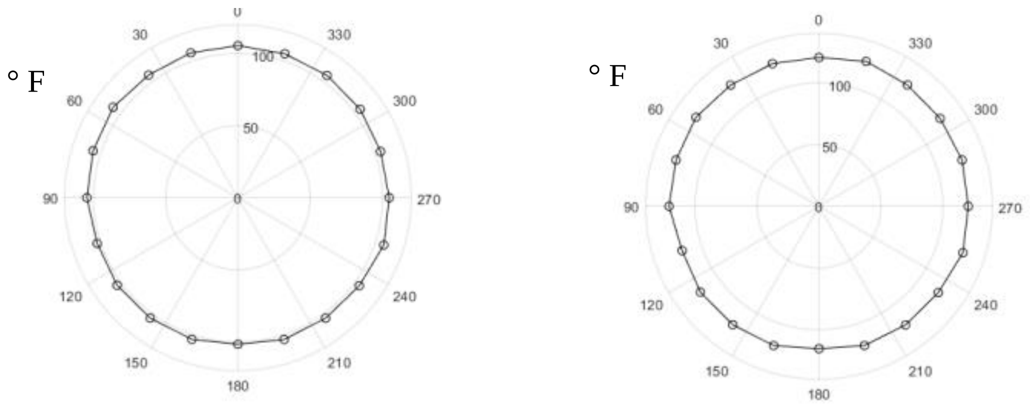

(a) (b)

Figure 6.8 Measured journal temperatures at (a) 3,000 rpm and (b) 4,200 rpm operating speed

Temperature data measured with RTD sensors are shown in Figure 6.8. The circumference of the journal is measured with 20 RTD sensors, and its values are drawn in the polar plot. The journal circumferential temperatures were measured at both 3,000 rpm and 4,200 rpm. At each operating speed, journal temperature differential about 1.2°C and 2°C were measured, respectively.

6.3. Vibration measurement

Five pad tilting pad journal bearing with load on pad configuration supports the rotor NDE side, and ball bearing is installed at the drive-end (DE) side. The oil system in the figure circulate the oil flow in the journal bearing. The temperature of the supply oil to the bearing is maintained at the room temperature (about 25°C) by cooling the circulating oil with the ice and water in the refrigerator. The measured bearing clearance of the tilting pad journal bearing is about 0.074 mm. The parameters for rotor and bearings are shown in Table 6.5.

Lubricant parameters		**Bearing parameters**	
Viscosity at 50 °C [$Ns/m2$]	0.0203	Pad type	Load on pad
Viscosity coefficients [$1/°C$]	0.031	No. pads	5
Supply temperature [$°C$]	50	Radius of shaft [m]	0.04
Inlet pressure [Pa]	$1.32{\times}10^{5}$	Bearing clearance (C_b) [m]	$7.4{\times}10^{-5}$
Reference temperature [$°C$]	50	Preload	0.25
Rotor Parameters		Bearing length [m]	0.06
Heat capacity [J/kg $°C$]	453.6	Thermal expansion coefficient [$1/°C$]	$1.22{\times}10^{-5}$
Heat conductivity [W/mK]	50	Reference Temperature [$°C$]	30
Thermal expansion coefficient [$1/°C$]	$1.22{\times}10^{-5}$	Pad pivot stiffness [N/m]	4e8
Reference temperature [$°C$]	25	Pivot offset	0.5
Rotor length [m]	1.215	**Linear Bearing**	
Rotor inner diameter [m]	0.0254	Kxx, Kyy [N/m]	$1.7{\times}10^{8}$
Rotor outer diameter [m]	0.08	Cxx, Cyy [Ns/m]	$1.0{\times}10^{5}$
Mass of wheel near bearing [kg]	90	**Thermal boundary conditions**	
Mass of overhung wheel [kg]	40	Temperature on shaft surface [$°C$]	30
Initial(mechanical) imbalance [$kg.m$]	6.5e-5	Temperature on bearing surface [$°C$]	30
		Convection coefficient [W/m^2K]	50
		Thermal rotor length [m]	0.18

Table 6.5 Parameters of Morton effect test rig

Rotor run-up/down tests has been conducted, and the speed of the rotor has been increased from 240 rpm to 4,800 rpm for the first test and to 5,640 rpm for the second test. Note that the slip ring is not installed at the NDE side for these run-up/down tests. In the first test, the rotor speed has been increased to the highest speed of 4,800 rpm for about 228 seconds and stayed at the speed for about 305 seconds. Then, the rotor was decelerated to the 240 rpm for 83 seconds. The vibration and temperature with respect time and rotor speed plots for first run-up/down test are shown in Figure 6.9.

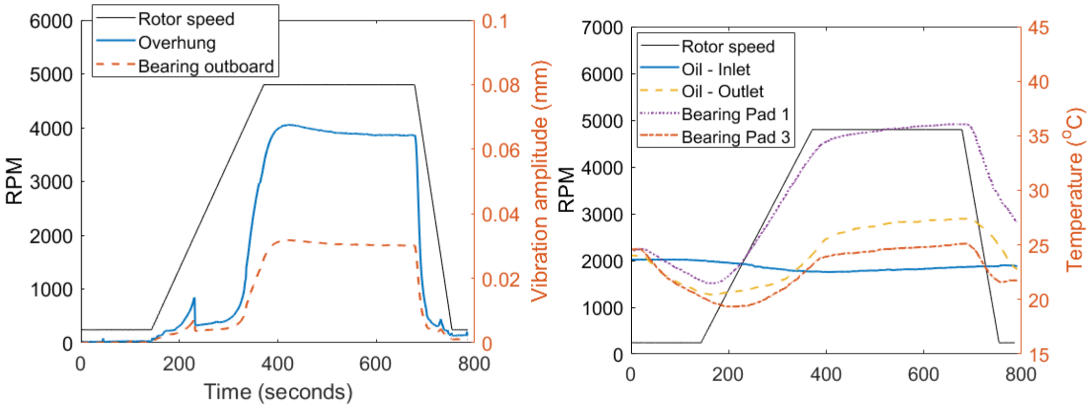

(a) (b)

Figure 6.9 (a) Rotor vibration amplitude and (b) temperatures of oil for the first test (4,800 rpm)

In Figure 6.9 (a), the vibration increases as the rotor speed reaches at 4,800 rpm at the rotor overhung end and bearing outboard locations. In the typical rotor run up/down testing, the vibration levels tend to decrease or stay at the similar levels at the constant operating speed because the rotor vibration converges to the steady-state with time. But the opposite phenomenon of increasing vibration at constant speed is normally observed in the rotor experiencing the Morton effect. The current test results show this vibration increase of the overhung end and bearing location at the constant speeds. In addition to the vibration change with rotor speeds, the temperatures of inlet/outlet oil temperatures and pad temperatures have been changed during the experiment. As the rotor speed increases, the temperatures of outlet oil and pads also increased due to the increased viscous heating in the journal. However, the inlet oil temperature has been maintained at the similar level during the whole testing using the oil cooling system. The control of inlet temperature is very important to accurately predict the Morton effect because the inlet oil temperature increase may induce the change in rotordynamic responses. The trend of the vibration increase at the 4,800 rpm is more clearly observed in the bode and 1x polar plots in Figure 6.10.

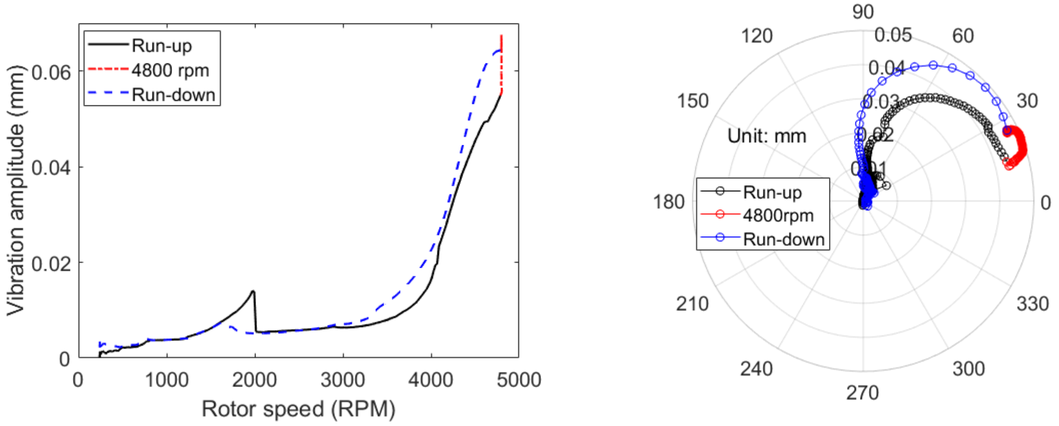

(a) (b)

Figure 6.10 (a) Bode (overhung end) and (b) 1x polar (bearing outboard X) plots for the first test (4,800 rpm)

In both figures of Figure 6.10 (a) and (b), the vibration increases until it reaches to the maximum operating speed of 4,800 rpm (black line). At the constant speed with red line, the vibration increases are seen to occur without changing operating speeds. The vibration level initially increases and decrease to the steady state position in the Figure 6.10 (a). Then the rotor speed was decreased to 240 rpm for 83 seconds, and the hysteresis vibration is shown during the run-down (blue line), where the vibration levels of the run-down are larger than those of the run-up. In the Figure 6.10 (b), the 1x polar plot also shows the phase changes of the bearing vibration (X direction) along with vibration amplitude changes at the constant speed (red line). These hysteresis phenomenon, vibration amplitude/phase changes at constant speed are normally observed in the rotor experiencing the Morton effect. Based on the vibration and temperature measurement results in Figure 6.9 and 6.10, it can be concluded that weak Morton effect is present in the tested rotor-bearing system.

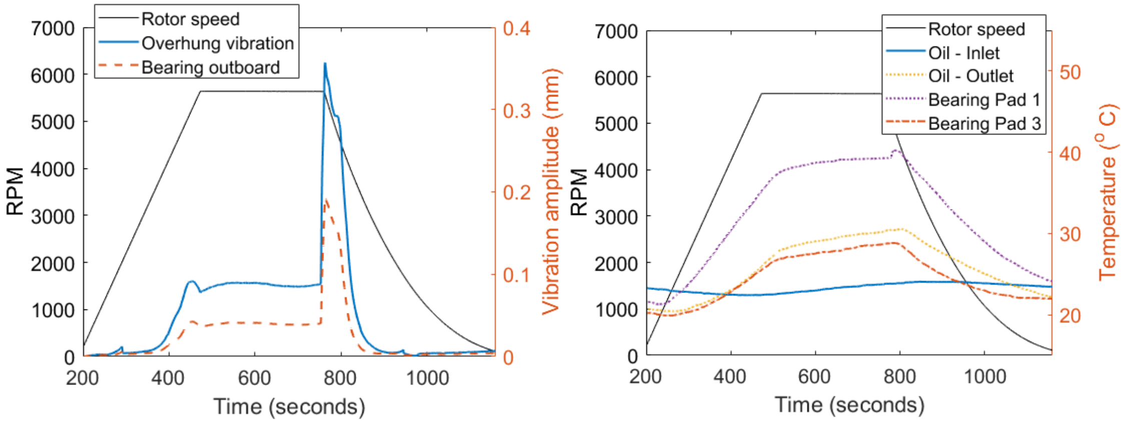

(a) (b)

Figure 6.11 (a) Rotor vibration amplitude and (b) temperatures of oil for the second test (5,640 rpm)

Second test has been conducted, and the maximum rotor speed was set to be 5,640 rpm in this case. The vibration and oil temperature changes during run-up/down and at 5,640 rpm are shown in Figure 6.11. At 5,640 rpm, the vibration amplitude of the overhung and bearing outboard locations changes with time, and the vibration level abruptly has increased to the high levels. The pk-pk vibration levels of the overhung end and bearing reach up to 0.3572mm and 0.1918mm, respectively. These vibration levels exceeded the trip level programmed in the rotor control system, and therefore the rotor spin speed was automatically decreased to 240rpm for about 359 seconds. The oil/pads temperatures at 5,640 rpm are also shown in Figure 6.11 (b). All oil and pad temperature values except the oil inlet increases at the speed and reaches to its maximum value at the timing when the rotor deceleration has started.

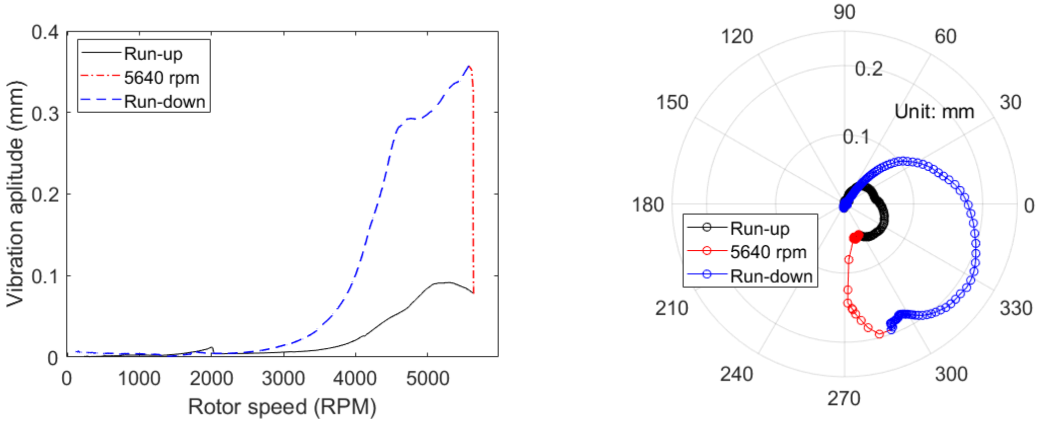

(a) (b)

Figure 6.12 (a) Bode (overhung end) and (b) 1x polar (bearing outboard X) plots for the second test (5,640 rpm)

The bode and 1x polar plots of the second test are shown in Figure 6.12. At 5,640 rpm with the red line in Figure 6.12 (a), the rotor vibration level increases from 0.077mm to 0.3572mm. In the rotor deceleration from 5,640 rpm to 240 rpm with blue line, large hysteresis phenomenon occurred at the vibration amplitudes in the run-down are much larger than the amplitude of the run-up. The vibration amplitude and phase changes are also represented in the 1x polar plot in Figure 6.12 (b).

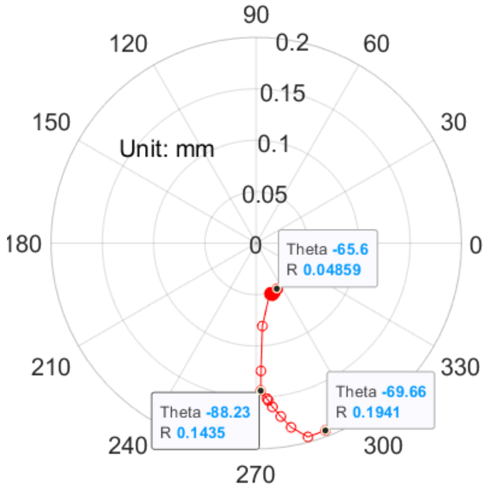

Figure 6.13 1x polar (bearing outboard X) plots at 5,640 rpm

To observe the changes in vibration amplitude and phase at the constant speed, the 1x polar plot is drawn only for the vibration measurement at 5,640rpm in Figure 6.13. At the point 1 in the figure, the vibration amplitude and phase are 0.048mm and -65.6°, respectively. At 756 seconds after the rotor starts (point 2), the vibration is measured, and its amplitude was increased from 0.048 mm to 0.143 mm. The phase also shifted from -65.6° to -88.2° during the testing. The vibration amplitude further increased to 0.194 mm after 762 seconds after the test starts, and the phase of the vibration also changed to -69.6° (point 3). These results clearly shows the vibration amplitude and phase changes at the constant speed of 5,640 rpm. The measured vibration at the three points are summarized in Table 6.6.

	Amplitude	**Phase**
Point 1 (422 Sec)	0.048 mm	-65.6°
Point 2 (756 Sec)	0.143 mm	-88.2°
Point 3 (762 Sec)	0.194 mm	-69.6°

Table 6.6 Vibration amplitude and phase changes at 5,640 rpm

Simulations have been conducted using the Morton effect codes developed in the previous sections, and its results are compared with the experimental results at 5,640 rpm in Figure 6.14. In the simulation, as similar to the measured data, vibration increase induced by the Morton effect was observed at 5,640 rpm as shown in the figure. However, the vibration increase was mainly observed right after when the rotor speed reaches to 5,640 rpm while the vibration change was observed after 3 minutes in the experimental measurement. The predicted maximum vibration amplitude at the rotor overhung end was 0.19mm, which was smaller than the measured maximum value of 0.35mm. The simulation results without Morton effect are also presented in the same figure for a comparison purpose. For the “exclude Morton effect case”, the induced thermal bow was set to be zero to exclude the effect from the thermal bow. In the figure, the “exclude Morton effect case” shows no noticeable vibration change at 5,640 rpm and maintains almost same vibration amplitude at the speed. These results confirms that the

Morton effect was the sole factor to induce the vibration changes in the simulation results of “include Morton effect” case.

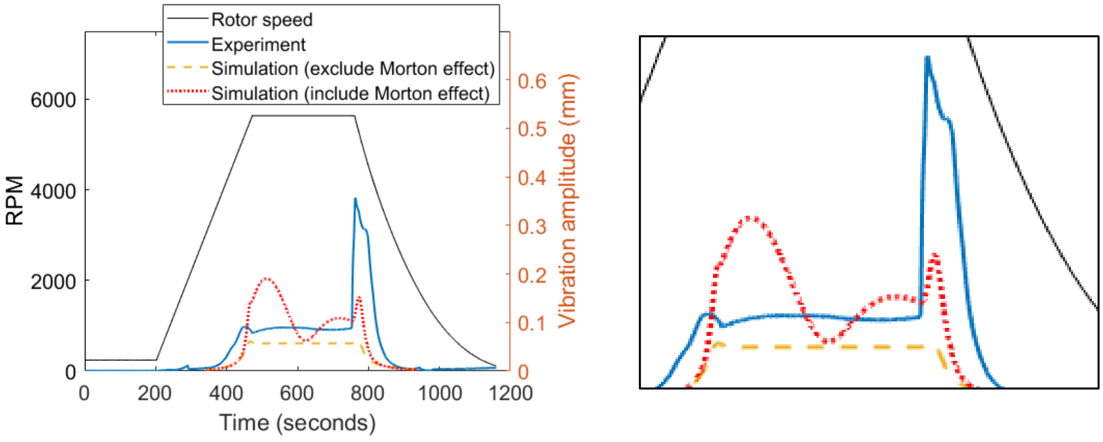

(a) (b)

Figure 6.14 (a) comparison between experimental measurements and simulation results (b) zoom of (a)

The vibration amplitudes of the rotor in rotor axial nodes with time are presented in Figure 6.15. Note that the vibration amplitudes at overhung end are largest among all rotor nodes. These results indicates that the induced large and fluctuating vibration is caused by the thermal bow effect induced at the overhung side of the rotor. The vibration amplitudes are also larger from 2 minutes to 8 minutes, which corresponds to the rotor operating speed of 5,640rpm.

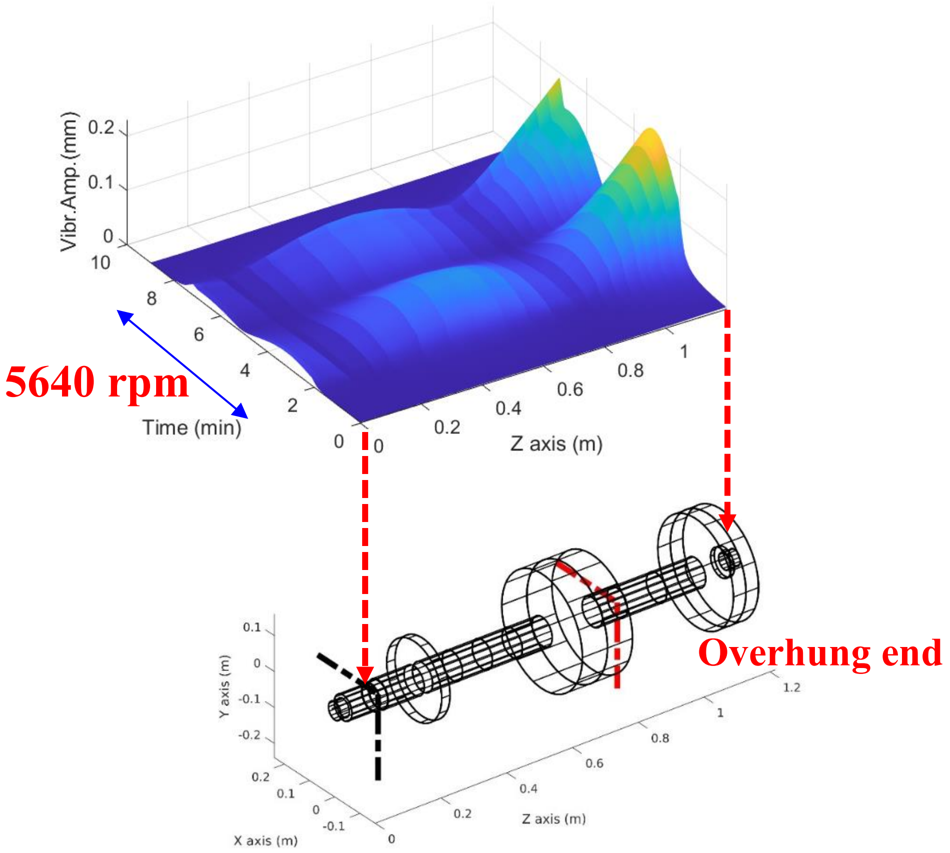

Figure 6.15 Simulated rotor vibration at each rotor node with time

Two measured vibration and oil/pad temperature values are presented. In both experiments, vibration amplitude and phase changes were observed. The hysteresis phenomena are also observed at both 4,800 rpm and 5,640 rpm. The hysteresis and spiral vibrations were more clearly observed at 5,640 rpm. These changing vibration amplitude/phase and hysteresis are the main characteristic of the rotor suffering from the Morton effect. Therefore, these results confirm that the tested rotor shows the thermal bow induced vibration problem (Morton effect). The simulations using the developed Morton effect codes have been conducted, and its results are compared with the measured data. Similar Morton effect vibrations have been observed in both cases, but the maximum vibration amplitude of the rotor overhung end was underpredicted compared to the measured vibration data. These discrepancy between the simulation and experiments may be caused from the unmodeled dynamics of rotor-bearing systems such as oil mixing coefficient, unknown unbalance amplitude/locations, inaccurate beam model, etc. The unknown parameters such as rotor unbalance distribution and journal misalignment should be also considered for better prediction results.

7. CONCLUSIONS

In Section 2, the nonlinear behavior and bifurcation of a geared rotor system supported by fluid film journal bearings were investigated employing a multiple shooting/continuation algorithm. Nonlinear effects included in the model are nonlinear fluid film force in journal bearing, gear backlash, and time-varying mesh stiffness. The present study confirms that the nonlinearities in a gear pair may induce nonlinear behaviors such as the jump phenomenon, co-existing responses, subharmonic resonances and chaotic responses in the five-degree-of-freedom, gear-journal bearing system model. The effect of the gear applied torque and journal bearing paramaters on the nonlinear phenomena were investigated. The simulation with varying gear input torque showed that the separation between jump-up and jump-down speed is reduced with high input torques. The high input torque also induced a hardening effect which is not observed in low torque values. It was also confirmed that as bearing L/D ratio and bearing lubricant viscosity are increased, or bearing clearances are decreased, the frequency where the gear nonlinearity-induced jump phenomenon occurs is lowered, and the number of multiple responses is increased, along with the double-sided contact of meshes. In addition, the influence of the input torque and journal bearing parameters on the subharmonic responses were investigated. The simulation results revealed that the high input torque gives rise to the hardening effect as well as the softening effect in the subharmonic resonance region. It is also shown that small bearing L/D ratio, lubricant viscosity and bearing clearance suppress the subharmonic resonances.

The impact of journal bearing parameters on the chaotic response were investigated via direct numerical integration, bifurcation diagrams, spectrums, Poincaré attractors and maximum Lyapunov exponents. As compared to the former studies, which used the linearized bearing stiffness and damping coefficients, the present study utilized the nonlinear journal bearing modeled with the finite element method. The results showed that the high-applied input torques to the gear suppress the chaotic response in the system. Chaotic motions and period-doubling bifurcations were observed at constant operating speed, as the value of lubricant viscosity and bearing clearance varied.

The effect of gear mesh stiffness on the oil whirl phenomenon of the journal bearing was also studied. Using the continuation algorithm, it was verified that the increased gear mesh stiffness delays the onset speed of oil whirl. In addition, the mesh stiffness effect on the oil whirl phenomenon was sensitive to the magnitude of the gear input torque, as the amount of the onset speed delay was found to be more significant with high input torques.

Future investigations for bifurcation and nonlinear dynamics of a gear supported by journal bearings will include thermal effect in the bearing lubricant, other types of hydrodynamic journal bearings such as pressure dam or tilting pad bearings. A more detailed gear-rotor model including a finite element shaft and a lubricant between gear meshes will also be developed. Experimental verification will be conducted to obtain validation results for the theoretical models.

Section 3 presents results of a study for the effects of bearing misalignment on the ME, utilizing high-fidelity rotordynamics and thermodynamics models, based on the 3D FEM. The following conclusions are made: (1) journal misalignment induces decreased film thickness and film thickness distribution asymmetry which increases the ME instability speed range ISR. Simulations for two rotor cases with different bearing clearances showed that the ISR was nearly invariant with respect to bearing radial clearance. It was also demonstrated that a rotor operating free from the ME may experience a ME instability if the journal becomes misaligned. (2) Severe ME instability was observed to occur when the misalignment ratio exceeded a certain amplitude ($r_m > 0.2$). High misalignment ratios ($r_m = 0.2\ and\ 0.3$) expanded the ME instability speed range and increased the ME severity. (3) Spherical pad-type pivot compensated the misalignment effect, as confirmed by the invariance of the ISR with misalignment ratio increase when spherical pivot models were included. The compensation effect was confirmed with the increased angular displacements of the pad rolling motions in accordance with the misalignment direction.

In section 4, the mitigation of the ME-induced vibration utilizing a squeeze film damper with a central groove has been presented. The ME model was benchmarked with an experimental result, and similar trends of spiral vibration were observed. However, the ME speed range and predicted vibration amplitudes depart from the experimental case under some conditions, due to un-modeled effects. The following conclusions are made based on convectional linear analysis and nonlinear transient ME simulations: (1) Based on conventional rotordynamic linear analysis, the SFD in series with the TPJB shifts the first forward critical speed of the overhung rotor. Mounting the SFD with low stiffness could raise the rotor's critical speed above the original one without SFD. However, this positive shift of critical speed could be unfavorably reduced if an improper SFD with a much higher stiffness is chosen. (2) The SFD with adequately designed parameters suppresses the ME-induced vibration. The cage stiffness of the SFD significantly affects the ME suppression capability of the SFD. In the current rotor-bearing-SFD case, a stiffer cage induces larger vibration at journal location in the linear unbalance response, which may cause increased viscous heating in a journal circumference and consequently more severe ME vibration in the nonlinear simulations. A cage stiffness of $1\times10^{8}\ N/m$ was shown to be optimal for suppressing the ME, compared with two other cases $4\times10^{8}\ N/m$ and $8\times10^{8}\ N/m$, for the particular rotor model presented. This may of course vary between machines considered. For comparison, the optimal cage stiffness was 25 % of the average x and y linear bearing stiffness values. (3) The installation of the cage stiffness without the SFD damping force was unable to control the ME vibration. The damping force from the SFD, along with the cage, increased the critical speed and suppressed the ME. (4) There exist optimal parameters for the SFD that offer the best suppression of the ME, and this is verified via the nonlinear ME simulations. Future work will include experimental verification of the ME suppression using the SFD with a central groove. SFD lubricant temperature variation and thermal conduction effect through SFD/TPJB housings will be considered in future work. In addition, an advanced optimization technique will be applied for the optimal SFD parameter identification to suppress the ME.

In section 5, nonlinear ME simulations are conducted to investigate the pivot design influences on the ME vibration. The rotor-bearing model is developed based on 3D FEM-based thermal and structural models, Reynolds equation, 3D Energy equation, and Euler beam model. The pivot design components such as the pivot type (cylindrical and spherical pivots), pivot flexibility, and pad-pivot friction are included in the TPJB models, and parametric studies have been carried out. The following conclusions are made based on the simulation results.

1) Spherical pivot type increases the minimum film thickness ratio and shows a better cooling effect compared with the cylindrical pivot type due to its pitching motion. This characteristic favorably works to avoid the rubbing effect when the ME occurs.
2) The pivot stiffness shifts the critical speed of the rotor as shown in the conventional linear rotor dynamic analysis. The critical speed change was more significant with the spherical pivot type compared with the cylindrical pivot due to its geometry.
3) The shift of the critical speed also affects the ME instability speed range, and it is demonstrated with the nonlinear transient ME analyses. With the shifted ME instability speed to the lower speed range, less severe ME vibration has been observed in general.
4) The pad-pivot friction in the spherical pivot shows a relatively suppressed vibration level compared with the case without the friction. The effect of the friction is over-predicted with the rigid pivot assumption. With the nonlinear pivot considering the

friction, the speed where maximum vibration level occurs has been shifted up with increasing friction coefficients.

5) The vibration reduction due to the pad-pivot friction does not occur monotonically with increasing friction coefficients, and there exists an optimal value of pad-pivot friction coefficients which effectively suppresses the ME vibration.

Future works include a more sophisticated prediction method of the friction coefficients between the pad and pivot using the finite element method. The effect of the pad's composite materials on the ME vibration will be also investigated. The experimental works to verify the numerical results will be conducted.

In the last section, the Morton effect test rig has been constructed and tested. The test has been conducted by increasing the rotor spin speed from 0 rpm to 5,600 rpm and 5,700 rpm. The vibration results show that the vibration increase at the rotor overhung end while the rotor operating speed is kept constant. The vibration phase also changes with time at the contact operating speed. Since vibration amplitude and phases changes at the constant operating speed are the main characteristics of the rotor experiencing Morton effect, the results from the test rig show the evidence of the Morton effect in the developed rotor-bearing test rig. Future works include the measurement of the journal temperature differential with a slip ring. The parameters and operating conditions such as unbalance, lubricant viscosity, supply oil temperature, etc. will be varied to investigate more obvious hysteresis effect and spiral vibrations.

REFERENCES

[1] Kahramant, A., and R. Sing. "Non-linear dynamics of a spur gear pair." Journal of Sound and Vibration (I990) 142, no. 1 (1990): 49-75.

[2] Kahraman, A., and R. Singh. "Non-linear dynamics of a geared rotor-bearing system with multiple clearances." Journal of Sound and Vibration 144, no. 3 (1991): 469-506.

[3] Karahman, A., and R. Singh. "Interactions between time-varying mesh stiffness and clearance nonlinearity in a gear pair." Journal of Sound and Vibration 146 (1991): 135-156.

[4] Blankenship, G. W., and A. Kahraman. "Steady state forced response of a mechanical oscillator with combined parametric excitation and clearance type non-linearity." Journal of Sound and Vibration 185, no. 5 (1995): 743-765.

[5] Kahraman, Ahmet, and G. Wesley Blankenship. "Interactions between commensurate parametric and forcing excitations in a system with clearance." Journal of Sound and Vibration 194, no. 3 (1996): 317-336.

[6] Kahraman, Ahmet, and G. Wesley Blankenship. "Experiments on nonlinear dynamic behavior of an oscillator with clearance and periodically time-varying parameters." Journal of Applied Mechanics 64, no. 1 (1997): 217-226.

[7] Raghothama, A., and S. Narayanan. "Bifurcation and chaos in geared rotor bearing system by incremental harmonic balance method." Journal of Sound and Vibration 226, no. 3 (1999): 469-492.

[8] Theodossiades, Stephanos, and Sotirios NATSIAVAS. "Non-linear dynamics of gear-pair systems with periodic stiffness and backlash." Journal of Sound and vibration 229, no. 2 (2000): 287-310.

[9] Al-Shyyab, A., and A. Kahraman. "Non-linear dynamic analysis of a multi-mesh gear train using multi-term harmonic balance method: period-one motions." Journal of Sound and Vibration 284, no. 1-2 (2005): 151-172.

[10] Al-Shyyab, A., and A. Kahraman. "Non-linear dynamic analysis of a multi-mesh gear train using multi-term harmonic balance method: sub-harmonic motions." Journal of Sound and Vibration 279, no. 1-2 (2005): 417-451.

[11] Zhou, Shihua, Jie Liu, Chaofeng Li, and Bangchun Wen. "Nonlinear behavior of a spur gear pair transmission system with backlash." Journal of Vibroengineering 16, no. 8 (2014): 3850-3861.

[12] Yang, Yi, Hang Li, and Yiping Dai. "Nonlinear vibration characteristics of spur gear system subjected to multiple harmonic excitations." Proceedings of the Institution of Mechanical Engineers, Part C: Journal of Mechanical Engineering Science 233, no. 17 (2019): 6026-6050.

[13] Yang, Yi, Mengjuan Xu, Yang Du, Pan Zhao, and Yiping Dai. "Dynamic analysis of nonlinear time-varying spur gear system subjected to multi-frequency excitation." Journal of Vibration and Control 25, no. 6 (2019): 1210-1226.

[14] Yang, Yi, Liyan Cao, Hang Li, and Yiping Dai. "Nonlinear dynamic response of a spur gear pair based on the modeling of periodic mesh stiffness and static transmission error." Applied Mathematical Modelling 72 (2019): 444-469.

[15] Wang, Zhong, Lei Zhang, Yuan-Qing Luo, and Chang-Zheng Chen. "Dynamic model of spur gear pair with modulation internal excitation." International Journal of Rotating Machinery (2017).

[16] Motahar, Habibollah, Farhad S. Samani, and Moslem Molaie. "Nonlinear vibration of the bevel gear with teeth profile modification." Nonlinear Dynamics 83, no. 4 (2016): 1875-1884.

[17] Yang, Junyi, and Teik Lim. "Dynamics of coupled nonlinear hypoid gear mesh and time-varying bearing stiffness systems." SAE International Journal of Passenger Cars-Mechanical Systems 4, no. 2011-01-1548 (2011): 1039-1049.

[18] Wang, Jun, and Teik C. Lim. "Effect of tooth mesh stiffness asymmetric nonlinearity for drive and coast sides on hypoid gear dynamics." Journal of Sound and Vibration 319, no. 3-5 (2009): 885-903.

[19] Ambarisha, Vijaya Kumar, and Robert G. Parker. "Nonlinear dynamics of planetary gears using analytical and finite element models." Journal of Sound and Vibration 302, no. 3 (2007): 577-595.

[20] Zhao, Mingming, and J. C. Ji. "Nonlinear torsional vibrations of a wind turbine gearbox." Applied Mathematical Modelling 39, no. 16 (2015): 4928-4950.

[21] Qiu, Xinghui, Qinkai Han, and Fulei Chu. "Investigation of parametric instability of the planetary gear under speed fluctuations." Shock and Vibration 2017 (2017).

[22] Gill-Jeong, Cheon. "Nonlinear behavior analysis of spur gear pairs with a one-way clutch." Journal of Sound and Vibration 301, no. 3-5 (2007): 760-776.

[23] Cheon, Gill-Jeong. "Numerical study on reducing the vibration of spur gear pairs with phasing." Journal of Sound and Vibration 329, no. 19 (2010): 3915-3927.

[24] Bonori, Giorgio, and Francesco Pellicano. "Non-smooth dynamics of spur gears with manufacturing errors." Journal of Sound and Vibration 306, no. 1-2 (2007): 271-283.

[25] Wei, S., Q. K. Han, X. J. Dong, Z. K. Peng, and F. L. Chu. "Dynamic response of a single-mesh gear system with periodic mesh stiffness and backlash nonlinearity under uncertainty." Nonlinear Dynamics 89, no. 1 (2017): 49-60.

[26] Kim, T. C., T. E. Rook, and R. Singh. "Effect of smoothening functions on the frequency response of an oscillator with clearance non-linearity." Journal of Sound and Vibration 263, no. 3 (2003): 665-678.

[27] Farshidianfar, Anoshirvan, and Amin Saghafi. "Global bifurcation and chaos analysis in nonlinear vibration of spur gear systems." Nonlinear Dynamics 75, no. 4 (2014): 783-806.

[28] Gou, Xiang-Feng, Ling-Yun Zhu, and Dai-Lin Chen. "Bifurcation and chaos analysis of spur gear pair in two-parameter plane." Nonlinear Dynamics 79, no. 3 (2015): 2225-2235.

[29] Li, Yinggang, Tianning Chen, and Xiaopeng Wang. "Non-linear dynamics of gear pair with dynamic backlash subjected to combined internal and external periodic excitations." Journal of Vibration and Control 22, no. 6 (2016): 1693-1703.

[30] Theodossiades, S., and S. Natsiavas. "On geared rotordynamic systems with oil journal bearings." Journal of Sound and Vibration 243, no. 4 (2001): 721-745.

[31] Baguet, Sébastien, and Guillaume Jacquenot. "Nonlinear couplings in a gear-shaft-bearing system." Mechanism and Machine Theory 45, no. 12 (2010): 1777-1796.

[32] Fargère, Romain, and Philippe Velex. "Influence of clearances and thermal effects on the dynamic behavior of gear-hydrodynamic journal bearing systems." Journal of Vibration and Acoustics 135, no. 6 (2013).

[33] Liu, Zhenxing, Zhansheng Liu, Jingming Zhao, and Guanghui Zhang. "Study on interactions between tooth backlash and journal bearing clearance nonlinearity in spur gear pair system." Mechanism and Machine Theory 107 (2017): 229-245.

[34] Kim, Sitae, and Alan B. Palazzolo. "Shooting With Deflation Algorithm-Based Nonlinear Response and Neimark-Sacker Bifurcation and Chaos in Floating Ring Bearing Systems." Journal of Computational and Nonlinear Dynamics 12, no. 3 (2017).

[35] Kim, Sitae, and Alan B. Palazzolo. "Effects of thermo hydrodynamic (THD) floating ring bearing model on rotordynamic bifurcation." International Journal of Non-Linear Mechanics 95 (2017): 30-41.

[36] Kim, Sitae, and Alan B. Palazzolo. "Bifurcation analysis of a rotor supported by five-pad tilting pad journal bearings using numerical continuation." Journal of Tribology 140, no. 2 (2018).

[37] Tong, Xiaomeng, Alan Palazzolo, and Junho Suh. "A Review of the Rotordynamic Thermally Induced Synchronous Instability (Morton) Effect." Applied Mechanics Reviews 69, no. 6 (2017).

[38] Jongh, Frits M. De, and Pieter Van Der Hoeven. "Application Of A Heat Barrier Sleeve To Prevent Synchronous Rotor Instability." In Proceedings of the 27th

Turbomachinery Symposium. Texas A&M University. Turbomachinery Laboratories, 1998.

[39] Keogh, P. S., and P. G. Morton. "The dynamic nature of rotor thermal bending due to unsteady lubricant shearing within a bearing." Proceedings of the Royal Society of London. Series A: Mathematical and Physical Sciences 445, no. 1924 (1994): 273-290.

[40] Lee, Jung Gu, and Alan Palazzolo. "Morton effect cyclic vibration amplitude determination for tilt pad bearing supported machinery." Journal of Tribology 135, no. 1 (2013).

[41] Suh, Junho, and Alan Palazzolo. "Three-dimensional dynamic model of TEHD tilting-pad journal bearing—part I: theoretical modeling." Journal of Tribology 137, no. 4 (2015).

[42] Suh, Junho, and Alan Palazzolo. "Three-dimensional dynamic model of TEHD tilting-pad journal bearing—Part II: Parametric studies." Journal of Tribology 137, no. 4 (2015).

[43] Suh, Junho, and Alan Palazzolo. "Three-Dimensional Thermohydrodynamic Morton Effect Simulation—Part I: Theoretical Model." Journal of Tribology 136, no. 3 (2014).

[44] Suh, Junho, and Alan Palazzolo. "Three-Dimensional Thermohydrodynamic Morton Effect Analysis—Part II: Parametric Studies." Journal of Tribology 136, no. 3 (2014).

[45] Tong, Xiaomeng, Alan Palazzolo, and Junho Suh. "Rotordynamic Morton effect simulation with transient, thermal shaft bow." Journal of Tribology 138, no. 3 (2016).

[46] Tong, Xiaomeng, and Alan Palazzolo. "Double Overhung Disk and Parameter Effect on Rotordynamic Synchronous Instability—Morton Effect—Part I: Theory and Modeling Approach." Journal of Tribology 139, no. 1 (2017).

[47] Tong, Xiaomeng, and Alan Palazzolo. "Double Overhung Disk and Parameter Effect on Rotordynamic Synchronous Instability—Morton Effect—Part II: Occurrence and Prevention." Journal of Tribology 139, no. 1 (2017).

[48] Tong, Xiaomeng, and Alan Palazzolo. "Measurement and prediction of the journal circumferential temperature distribution for the rotordynamic Morton effect." Journal of Tribology, 140, no. 3 (2018).

[49] Tong, Xiaomeng, and Alan Palazzolo. "Tilting pad gas bearing induced thermal bow-rotor instability (Morton effect)." Tribology International 121 (2018): 269-279.

[50] Bouyer, J., and M. Fillon. "An experimental analysis of misalignment effects on hydrodynamic plain journal bearing performances." Journal of Tribology, 124, no. 2 (2002): 313-319.

[51] Sun, Jun, and Gui Changlin. "Hydrodynamic lubrication analysis of journal bearing considering misalignment caused by shaft deformation." Tribology International, 37, no. 10 (2004): 841-848.

[52] El-Butch, A. M., and N. M. Ashour. "Transient analysis of misaligned elastic tilting-pad journal bearing." Tribology International 38, no. 1 (2005): 41-48.

[53] Sun, Jun, Mei Deng, Yonghong Fu, and Changlin Gui. "Thermohydrodynamic lubrication analysis of misaligned plain journal bearing with rough surface." Journal of Tribology, 132, no. 1 (2010).

[54] Xu, Guohui, Jian Zhou, Haipeng Geng, Mingjian Lu, Lihua Yang, and Lie Yu. "Research on the static and dynamic characteristics of misaligned journal bearing considering the turbulent and thermohydrodynamic effects." Journal of Tribology, 137, no. 2 (2015).

[55] Suh, Junho, and Yeon-Sun Choi. "Pivot design and angular misalignment effects on tilting pad journal bearing characteristics: Four pads for load on pad configuration." Tribology International 102 (2016): 580-599.

[56] Leader, Malcolm E., John K. Whalen, Godfrey G. Grey, and Thomas D. Hess. "The Design And Application Of A Squeeze Film Damper Bearing To A Flexible Steam Turbine Rotor." In Proceedings of the 24th Turbomachinery Symposium. Texas A&M University. Turbomachinery Laboratories, 1995.

[57] Edney, Stephen L., and John C. Nicholas. "Retrofitting A Large Steam Turbine With A Mechanically Centered Squeeze Film Damper." In Proceedings of the 28th Turbomachinery Symposium. Texas A&M University. Turbomachinery Laboratories, 1999.

[58] Kanki, H., Y. Kaneko, M. Kurosawa, and T. Yamamoto. "Prevention of low-frequency vibration of high-capacity steam turbine units by squeeze-film damper." Journal of Engineering for Gas Turbines and Power 120, no. 2 (1998).

[59] Ferraro, Riccardo, Michael Catanzaro, Jongsoo Kim, Michela Massini, Davide Betti, and Richard Livermore-Hardy. "Suppression of Subsynchronous Vibrations in a 11 MW Steam Turbine Using Integral Squeeze Film Damper Technology at the Exhaust Side Bearing." In Turbo Expo: Power for Land, Sea, and Air, vol. 49835, p. V07AT30A011. American Society of Mechanical Engineers, 2016.

[60] Ertas, Bugra, Vaclav Cerny, Jongsoo Kim, and Vaclav Polreich. "Stabilizing a 46 MW multistage utility steam turbine using integral squeeze film bearing support dampers." Journal of Engineering for Gas Turbines and Power 137, no. 5 (2015).

[61] Barrett, L. E., E. J. Gunter, and P. E. Allaire. "Optimum bearing and support damping for unbalance response and stability of rotating machinery." Journal of Engineering for Gas Turbines and Power 100, no. 1 (1978).

[62] Chu, Fulei, and Roy Holmes. "The damping capacity of the squeeze film damper in suppressing vibration of a rotating assembly." Tribology International 33, no. 2 (2000): 81-97.

[63] San Andres, L. A., and J. M. Vance. "Experimental measurement of the dynamic pressure distribution in a squeeze-film bearing damper executing circular-centered orbit." ASLE Transactions 30, no. 3 (1987): 373-383.

[64] Lund, Jørgen W., Claus M. Myllerup, and Henning Hartmann. "Inertia effects in squeeze-film damper bearings generated by circumferential oil supply groove." Journal of Vibration and Acoustics. 125, no. 4 (2003): 495-499.

[65] Kim, Keun-Joo, and Chong-Won Lee. "Dynamic characteristics of sealed squeeze film damper with a central feeding groove." Journal of Tribology, 127, no. 1 (2005): 103-111.

[66] San Andrés, Luis. "Damping and inertia coefficients for two open ends squeeze film dampers with a central groove: measurements and predictions." Journal of Engineering for Gas Turbines and Power 134, no. 10 (2012).

[67] San Andrés, Luis, and Sanjeev Seshagiri. "Damping and inertia coefficients for two end sealed squeeze film dampers with a central groove: measurements and predictions." Journal of Engineering for Gas Turbines and Power 135, no. 11 (2013).

[68] San Andrés, Luis, Sung-Hwa Jeung, and Gary Bradley. "Experimental Performance of an Open Ends, Centrally Grooved, Squeeze Film Damper Operating With Large Amplitude Orbital Motions." In Turbo Expo: Power for Land, Sea, and Air, vol. 45776, p. V07BT32A005. American Society of Mechanical Engineers, 2014.

[69] Delgado, Adolfo, and Luis San Andrés. "A model for improved prediction of force coefficients in grooved squeeze film dampers and oil seal rings." Journal of Tribology 132, no. 3 (2010).

[70] Andrés, Luis San, and Adolfo Delgado. "A novel bulk-flow model for improved predictions of force coefficients in grooved oil seals operating eccentrically." Journal of Engineering for Gas Turbines and Power 134, no. 5 (2012).

[71] Kang, Xiao. "Simulation and Test of the Auxiliary Bearings and Their Dampers in Magnetic Bearing Systems." Ph.D. Dissertation, Texas A&M University, College Station, TX, 2019.

[72] Bonello, Philip, Michael J. Brennan, and Roy Holmes. "A study of the nonlinear interaction between an eccentric squeeze film damper and an unbalanced flexible rotor." Journal of Engineering for Gas Turbines and Power 126, no. 4 (2004): 855-866.

[73] He, Feng. "Forced Response with Stability of Flexible Rotor-Bearing Systems with Squeeze Film Dampers." Ph.D. Dissertation, University of Virginia, Charlottesville, VA, 2013.

[74] Cao, Jianming, Paul Allaire, and Timothy Dimond. "Coupled lateral and torsional nonlinear transient rotor–bearing system analysis with applications." Journal of Dynamic Systems, Measurement, and Control 137, no. 9 (2015).

[75] San Andrés, Luis, and Yujiao Tao. "The role of pivot stiffness on the dynamic force coefficients of tilting pad journal bearings." In Turbo Expo: Power for Land, Sea, and Air, vol. 55270, p. V07BT30A013. American Society of Mechanical Engineers, 2013.

[76] Dang, Phuoc Vinh, Steven Chatterton, and Paolo Pennacchi. "The Effect of the Pivot Stiffness on the Performances of Five-Pad Tilting Pad Bearings." Lubricants 7, no. 7 (2019): 61.

[77] Childs, Dara, and Joel Harris. "Static performance characteristics and rotordynamic coefficients for a four-pad ball-in-socket tilting pad journal bearing." Journal of Engineering for Gas Turbines and Power 131, no. 6 (2009).

[78] Kulhanek, Chris D., and Dara W. Childs. "Measured Static and Rotordynamic Coefficient Results for a Rocker-Pivot, Tilting-Pad Bearing With 50 and 60% Offsets." Journal of Engineering for Gas Turbines and Power 134, no. 5 (2012).

[79] Mehdi, Syed Muntazir, Kyung Eun Jang, and Tae Ho Kim. "Effects of pivot design on performance of tilting pad journal bearings." Tribology International 119 (2018): 175-189.

[80] Young, Warren Clarence, Richard Gordon Budynas, and Ali M. Sadegh. Roark's formulas for stress and strain. Vol. 7. New York: McGraw-Hill, 2002.

[81] Kirk, R. G., and S. W. Reedy. "Evaluation of pivot stiffness for typical tilting-pad journal bearing designs." Journal of Vibration and Acoustics 110, no. 2 (1988).

[82] Nicholas, John C., and Karl D. Wygant. "Tilting Pad Journal Bearing Pivot Design For High Load Applications." In Proceedings of the 24th turbomachinery symposium. Texas A&M University. Turbomachinery Laboratories, 1995.

[83] Shi, Zhaoyang, Yingze Jin, and Xiaoyang Yuan. "Influence of pivot design on nonlinear dynamic analysis of vertical and horizontal rotors in tilting pad journal bearings." Tribology International 140 (2019): 105859.

[84] Wygant, Karl D., Ronald D. Flack, and Lloyd E. Barrett. "Influence of pad pivot friction on tilting-pad journal bearing measurements—Part I: steady operating position©." Tribology Transactions 42, no. 1 (1999): 210-215.

[85] Wygant, Karl D., Lloyd E. Barrett, and Ronald D. Flack. "Influence of pad pivot friction on tilting-pad journal bearing measurements—Part II: dynamic coefficients©." Tribology Transactions 42, no. 1 (1999): 250-256.

[86] Pettinato, Brian, and Pranabesh De Choudhury. "Test Results of Key and Spherical Pivot Five-Shoe Tilt Pad Journal Bearings—Part I: Performance Measurements." Tribology Transactions 42, no. 3 (1999): 541-547.

[87] Pettinato, Brian, and Pranabesh De Choudhury. "Test results of key and spherical pivot five-shoe tilt pad journal bearings—part II: dynamic measurements." Tribology Transactions 42, no. 3 (1999): 675-680.

[88] Sabnavis, Giridhar. "Test Results for Shaft Tracking Behavior of Pads in a Spherical Pivot Type Tilting Pad Journal Bearing." Ph.D. Dissertation, University of Virginia, Charlottesville, VA, 2005.

[89] Kim, Sung-Gi, and Kyung-Woong Kim. "Influence of pad–pivot friction on tilting pad journal bearing." Tribology International 41, no. 8 (2008): 694-703.

[90] He, Feng. "Including Pivot Friction in Pad Motion for a Tilting Pad Journal Bearing With Ball-Socket Pivots." In Turbo Expo: Power for Land, Sea, and Air, vol. 50923, p. V07AT34A036. American Society of Mechanical Engineers, 2017.

[91] Kim, Sitae, and Alan B. Palazzolo. "Pad-Pivot Friction Effect on Nonlinear Response of a Rotor Supported by Tilting-Pad Journal Bearings." Journal of Tribology (2019): 1-21.

[92] Lu X, Khonsari MM, Gelink ER. The Stribeck curve: experimental results and theoretical prediction. Journal of Tribology (2006): 128(4): 789-94.

[93] D. Shin, A. Palazzolo, Multiple steay state response solver for nonlinear gear, bearing and mafunction simulation, Texas A&M University, College Station, TX, USA, Techincal report no. TRC-400124-00073 (2017)

[94] Nayfeh, Ali H., and Balakumar Balachandran. Applied nonlinear dynamics: analytical, computational, and experimental methods. John Wiley & Sons, 2008.

[95] Ma, Qinglong, and A. Kahraman. "Subharmonic resonances of a mechanical oscillator with periodically time-varying, piecewise-nonlinear stiffness." Journal of Sound and Vibration 294, no. 3 (2006): 624-636.

[96] Wang, Jun, Teik C. Lim, and Mingfeng Li. "Dynamics of a hypoid gear pair considering the effects of time-varying mesh parameters and backlash nonlinearity." Journal of Sound and Vibration 308, no. 1-2 (2007): 302-329.

[97] Bonori, Giorgio, and Francesco Pellicano. "Non-smooth dynamics of spur gears with manufacturing errors." Journal of Sound and Vibration 306, no. 1-2 (2007): 271-283.

[98] Theodossiades, S., and S. Natsiavas. "On geared rotordynamic systems with oil journal bearings." Journal of Sound and Vibration 243, no. 4 (2001): 721-745.

[99] Xiang, Ling, Yi Jia, and Aijun Hu. "Bifurcation and chaos analysis for multi-freedom gear-bearing system with time-varying stiffness." Applied Mathematical Modelling 40, no. 23-24 (2016): 10506-10520.

[100] Zhou, Shihua, Guiqiu Song, Mengnan Sun, and Zhaohui Ren. "Nonlinear dynamic response analysis on gear-rotor-bearing transmission system." Journal of Vibration and Control 24, no. 9 (2018): 1632-1651.

[101] Das, Santanu, S. K. Guha, and A. K. Chattopadhyay. "On the steady-state performance of misaligned hydrodynamic journal bearings lubricated with micropolar fluids." Tribology International 35, no. 4 (2002): 201-210.

[102] Ebrat, Omidreza, Zissimos P. Mourelatos, Nickolas Vlahopoulos, and Kumar Vaidyanathan. "Calculation of journal bearing dynamic characteristics including journal

misalignment and bearing structural deformation©." Tribology Transactions 47, no. 1 (2004): 94-102.

[103] Ahmed, A. M., and A. El-Shafei. "Effect of misalignment on the characteristics of journal bearings." Journal of Engineering for gas Turbines and Power 130, no. 4 (2008).

[104] Lee, Donghyun, Kyung Ho Sun, Byungock Kim, and Donghyuk Kang. "Thermal behavior of a worn tilting pad journal bearing: Thermohydrodynamic analysis and pad temperature measurement." Tribology Transactions 61, no. 6 (2018): 1074-1083.

[105] Sim, Kyuho, and Daejong Kim. "Thermohydrodynamic analysis of compliant flexure pivot tilting pad gas bearings." Journal of Engineering for Gas Turbines and Power 130, no. 3 (2008).

[106] Khonsari, Michael M., and E. Richard Booser. Applied tribology: bearing design and lubrication. John Wiley & Sons, 2017.

[107] Heinrich, J. C., P. S. Huyakorn, O. C. Zienkiewicz, and A. R. Mitchell. "An'upwind'finite element scheme for two-dimensional convective transport equation." IJNME 11, no. 1 (1977): 131-143. https://doi.org/10.1002/nme.1620110113

[108] Keogh, P. S., and P. G. Morton. "The dynamic nature of rotor thermal bending due to unsteady lubricant shearing within a bearing." Proceedings of the Royal Society of London. Series A: Mathematical and Physical Sciences 445, no. 1924 (1994): 273-290.

[109] ISO 286-1. "ISO system of limits and fits–Part1: bases of tolerances, deviations and fits." (1988).

[110] Zeidan, Fouad Y., Luis San Andres, and John M. Vance. "Design And Application Of Squeeze Film Dampers In Rotating Machinery." In Proceedings of the 25th Turbomachinery Symposium. Texas A&M University. Turbomachinery Laboratories, 1996.

[111] De Jongh, F. M., and P. G. Morton. "The synchronous instability of a compressor rotor due to bearing journal differential heating." Journal of Engineering for Gas Turbines and Power 118, no. 4 (1996).

[112] Kocur, J. A., and F. M. De Jongh. "Thermal Rotor Instability in Gas Compressors." In Proceedings of the XIV International Gas Convention, Caracas, Venezuela. 2000.

[113] Panara, Daniele, Leonardo Baldassarre, Duccio Griffin, Alessandro Mattana, Simone Panconi, and Enrico Meli. "Numerical prediction and experimental validation of rotor thermal instability." In Proceedings of the 44th Turbomachinery Symposium. Turbomachinery Laboratories, Texas A&M Engineering Experiment Station, 2015.

[114] Yang, Jongin, and Alan Palazzolo. "Three-Dimensional Thermo-Elasto-Hydrodynamic Computational Fluid Dynamics Model of a Tilting Pad Journal Bearing—Part I: Static Response." Journal of Tribology 141, no. 6 (2019).

[115] Yang, Jongin, and Alan Palazzolo. "Three-Dimensional Thermo-Elasto-Hydrodynamic Computational Fluid Dynamics Model of a Tilting Pad Journal Bearing—Part II: Dynamic Response." Journal of Tribology 141, no. 6 (2019).

[116] Yang, Jongin, and Alan Palazzolo. "Computational Fluid Dynamics Based Mixing Prediction for Tilt Pad Journal Bearing TEHD Modeling—Part I: TEHD-CFD Model Validation and Improvements." Journal of Tribology 143, no. 1 (2020).

[117] Yang, Jongin, and Alan Palazzolo. "Computational Fluid Dynamics Based Mixing Prediction for Tilt Pad Journal Bearing TEHD Modeling—Part II: Implementation With Machine Learning." Journal of Tribology 143, no. 1 (2020).

[118] Oh, Joseph, Alan Palazzolo, and Lingnan Hu. "Stability of Non-Axisymmetric Rotor and Bearing Systems Modeled With Three-Dimensional-Solid Finite Elements." Journal of Vibration and Acoustics 142, no. 1 (2020).

[119] Oh, Joseph, Baik Jin Kim, and Alan Palazzolo. "3D Solid Finite Element Contact Model for Rotordynamic Analysis: Experiment and Simulation." Journal of Vibration and Acoustics (2020): 1-41.